

UNIVERSITY OF WOLLONGONG

DOCTORAL THESIS

**Constraining natural contributions to
tropospheric ozone production over
Australia and selected areas of the
Southern Ocean**

Author:
Jesse GREENSLADE

Supervisors:
Jenny Fisher
Clare Murphy

*A thesis submitted in fulfillment of the requirements
for the degree of Doctor of Philosophy
in the*

*Centre of Atmospheric Chemistry
School of Earth, Atmospheric, and Life Sciences*

June 28, 2019

Declaration of Authorship

I, Jesse GREENSLADE, declare that this thesis titled, "Constraining natural contributions to tropospheric ozone production over Australia and selected areas of the Southern Ocean" and the work presented in it are my own. I confirm that:

- This work was done wholly or mainly while in candidature for a research degree at this University.
- Where any part of this thesis has previously been submitted for a degree or any other qualification at this University or any other institution, this has been clearly stated.
- Where I have consulted the published work of others, this is always clearly attributed.
- Where I have quoted from the work of others, the source is always given. With the exception of such quotations, this thesis is entirely my own work.
- I have acknowledged all main sources of help.
- Where the thesis is based on work done by myself jointly with others, I have made clear exactly what was done by others and what I have contributed myself.

Signed:

Date:

“Thanks to my solid academic training, today I can write hundreds of words on virtually any topic without possessing a shred of information, which is how I got a good job in journalism.”

Dave Barry

UNIVERSITY OF WOLLONGONG

Abstract

Science Medicine And Health
School of Earth, Atmospheric, and Life Sciences

Doctor of Philosophy

**Constraining natural contributions to tropospheric ozone production over
Australia and selected areas of the Southern Ocean**

by Jesse GREENSLADE

Jenny Comment: I would prefer each of these 3 main paragraphs to be a super-mini version of the main chapters, with one-two sentences each for: intro/context; what you did, what you found, what makes it meaningful/important.

Ozone in the troposphere is a toxic pollutant which causes respiratory and agricultural damage. The two main sources are chemical production, and transport from the stratosphere. Chemical production can occur following biogenic emissions of volatile organic compounds (BVOCs) when they mix with polluted urban air. Most tropospheric ozone is formed through chemical reactions involving nitrogen oxides, the hydroxy radical, and volatile organic compounds (such as isoprene). Contributions to ozone levels in the troposphere over Australia are highly uncertain, affecting our ability to model important atmospheric processes. Isoprene, formaldehyde, and ozone in the troposphere are linked by oxidative chemistry and are all important to air quality, climate, and radiation budgets. This thesis has three aims: to quantify formaldehyde amounts over Australia observed by satellite using a global CTM (GEOS-Chem), to determine Australian isoprene emissions using modelled isoprene-to-formaldehyde yields along with satellite formaldehyde amounts, and to attribute ozone in the troposphere to the contributions from chemical production and stratospheric transport. Model and observations are combined for each aim in this thesis.

To quantify isoprene emissions (the dominant BVOC), formaldehyde (one of the main products of isoprene oxidation) is used as a proxy. Formaldehyde observed by satellite over Australia is calculated based on modelled a priori vertical distributions using a CTM and a radiative transfer model. In order to compare satellite formaldehyde products against models or other measurements, corrections are required to remove the influence of the a priori profile. Impacts on formaldehyde levels from anthropogenic and pyrogenic sources are determined and filtered out to determine the biogenic footprint and minimise bias in isoprene emissions quantification.

Isoprene is predominantly emitted by trees and shrubs, and Eucalypts are potentially very high emitters. Subsequent oxidation reactions form formaldehyde which has a sufficiently short lifetime in the atmosphere to establish chemical equilibrium. Using a simple linear model and assuming minimal transport and a chemical steady state allows an estimate of the yield of formaldehyde from isoprene emissions. This yield is modelled over Australia and then applied to the recalculated satellite formaldehyde to create a new estimate of Australian isoprene emissions. This technique is used to improve isoprene emissions estimates without extensive measurement campaigns. Results are compared against existing measurement campaigns for validation and analysis. Isoprene emissions from Australian forests are found to be substantially lower than previous estimates have predicted.

The second most abundant source of tropospheric ozone is the stratosphere, which occasionally mixes into the troposphere bringing ozone-rich air masses down towards the earth's surface. Analysing the local weather patterns and ozone seasonality, most transport is found to occur during low pressure frontal weather systems. This work provides a novel technique using a mathematical (Fourier band-pass) filter on ozonesonde profiles for estimation and quantification of tropospheric ozone transported from the stratosphere. An estimate encompassing three measurement stations over the Southern Ocean near Australia of about 7.2×10^{17} molec cm⁻² per year is derived.

Overall, this work improves knowledge of tropospheric ozone and its sources for Australia.

Acknowledgements

Thanks to my supervisor Jenny Fisher, the whole Atmospheric Chemistry team at Wollongong who made me feel at home: Beata, Clare Murphy, Dagmar, Doreena, Elise, Joel, Kaitlyn, Max, Nick Deutscher, Nicholas Jones, Ruhi, Stephen Wilson, and Voltaire.

Contents

Declaration of Authorship	iii
Abstract	viii
Acknowledgements	xi
1 Introduction and Literature Review	1
1.1 The atmosphere	1
1.1.1 Structure	1
1.1.2 Composition and chemistry	2
1.2 Ozone	3
1.2.1 Stratospheric ozone	3
1.2.2 Tropospheric ozone	4
1.2.2.1 Stratosphere to troposphere transport	6
1.2.2.2 Chemical production	6
1.3 Volatile Organic Compounds	8
1.3.1 Emissions	10
1.3.2 Isoprene	11
1.3.3 Isoprene chemistry	12
1.3.3.1 High NO _x pathway	13
1.3.3.2 Low NO _x pathway	14
1.3.3.3 Night time processes	14
1.3.4 Radiative Forcing	15
1.4 Formaldehyde	15
1.4.1 Sources and sinks	17
1.4.2 Measurement techniques	18
1.4.2.1 Satellite measurements	19
1.5 Atmospheric Chemistry Modelling	20
1.5.1 Box models	21
1.5.2 Chemical transport models	21
1.5.3 Emissions	23
1.5.4 Uncertainties	23
1.5.4.1 Emissions Inventories	23
1.5.4.2 Resolution	24
1.5.4.3 Chemistry mechanisms	24
1.5.4.4 Clouds	25
1.6 Australia and the southern hemisphere	25
1.6.1 Ozone	25
1.6.2 Biogenic VOCs	26

1.7 Aims	28
2 Data and Modelling	31
2.1 Introduction	31
2.2 Datasets	32
2.2.1 Satellite	32
2.2.1.1 Formaldehyde	33
2.2.1.2 Nitrogen dioxide	34
2.2.1.3 Aerosol optical depth	36
2.2.1.4 Active fires	36
2.2.1.5 Carbon monoxide	36
2.2.1.6 Uncertainties	36
2.2.2 Model datasets	37
2.2.2.1 GEOS-Chem output	37
2.2.2.2 Meteorological reanalysis	37
2.2.2.3 Surface temperatures	38
2.2.3 Campaign datasets	38
2.2.3.1 Measurements of Urban, Marine and Biogenic Air (MUMBA) .	38
2.2.3.2 Sydney Particle Studies (SPS1, SPS2)	41
2.2.3.3 Ozonesondes	43
2.2.3.4 Wollongong	43
2.2.3.5 Uncertainties	44
2.3 Satellite formaldehyde	46
2.3.1 Pixel filtering	48
2.3.2 DOAS	50
2.3.3 Air mass factor (AMF)	52
2.3.4 LIDORT	53
2.3.5 Uncertainty	53
2.4 GEOS-Chem	55
2.4.1 Overview	55
2.4.2 Installing and running GEOS-Chem	56
2.4.3 Chemical Mechanism	56
2.4.4 GEOS-Chem isoprene	58
2.4.4.1 Oxidation	59
2.4.4.2 Nitrogen oxide impacts	59
2.4.4.3 OH	60
2.4.5 Emissions from MEGAN	60
2.4.6 Nitrogen oxides	62
2.4.7 GEOS-Chem simulations	63
2.4.7.1 GEOS-Chem outputs	63
2.4.7.2 GEOS-Chem runs	67
2.4.7.3 UCX vs tropchem	68
2.5 Calculating new AMF	74
2.6 Recalculation of OMI HCHO	76
2.6.1 Outline	77
2.6.2 Creating new shape factors	78
2.6.3 Creating new AMF using GEOS-Chem	79

2.6.3.1	Updating shape factors	79
2.6.3.2	Recalculating the AMF using PP code	79
2.6.3.3	Saving the AMF with satellite pixels	80
2.6.4	Vertical columns from AMF	80
2.6.5	Reference sector correction	80
2.6.6	Corrected vertical columns	84
2.6.7	Binning the results daily	84
2.6.8	Difference between original and corrected OMI HCHO columns	86
2.7	Filtering Data	89
2.7.1	Pyrogenic filter	89
2.7.2	Anthropogenic filter	95
2.7.3	Smearing filter	100
2.7.3.1	Calculation of smearing	100
2.7.3.2	NO_x dependence	104
2.8	Relationship between temperature and HCHO	104
2.9	Process schematic	107
2.10	Data Access	113
3	Biogenic Isoprene emissions in Australia	117
3.1	Introduction	117
3.1.1	Aims	118
3.1.2	Existing emissions estimates	118
3.1.3	Top-down isoprene emissions estimates	119
3.1.3.1	Bayesian inversion	119
3.1.3.2	Linear inversion	120
3.2	Methods	121
3.2.1	Outline	121
3.2.2	Masks and reprocessed satellite HCHO	122
3.2.3	GEOS-Chem emissions	124
3.2.4	Relationship between isoprene emissions and formaldehyde	124
3.2.5	Calculation of modelled slope	126
3.2.6	Modelled background HCHO	128
3.2.7	Calculation of Emissions	128
3.2.8	Sensitivity to smearing	132
3.2.8.1	Modelled HCHO lifetimes	132
3.2.9	Running GEOS-Chem using a posteriori emissions	134
3.2.10	Conversion to emissions by kg	136
3.3	Results	136
3.3.1	A posteriori emissions	136
3.3.1.1	Diurnal emissions	143
3.3.1.2	Trends	144
3.3.2	Modelled impacts of reduced isoprene emissions	147
3.3.2.1	Implications for HCHO	147
3.3.2.2	Implications for ozone	147
3.3.3	Comparison with in situ measurements	153
3.4	Uncertainty	157
3.4.1	Top down emissions	159

3.4.2	Model Uncertainty	160
3.4.3	Satellite Uncertainty	163
3.4.4	Sensitivity to AMF recalculation	169
3.4.5	Sensitivity to filtering	169
3.5	Conclusions and implications	171
4	Stratospheric ozone intrusions	175
4.1	Foreword	175
4.2	Introduction	175
4.3	Data and Methods	177
4.3.1	Ozonesonde record in the Southern Ocean	177
4.3.2	Model description	181
4.3.3	Characterisation of STT events and associated fluxes	181
4.3.4	Biomass burning influence	183
4.3.5	Classifying synoptic conditions during STT events	184
4.4	STT event climatologies	185
4.5	Simulated ozone columns	188
4.6	Stratosphere-to-troposphere ozone flux from STT events	192
4.6.1	Method	192
4.6.2	Results	194
4.6.3	Comparison to literature	199
4.7	Sensitivities and limitations	200
4.7.1	Event detection	200
4.7.2	Flux calculations	200
4.8	Conclusions	202
4.9	Contributions and Acknowledgements	203
5	Summary and Concluding remarks	205
5.1	Outcomes	205
5.2	Isoprene emissions	206
5.3	Ozone over Australia	206
5.4	Outputs	208
5.5	Future work	210
Bibliography		213

List of Figures

1.1 Pressure (red) logarithmically decreasing, shown with percentage of atmosphere below at several points. Temperature (green) changes throughout the atmosphere. Figure modified from https://climate.ncsu.edu/edu/Structure	2
1.2 Tropospheric ozone processes, Figure 1 in Young et al. (2017). DOI: https://doi.org/10.1525/elementa.265.f1	5
1.3 NO - NO ₂ - O ₃ photoequilibrium cycle without and with (A, B respectively) influence from VOCs. Figure reproduced from Atkinson (2000).	8
1.4 Dependence of ozone production rate on NO _x and VOC concentrations reproduced from Mazzuca et al. (2016).	9
1.5 Simplified isoprene products following oxidation by OH, reproduced from Mao et al. (2013).	12
1.6 The overall radiative forcings and uncertainties of several atmospheric constituents This is an image taken from Stocker et al. (IPCC, 2013: <i>Climate Change 2013: The Physical Science Basis. Contribution of Working Group I to the Fifth Assessment Report of the Intergovernmental Panel on Climate Change</i>), chapter 8.	16
1.7 HCHO spectrum, with a typical band of wavelengths used for DOAS path measurements. Reproduced from Davenport et al. (2015).	19
1.8 An example spectrum showing absorption features used for species concentration measurements by GOME-2. Image reproduced from EU-METSAT and ESA (EUMETSAT 2015).	20
1.9 Standard box model parameters, reproduced from Jacob (1999).	22
1.10 Forest types in Australia reproduced from http://www.agriculture.gov.au/abares/forestsaustralia/australias-forests	27
1.11 Global and Australian isoprene emission factors modified from Guenther et al. (2006).	27
2.1 Example of NO ₂ tropospheric columns taken from the OMNO2d product.	34
2.2 Average 2005 tropospheric NO ₂ from OMNO2d with pixels screened for < 30% cloud cover.	35
2.3 CPC daily maximum temperature dataset output for 1, Jan, 2005.	38
2.4 Locations of VOC measurements (top panel) and ozonesonde release sites (bottom panel). Inlaid in top panel is the flight paths over Australia of the HIPPO campaign.	39

2.5	Top: MUMBA, SPS1, and SPS2 time-series for HCHO (orange) and isoprene (magenta), along with detection limits (dashed). Bottom: isoprene measurements superimposed onto a single year.	40
2.6	SPS HCHO (yellow) and isoprene (green) time series, along with detection limits (dashed). SPS 1 (left) took place in late summer 2011, while SPS 2 (right) occurred during autumn 2012.	42
2.7	Mean midday FTIR profile (x_{ret}) and a priori profile (x_{apri}). Shaded area shows the inter-quartile range over the same time period. Profile is averaged between November 2007 to April 2013.	44
2.8	Left panel shows the mean midday (13:00 - 14:00 local time) total column averaging kernel, along with the inter-quartile range (IQR) between November 2007 and April 2013. Right panel shows the mean averaging kernel for the vertical profile over the same time period, coloured by vertical level. One in six vertical levels are labelled and plotted with a solid line, the rest are shown with dashed lines. The x-axes are unitless in the two plots shown here.	45
2.9	Figure 1 and Table 1 from Schenkeveld et al. (2017), with the following caption “An impression of OMI flying over the Earth. The spectrum of a ground pixel is projected on the wavelength dimension of the charge-coupled device (CCD; the columns). The cross-track ground pixels are projected on the swath dimension of the CCD (the rows). The forward speed of 7 km s^{-1} and an exposure time of 2 s lead to a ground pixel size of 13 km in the flight direction. The viewing angle of 114° leads to a swath width on the ground of 2600 km.” The table shows the optical properties for OMIs three channels.	47
2.10	Solar and viewing zenith angles, image copied from Wikipedia (2016), originally from a NASA website.	48
2.11	HCHO Column amount histograms for a subset of OMI swaths over Australia on the 18th of March 2013. Negative entries are shown in the left panel, positive in the right. Note the different scale between negative and positive panels.	51
2.12	Top row shows $0.25^\circ \times 0.3125^\circ$ binned OMHCHO columns with one day, one month, and one month with non-biogenic masking applied from left to right respectively. Bottom row shows the uncertainty for each grid square after averaging.	54
2.13	MEGAN schematic, from http://lar.wsu.edu/megan/	61
2.14	Left to right columns show tropospheric NO_2 columns (Ω_{NO_2} ; molec cm^{-2}) from GEOS-Chem (GC), OMNO2d (OMI), and the differences. Each row shows one season from 2005, the left two columns use the left colour scale, while the third column uses the right colour scale.	64
2.15	Left and right columns show anthropogenic and soil emissions of NO respectively from GEOS-Chem in molec $\text{cm}^{-2} \text{s}^{-1}$. Each row shows one season from 2005. Anthropogenic and soil emissions use a logarithmic and linear colour scale respectively.	65

2.16	The first column shows the scatter plots of tropospheric NO ₂ columns between GEOS-Chem (y-axis) and OMNO2d (x-axis) at 2° × 2.5°. The reduced major axis linear regression is drawn in red, and the equation, regression coefficient (r), and number of grid squares (n) used is inlaid as a legend. The second and third columns show the scatter between emissions and the bias between GEOS-Chem and OMNO2d (GC-OMI), for anthropogenic and soil emissions respectively. These two columns share the far right axis; however, emissions are from anthropogenic and soil sources respectively. All scatter points are coloured by the sum of anthropogenic and soil NO emissions (from GEOS-chem), as per the colour bar shown at the bottom.	66
2.17	Surface HCHO simulated by GEOS-Chem with UCX (A: top left), and without UCX (B: top right), along with their absolute and relative differences (bottom left, right respectively). Amounts are the average of all times between 1 Jan and 28 Feb 2007.	69
2.18	As Figure 2.17 using total column amounts instead of surface concentrations.	70
2.19	As Figure 2.17, except showing isoprene surface concentrations.	71
2.20	As Figure 2.19, except showing isoprene total column amounts.	72
2.21	Total column ozone simulated by GEOS-Chem with UCX (A: top left), and without UCX (B: top right), along with their absolute and relative differences (bottom left, right respectively). Amounts are the average of all times between 1 Jan and 28 Feb 2007.	73
2.22	Top row: averaged OMI Satellite AMF for 2005, from the OMHCHO data set (left, AMF_{OMI}), recalculated using GEOS-Chem shape factors (middle, AMF_{GC}), and recalculated using GEOS-Chem shape factors and scattering weights (right, AMF_{PP}). Middle row: AMF time series over 2005 for each recalculation. Bottom row: AMF frequency distributions over January and February. Oceanic pixels are filtered out, only land pixels are included in this figure.	81
2.23	Example of remote Pacific RSC using 8-day average measurements and one month modelled data. <i>OMIVC</i> shows the uncorrected vertical columns, while <i>Corrected</i> shows the corrected vertical columns. OMI corrections shows the correction applied globally based on latitude and OMI track number(sensor). Ω_{GC} shows the GEOS-Chem modelled HCHO VC over the reference sector (region within black vertical lines), with Ω_{VCC} showing the corrected VC over the same area.	83
2.24	Example of track correction interpolations for January 1st 2005, points represent the difference between satellite slant column measurements and modelled slant columns over the remote Pacific.	85
2.25	Row 1: regridded corrected Ω_{HCHO} from OMHCHO on January 1, 2005: original (left), recalculated using new shape factors (middle), and additionally using updated scattering weights (right). Row 2: shows the monthly average for January 2005. Row 3: shows the distribution over the month for each of the three column amounts. Distribution bins are logarithmic, resulting in wider bins for higher column amounts.	87

2.26	Monthly pixel counts over Australia (non-oceanic) used in recalculations of vertical columns. N_{GC} refers to the number of pixels used in AMF recalculation without running code from Paul Palmer, N_{PP} refers to those which have been recalculated using their code. Filters applied are described in Section 2.7,	88
2.27	Top row: averaged OMI Satellite VCC for 2005, from the OMHCHO data set (left, VCC_{OMI}), recalculated using GEOS-Chem shape factors (middle, VCC_{GC}), and recalculated using GEOS-Chem shape factors and scattering weights (right, VCC_{PP}). Middle row: VCC time series over 2005 for each recalculation. Bottom row: VCC frequency distributions over January and February. Oceanic pixels are filtered out, only land pixels are included in this figure.	90
2.28	Top row shows grid squares filtered out by anthropogenic (left) and pyrogenic (right) influence masks over 2005. Bottom row shows portion of Australian grid squares filtered out each day.	91
2.29	Recalculated OMI vertical HCHO columns and pixel counts for January 2005. Column 1: VCC_{PP} amounts after applying the active fire filter. The filter is applied at $0.25^\circ \times 0.3125^\circ$ resolution, before output is averaged into $2^\circ \times 2.5^\circ$ bins. Column 2: Pixel counts after applying the active fire filter (summed into $0.25^\circ \times 0.3125^\circ$ bins). Row 1-4: increasing number of prior days which have active fires are included when masking fire influence. The first row shows the values without applying any active fire filter. The average and maximum VCC column amount (at $0.25^\circ \times 0.3125^\circ$ resolution), and number of pixels, is inset as text in column 1 of each row.	93
2.30	AAOD from OMAERUVd (columns 1, 2, 3) over Australia for four different scenarios (rows 1-4). Black Saturday (row 2) demarks the occurrence of widespread bush fires across Victoria. The transported plume in row three can be seen in the overlaid AOD shown in the last column, Indonesia (northwards from Darwin) suffered from wide-spread forest fires around this time. Scenes in the final column are created using the EOS Worldview website https://worldview.earthdata.nasa.gov/ from satellite products provided therein. AAOD = 0.03 is demarked by a horizontal line in the density plots in column 3. Density plots show normalised AAOD frequencies (scale not shown).	94
2.31	Top: percentage of pixels filtered out by fire and smoke masks in 2005 (left) and 2012 (right). Bottom: percentage filtered out each day from land squares in Australia for the two years shown.	96
2.32	Top: gas fields and pipelines (2018) for Australia (http://www.ga.gov.au/scientific-topics/energy/resources/petroleum-resources/gas). Bottom: petrol Well locations over Australia (as of 2018) (http://dbforms.ga.gov.au/www/npm.well.search).	97
2.33	Forest coverage, coloured by predominant tree species.	98

2.34 Mean (top left) and standard deviation (top right) of OMNO2d daily $0.25^\circ \times 0.25^\circ$ tropospheric cloud filtered NO ₂ columns. Time series for Australia, and each region (by colour) shown in the bottom panel, with mean for that region shown on the right. The grey shaded area depicts the 25th to 75th percentiles of Australia averaged NO ₂ columns for each day in the time series, with a thicker black line showing the Australia-wide mean value.	99
2.35 Top row: 2005 OMNO2d NO ₂ column mean before (left) and after (right) applying the threshold filters as described in the text. Bottom row: time series for Australia, and each region (by colour) shown in the bottom panel, with mean for that region shown on the right. The time series before (left) and after (right) applying the anthropogenic filter are shown, the dashed and dotted horizontal lines show daily and yearly mean thresholds respectively.	101
2.36 2005 OMNO2d NO ₂ column means (top left) and distributions (top right) for Australia, and each region shown in the area map (by colour). Vertical dashed lines show the threshold for anthropogenic influence, any columns above this value are filtered out. The vertical axis is normalised so that area under the curve adds up to unity, and as such is not important except as a visual measure of the relative width between the distributions.	102
2.37 Top: OMNO2d tropospheric NO ₂ columns averaged into $2^\circ \times 2.5^\circ$ horizontal bins for Jan, 2005. Bottom: Scatter plot of NO ₂ against smearing calculations from GEOS-Chem (\hat{S}), with points above and below the smearing threshold range of 800-4600 s coloured red and blue respectively. Points are binned by NO ₂ with and without the smearing filter applied (orange and magenta respectively). Overplotted is the mean and standard deviation (error bars) within each bin. Due to the logarithmic Y scale we only show the positive direction of standard deviations for unfiltered data.	106
2.38 Top row (left): surface temperature averaged over January and February 2005. Top row (right): correlation between spatially averaged GEOS-Chem temperatures and recalculated satellite vertical columns. Second row: GEOS-Chem surface temperatures correlated against GEOS-Chem HCHO, with different colours for each grid box, and black showing the spatially averaged correlation over time. Third row: as second row, except GEOS-Chem HCHO comes from the biogenic emissions only simulation. A reduced major axis regression is used within each gridbox using daily overpass time surface temperature and HCHO. The distribution of slopes (solid) and regression correlation coefficients (dashed) for the exponential regressions is shown in the inset panels in rows 2 and 3.	108
2.39 As Figure 2.38 but for northern Australia.	109
2.40 As Figure 2.38 but for south-western Australia. TODO: Fix y axis in subplot 322	110

2.41	Surface HCHO from GEOS-Chem overpass output (midday) on the Y axis vs surface temperatures at midday (T_{GC}) and vs maximum daily temperatures from the CPC data set (T_{CPC}). Top row: Sydney grid square scatter plot and regression with one data point for each day in the summer of 2005-2006. Bottom row: as top row except averaging over several grid boxes covering south eastern Australia (SEA: 37°S to 29°S, 146°E to 153.5°W). Grid squares with pyrogenic influence detected are removed (prior to any averaging) in the right column.	111
2.42	OMI recalculated vertical columns of HCHO on the Y axis vs surface temperatures at midday (T_{GC}) and vs maximum daily temperatures from the CPC data set (T_{CPC}). Top row: Sydney grid square scatter plot and regression with one data point for each day in the summer of 2005-2006. Bottom row: as top row except averaging over several grid boxes covering south eastern Australia (SEA: 37°S to 29°S, 146°E to 153.5°W). Grid squares with pyrogenic influence detected are removed (prior to any averaging) in the right column.	112
2.43	Flow diagram showing how OMHCHO level two swath data is read, processed, and gridded in this thesis.	114
3.1	Top-down isoprene emissions estimate formation using OMHCHORP and GEOS-Chem outputs.	123
3.2	Top left: RMA slope between modelled tropospheric column HCHO and isoprene emissions (E_{GC}) using midday (13:00-14:00 LT) values over for January 2005, per grid square at $2^\circ \times 2.5^\circ$ horizontal resolution. Top right: Squared RMA correlation coefficient for regression in top left. Bottom: Sample of correlations from four grid squares. Coloured dots in top panels correspond to the colour of the regressions shown in bottom panel.	127
3.3	Row 1: monthly slope along with 95% confidence interval both before (left) and after (right) applying the smear filter for the model grid square containing Sydney over 2005-2012. Limits used in creation of the smear filter are shown with dashed lines. Row 2: regression coefficient and data-point counts for slope shown in row 1. Additionally limits for r and n used in slope utilisation (see text) are shown with dashed lines. Row 3: slope and confidence interval using the multi-year dataset for each month. Row 4: regression coefficient and data-point counts for row 3.	129
3.4	Top left: Background total column HCHO based on longitudinally averaged values over the remote Pacific Ocean. Top right: Background total column HCHO based on GEOS-Chem output with isoprene emissions set to zero. Bottom left: Distributions of column amounts over land squares in Australia from the two background definitions and the monthly HCHO average from GEOS-Chem (standard tropchem run). Bottom right: Absolute difference between the two background defined value maps.	130

3.5	Top row: isoprene emissions from GEOS-Chem (a priori, left) simulation and top-down (a posteriori, right) calculations averaged over the month of January, 2005. Bottom row: the absolute (left) and relative (right) differences between the two.	131
3.6	Seasonally averaged smearing (\hat{S} , see text) over 2005. Diamonds represent grid squares which have had at least 10 (pink) or 30 (red) days removed due to the smearing filter over the season. Red crosses show where the filter has removed all data.	133
3.7	Monthly area averaged HCHO lifetime (τ in hours), with IQR shaded. Solid lines show lifetime assuming yield is 0.2, and 0.4 (higher and lower lines respectively). Coloured by regions shown in Figure 3.10.	134
3.8	Row 1: α for the average January (left) and June (right) over 2005-2012. Row 2: a priori (magenta, left axis), a posteriori (cyan, left axis), and α (black, right axis) multi-year monthly averages calculated for Sydney. Row 3: Monthly averages of the same terms in Row 2.	135
3.9	Total daily isoprene emissions (in kg) is represented by the area under the sine wave.	136
3.10	Sub-regions used in subsequent figures: Northern, North Eastern, South Eastern, South Western, and Middle. Australia-wide averages will be black or grey, while averages from within the coloured rectangles will match the colour shown here.	137
3.11	Row 1: Biogenic emissions of isoprene from GEOS-Chem (a priori, E_{GC}). Row 2: Emissions calculated using the OMI top down inversion (a posteriori, E_{OMI}). Row 3: Absolute differences between the first two rows. Midday emissions are averaged for each season (DJF, MAM, JJA, SON), and colours represent averaged areas from subregions shown in Figure 3.10. Grey dashed horizontal bars are added highlighting the scale between rows.	138
3.12	Regional multi-year seasonal mean a priori emissions (magenta) compared to a posteriori emissions (cyan). Error bars show the regionally averaged uncertainty. Additional horizontal dashes show the uncertainty plus effects from potential HCHO biases (discussed in Section 3.4.1) from satellite underestimation (40%) and monthly clear sky overestimation (13%).	139
3.13	The multi-year monthly mean (lines) and IQR (shaded) of midday (13:00-14:00 LT) isoprene emissions estimates. A priori emissions are shown by the dashed lines and hatched shaded areas show the IQR. A posteriori emissions are shown using the solid lines, with IQR shown by unhatched shaded areas. Colours denote the region over which the monthly average was taken, as in Figure 3.10.	141

3.14 Scatter plot of a priori emissions against a posteriori using monthly averaged grid squares as regression datapoints. Data points are created using monthly averages (of midday emissions) for each grid box for each month of summer (DJF) within each region shown. Multiple years of data are used, meaning if a region has 10 grid boxes, the 8 years of data will add up to 10 boxes \times 3 months \times 8 years = 240 data points minus filtered and zero emission squares. Plots are coloured by regions matching those shown in Figure 3.10. The linear best fit regression is inset into each plot along with the line equation and regression coefficient. The normalised distribution of each population is shown at the top and right spine of each subplot, with the right spine (facing the a priori axis) using the a priori axis and scale, and the top spine using the a posteriori axis and scale.	142
3.15 Top row: multi-year mean a priori emissions in Tg yr ⁻¹ from E_{GC} (GEOS-Chem; running MEGAN) and E_{OMI} (top-down emissions) respectively. E_{OMI} uses an assumed sinusoidal daily cycle, with daylight hours prescribed for each month: see Section 3.2.10). Bottom left and right show the absolute and relative differences, respectively.	143
3.16 The diurnal cycle of GEOS-Chem a priori emissions (solid line) averaged by month into hourly bins over from 2005 to 2013 are shown against top-down a posteriori (dashed line) emissions. Standard deviations for the monthly average are shaded for the a priori, and shown with error bars at 13:30 LT for the a posteriori. Top down emissions shown here are based on monthly midday emissions being the peak of a sine wave which drops to zero after and before daylight hours (see Section 3.2.10).	145
3.17 A priori (row 1) and a posteriori (row 2) emissions anomaly from multyear monthly mean, split by region (see Figure 3.10).	146
3.18 Daily mean total column HCHO amounts from GEOS-Chem with a priori (new emissions run) and a posteriori (tropchem run) a posteriori scaled isoprene emissions, along with the recalculated OMI HCHO columns. Each row shows the average over regions in Figure 3.10.	148
3.19 Total column HCHO before (left) and after (middle) scaling isoprene emissions, and their relative differences (right). Top row shows summer (DJF) averaged total columns, while bottom row shows the winter (JJA).	149
3.20 Regionally and seasonally averaged HCHO total columns from GEOS-Chem and recalculated OMI measurements side by side. Each row represents one region within Australia, while each column represents from left to right: summer, autumn, winter, spring. Standard deviations are shown with error bars.	150
3.21 Monthly averaged HCHO profile over Wollongong modelled by GEOS-Chem before (VMR) and after (VMR ^a) scaling isoprene emissions. Shaded areas represent the inter-quartile range over the month.	151
3.22 Surface ozone concentrations (ppb) per region over 2005. Concentrations are shown using the left axis, and absolute differences (tropchem run - scaled run) shown in grey using the right axis.	152

3.23 Surface (up to ~ 150 m) ozone before (left) and after (middle) scaling isoprene emissions, and their relative differences (right). Top row shows summer (DJF) averaged total columns, while bottom row shows the winter (JJA).	153
3.24 GEOS-Chem grid box ($2^\circ \times 2.5^\circ$) containing Wollongong FTIR, SPS, and MUMBA campaign data.	154
3.25 SPS1, SPS2, and MUMBA (left to right columns respectively) midday (13:00-14:00 local time) measurements of isoprene, HCHO, and ozone (top to bottom rows respectively). Shown in magenta and brown are the a priori and a posteriori GEOS-Chem surface outputs for the matching grid square at midday for days containing measurements.	156
3.26 Multi-year (from all days where both measurements and model data exist) monthly mean total column (Ω) HCHO from the FTIR instrument, and the colocated convolved GEOS-Chem equivalent before (Ω_{GC}) and after (Ω_{GC}^a) scaling isoprene emissions. Shaded areas show inter quartile range.	158
3.27 Median and inter-quartile range of multi-year monthly relative uncertainty in the a posteriori. Median relative uncertainty in S and Ω are added as dashed and dotted lines respectively.	161
3.28 Summer (DJF, top row) and winter (JJA, bottom row) a posteriori emissions (left column) and relative error (right column).	162
3.29 Median and inter-quartile range of monthly binned uncertainty in S	164
3.30 Mean and standard deviation (vertical error bars) of total pixel counts per region per season, before (magenta) and after (cyan) applying smearing, pyrogenic, and anthropogenic filters.	166
3.31 Median and inter-quartile range for monthly binned relative uncertainty in satellite vertical columns.	168
3.32 Top row: averaged OMI Satellite AMF for 2005, from the OMHCHO data set (left, AMF_{OMI}), recalculated using GEOS-Chem shape factors (middle, AMF_{GC}), and recalculated using GEOS-Chem shape factors and scattering weights (right, AMF_{PP}). Middle row: mean and inter-quartile range over 2005 for each season. Bottom row: mean and inter-quartile range of non-zero emissions based on the three recalculations (with matching subscripts) next to the a priori emissions from GEOS-Chem.	170
3.33 Multi-year monthly mean values for a posteriori emission estimates calculated with (solid) and without (dashed) applying filters for anthropogenic, pyrogenic, and smearing influences. The portion of pixels within each region which are filtered is shown on the right axis with a blue dotted line.	171
4.1 Ozonesonde release sites and the regions used to examine STT effect on tropospheric ozone levels.	178

4.2	Multi-year monthly median tropopause altitude (using the ozone defined tropopause) determined from ozonesondes measurements at Davis (2006-2013), Macquarie Island (2004-2013), and Melbourne (2004-2013) (solid lines). Dashed lines show the 10th to the 90th percentile of tropopause altitude for each site.	179
4.3	Multi-year mean seasonal cycle of ozone mixing ratio over Davis, Macquarie Island, and Melbourne as measured by ozonesondes. Measurements were interpolated to every 100 m and then binned monthly. Black and red solid lines show median ozone and lapse-rate defined tropopause altitudes (respectively), as defined in the text.	180
4.4	An example of the STT identification and flux estimation methods used in this work. The left panel shows an ozone profile from Melbourne on 8 January 2004 from 2 km to the tropopause (blue dashed horizontal line). The right panel shows the perturbation profile created from bandpass filtering of the mixing ratio profile. The STT occurrence threshold calculated from the 95th percentile of all perturbation profiles is shown as the orange dashed line, and the vertical extent of the event is shown with the purple dashed lines (see details in text). The ozone flux associated with the STT event is calculated using the area outlined with the orange dashed line in the left panel.	182
4.5	Seasonal cycle of STT event frequency at Davis (top), Macquarie Island (middle), and Melbourne (bottom). Events are categorised by associated meteorological conditions as described in the text, with low pressure fronts ("frontal") in dark blue, cut-off low pressure systems ("cut-off") in teal, and indeterminate meteorology ("misc") in cyan. Events that may have been influenced by transported smoke plumes are shown in red (see text for details).	186
4.6	Seasonal distribution of STT events using the alternative STT proxy, obtained from consideration of the static stability at the ozone and lapse rate tropopauses, for Davis (2006-2013), Macquarie Island (2004-2013), and Melbourne (2004-2013).	187
4.7	The distribution of STT events' altitudes at Davis (top), Macquarie Island (middle), and Melbourne (bottom), determined as described in the text. Events are coloured as described in Fig. 4.5.	188
4.8	The distribution of STT events' depths, defined as the distance from the event to the tropopause, at Davis (top), Macquarie Island (middle), and Melbourne (bottom), determined as described in the text. Events are coloured as described in Fig. 4.5.	189
4.9	Comparison between observed (black) and simulated (pink, red) tropospheric ozone columns (Ω_{O_3} , in molecules cm ⁻²) from 1 January 2004 to 30 April 2013. For the model, daily output is shown in pink, while output from days with ozonesonde measurements are shown in red. For each site, the model has been sampled in the relevant grid square.	190

4.10 Observed and simulated tropospheric ozone profiles over Davis, Macquarie Island, and Melbourne, averaged seasonally. Model medians (2005-2013 average) are shown as red solid lines, with red dashed lines showing the 10th and 90th percentiles. Ozonesonde medians (over each season, for all years) are shown as black solid lines, with coloured shaded areas showing the 10th and 90th percentiles. The horizontal dashed lines show the median tropopause heights from the model (red) and the observations (black).	191
4.11 Example comparisons of ozone profiles from ozonesondes (black) and GEOS-Chem (red) from three different dates during which STT events were detected from the measurements. The dates were picked based on subjective visual analysis. The examples show the best match between model and observations for each site. GEOS-Chem and ozonesonde pressure levels are marked with red and black dashes respectively.	193
4.12 Top panel: tropospheric ozone attributed to STT events. Bottom panel: percent of total tropospheric column ozone attributed to STT events. Boxes show the inter-quartile range (IQR), with the centre line being the median, whiskers show the minimum and maximum, circles show values which lie more than 1.5 IQR from the median. Values calculated from ozonesonde measurements as described in the text.	195
4.13 (Top) Tropospheric ozone, (<i>I</i>)mpact per event, and (<i>P</i>)robability of event detection per sonde launch, averaged over the region above Davis. The tropospheric ozone column Ω_{O_3} (black, left axis) is from GEOS-Chem, while the STT probability P (magenta, right axis) and impact I (teal, right axis) are from the ozonesonde measurements. The STT impact is multiplied by ten to better show the seasonality. (Bottom) Estimated contribution of STT to tropospheric ozone columns over the region, with uncertainty (shaded area) estimated as outlined in Sect. 4.7. The black line shows STT ozone flux if event lifetime is assumed to be two days, with dashed lines showing the range of flux estimation if we assumed events lasted from one day to one week.	196
4.14 As described in 4.13, for the region containing Macquarie Island.	197
4.15 As described in 4.13, for the region containing Melbourne.	198
5.1 Top row: ozone maps before (left) and after (right) scaling isoprene emissions in GEOS-Chem for summer. Middle row: absolute (left) and relative (right) differences. The bottom panel shows the linear regression between the runs along with a black dashed line representing the 1-1 ratio.	207
5.2 Sub-regions used in subsequent figures. Australia-wide averages will be black or grey, while results from within the coloured rectangles will match the colours shown here.	209

List of Tables

2.1	Detection limits for MUMBA	41
2.2	OMI quality flag values table from Kurosu and Chance (2014)	49
2.3	Species or classes from the GEOS-Chem mechanism.	58
2.4	Satellite pixels remaining after filtering by active fires, smoke, and anthropogenic masking. In parenthesis are the portion of pixels filtered. . .	91
2.5	NO_2 averages (molec $\text{cm}^{-2} \times 10^{14}$) by region before and after filtering for anthropogenic emissions using 2005 data from the OMNO2d product.	100
2.6	Smearing filters or typical slopes (S) from literature.	104
2.7	Isoprene to HCHO yields and lifetime.	105
3.1	Isoprene emissions (Tg/yr) from Australia	144
3.2	Yearly trend in surface amounts (ppbvC) before and after scaling isoprene emissions.	146
3.3	Campaign measurements compared to model output [ppb].	155
3.4	Mean total column HCHO amounts in 10^{15} molec cm^{-2}	157
3.5	Relative uncertainty estimates.	159
3.6	Uncertainties in satellite total column HCHO.	167
4.1	Number of sonde releases at each site over the period of analysis.	178
4.2	Total number of ozonesonde detected STT events, along with the number of events in each category (see text).	185
4.3	Seasonal STT ozone contribution in the regions near each site, in $\text{kg km}^{-2} \text{ month}^{-1}$. In parentheses are the relative uncertainties.	199
5.1	Isoprene emissions from MEGAN and top-down estimation in Tg a^{-1} , along with ozone tropospheric column amounts in $\text{O}_3 \text{ cm}^{-2} \times 10^{17}$	208

List of Abbreviations

ACCMIP	Atmospheric Chemistry and Climate Model Inter-comparison Project
AAOD	Aerosol Absorption Optical Depth
AMF	Air Mass Factor
AOD	Aerosol Optical Depth
BVOC	Biogenic Volatile Organic Compound
CCD	Charged Coupled Device spectrometer
CPC	Climate Prediction Center
CTM	Chemical Transport Model
DOAS	Differential Optical Absorption Spectroscopy
ECMWF	European Centre for Medium-range Weather Forecasts
EDGAR	Emission Database for Global Atmospheric Research
ERA-I	ECMWF ReAnalysis (Interim)
GC-FID	Gas Chromatographer Flame Ionisation Detector
FTIR	Fourier transform Infra-Red spectrometer
GEOS	Goddard Earth Observing System
GMAO	Global Modeling and Assimilation Office
GOME	Global Ozone Monitoring Experiment
GPH	GeoPotential Height
HEMCO	Harvard-NASA Emissions Component
IQR	Inter-Quartile Range
LAI	Leaf Area Index
LT	Local Time
OMHCHO	OMI satellite HCHO product
OMHCHORP	OMI satellite HCHO product re-processed
OMI	Ozone Monitoring Instrument
MEGAN	Model of Emissions of Gases and Aerosols from Nature
MUMBA	Measurements of Urban, Marine, and Biogenic Air
NCO	National Computing Infrastructure
NDACC	Network for the Detection of Atmospheric Composition Change
NH	Northern Hemisphere
NMVOC	Non-Methane Volatile Organic Compound
(S,P)OA	(Secondary, Primary) Organic Aerosols
OMR	Ozone Mixing Ratio
PAN	PeroxyAcetyl Nitrate
PFT	Plant Functional Type
PM	Particulate Matter
PTR-MS	Proton-Transfer-Reaction Mass spectrometer
PV	Potential Vorticity
RA	Row Anomaly

RF	Radiative Forcing
RMA	Reduced Major Axis
RMSA	Root Mean Square Error
RSC	Reference Sector Correction
RTM	Radiative Transfer Model
SAO	Smithsonian Astrophysical Observatory
SH	Southern Hemisphere
SHADOZ	Southern Hemisphere Additional OZonesonde
SPS(1,2)	Sydney Particulate Studies
STT	Stratosphere to Troposphere Transport
SZA	Solar Zenith Angle
TOA	Top Of the Atmosphere
TOMS	Total Ozone Mapping Spectrometer
VOC	Volatile Organic Compounds
UCX	Universal tropospheric-stratospheric Chemistry eXtension
UV-Vis	Ultraviolet and visible
VCC	Vertical Column Corrected
VMR	Vertical Mixing Ratio
WOUDC	World Ozone and Ultraviolet Data Centre

List of Symbols

C_x	mixing ratio or mole fraction of gas x	molecules of x per molecule of air
n_x	Number density of gas x	molecules of x per unit volume of air
Ω	Vertical column	molecules per square centimetre

Chapter 1

Introduction and Literature Review

1.1 The atmosphere

The atmosphere is made up of gases held to the earth's surface by gravity. These gases undergo transport on all scales, from barbecue smoke being blown about the garden, to smoke plumes from forest fires travelling across the world and depositing in the Antarctic snow. They take part in innumerable chemical reactions along the way, largely driven by solar input and interactions with each other. Many gases are emitted into the atmosphere by soil, trees, factories, cars, seas and oceans. They are also deposited back to the surface both directly and in rainfall.

The atmosphere is made up of nitrogen (N_2 : $\sim 78\%$), oxygen (O_2 : $\sim 21\%$), and argon (Ar : $\sim 1\%$), along with water (H_2O) and *trace gases* (those that make up less than 1% of the atmosphere). Atmospheric H_2O content can be as high as 4% depending on local conditions. Beyond these major constituents the atmosphere has a vast number of trace gases, including carbon dioxide (CO_2 : $\sim 0.4\%$), ozone (O_3 : $.000001\%$ to 0.001%), and methane (CH_4 : $\sim 0.00018\%$) (*Earth System Research Laboratory; Global Monitoring Division*; Brasseur and Jacob 2017, Ch. 2). Trace gases in the atmosphere can have a large impact on conditions for life on earth. They combine, break apart, and react with each other affecting all surface ecosystems upon which life depends.

One important trace gas is ozone (O_3), which affects climate, human health, and ecosystem productivity. The ozone budget (production, loss, and transport) is relatively uncertain over Australia. This thesis focuses on ozone in the troposphere over Australia and sites in the nearby Southern Ocean. It also estimates emissions of isoprene, one of the important precursors to tropospheric ozone production. This chapter provides background on the structure and composition of the atmosphere and introduces the key atmospheric species examined in this thesis, as well as relevant techniques used to measure and model chemistry in the atmosphere.

1.1.1 Structure

Most of the atmosphere ($\sim 85\%$) is within 10 km of the earth's surface. This is due to gravity, which causes air pressure to decrease logarithmically with altitude. Any entity is subjected to the weight of the air above it, and the structure of the atmosphere is driven by this pressure.

The atmosphere extends above the earth's surface to the edges of space. This is split into various layers, defined by the *lapse rate*: the decrease in temperature (T) with

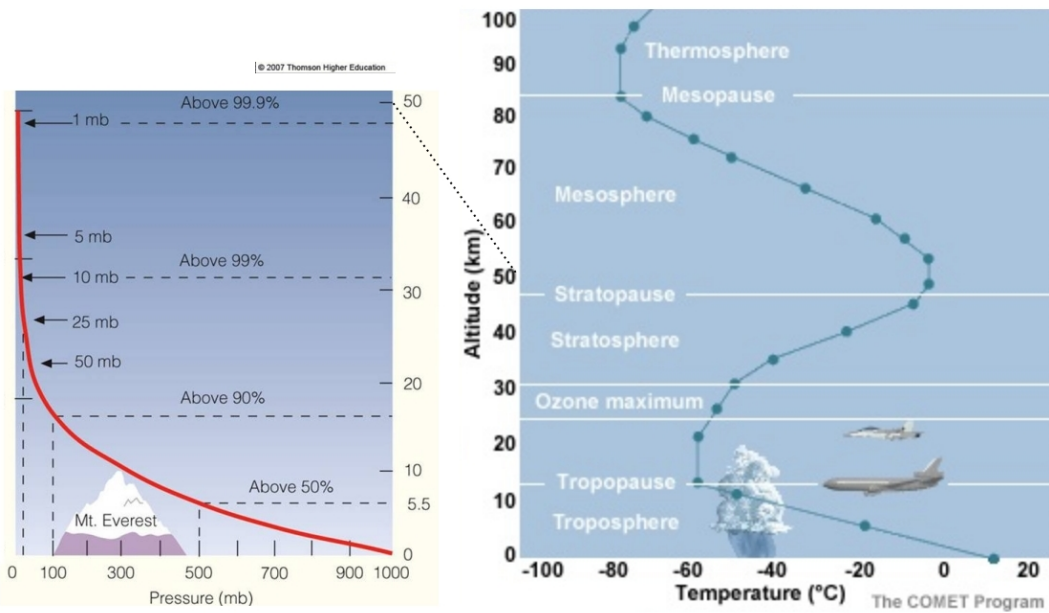


FIGURE 1.1: Pressure (red) logarithmically decreasing, shown with percentage of atmosphere below at several points. Temperature (green) changes throughout the atmosphere. Figure modified from <https://climate.ncsu.edu/edu/Structure>.

increasing altitude (z), or $\frac{-dT}{dz}$. Figure 1.1 shows the pressure and temperature profiles against altitude through the atmosphere. The first layer is the troposphere, which extends to roughly 10 km and is characterised by positive lapse rate (or decreasing temperature with altitude). At the top of the troposphere (the tropopause) the temperature stops decreasing, and then the stratosphere is defined by a negative lapse rate. This is due to ultraviolet radiation being absorbed by ozone, and leads to a very vertically stable environment.

In addition to these atmospheric layers, the troposphere can be subset into the *boundary layer* and the *free troposphere*. The *boundary layer* is the lowest layer and involves increased atmospheric mixing due to ground heating and friction effects. It generally extends from the surface up to 200 m - 1000 m, above which the ground effects have fewer direct impacts. The *free troposphere* is the remainder of the troposphere, where trace gas concentrations are more affected by transport and chemistry. Transported trace gases (and particulates) can come from the stratosphere or local to global scale winds and jet streams.

1.1.2 Composition and chemistry

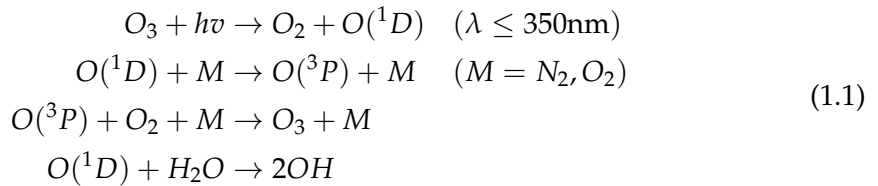
There are myriad trace gases in the atmosphere, emitted by plants, animals, earth, and water. These gases react with one another and over time they either deposit back onto the earth or form more stable compounds such as carbon dioxide (CO_2). Oxidation

and photolysis (the process of being broken apart by photons) are the two main processes whereby compounds are broken down in the atmosphere. Products formed in these reactions are sometimes called child products.

Hydroxyl radicals (OH) and hydrogen dioxide (HO_2) concentrations largely determine the oxidative capacity of the atmosphere. The OH radical drives many processes in the atmosphere, especially during the day when it is produced by the photolysis of ozone (Atkinson 2000). OH is a key species that reacts with nearly all the organic compounds in the troposphere, with only a few exceptions (Atkinson 2000). Over land, isoprene (C_5H_8) and monoterpenes ($\text{C}_{10}\text{H}_{16}$) account for 50% and 30% of the OH reactivity respectively (Fuentes et al. 2000).

Since radicals are involved in all oxidative chemistry in the atmosphere it is important for models to accurately represent them (e.g., Travis et al. 2016). This is difficult as they are coupled with so many other species and measurements of OH are not readily available on a global scale. In the late 1990s it was thought that OH radicals were formed exclusively from photolysis of O_3 , HONO , HCHO , and other carbonyls ($\text{R}_2\text{C}=\text{O}$) (Atkinson 2000). It has been shown since that OH is recycled in various processes. For example isoprene (C_5H_8) was thought to be a sink of OH until it was shown by Paulot et al. (2009b) that the radicals are recycled. This recycling process is discussed in more detail in section 1.3.3.

Ozone is an important precursor to OH , as excited oxygen atoms ($\text{O}^{(1D)}$) are created through its photolysis, which then go on to react with water to form OH , as shown in reaction sequence 1.1 (Atkinson 2000; Atkinson and Arey 2003):



where $h\nu$ represents radiation and M is an inert molecule. This shows that some of the $\text{O}^{(1D)}$ recycles back to ozone, while some forms OH .

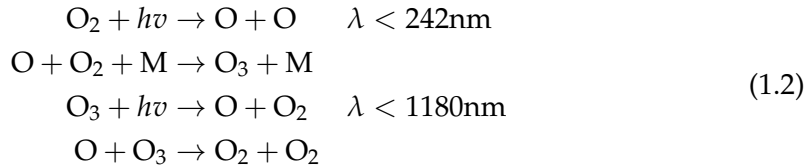
1.2 Ozone

Ozone (O_3) is an important greenhouse gas and oxidant. It is mostly located in the stratosphere and prevents much of the shorter wavelength solar radiation from reaching the earth's surface. Ozone in the troposphere is less beneficial, leading to health issues, radiative forcing, and crop death (Stevenson et al. 2013). Understanding and accurately portraying ozone concentrations in the troposphere is important to allow accurate predictions of future climate. This will become even more important as climate change alters the atmosphere (Hegglin and Shepherd 2009).

1.2.1 Stratospheric ozone

In the stratosphere, ozone production is driven by the Chapman mechanism, as high energy radiation (with wavelengths $\lambda < 242$ nm) photolyses the molecular oxygen (O_2) in the atmosphere (Brasseur and Jacob 2017, Chapter 3, section 2). The Chapman

mechanism involves several reactions that lead to rough equilibrium of O, O₂, O₃ and pressure, as follows:



The high energy photons ($\lambda < 242$ nm) are present from the top of the atmosphere but are mostly removed before reaching the troposphere as their energy is used to split the O₂ molecules. The lifetime of O against loss by O₂ is less than a second in the troposphere, and produced O₃ quickly returns to O and O₂, as low energy ($\lambda < 1180$ nm) photons and M are abundant. The reduced light penetration towards the surface, in addition to the logarithmic increase in atmospheric pressure (which affects M abundance) drives the vertical profile of ozone into what is called the *ozone layer*. This is a layer of relative ozone abundance within the stratosphere.

Satellite based measurements of ozone were instrumental in identifying the ozone hole. Since the Montreal Protocol on Substances that Deplete the Ozone Layer was established in August 1987, and ratified in August 1989, new satellites and measurement stations were set up to monitor ozone in the stratosphere. Detecting ozone from the surface up to the top of the stratosphere requires techniques such as remote sensing and ozonesonde releases. Ozonesondes are weather balloons (with attached ozone detectors) that detect ozone concentrations up to the mid stratosphere (~ 30 km), providing a vertical profile over a single location. Ozonesondes have been released periodically for decades over some cities, allowing long term ozone concentration profile analysis (e.g., Brinksma et al. 2002). A small network of ozonesonde release sites (including Davis, Macquarie Island, and Melbourne) is available from the world ozone and ultraviolet radiation data centre <http://woudc.org/data/explore.php> and is used in Chapter 4 to examine stratospheric impacts on tropospheric ozone (see Section 2.2.3.3 for more info on these ozonesondes).

1.2.2 Tropospheric ozone

Ozone in the lower atmosphere is a serious hazard that causes health problems (Hsieh and Liao 2013), causes billions of dollars of damage to agricultural crops (Avnery et al. 2013; Yue et al. 2017), and increases the rate of climate warming (Myhre and Shindell 2013). Around 5 to 20 percent of all air pollution related deaths are due to ozone (Monks et al. 2015), which translates to roughly 800 thousand deaths per year (Lelieveld et al. 2013). In the short term, ozone concentrations of ~50-60 ppbv over eight hours or ~80 ppbv over one hour are agreed to constitute a human health hazard (Ayers and Simpson 2006; Lelieveld et al. 2009). Long term exposure causes problems with crop loss and ecosystem damage (Ashmore, Emberson, and Murray Frank 2003), and concentrations may get worse in the future (Lelieveld et al. 2009; Stevenson et al. 2013). For example, future tropospheric ozone enhancements are projected to drive reductions in global crop yields equivalent to losses of up to \$USD₂₀₀₀ 35 billion (US dollars in the year 2000) per year by 2030 (Avnery et al. 2013), along with detrimental health outcomes equivalent to ~\$USD₂₀₀₀ 11.8 billion per year by 2050 (Selin et al.

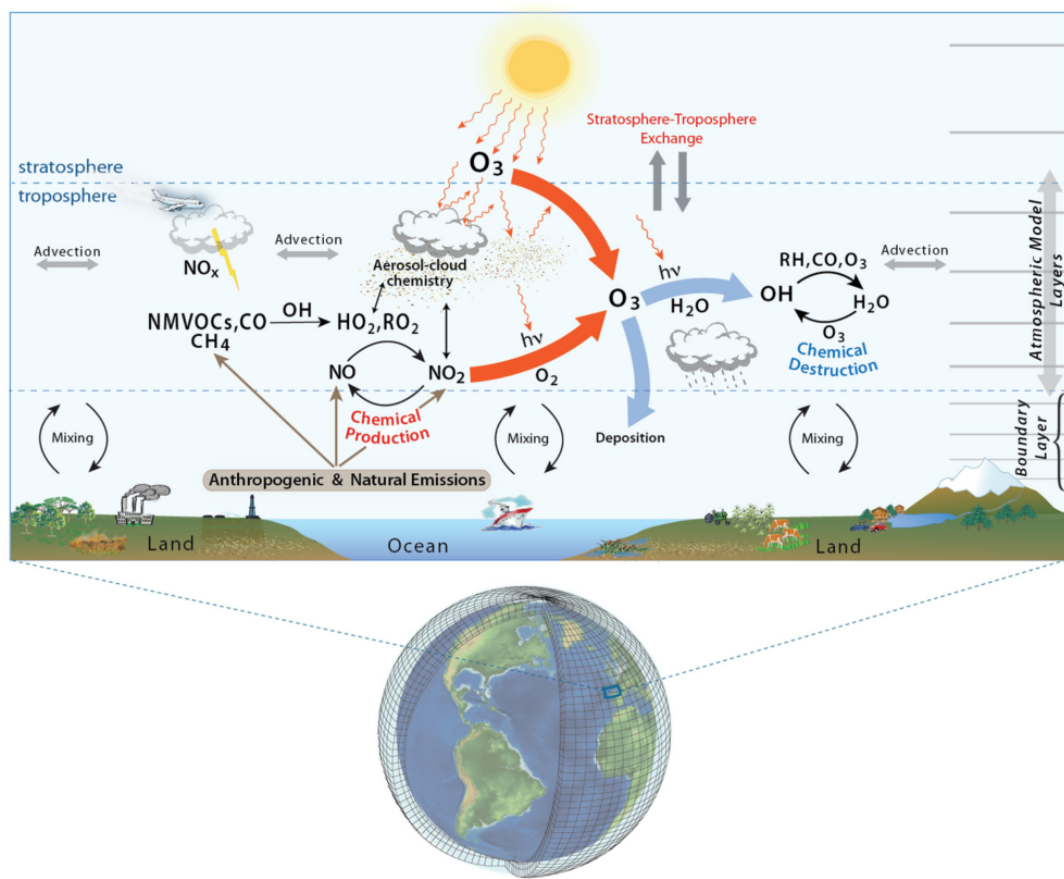


FIGURE 1.2: Tropospheric ozone processes, Figure 1 in Young et al. (2017). DOI: <https://doi.org/10.1525/elementa.265.f1>

2009). Recently Yue et al. (2017) showed that the net effect of near-surface ozone is an approximately 14% decrease in net primary productivity in China. They also state that in order to wind back most of this productivity decrease, drastic measures are required.

Figure 1.2, reproduced from Young et al. (2017), shows a summary of the major processes and emissions affecting tropospheric ozone. This thesis focuses on improving the highly uncertain natural emissions of non-methane volatile organic compounds (NMVOCs) from Australia, and estimating how much ozone is transported down from the stratosphere.

Generally there are two main drivers of tropospheric ozone concentrations: transport from the stratosphere and chemical production due to emissions of precursors. Tropospheric ozone is lost via chemical destruction and dry deposition, estimated to be $4700 \pm 700 \text{ Tg yr}^{-1}$ and $1000 \pm 200 \text{ Tg yr}^{-1}$, respectively (Stevenson et al. 2006; Young et al. 2017). The main loss channel is through photolysis and collisions, and leads to OH production (equation 1.1).

1.2.2.1 Stratosphere to troposphere transport

Historically, ozone transported down from the stratosphere was thought to contribute 10–40 ppb to tropospheric ozone levels, making up 50% of tropospheric concentrations (Atkinson 2000; Stohl et al. 2003). The proportion was revised down to around 10% over the years as measurement and modelling campaigns improved our understanding of global scale transport, mixing, and chemistry (Guenther et al. 2006; Monks et al. 2015). Intrusions of stratospheric air into the troposphere are often called Stratosphere to Troposphere Transport (STT) events. Although most tropospheric ozone comes from production, STT enhancements of ozone are measurable and can be regionally important (eg., Jacobson and Hansson 2000; Lelieveld et al. 2009; Kuang et al. 2017). Additionally, upper tropospheric ozone can be transported long distances (Cooper et al. 2004), affecting measurements far downwind of where stratospheric mixing may be taking place. An analysis of the Atmospheric Chemistry and Climate Model Inter-comparison Project (ACCMIP) simulations showed STT enhances tropospheric ozone by $540 \pm 140 \text{ Tg yr}^{-1}$ (Young et al. 2013), equivalent to ~11% of the tropospheric ozone column (Monks et al. 2015).

Ozone transported to the troposphere from the stratosphere can occur through diffusion (relatively slowly) or direct mixing (as STT). STT often occur as tongues of stratospheric air that descend into the troposphere before becoming detached. These can be due to low pressure systems and jet streams (Sprenger, Croci Maspoli, and Wernli 2003). It is possible to model this process and estimate how much ozone is being transported by STT (e.g., Young et al. 2013; Ojha et al. 2016). Model based estimates require validation against actual measurements, such as those from ozonesondes or satellites. It has been estimated that climate change will lead to increased STT through acceleration of the Brewer Dobson circulation (Hegglin and Shepherd 2009), a large scale transport system that affects the structure and composition of the atmosphere, and meteorology, in the tropics. Hegglin and Shepherd (2009) estimated that ozone transport would increase by 23% globally by 2095 (relative to 1965), $\sim 30 \text{ Tg yr}^{-1}$ in the southern hemisphere and $\sim 121 \text{ Tg yr}^{-1}$ in the northern hemisphere.

STT mostly impacts the upper troposphere, although some areas are impacted down to the surface. Over both ocean and land STT can lead to seasonal enhancements of upper and lower tropospheric ozone concentrations (Lin et al. 2015; Liu et al. 2017a; Kuang et al. 2017). A confounding factor is that stratospheric based ozone enhancement can be transported horizontally, and is not confined to the area where intrusion into the troposphere occurred. Understanding of STT needs to be improved to allow source attribution of the causes of local ozone enhancements (Lin et al. 2015).

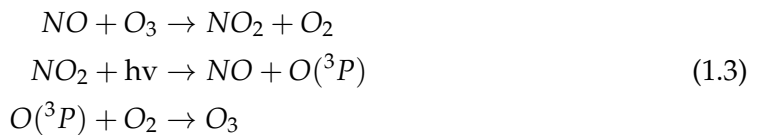
1.2.2.2 Chemical production

Tropospheric ozone concentrations are enhanced by ozone precursor emissions; including NO, NO₂, CO, and VOCs such as isoprene (Atkinson 2000; Young et al. 2013; Marvin et al. 2017). Ozone predictions are uncertain and changing climate affects transport, deposition, destruction, and natural precursor emissions. All of these processes are tightly coupled and difficult to accurately model, as they depend on uncertain assumptions such as CO₂ dependency (Young et al. 2013). Despite significant

advances over the prior decades, there remain large uncertainties about ozone precursors in the troposphere (Mazzuca et al. 2016). Tropospheric ozone is regulated by NO and NO_x concentrations, which form an equilibrium (Cape 2008; Young et al. 2017). At all scales, pyrogenic (fire) and anthropogenic (man-made) emissions can be important; however, biogenic VOC emissions are a nearly constant source of potential production during the day. Smoke plumes from biomass burning can carry ozone precursors, creating higher ozone concentrations downwind of the plume's source. Emissions of precursors from large cities (primarily from traffic and power production) can impact ozone concentrations. These impacts are not always straightforward due to the nonlinear relationship between ozone and its precursors. Recently, modelled ozone concentrations have been shown to be most sensitive to NO_x (\equiv NO₂ + NO) sources (such as lightning and car exhaust emissions) and isoprene emissions (Christian et al. 2018).

NO_x is an important chemical family in the atmosphere, which interacts with ozone and regulates the atmospheric oxidative capacity. NO_x and VOC emissions affect the tropospheric ozone equilibrium and can lead to enhanced ozone formation, shown in figure 1.2. NO_x compounds are short-lived, with emissions from power generation and transport being the main driver of concentrations (Delmas, Serca, and Jambert 1997). NO_x is removed primarily by conversion to nitric acid (HNO₃) or alkyl nitrates (RONO₂) followed by wet or dry deposition (Ayers and Simpson 2006; Romer Present, Zare, and Cohen 2019). Ozone in rural areas is often higher than in populous cities, due to titration (removal) of ozone by NO in areas with high anthropogenic emissions (Cooper, Gilge, and Shindell 2014; Monks et al. 2015).

As discussed above, STTs are responsible for $\sim 11\%$ of the tropospheric column of ozone, with the remainder produced photochemically. A recent summary by Young et al. (2017) estimated ozone production and loss in the troposphere to be $\sim 4900 \text{ Tg yr}^{-1}$, and $\sim 4500 \text{ Tg yr}^{-1}$ respectively. These numbers are at the global scale, and it should be noted that meteorology and topography can play dominant roles at local to regional spatial scales (e.g., Kuang et al. 2017). The main processes involved are shown in figure 1.2, with ozone and NO_x concentrations regulated by the following reactions (Sillman 1999; Atkinson 2000):



VOC emissions can alter this process, essentially replacing ozone in the first stage of the above equation. The process without and with the influence of VOCs (panel A and B respectively) is summarised in figure 1.3.

Net formation or loss of O₃ is determined by interactions between VOCs, NO_x, and HO_x, and is a complicated system of positive and negative feedbacks (Atkinson 2000). Figure 1.4 shows an example of this non-linear relationship between NO_x, VOCs, and ozone production as modelled in Mazzuca et al. (2016). Essentially increasing NO_x and VOC concentrations will increase ozone production; however, increasing one or the other may or may not increase production depending on current conditions. This is a short time scale relationship and ozone production can be more or less sensitive

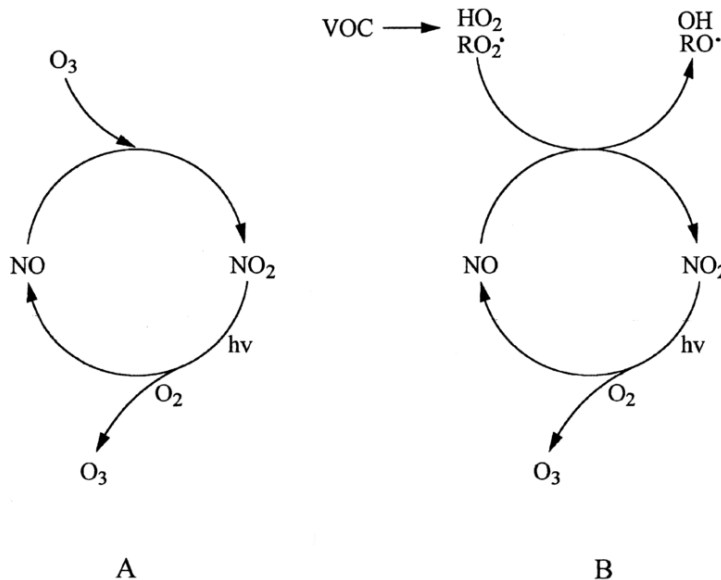


FIGURE 1.3: NO - NO₂ - O₃ photoequilibrium cycle without and with (A, B respectively) influence from VOCs. Figure reproduced from Atkinson (2000).

to VOCs at different hours of the day (Mazzuca et al. 2016). It is important to correctly determine the precursor concentrations in order to estimate ozone levels and production. This non-linear relationship is examined in more detail in the following section (1.3).

1.3 Volatile Organic Compounds

The least well understood precursors to tropospheric ozone production belong to a subclass of organic compounds. Organic compounds are a class of chemicals whose molecules contain carbon, with the exception of a few compounds such as carbides, carbonates, and simple oxides of carbon and cyanide. Organic compounds can be categorised based on their vapour pressure, which is the tendency of a liquid or solid to vaporise. Compounds with high vapour pressures at standard temperature are classed as volatile (volatile organic compounds: VOC), and are likely to vaporise at surface pressure. Gas phase compounds with higher vapour pressures can be oxidised into lower vapour pressure products that partition between gas and particle phase, often called semi or non-volatile. Atmospheric organic compounds are legion and differ by orders of magnitude with respect to their fundamental properties, such as volatility, reactivity, and cloud droplet formation propensity.

VOCs have vapour pressure greater than 10^{-5} atm, and are mostly generated naturally by plants, which emit around 1000 Tg yr⁻¹ (Guenther et al. 1995; Glasius and Goldstein 2016). Due to their high volatility these compounds generally exist in the gas phase. Organic compounds with a lower volatility are classed as semi-volatile (SVOCs: vapour pressure between 10^{-5} and 10^{-11} atm) and are found in both gas and

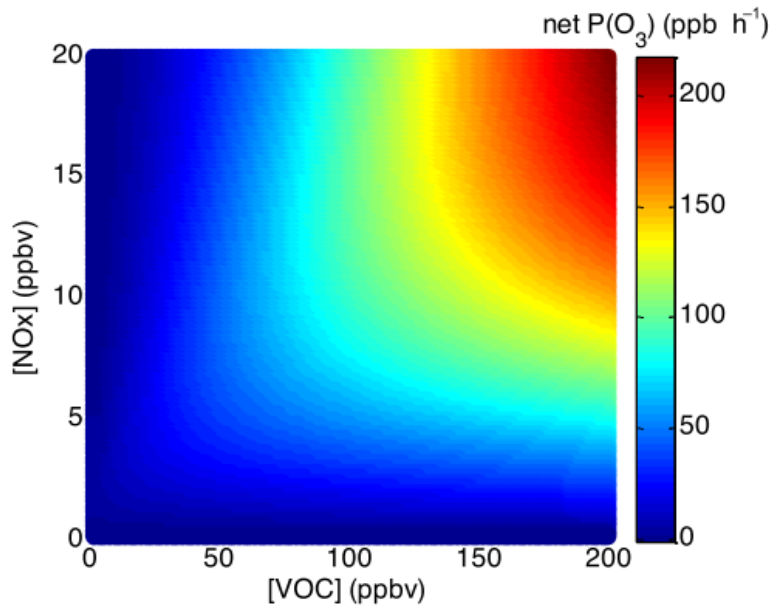


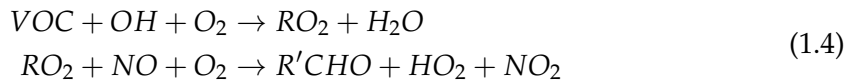
FIGURE 1.4: Dependence of ozone production rate on NO_x and VOC concentrations reproduced from Mazzuca et al. (2016).

particle phase depending on temperature and pressure. Plants contain tens of thousands of organic compounds, with fewer than 40 having high enough volatility to be emitted (Guenther et al. 2000). VOCs are oxidised in the atmosphere (mainly by OH), forming HCHO, O_3 , CO_2 and many other species.

Organic compounds with even lower vapour pressure are generally found in the particle phase (Glasius and Goldstein 2016). Understanding the drivers of trends in biogenic VOC emissions (BVOCs) is required in order to estimate future carbon fluxes, changes in the water cycle, ozone production, air quality, and other climate responses (Yue, Unger, and Zheng 2015). In the last 20 years, anthropogenic emissions of VOCs have been increasing while biogenic VOC emissions have decreased, due to rapid economic growth and lower annual temperatures (Stavrakou et al. 2014; Kwon et al. 2017).

Methane (CH_4) is one of the more abundant VOCs, however it is often classified separately from non-methane VOCs (NMVOCs). NMVOCs include alkanes, alkenes, and aromatic hydrocarbons, with isoprene (an alkene) being the most abundant (Guenther et al. 1995). Methane is relatively long lived (years) and is well mixed in the atmosphere, while other VOCs have shorter lifetimes and therefore their concentrations are more spatially variable. VOCs with short lifetimes are generally only found in high concentrations near their emission sources.

In areas with high VOC concentrations, ozone production may be enhanced through the following reaction sequence (Sillman 1999):



with R and R' representing organic species. The reactions of VOCs with OH convert NO to NO₂, which leads to ozone formation as NO₂ production in reaction 1 of 1.3 is bypassed.

One aspect associated with VOC emissions is the production of aerosols. Aerosols are suspended particulates and liquid compounds in the atmosphere, often called particulate matter (PM). PM in the atmosphere is a major problem, causing an estimated 2-3 million deaths annually (Avnery et al. 2013; Hoek et al. 2013; Krewski et al. 2009; Silva et al. 2013; Lelieveld et al. 2015). Fine particulate matter (PM_{2.5}) penetrates deep into the lungs and is detrimental to human health. Some PM comes from small organic aerosols (OA) that are directly emitted to the atmosphere in the particulate phase, referred to as primary OA (POA).

A substantial amount of PM is due to gaseous organic compounds transforming into what is known as secondary OA (SOA) (Atkinson 2000; Kanakidou et al. 2005; Kroll and Seinfeld 2008). Formation of SOA is generally due to VOC oxidation and subsequent reactions, while removal from the atmosphere is largely due to wet or dry deposition, and cloud scavenging (Kanakidou et al. 2005). Most of the tropospheric SOA comes from biogenic precursors, and the evidence for this has grown over the last two decades (Guenther et al. 1995; Kanakidou et al. 2005; Guenther et al. 2012). Improved concentration estimates of these precursors requires a better understanding of their emissions, which is one of the foci in this thesis.

VOCs are removed mainly by photolysis and oxidation by OH, forming alkyl radicals (R'). Additional losses are caused by wet and dry deposition, reaction with NO₃, and ozonolysis (at night time or in polluted areas) (Atkinson and Arey 2003; Brown et al. 2009). Deposition only accounts for a small fraction of the VOC loss (Atkinson and Arey 2003).

1.3.1 Emissions

VOC emissions are classified as either biogenic (BVOC), anthropogenic, or pyrogenic. Global NMVOC emissions are estimated to come from 85 % biogenic, 13 % anthropogenic, and 3 % pyrogenic sources respectively (Kanakidou et al. 2005; Kefauver, Filella, and Peñuelas 2014). The ocean also plays a role in VOC emissions, with the Oceanic Niño Index showing positive VOC emission anomalies associated with neighbouring countries (Stavrakou et al. 2014). Due to the lack of in-situ ground based measurements, estimates of VOC emissions are uncertain, with large scale extrapolation required (Millet et al. 2006).

There is ten times as much mass of NMVOCs emitted from natural sources as from anthropogenic sources (Guenther et al. 2006; Kanakidou et al. 2005; Millet et al. 2006). Major emitters are broadleaves (notably Eucalyptus), and shrubs (Guenther et al. 2006; Arneth et al. 2008; Niinemets et al. 2010; Monks et al. 2015). NMVOC emissions are a byproduct of photosynthesis, and also a response to various environmental factors, including temperature, atmospheric CO₂, soil moisture, and drought stress. Land use changes can drastically affect isoprene sources, for instance in the tropics where large scale deforestation has converted forest into crop lands (Kanakidou et al. 2005). In this thesis I focus on emissions of isoprene in Australia.

Globally around 710 - 1150 Tg C yr⁻¹ of BVOCs are emitted (Guenther et al. 1995; Lathière et al. 2006; Guenther et al. 2012; Messina et al. 2016). BVOCs are emitted by

vegetation, with the most dominant emitters being tropical trees. The main VOCs emitted are isoprene (C_5H_8) (~ 50 – 70%), and monoterpenes ($C_{10}H_{16}$) (~ 30%), which have different emission amounts depending on the tree species(Guenther et al. 2012; Sindelarova et al. 2014). Other emissions include methanol (CH_3OH), ethanol (C_2H_6O), acetaldehyde (CH_3CHO), acetone ($(CH_3)_2CO$), ethene (C_2H_4) and propene (C_3H_6) (Guenther et al. 2012). Many of these estimates come from Model of Emissions of Gases and Aerosols from Nature (MEGAN), a bottom-up biogenic emissions model. MEGAN parameterises BVOC emissions as a function of temperature, land cover, plant functional type, etc., with descriptions given in Guenther et al. (2012).

1.3.2 Isoprene

Isoprene (2-methylbuta-1,3-diene) is the dominant BVOC emitted to the atmosphere.. It is of major importance to the atmosphere, as it is involved in various processes that alter the oxidative capacity of the atmosphere. Isoprene affects NO_x and HO_x cycling, see for example reactions 1.1, 1.3. In the presence of NO_x , isoprene forms tropospheric ozone and SOA (Wagner 2002; Millet et al. 2006). It has a short lifetime during the day, roughly an hour due to OH oxidation (Atkinson and Arey 2003). Ozonolysis and photolysis are lesser oxidation pathways, which can form similar products (Nguyen et al. 2016; Wolfe et al. 2016).

Measurements of isoprene are often uncertain, as the compound is reactive and short lived. Chamber experiments are used to determine how isoprene behaves once it is emitted into the atmosphere; however, laboratory derived reaction rates may be unsuitable when modelling the natural atmosphere, which is often very different (Kanakidou et al. 2005; Nguyen et al. 2014). In the absence of extensive measurements, isoprene emissions and subsequent atmospheric oxidative chemistry are often modelled.

MEGAN (Guenther et al. 1995), and subsequent updates (Guenther et al. 2000; Guenther et al. 2006; Guenther et al. 2012), have been used ubiquitously by the atmospheric community as a global estimate of isoprene emissions, at roughly 500-600 Tg yr^{-1} , emitted mostly during the day. Other models also exist which estimate similar isoprene amounts, such as LPJ-GUESS (Lund-Potsdam-Jena General Ecosystem Simulator) (Arneth et al. 2007), and ORCHIDEE (Organizing Carbon and Hydrology in Dynamic EcosystEm) (Messina et al. 2016). There is a potential issue caused by shared underlying algorithms and assumptions between the models, which lead to an unrealistic convergence on isoprene emission estimation (Arneth et al. 2008). The global emission factors used to derive these estimates are based on modelling emissions from different plant species (phenotypes), and relatively few Australian species were used when forming these estimates. This leads to increased uncertainty for Australian emissions. Due to the highly reactive nature of isoprene, modelling of related chemical products is sensitive to uncertainties, for example the diurnal pattern of isoprene emissions affects modelled ground level ozone (Hewitt et al. 2011; Fan and Zhang 2004).

The global uncertainty of isoprene emission was estimated to be a factor of 2 to 5 (250-750 Tg yr^{-1}) (Kanakidou et al. 2005). Improvements over the years have been incremental, and generally localised to regions of particular interest for air quality such as China and the USA (Guenther et al. 2012; Jiang et al. 2018).

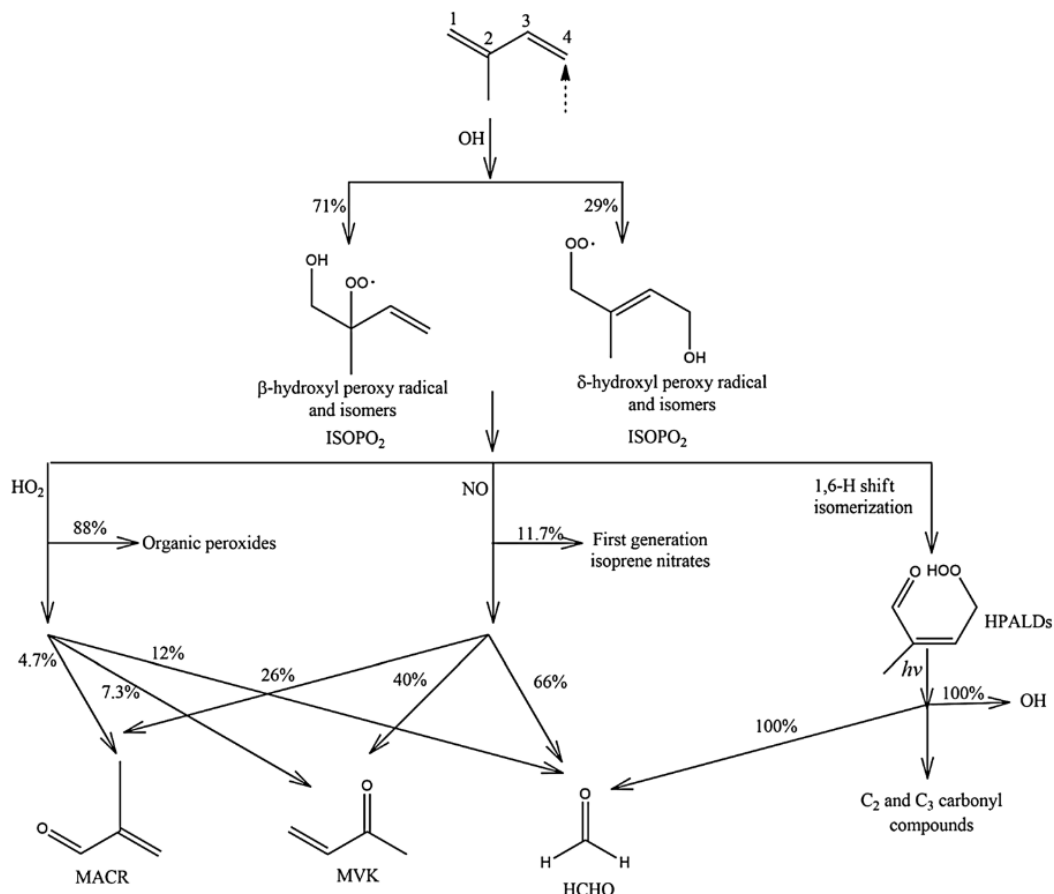
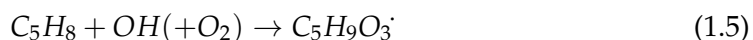


FIGURE 1.5: Simplified isoprene products following oxidation by OH, reproduced from Mao et al. (2013).

1.3.3 Isoprene chemistry

Isoprene is emitted and enters the atmosphere in the gas phase, where it reacts quickly with OH and other radicals. One common compound that is produced by these reactions is HCHO, which can be measured from satellites and is often used to estimate how much isoprene is being emitted. Isoprene reacts with OH, ozone, or NO₃, leading to organic peroxy radicals (ROO[·]). These go on to form many products and lead to (amongst other things) aerosol, formaldehyde, and ozone formation, depending on sunlight and NO_x concentrations (Atkinson 2000). Reactions with NO can lead to ozone production within environments rich in isoprene or other NMVOCs (Patchen et al. 2007; Atkinson and Arey 2003).

Figure 1.5 shows the first stages of oxidation of isoprene by OH. The primary first step for atmospheric isoprene is photooxidation, reacting with OH to form isoprene hydroxyperoxy radicals (ISOPPOO: C₅H₉O₃) (Patchen et al. 2007; Wolfe et al. 2016; Marvin et al. 2017). Isomers form based on which carbon the OH adducts to (for example, Figure 1.5).



The subsequent processes that begin with isoprene oxidation are often called the isoprene (photochemical) cascade (e.g., Crounse et al. 2012; Paulot, Henze, and Wennberg 2012; Wolfe et al. 2016).

ISOPOO reacts with HO₂ or NO, producing stable products. This pathway also produces HCHO (with varying yields):



During the day HCHO has a lifetime of 1-2 hrs, while ROO' lasts ~ 100 s, making reaction 1.5 a rate limiting factor in HCHO production (Wolfe et al. 2016). Additionally, ISOPOO can isomerise and produce hydroperoxy-methyl-buteneals (HPALDS) (see figure 1.5), which also leads to HCHO. At higher NO mixing ratios (at least a few hundred pptv), ROO react mostly with NO. At low NO (less than 50 pptv), ROO' is more likely to either isomerise, react with HO₂, or react with another ROO'.

There is uncertainty about which pathways are most important following ISOPOO production, affecting predictions by atmospheric models (Nguyen et al. 2014). This limits understanding of the relative importance of some chemical processes, such as auto-oxidation of ISOPOO (Crounse et al. 2013). The reaction pathways depend on local concentrations of NO_x: the high and low NO_x pathways are dominated by NO and HO₂ reactions respectively. HO₂ reactions predominantly produce hydroxyhydroperoxides (ISOPOOH), while NO reactions produce isoprene nitrates (ISOPN) (Crounse et al. 2006). If measured, first generation ISOPN and ISOPOOH products can be used to determine the portion of isoprene oxidation following each pathway (e.g., Yu et al. 2016). Globally around one third of ISOPOO react with HO₂, and two thirds react with NO (Paulot et al. 2009b). Most of these reaction pathways produce HCHO, however this along with methyl vinyl ketone (MVK), and methacrolein (MACR) are formed at different yields between the two pathways (Marais et al. 2012; Liu et al. 2016b; Wolfe et al. 2016).

1.3.3.1 High NO_x pathway

In the presence of NO_x, ISOPOO reacts with NO and forms ISOPN, which affect levels of both HO_x (OH+HO₂) and NO_x. ISOPN generally act as a sink of HO_x, and can be a sink or reservoir for NO_x (Mao et al. 2013; Fisher et al. 2016). A portion of the ISOPN are recycled back to NO_x, serving as a reservoir of nitrogen and allow its transport to the boundary layer of remote regions (Patchen et al. 2007; Paulot et al. 2009a). The nitrates can also build up in the winter, when removal processes are not as dominant (Lelieveld et al. 2009).

Under high NO_x conditions there is a large and rapid yield of HCHO, with most of the ultimate HCHO production occurring within one day (Palmer et al. 2006). First generation ISOPN produce MVK(~ 40%), MACR(~ 26%), and HCHO(~ 60%) at higher yields than are produced by ISOPOOH (Liu et al. 2013; Mao et al. 2013). The MVK and MACR products form additional HCHO within a few hours due to oxidation by OH (Palmer et al. 2006).

1.3.3.2 Low NO_x pathway

In low NO_x environments, ISOPOOH is formed in yields > 70%, while MACR, MVK, and HCHO are formed at ~ 5%, ~ 7%, and ~ 12% respectively (Paulot et al. 2009b; Mao et al. 2013). This ISOPOOH mostly reacts with OH to form dihydroxyperoxides (IEPOX) while regenerating OH (Mao et al. 2013). This pathway has lower and slower ultimate yields of HCHO from isoprene when compared to the high-NO_x pathway (Palmer et al. 2006).

Isoprene oxidation and subsequent reactions are less well understood when lower concentrations of NO are present in the atmosphere. It was thought that in low NO environments, like those far from anthropogenic pollution and fires, oxidation of isoprene would create ISOPOOH and reduce local concentrations of OH and HO₂ (Guenther et al. 2000; Paulot et al. 2009b). However this reduction was not seen in measurements and HO_x levels have been shown to be largely unaffected by isoprene concentrations (Paulot et al. 2009b). HO_x is recycled through IEPOX, formed from ISOPOOH oxidation, and some HO_x is produced in the formation of MACR and MVK (Paulot et al. 2009b). Though uncertain, OH and HO₂ production or regeneration mechanisms have improved model outcomes when compared against campaigns (Peeters and Muller 2010; Crounse et al. 2012).

Uncertainties and bias from measurements have made it more difficult to understand what happens in low NO_x conditions, and many observations of OH remain under-predicted in models (Mao et al. 2012). Due to OVOC interference, measurements in low NO_x environments can lead to massively overestimated MVK and MACR yields (Nguyen et al. 2014). Nguyen et al. (2014) show preliminary estimates of low-NO yields of MVK and MACR to be 6±3% and 4±2% respectively, consistent with Liu et al. (2013), but only when cold-trapping methods are employed. Many instruments have been shown to generate OH internally, creating anomalous VOC readings due to within-instrument oxidation (Mao et al. 2012).

Improved understanding of both the chemistry and instrument sensitivities has helped closed the gap between model predictions and detected concentrations of VOCs and OH (Mao et al. 2012), but uncertainties remain in isoprene oxidation mechanisms. Examples (taken from Nguyen et al. (2014)) include:

- isoprene nitrate yields, which range from 4-15% (Fisher et al. 2016)
- 90% disagreements in MACR and MVK yields (Liu et al. 2013)
- unknown HPALD fates (Peeters, Nguyen, and Vereecken 2009; Crounse et al. 2013)
- poorly-characterised RO₂ lifetime (Wolfe et al. 2012).

1.3.3.3 Night time processes

At night when OH concentrations have dropped, isoprene can remain in the atmosphere. Typically less than half of this night time isoprene is removed through ozonolysis (Atkinson and Arey 2003). A build up of NO₃ radicals can be seen at night, when photolysis is not removing them (Atkinson 2000; Brown et al. 2009). This build up is

enhanced in polluted (high NO_x) areas. NO_3 are largely formed through ozone reactions. In these conditions isoprene is consumed by NO_3 radicals that join to one of the double bonds, producing organic nitrates (RONO_2) in high yield (65% to 85%) (Mao et al. 2013).

In areas with high NO_x levels, greater than 20% of the isoprene emitted late in the day ends up being oxidised by the NO_3 radical overnight (Brown et al. 2009). At night isoprene affects both NO_x concentrations and ozone levels, and can form harmful organic nitrates and SOA (Brown et al. 2009; Mao et al. 2013). These nitrates go on to produce further SOA, largely due to NO_3 reacting with first generation isoprene oxidation products (Rollins et al. 2009). The night-time concentrations of OH and ozone also have a complex effect on NO_x removal in high latitude winters, when photolysis and NO reactions are reduced (Ayers and Simpson 2006).

1.3.4 Radiative Forcing

Another reason for interest in VOCs is that they are a dominant source of organic aerosol, which are a major source of uncertainty in radiative forcing. VOC emissions affect ozone along with several atmospheric parameters that directly and indirectly alter radiative forcing rates (e.g., Arneth et al. 2008). This is even more important in Australia where VOCs are so poorly represented by contemporary modelling (Emmerson et al. 2016). Aerosols are particles in the atmosphere, and they affect radiative forcing in ways that are difficult to accurately quantify. For some years it has been understood that aerosols have an overall cooling effect within the atmosphere. Smaller particles can match the wavelengths of visible light, interfering with incoming radiation (Kanakidou et al. 2005). Aerosol products from gas phase emissions (or the children thereof) also play an indirect and complex role in cloud properties, with a net cooling effect (Kanakidou et al. (2005), Stocker et al. (IPCC, 2013: *Climate Change 2013: The Physical Science Basis. Contribution of Working Group I to the Fifth Assessment Report of the Intergovernmental Panel on Climate Change, Chapter 7,8*)). Aerosol and cloud formation remain as large uncertainties in recent IPCC reports (Forster et al. 2007). Figure 1.6 shows that uncertainty from aerosol effects dominate the uncertainty in radiative forcing.

1.4 Formaldehyde

In conjunction with atmospheric chemistry and radiative models, satellite measurements quantify the abundance of HCHO in the atmosphere. Isoprene is hard to measure directly due to its short lifetime and weak spectral absorption, instead HCHO is often used as a proxy (Millet et al. 2006; Fu et al. 2007; Dufour et al. 2008; Marais et al. 2012; Bauwens et al. 2013; Kefauver, Filella, and Peñuelas 2014; Bauwens et al. 2016; Surl, Palmer, and Abad 2018). The existence of satellite data covering remote areas provides an opportunity to improve VOC emissions estimates leading to more robust models of global climate and chemistry. This method is implemented within this thesis (Section 3.2), and relevant information dealing with HCHO is provided here.

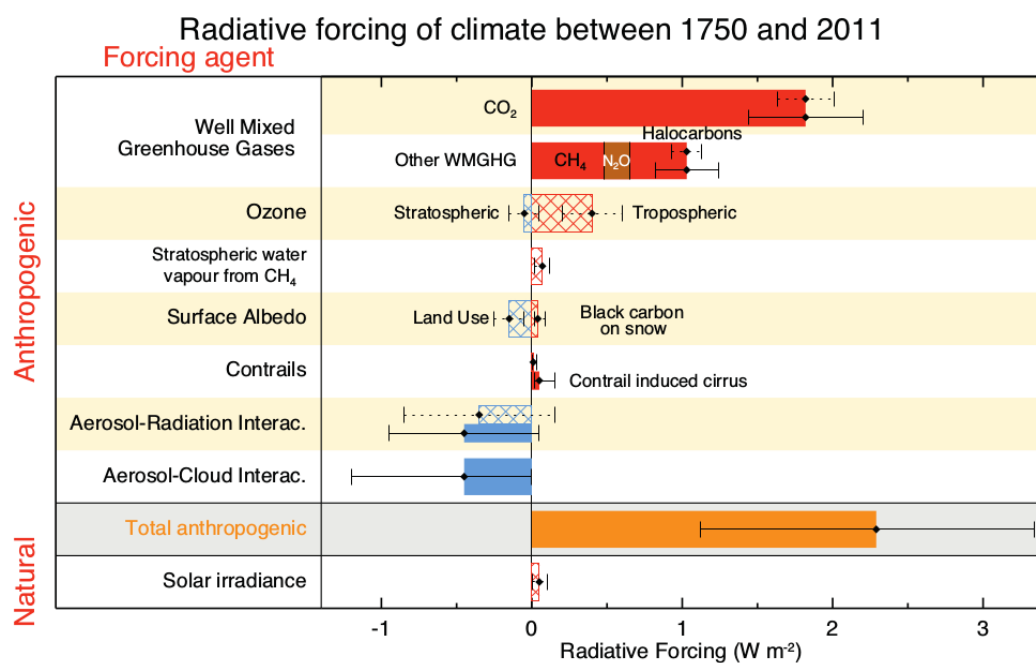
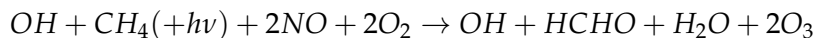


FIGURE 1.6: The overall radiative forcings and uncertainties of several atmospheric constituents This is an image taken from Stocker et al. (IPCC, 2013: *Climate Change 2013: The Physical Science Basis. Contribution of Working Group I to the Fifth Assessment Report of the Intergovernmental Panel on Climate Change*), chapter 8.

Formaldehyde (HCHO), also known as methanal, methyl aldehyde, or methylene oxide, is part of the aldehyde family. HCHO is an oxygenised VOC that is toxic, allergenic, and a potential carcinogen. Generally, HCHO is not dangerous at low background atmospheric levels. Globally, HCHO production is mainly due to the oxidation of methane; however, over continental regions, HCHO enhancement above the background level is largely due to isoprene emissions. HCHO production also depends on NO_x concentrations, which affect the yield from isoprene oxidation. HCHO yield is higher in the high-NO_x pathway (compared to the low-NO_x pathway) from isoprene reactions (Marais et al. 2012). HCHO measurements are often used to evaluate how well isoprene chemistry is simulated by models, as HCHO levels depend on initial VOCs and oxidants (which can be prescribed) (Marvin et al. 2017).

1.4.1 Sources and sinks

Background levels of HCHO in the atmosphere are driven by the oxidation of CH₄ by the OH, which produces $\sim 970 \text{ Tg yr}^{-1}$ (Fortems-Cheiney et al. 2012). Atkinson (2000) summarised the background formation of HCHO with the following reaction:



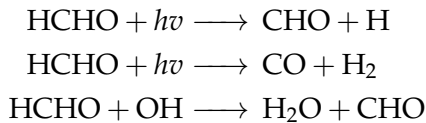
This shows that photolysis and oxidation of methane forms HCHO and ozone in a process that regenerates the OH radicals. CH₄ concentrations are relatively well constrained in models, with the ACCMIP comparison showing only $\sim 3\%$ inter-quartile range (Young et al. 2013).

Within the continental boundary layer, HCHO is enhanced above background levels, due to NMVOC emissions reacting with OH radicals in the presence of NO_x (Wagner 2002; Millet et al. 2006; Kefauver, Filella, and Peñuelas 2014). The total contribution from NMVOC oxidation is $\sim 358 \text{ Tg yr}^{-1}$ (Fortems-Cheiney et al. 2012). Enhancements to regional and continental HCHO are largely driven by emissions of isoprene (Guenther et al. 1995; Palmer et al. 2003; Shim et al. 2005; Kefauver, Filella, and Peñuelas 2014). The exception is where emissions of HCHO or precursors occur due to fires or anthropogenic activities such as fossil fuel combustion, natural gas flaring, ethanol refining, and agricultural activity (Guenther et al. 1995; Kefauver, Filella, and Peñuelas 2014; Wolfe et al. 2016). Other terpenoids (monoterpenes, sesquiterpenes, etc.) can also produce HCHO, although generally to a lesser extent than isoprene, methane and biomass burning (Guenther et al. 2012). Anthropogenic sources of HCHO are largely negligible; however, their signals can be seen in very large cities or near large industrial sources (Millet et al. 2008; Zhu et al. 2014).

In the past, HCHO levels were underestimated by models, often with large discrepancies, due to the poor understanding of methyl peroxy radical (CH₃OO) chemistry (Wagner 2002). Now HCHO concentrations are better understood, however precursor emissions are one of the main unknowns (e.g., Emmerson et al. 2016; Marvin et al. 2017). The primary source of discrepancy between modelled and measured HCHO concentrations is second and later generational isoprene oxidation chemistry (Marvin et al. 2017).

HCHO has two major sinks totalling $\sim 1210 \text{ Tg yr}^{-1}$, reactions with OH (oxidation), and photolysis (Levy 1972; Crutzen, Lawrence, and Poschl 1999; Wagner 2002;

Fortems-Cheiney et al. 2012; Kefauver, Filella, and Peñuelas 2014). The other sinks are wet and dry deposition, although these are not as significant ($\sim 32 \text{ Tg yr}^{-1}$) (Atkinson 2000; Fortems-Cheiney et al. 2012). Oxidation and photolysis reactions begin as follows (Ayers et al. 1997):



These reactions lead to a daytime lifetime of a few hours (Atkinson 2000; Millet et al. 2006). Both these loss processes (photolysis, oxidation) form CO, and lead to production of hydroperoxyl radicals (HO_2). These products have global significance to radiative forcing and oxidative capacity (Franco et al. 2015).

1.4.2 Measurement techniques

HCHO measurements are used extensively throughout this thesis, and a brief introduction to the relevant techniques is provided here. HCHO data used in this thesis have been measured using two different techniques: Fourier Transform Infra-Red (FTIR) Spectrometry and Differential Optical Absorption Spectroscopy (DOAS). FTIR uses the Fourier transform of a measured spectrum to quantify species which interfere with the spectrum in the infra-red region. DOAS methods are based on light interference and absorption through air masses.

The DOAS technique takes advantage of the optically thin nature of HCHO in order to linearise the radiance differential through air masses with and without HCHO, using the Beer-Lambert intensity law. This method is used globally both from ground-based and space-based instruments for HCHO detection (Guenther et al. 1995; Gonzalez Abad et al. 2015; Davenport et al. 2015). As a trace gas, HCHO absorbs light over a few wavelength bands, which allows instruments to detect concentrations between a known light source and a detector. Figure 1.7 shows the interference spectrum of HCHO along with a typical band used to examine interference in the DOAS technique. FTIR and DOAS measurements have a range of uncertainties, including systematic and random measurement errors and uncertain a priori shape factors and water vapour profiles (e.g., Franco et al. 2015). One difficulty is that this interference is relatively small (HCHO is optically thin) and other compounds absorb light at similar wavelengths (Davenport et al. 2015).

Other types of measurement involve directly measuring the air, and determining chemical compounds through their physical properties such as by mass spectrometry analysis of mass to charge ratios (m/z) of ionised air masses. Two examples of this include proton transfer reaction mass spectrometers (PTR-MS), and gas chromatography mass spectrometers (GC-MS). These instruments can be also used to determine the gas phase evolution of other isoprene and monoterpene products (e.g., Lee et al. 2006; Nguyen et al. 2014; Wolfe et al. 2016; Lerner et al. 2017). Reasonable agreements between different instruments and techniques can be achieved, although titration and calibration differences can lead to large ($\sim 30\%$) discrepancies (e.g., Hak et al. 2005).

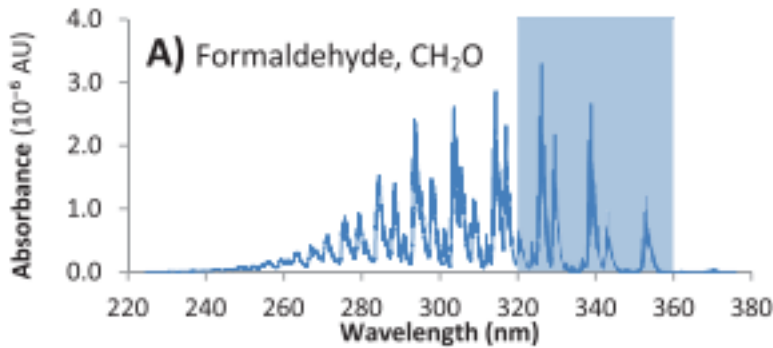


FIGURE 1.7: HCHO spectrum, with a typical band of wavelengths used for DOAS path measurements. Reproduced from Davenport et al. (2015).

These differences and non-uniformities between measurements (even among identical instruments) are part of the reason HCHO does not have a consistent network for global measurements like those for greenhouse gases or ozone (Fortems-Cheiney et al. 2012).

1.4.2.1 Satellite measurements

Satellites remotely sense atmospheric HCHO through irradiance measurements of solar light that has reflected off the earth's surface. These irradiances are affected by gases that absorb radiation along the reflected path of light between the detector, earth, and sun. The irradiance is then used to estimate how much of a particular gas exists along this path, which gives an estimate called the slant column (SC). The retrieved SC of a particular gas (species) can be transformed into a vertical column (VC) by scaling the path length in conjunction with accounting for the light scattering properties of the trace gas. The scaling coefficient created to transform from SC to VC is called the Air Mass Factor (AMF).

Several satellites provide long term HCHO observations with near complete global coverage. Some of these are:

- ERS-2 launched in April 1995, housing the GOME ultraviolet and visible (UV-Vis) spectrometer
- AURA launched in July 2004, housing the OMI UV-Vis spectrometer
- MetOp-A and B launched in October 2006 and September 2012 respectively, both housing a GOME-2 UV-Vis spectrometer.

These satellites are on low earth orbit trajectories and overpass any area up to once per day. Satellites use DOAS techniques with radiative transfer calculations on solar radiation absorption spectra to measure column HCHO. An example of a spectrum retrieved from the GOME-2 instrument is given in figure 1.8.

Satellite observations often require both remote-sensing and in situ measurements combined with modelled data for validation (Marais et al. 2014). There is less information available from satellite measurements at higher latitudes due to increased error in

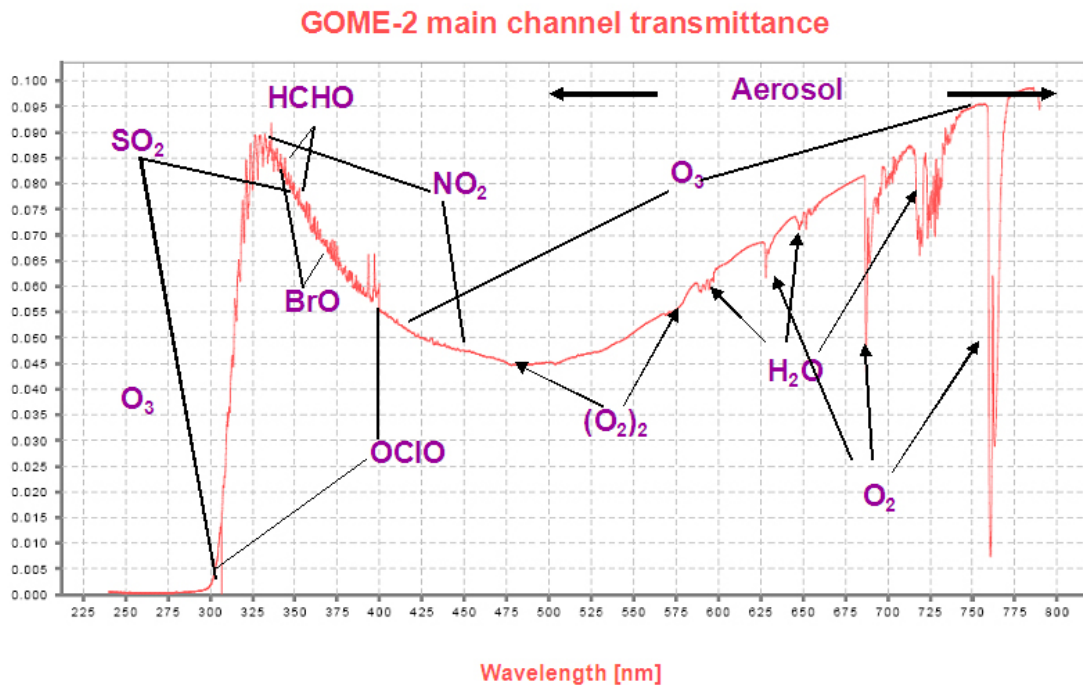


FIGURE 1.8: An example spectrum showing absorption features used for species concentration measurements by GOME-2. Image reproduced from EUMETSAT and ESA (EUMETSAT 2015).

measurements over the more slanted column paths (De Smedt et al. 2015). Validation is important due to the various uncertainties in the satellite remote sensing process. This can be done using aircraft data such as from the Studies of Emissions and Atmospheric Composition, Clouds and Climate Coupling by Regional Surveys HCHO measurements over the southeastern US to provide model validation (e.g., Zhu et al. 2016). Satellites use an assumed shape factor to improve the vertical column estimate, however this can lead to a bias between satellite data and other measurements (Zhu et al. 2016). Different satellites, instruments, or techniques that measure HCHO (or any trace gas) can give different results due to differing a priori assumptions (Lorente et al. 2017). The concept of differences that arise between datasets based on measurement techniques or underlying instrument biases is called structural uncertainty.

1.5 Atmospheric Chemistry Modelling

Models can fill the gaps (both spatial and temporal) in measurement records, and can help us improve our understanding of the natural world. For example, they can be used to examine future outcomes resulting from changing our emissions. They can be used to increase measurement accuracy (for instance in satellite measurements) and determine where we lack information, while also evaluating the performance of new instruments. Precisely representing various chemicals and reactions in the atmosphere allows efficient mitigation of pollution, since we can compare scenarios against

one another. Currently, models require improved isoprene emissions and subsequent chemistry for effective air quality determination (Marvin et al. 2017).

1.5.1 Box models

Box models simulate chemistry in a singular set of conditions without transport or spatial gradients. These models often parameterise things such as transport and emissions that would realistically take place at the edges of the box. Box models can be used to test chemical mechanisms in specific scenarios, such as high or low NO_x environments. For example, Marvin et al. (2017) used a box model matching conditions in southeast USA to evaluate isoprene mechanisms from several models.

By allowing for interactions between boxes this concept can be extended to multiple-box models. Multiple-box models are simply multiple instances of single boxes with the addition of transport between them. Transport requires meteorological fields such as wind velocities and turbulence. The meteorology fields can be modelled, and/or input as parameters.

1.5.2 Chemical transport models

Chemical transport models (CTMs) provide a simulation of chemical densities and transport over time, through the atmosphere. Chemistry in the atmosphere is a complex system of coupled reactions and dynamics, which can be solved using numerical partial differential equation solvers. Chemical models require many inputs such as meteorological conditions and emissions. Initial (atmospheric starting state) and boundary (inputs and outputs at the edge of the modelled system) conditions are required, and models or inventories of emissions often make up inputs at the surface of the atmosphere.

CTMs simulate production, loss, and transport of chemical species. This is generally calculated using one or both of the Eulerian (box) or Lagrangian (puff) frames of reference. Eulerian models use equations of chemistry within and transport between volumes in a gridded spatial coordinate system, while Lagrangian models evaluate behaviour within a potentially changing frame of reference (for example within a cloud). CTMs normally solve continuity equations simultaneously for many coupled species. The continuity equations describe transport of a conserved quantity such as mass or energy, which, solved together with production and loss of a chemical can provide detailed simulations of natural processes.

The general continuity equation links a quantity of a substance (q) to the field in which it flows and can be described by the formula:

$$\frac{\partial \rho}{\partial t} + \nabla \cdot j = \sigma$$

where ρ is density of q in the field, t is time, ∇ is divergence, j is the flux (q per unit area per unit time entering or leaving the field), and σ is the generation or loss of q per unit volume per unit time.

The type of model best suited to modelling the entire earth uses the Eulerian frame of reference, where the atmosphere is broken up into 3-D boxes with densities and

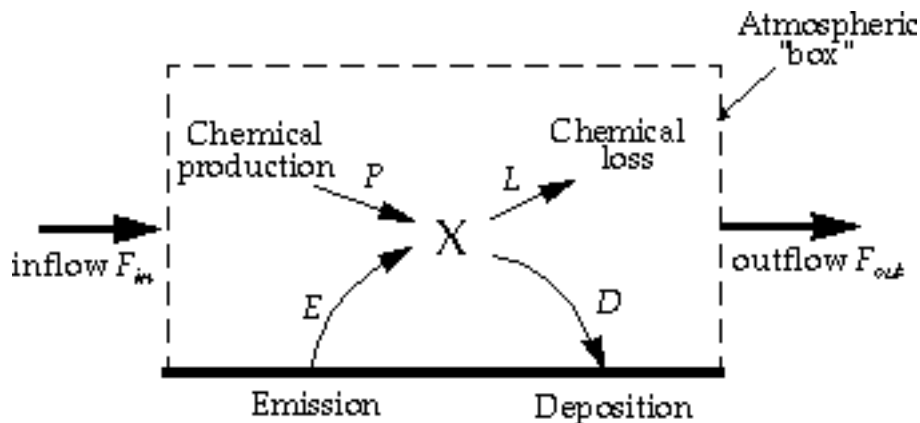


FIGURE 1.9: Standard box model parameters, reproduced from Jacob (1999).

transport calculated and stored for sequential steps in time at each location. The mass balance equation must be satisfied in any realistic long term model and is as follows:

$$\begin{aligned}\frac{dm}{dt} &= \sum \text{sources} - \sum \text{sinks} \\ &= F_{in} + E + P - F_{out} - L - D\end{aligned}$$

where m is mass of a chemical, E and D are emission and deposition, P and L are production and loss, and F is chemical transport in and out, as shown in figure 1.9. Many chemical species interact with each other through production and loss. Any large chemical model will solve this mass balance equation over highly coupled arrays of partial differential equations, which becomes computationally expensive as complexity increases.

Contemporary models generally use mathematical differential solving tools of various complexity (often called chemical mechanisms) to solve chemical equations in order to predict chemical species evolution over time. Different solvers may be slower or faster, and some are more suited to particular situations. The choice of chemical mechanism is normally driven by the mathematical properties of the equations and systems being modelled (such as stability and stiffness), as well as limitations around processing power. Grouping together subsets of model equations or chemical species is often performed and it is possible to use different solvers on each grouping. For example: since $[O] \ll [O_3]$ the chemical family O_X ($O_X \equiv O + O_3$) can be used to simplify chemistry simulations and approximate O_3 concentrations (Brasseur and Jacob 2017, Chapter 3). Different chemical mechanisms may find different solutions to the same problems, due to how the numerical solvers are implemented, which can affect model output (Zhang et al. 2012).

1.5.3 Emissions

The general formula governing modelled emissions E for a species i (from Brasseur and Jacob (2017)) is as follows:

$$E_i = A \times EF_i \times S_i \quad (1.7)$$

with A the activity rate, EF_i being the emission factors, and S_i is a scaling factor accounting for meteorology and other effects not included in A or F (eg. seasonal temperature). For example, to estimate isoprene emission E_{isop} per second for an area, the equation becomes A = how many trees in an area multiplied by EF_{isop} = isoprene emitted per tree per second multiplied by S_{isop} = a scaling factor based on temperature and soil moisture. This is a simplified example of a bottom-up estimate, one commonly used technique for estimating isoprene emissions. Bottom-up emission estimates use information about the flora that emit isoprene, along with the rates of emissions and meteorological parameters that affect these rates. The other common emission estimation technique is termed top-down. Top-down emissions estimates are derived from measurements of the child products of emitted VOCs. For example, GOME satellite HCHO and a Bayesian inversion technique have been used to estimate isoprene emissions of $\sim 566 \text{ Tg C yr}^{-1}$ globally (Shim et al. 2005).

1.5.4 Uncertainties

This section summarises the major uncertainties models have in relation to VOCs, and ozone. Atmospheric chemical models by necessity use simplifications of real world processes, and also utilise information that may be itself uncertain or extrapolated. Uncertainty is introduced through both of these channels as well as through computational limitations.

1.5.4.1 Emissions Inventories

Model results can be greatly affected by the choice of emissions inventory used to provide boundary conditions. Natural (biogenic or pyrogenic) and anthropogenic emissions often drive a large fraction of atmospheric oxidation and radical chemistry, especially in the continental boundary layer. Emissions inventories have been found to be reliable at larger (regional to global) scales, as long as they are derived from accurate input measurements (Zeng et al. 2015). Modelled ozone concentrations have been found to be sensitive to isoprene emissions and NO_x sources, both of which are uncertain within approximately a factor of 2 (Christian, Brune, and Mao 2017). Bottom up inventories of biogenic VOCs (BVOCs) remain largely uncertain due to missing or extrapolated plant functional type information, changing land cover, and parameterised environmental stressors (Guenther et al. 2000; Kanakidou et al. 2005; Millet et al. 2006). Global emissions inventories like MEGAN often implement data extrapolation, which also introduces uncertainties (Miller et al. 2014).

Modelled surface ozone may be overestimated if NO_x emissions are too high, due to their affects on the oxidative capacity of the atmosphere (Travis et al. 2016). NO_x and isoprene emissions have been shown to be the most significant sources of uncertainty for ozone concentrations near the surface over the US, while isoprene-derived

products and lightning NO_x drives uncertainty in the upper atmosphere (Christian, Brune, and Mao 2017).

Estimates of isoprene emission are based on a few algorithms that can depend greatly on parameterised inputs such as temperature, sunlight, plant type, plant coverage, plant health, etc. (Arneth et al. 2008; Niinemets et al. 2010). Sensitivity to these factors is pervasive in bottom up emissions models (e.g., Marais et al. 2014; Miller et al. 2014; Messina et al. 2016). Arneth et al. (2008) argue that the monopoly of isoprene emission estimates may be leading us to an incorrect understanding of isoprene chemistry. VOC emissions form an integral part of many chemistry models, and poor characterisation of these can lead to many more problems in other models (Yue, Unger, and Zheng 2015, e.g.). Models that depend on VOC emissions acquire the uncertainties and sensitivities (for example, to light and temperature parameters) found in VOC emissions (Yue, Unger, and Zheng 2015). This can be mitigated where measurements are used to constrain parameters (e.g., Stavrakou et al. 2014).

Modelled emissions are sensitive to soil moisture, especially near the wilting point, below which trees stop emitting isoprene and other VOCs completely as they can no longer draw water (Bauwens et al. 2016). MEGAN accounts for soil moisture through a parameterisation that drops plant emissions to zero below a prescribed soil moisture level (the wilting point). Jiang et al. (2018) found that improving the parameterisation of drought based on a measurement campaign in the U.S. would lower isoprene emissions globally by $\sim 17\%$.

Chamber studies are often used to inform modelled isoprene reactions (e.g., Paulot et al. 2009b). However these results come with their own uncertainties, not the least of which comes from the difficulty of reproducing ambient air in laboratory conditions (Nguyen et al. 2014). Structural uncertainties (differences between different measurement techniques) in measurements also occur, which increases the difficulty of assessing isoprene data-sets.

1.5.4.2 Resolution

Atmospheric chemistry simulations are somewhat sensitive to the gridbox resolution. Reducing model resolution can increase OH concentrations and ozone production rates (Wild and Prather 2006). Increasing model resolution can also impact OH, HO₂, and ozone concentrations (e.g., Christian, Brune, and Mao 2017). Yu et al. (2016) show that only at higher resolution (0.25 by 0.3125°) does isoprene oxidise under the correct NO_x pathway (through high or low NO_x pathways, see Section 1.3.3) in variable NO_x environments. This leads to an increase of high NO_x pathway oxidation of isoprene at the lower resolutions, which leads to an overestimation of HCHO but not ozone at coarser resolutions. However, for many global scale analyses, errors from resolution are less important than those from chemistry, meteorology, and emissions (Christian, Brune, and Mao 2017; Christian et al. 2018).

1.5.4.3 Chemistry mechanisms

Chemical mechanisms in several contemporary models are likely inadequate (Marvin et al. 2017), especially for isoprene oxidation, with changes to reaction rates being

inadequate to fix discrepancies from measurements. Ozone uncertainties are also affected by inadequate mechanisms, with for example ozone concentrations simulated by one model (GEOS-Chem) most sensitive to NO_2 photolysis, the $\text{NO}_2 + \text{OH}$ reaction rate, and precursor emissions (Christian, Brune, and Mao 2017).

1.5.4.4 Clouds

One of the major uncertainties in chemical models is cloud formation and dynamics. Clouds are remarkably complex at a much finer scale than can be accurately modelled by global chemistry models (with current processing power). Globally over half (50-60%) of the world is covered by clouds, with $\sim 10\%$ of them being rain-clouds (Kanakidou et al. 2005). Wet scavenging in clouds not only depends on large scale cloud processes, but also on the microphysics of aerosols being scavenged, and these processes must be parameterised in coarse resolution models.

1.6 Australia and the southern hemisphere

Australia is unique, with its own climate, soil moisture, clay content, plant species, ecosystem life-cycles, agricultural and mining practices, transport corridors, and many other important properties that affect emissions, atmospheric chemistry, and ultimately atmospheric composition. Many regions in Australia are difficult or expensive to reach, and measurement campaigns are limited. In Australia, most long term air quality or composition measurements are performed in or near large cities. Australia is dominated by areas with little anthropogenic influence, and few ground based measurements of natural emissions take place (VanDerA et al. 2008). Since many Australian cities are on the edge of regions with rich VOC emissions, it is very important to clarify the quantity, type, and cause of VOC emissions. Understanding of emissions from these areas is necessary to inform national policy on air pollution levels.

Ozone enhancements above the background levels are most sensitive to emissions (of precursor gases), with meteorology, and atmospheric composition also important. Anthropogenic emissions of ozone precursors are important but relatively stable, while pyrogenic sources are greatly variable and dependent on weather, fuel, and fire intensity (e.g., Lawson et al. 2017). Biomass burning in southern Africa and South America has previously been shown to have a major influence on atmospheric composition in Australia (Oltmans et al. 2001; Gloudemans et al. 2006; Edwards et al. 2006), particularly from July to December (Pak et al. 2003; Liu et al. 2016a). Local fires are even more influential and the burning season for Australia can be all year, although distinct burning seasons for different regions are also apparent (Russell-Smith et al. 2007). Bushfire severity depends on regional vegetation, recent and current weather, and El Niño phase.

1.6.1 Ozone

Surface ozone levels over Australia are relatively low (~ 20 ppb) (Young et al. 2017). It remains unclear how ozone will change in the future as relatively little is known about precursors and influx for the continent. Australian air quality is monitored independently within each state. Measurement stations are generally located in population

centres, which means there is a lack of natural emissions. Natural emissions can be important in urban regions as they can characterise the inflow, and affect air quality through production of O₃ and other pollutants. Overall in the southern hemisphere there are relatively few records of ozone (Huang et al. 2018). This affects our ability to accurately determine sources of ozone in the troposphere, with current southern hemisphere trends lacking full explanation (Zeng et al. 2017).

Generally STT of ozone over Australia only affects the upper troposphere; however, ozone enhancements can reach low altitudes during heavy storms and cyclonic weather patterns (Alexander et al. 2013). The contribution of STT to overall tropospheric ozone budgets remains uncertain, especially in the southern hemisphere (Škerlak, Sprenger, and Wernli 2014). STT can enhance surface ozone concentrations above legal air quality limits (e.g., Lelieveld et al. 2009; Lin et al. 2015). Detecting ozone enhancements over the background profile in the relatively clean southern ocean atmosphere is simple. However, measurements of ozone over this region are sparse (Škerlak, Sprenger, and Wernli 2014), and quantification of transported ozone is difficult without large scale extrapolations. Ozone enhancements over the southern ocean signify either transported pollution or stratospheric influx (Jacobson and Hansson 2000). Quantifying ozone processes over the southern ocean could improve our understanding of chemistry in the “clean background environment”, while additionally helping to validate model and satellite datasets. This poorly understood background composition forms the inflow of air into urban areas, and an improved understanding is required in order to model and attribute pollution and composition in these areas also.

1.6.2 Biogenic VOCs

The vegetation in Australia is diverse. Figure 1.10 shows the different forest types and their locations within Australia, highlighting that much of our forested lands are frequently found near population centres along the east coast. 16% of Australia is covered by forest, most (75%) of which is Eucalyptus, a major emitter of VOCs (Guenther et al. 2012).

It has been estimated by MEGAN that Australian vegetation is among the world’s strongest isoprene emitters, with forests in SE Australia having emission factors greater than 16 mg m⁻² h⁻¹ (see figure 1.11) (Guenther et al. 2006; Guenther et al. 2012). Measurement campaigns in SE Australia have since cast doubt on the emission factors used by MEGAN, potentially due to poor characterisation of Eucalyptus trees and soil moisture (Emmerson et al. 2016; Emmerson et al. 2019). These emissions factor estimates are not well verified and measurements of isoprene (or other BVOC) emissions are sparse and infrequent in Australia (Sindelarova et al. 2014; Bauwens et al. 2016).

Australia has a much greater diversity of tree species than is represented by MEGAN, however sparse measurements of emissions and BVOC concentrations makes model improvement difficult. Uncertainties in isoprene emissions could explain why models of HCHO over Australia are poor at reproducing satellite measurements (Stavrakou et al. 2009).

Australia suffers from poor characterisation of plant emissions, partly because many of the emission factors are based on northern hemispheric data. Many plant emissions rates have not been published, such as those for any Australian acacias.

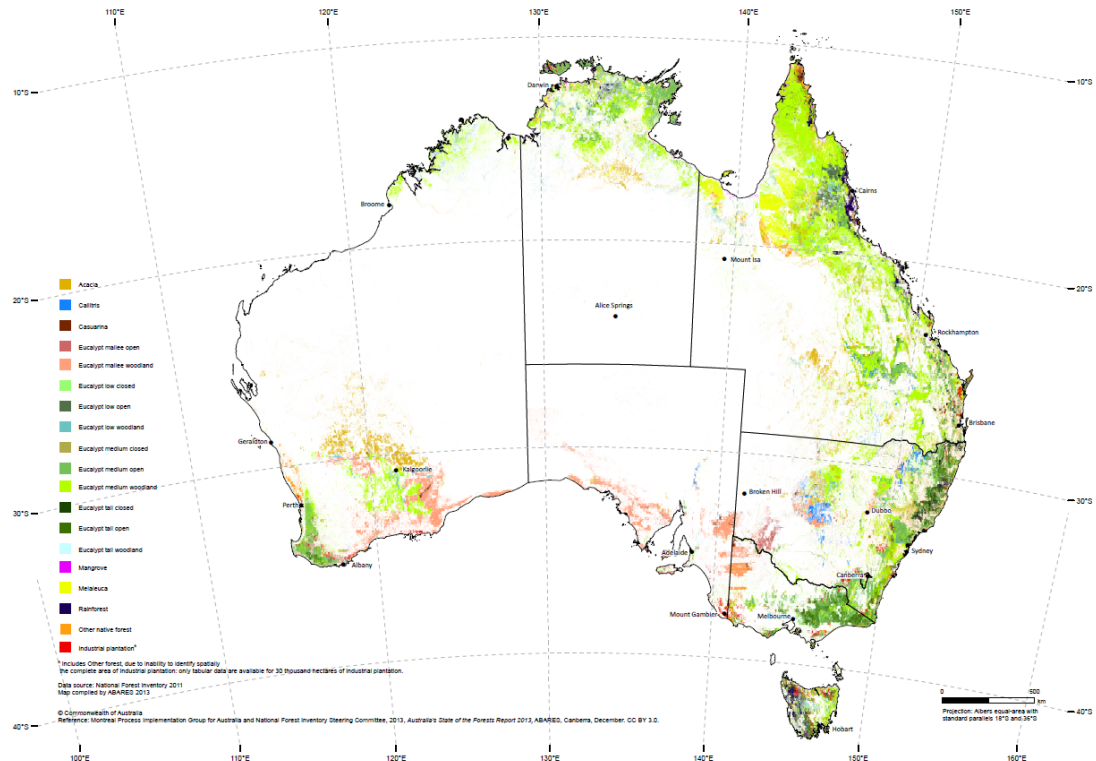


FIGURE 1.10: Forest types in Australia reproduced from <http://www.agriculture.gov.au/abares/forestsaustralia/australias-forests>.

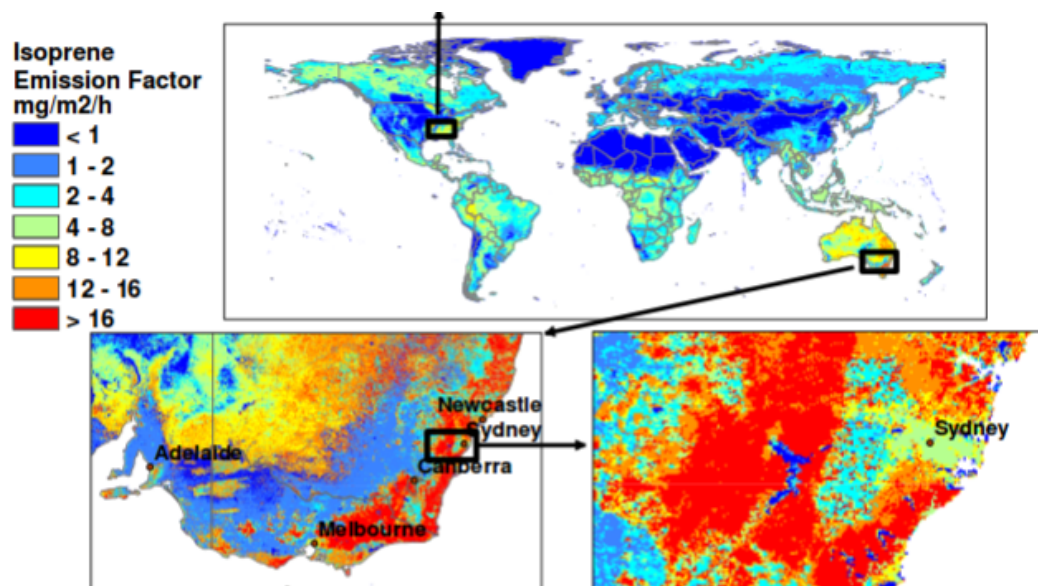


FIGURE 1.11: Global and Australian isoprene emission factors modified from Guenther et al. (2006).

Some Eucalypt emissions are based on samples from young trees, which may emit more isoprene than older trees (Emmerson et al. 2016). Changes in parameterisation of soil moisture in the MEGAN model lead to large reductions (38 – 58%) in Australian isoprene emission estimates, although errors remain (Sindelarova et al. 2014; Emmerson et al. 2019).

The only VOC emission information currently available come from three campaigns: the Measurements of Urban, Marine and Biogenic Air (MUMBA), and the two Sydney Particulate Studies (SPS1 and SPS2) (see Section 2.2). These measurements take place in south eastern Australia, and have suggested lower isoprene emissions than seen in models (by a factor of 2-6) (Emmerson et al. 2016). Several improvements are required as no simple scaling factor can completely fix the misrepresentation of isoprene emissions (Emmerson et al. 2016). These measurements focus on air quality and biogenic VOCs and use several different instruments (including PTR-MS and GC-FID) to detect metrics such as air particulates, HCHO, isoprene, and meteorological information. Isoprene and many of its products can be difficult to measure accurately due to their short lifetimes, high reactivity, and optically thin natures. There is also an instrument at University of Wollongong (see Section 2.2.3.4) that provides 20 years of HCHO measurements, which is the only available long term HCHO vertical column measurement comparable to satellite data. Satellite HCHO column measurements can be limited by various factors including interfering species, water, clouds, orography, etc, and independent in-situ measurements are required to validate the data. For further details on these campaigns and measurements, see Section 2.2.

Improvements to emissions models require improved understanding of emissions from Australian vegetation and how they respond to meteorological and chemical parameters. However, constraining these processes is difficult given the lack of available isoprene measurements. Satellite measurements of HCHO can instead be used to estimate and improve Australian isoprene emissions without costly measurement campaigns. This is due to the near-linear relationship between HCHO and isoprene emissions (e.g., Palmer et al. 2001; Millet et al. 2006; Bauwens et al. 2016). This method is explored in this thesis as described in Chapter 3.

1.7 Aims

In this thesis I aim to improve understanding of natural contributions to ozone over Australia and the southern ocean. The two largest contributors to tropospheric ozone concentrations are chemical production (driven by precursor emissions) and transport from the stratosphere. I aim to improve understanding of both of these sources using existing satellite and ground-based datasets along with modelled outputs from the GEOS-Chem chemical transport model.

Estimation of BVOC emissions in Australia can be improved through satellite measurements of HCHO, one of isoprene's primary oxidation products. Satellites that overpass daily record measurements over all of Australia. Combining satellite data with model outputs provides a platform for the understanding of natural processes, which are uncertain over Australia. Satellite measurements require modelled a priori vertical profiles of HCHO to estimate total column amounts. **I aim to recalculate satellite vertical columns of HCHO using updated model a priori information.** In this

effort I aim to improve the understanding of the importance of relevant parameters (within GEOS-Chem) in calculating vertical columns of HCHO measured by satellite. This includes an examination of how well GEOS-Chem simulates several species such as NO_x , isoprene, and HCHO compared to both in-situ and remote measurement data that exists for Australia. Additionally, I detail the construction and effects of satellite data filters. The work towards this aim is detailed in Chapter 2.

The technique of determining isoprene emissions from satellite detected HCHO is called satellite inversion. **I aim to determine isoprene emissions in Australia using a top-down inversion of satellite HCHO, through a modelled yield from isoprene to HCHO.** HCHO amounts and the yield of isoprene to HCHO over Australia is required to create top-down estimates. This process also requires careful examination of when the assumptions required within the inversion process are not valid. Due to the low availability of in-situ data over most of the Australian continent, a combination of modelled and satellite data can reduce the uncertainties of isoprene emissions from Australian landscapes. Improved emissions estimates will in turn improve the accuracy of CTMs, providing better predictions of atmospheric composition and its response to ongoing environmental change. The work towards fulfilling this aim is in Chapter 3.

Stratospheric transport is the second largest driver of tropospheric ozone concentrations, and an improved understanding of transported ozone can be determined from ozonesonde measurements. **I aim to improve understanding of ozone transported to the troposphere from the stratosphere in Australia and the southern ocean.** Ozonesondes provide a glimpse of the vertical ozone profile up to ~ 30 km, and I use a Fourier filter to determine how often stratospheric transport is occurring at three sites: Melbourne, Macquarie Island, and Davis Station. Transport event frequency analysis combined with modelled ozone distributions is used to derive a new method of detection and quantification of transported ozone as described in Chapter 4.

Overall, I aim to describe relative importance of sources of tropospheric ozone in Australia, as well as their seasonality. I will describe how modelled ozone is affected by updated isoprene emissions, comparing changes in GEOS-Chem outputs, and by ozone transport from the stratosphere.. This thesis will provide new insight into tropospheric ozone in Australia.

Chapter 2

Data and Modelling

2.1 Introduction

In this thesis the word model is used in lieu of chemical transport model (CTM), a class of model that simulates chemistry and chemical transport through the atmosphere. Models of the atmosphere can be used to interpret measurements, estimate chemical concentrations at any scale, and predict atmospheric composition in the future. Some advanced measurement techniques make use of modelled a priori information in order to produce useful outputs. Models of ozone in the atmosphere are used broadly for international assessments of ozone precursor emissions, and estimating effects from related processes (such as radiation) (Young et al. 2017). Models provide an estimate of many trace gas concentrations; however, verification is required, and is generally performed using results from measurement campaigns. In situ measurements from campaigns or measurement stations can be used to examine what is happening at a particular location. These data are used to determine how accurate models or estimates are - however the utility is limited to where and when the measurements took place. In this thesis data from several campaigns are compared against model outputs and satellite datasets. Satellite datasets provide large amounts of data over most of the planet. However, they can have high uncertainty due to instrument limitations. In this chapter several satellite datasets are combined to estimate biogenic HCHO amounts over Australia.

The first goal is to analyse Australia-specific HCHO concentrations measured by satellite. This leads into Chapter 3 where biogenic HCHO columns are used to estimate isoprene emissions. The second goal is to quantify ozone transported from the stratosphere down into the troposphere (Chapter 4). The focus in this chapter is to describe and analyse model outputs and measurements along with how they are recalculated and compared. Section 2.2 details satellite and campaign datasets, and describes model outputs. Measurement techniques used to retrieve the most utilised satellite dataset are outlined in Section 2.3. Section 2.4 describes the GEOS-Chem model, how it is run and what setup and outputs are used in this thesis. In Section 2.5 the process of using model outputs to recalculate satellite vertical columns is defined and analysed. In order to compare satellite data with other datasets, some work must be undertaken to avoid introducing bias (e.g., Palmer et al. 2001; Eskes and Boersma 2003; Marais et al. 2012; Lamsal et al. 2014). One key step is to recalculate the satellite information using modelled data, detailed in Section 2.6. The effects of these recalculations on satellite HCHO is also examined. The creation and effects of filters used to remove non-biogenic influences are described in Section 2.7.

2.2 Datasets

This section describes the datasets used in this thesis, along with an overview of the measurement techniques used for each. This includes modelled output, satellite measurements, and measurement campaigns. These datasets serve four purposes:

1. Model output validation in this chapter
2. Calculation of biogenic HCHO distribution over Australia in this chapter
3. Recalculated OMI formaldehyde columns are used as a basis for estimating isoprene emissions in Chapter 3
4. Extrapolation of ozone transport in Chapter 4

Details on filtering and interpolations which are undertaken when reading data are also provided, as each dataset has its own resolution. While no measurements are made throughout this thesis, it is important to understand the techniques used to create utilised datasets in order to understand possible anomalous datapoints or trends.

Horizontal geographical coordinates are always discussed in terms of degrees north and east, from -180° to 180° spanning west to east around the globe and -90° to 90° spanning the latitudes from the Antarctic to the Arctic. Vertical resolution is sometimes discussed in terms of metres, sometimes in terms of pressure (hPa), and sometimes in terms of sigma (σ) coordinates. Sigma coordinates represent the fraction of the atmosphere vertically above, with $\sigma = 1$ being the surface and $\sigma = 0$ being the top of the atmosphere (TOA). This can be useful when running global atmospheric models as the ground altitude is always at $\sigma = 1$ and we need not worry about topography. Conversion between σ and pressure (p) coordinates is as follows:

$$\sigma = \frac{p_s - p}{p_s - p_T} \quad (2.1)$$

where p_s and p_T is surface pressure and pressure at the TOA respectively.

Uncertainty (or error) is present in each dataset and where possible the causes are explained. There are two types of error: systematic and random. Arguably the worst of these is systematic error (or bias). Bias normally indicates a problem in calculation or instrumentation. If the systematic error is known, it can be corrected for by either offsetting data in the opposite direction, or else fixing the cause. A proper fix can only be performed if the sources of error are known and there is a way of correcting or bypassing it. Random error is often reported as some function of a datasets variance, or uncertainty. It can be reduced through averaging either spatially or temporally. Temporal and/or spatial averaging decreases uncertainty by a factor of $1/\sqrt{N}$ where N is the number of observations being averaged.

2.2.1 Satellite

Satellite data products are generally classed into several categories, level 0 through to level 3. Level 0 products are sensor counts and orbital swath data, level 1B data calibrates and geo-locates the level 0 data. Level 2 products additionally have temporal, spatial, solar, and viewing geometry information, as well as quality flags. To

create level 2 data slant column density is determined and then translated into vertical column density. Level 3 data is a temporally aggregated subset of level 2 data, for instance monthly or yearly averages.

Satellites record near nadir (vertical) reflected spectra between around 250-700 nm split into spectral components at around 0.3 nm in order to calculate trace gases including O₃, NO₂, and HCHO (e.g., Leue et al. 2001). Satellite measurements are generally performed using spectral fitting followed by conversion to vertical column densities. Several public data servers are available which include products from satellites, including NASA's Earthdata portal (<https://earthdata.nasa.gov/>) and the Belgian Institute for Space Aeronomy (IASB-BIRA) Aeronomie site (<http://h2co.aeronomie.be/>).

Rayleigh and Mie scattering describe two kinds of particle effects on radiation passing through a medium. Rayleigh scattering is heavily wavelength dependent, and is the dominant form of scattering from particles up to roughly one tenth of the wavelength of the scattered light. Mie scattering mostly involves larger particles, and has less wavelength dependence. The effects of scattering provide information about substances in the atmosphere, as different particles and gases in the air have measurable properties seen by remote sensing devices (such as a satellite). Instruments are more or less sensitive to these properties depending on altitude, radiation, and other parameters (e.g., Martin et al. 2002b).

Difficulties can arise when aerosols (e.g., clouds, smoke, dust) interfere with recorded spectra; however, some of these can be detected and filtered out. Instruments including MODIS onboard the Aqua and Terra satellites are able to determine aerosol optical depth (AOD), a measure of atmospheric scatter and absorbance. An AOD under 0.05 indicates a clear sky, while values of 1 or greater indicate increasingly hazy conditions. This is important in order to determine where measurements from other instruments may be compromised by high interference. Cloud filtering is performed on several satellite products used in this thesis, which reduces uncertainty at the cost of measurement quantity. This has been seen to introduce a clear-sky bias in monthly averages since measurements do not include cloudy days (Surl, Palmer, and Abad 2018).

Satellite measured AOD requires validation by more accurate ground based instruments like those of AERONET which uses more than 200 sun photometers scattered globally. Soon much more satellite data will be available in the form of geostationary satellite measurements (Kwon et al. 2017). Geostationary satellites can provide temporally rich measurements over an area, as they are not sweeping around the earth but fixed relative to one latitude and longitude.

2.2.1.1 Formaldehyde

OMI spectra are used in several products used in this thesis, including OMHCCHO, OMNO2d, and OMAERUVd. Satellite based formaldehyde measurements from the OMI instrument onboard Aura are stored in the OMHCCHO product. OMHCCHO data is used and modified extensively throughout this thesis, and so is discussed in more detail in Section 2.3. Calculation of column density and AMF are discussed respectively in sections 2.3.2 and 2.3.3.

HCHO products can be found in four satellite instruments: GOME on ERS-2, SCIAMACHY on ENVI-SAT, OMI on EOS Aura, and GOME2 on MetOp-A. These

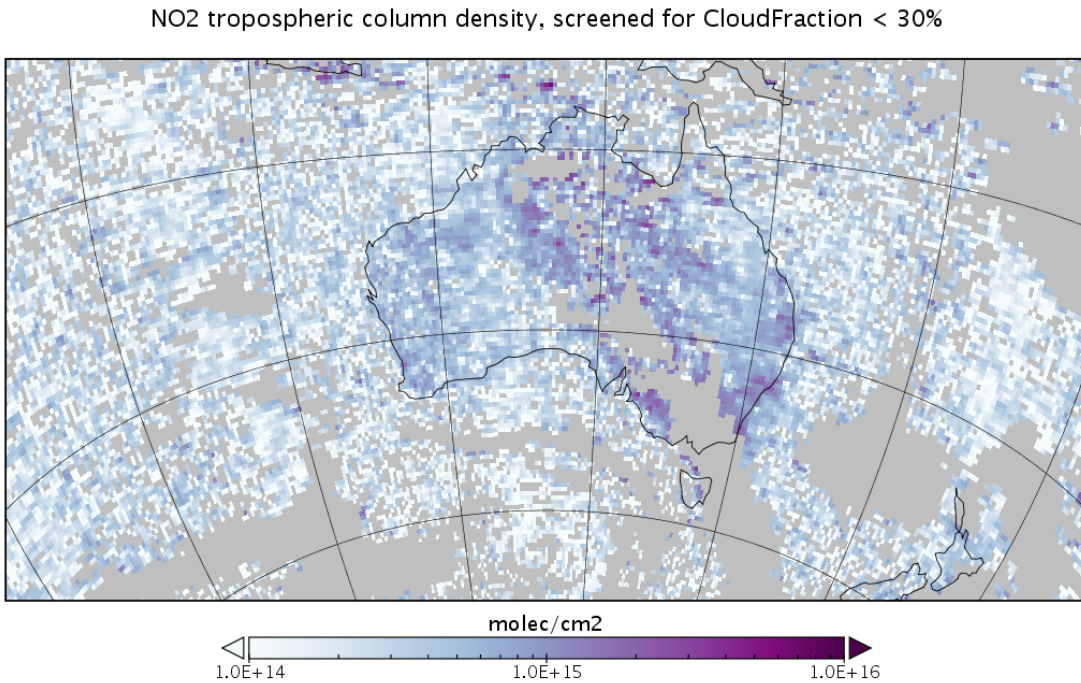


FIGURE 2.1: Example of NO₂ tropospheric columns taken from the OMNO2d product.

satellites have slightly different spectral and spatial resolutions, as well as using varied processes to estimate HCHO from detected radiances. This leads to different measurements between instruments (Lorente et al. 2017), and both validation and comparison become more important when using these remotely sensed data. The data set used in this thesis is from the Ozone Monitoring Instrument (OMI) onboard the Aura satellite, as it has data over the time period covered by GEOS5 modelled meteorological information used in GEOS-Chem, and sufficiently covers the southern hemisphere.

2.2.1.2 Nitrogen dioxide

OMNO2d is a gridded daily level three NO₂ product of satellite measurements averaged into $0.25 \times 0.25^\circ$ horizontally resolved bins. An example figure from Jan 29, 2005 is shown in Figure 2.1, while an average for 2005 (global) is shown in Figure 2.2. OMNO2 measurement resolution is 40 km by 130 km. NO₂ measured by OMI is used to check whether NO₂ is well represented by GEOS-Chem (see Section 2.4.6 for the comparison between this product and GEOS-Chem calculations). It is also used to form the anthropogenic influence filter for OMHCHO (See Section 2.7.2).

Like other satellite products, OMNO2d is influenced by a priori modelling which is required to convert slant path radiance to vertical columns. These models are generally low resolution ($\sim 110 \text{ km} \times 110 \text{ km}$), which leads to column smearing and difficulty detecting point sources of high NO emissions (Goldberg et al. 2017). Uncertainty in this product arises mostly from the calculation of the AMF (up to 50% of total error) (Lorente et al. 2017).

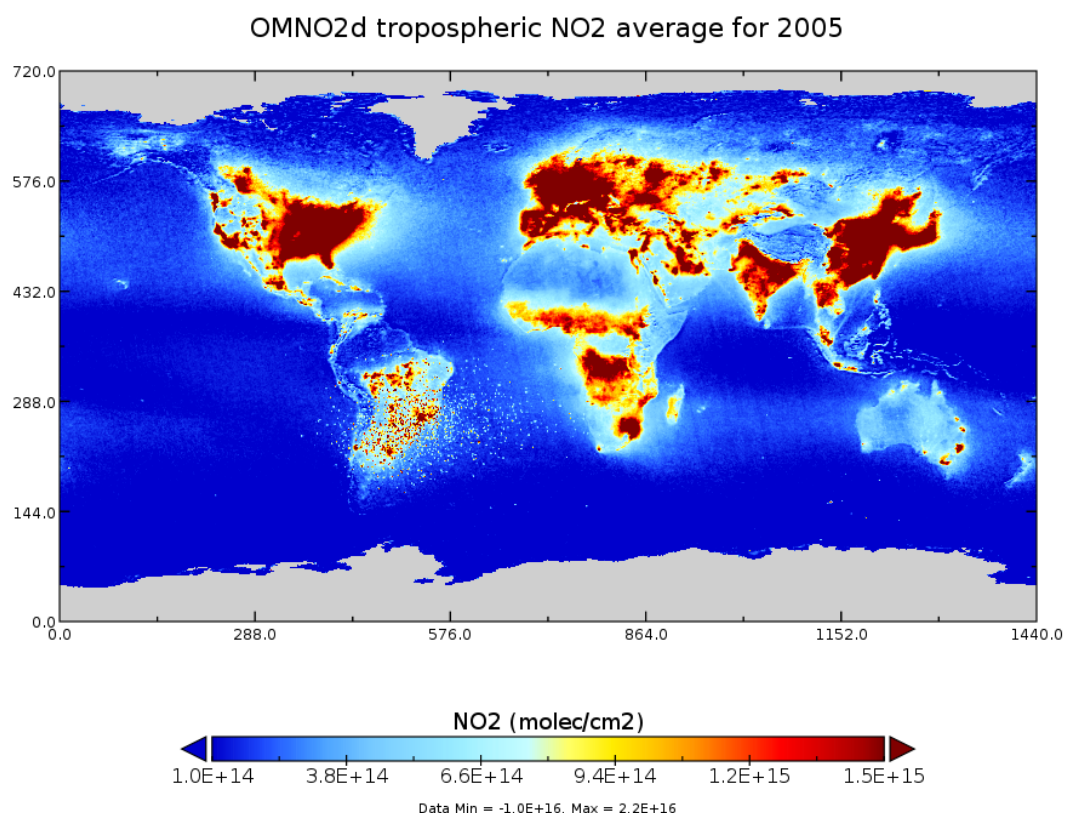


FIGURE 2.2: Average 2005 tropospheric NO₂ from OMNO2d with pixels screened for < 30% cloud cover.

2.2.1.3 Aerosol optical depth

Aerosols in the atmosphere can be seen through their affects on light. Smoke and dust can be seen as an increase in aerosol optical depth (AOD) (see Section 2.3.2). This is due these particles scattering and absorbing UV radiation (Ahn, Torres, and Bhartia 2008). A data product provided by Earthdata (https://disc.gsfc.nasa.gov/datasets/OMAERUVd_V003/summary) called OMAERUVd (DOI: 10.5067/Aura/OMI/DATA3003) is used in this thesis.

OMAERUVd allows detection of areas which may be smoke affected. The product contains AOD and aerosol absorption optical depths (AAOD) at three wavelengths (354, 388, and 500 nm), along with UV aerosol index. The OMAERUVd product is level three, based on quality filtered level two swath pixels which are then gridded by daily averaging. The product is most sensitive to error in the form of sub-pixel scale cloud interference, so AAOD is used in this thesis to create as it is least affected by clouds (Ahn, Torres, and Bhartia 2008).

In this work AAOD is mapped from $1 \times 1^\circ$ horizontal resolution to $0.25^\circ \times 0.3125^\circ$ using nearest value mapping. The AAOD at 500 nm wavelength is used to determine smoke influence, although any of the provided wavelengths would be affected by smoke plumes and could also be used. This daily AAOD is compared to a threshold to create a daily smoke filter, any areas with $\text{AAOD} > 0.03$ are considered to be potentially smoke plume affected (see Section 2.7.1).

2.2.1.4 Active fires

MOD14A1 is a gridded daily satellite based dataset of fire counts at $1 \times 1 \text{ km}^2$ horizontal resolution. Fire observations are performed four times daily from Terra (10:30 LT, 22:30 LT) and Aqua (01:30 LT, 13:30 LT). The fire pixels are detected based on parameters including apparent pixel temperature and the nearby background temperature. The dataset is obtained from NASA Earth Observations that is part of the EOS Project Science Office at the NASA Goddard Space Flight Center https://neo.sci.gsfc.nasa.gov/view.php?datasetId=MOD14A1_M_FIRE. This product is downloaded and binned into a lower resolution (using the sum of fire pixels) to create an active fire influence mask (see Section 2.7.1).

2.2.1.5 Carbon monoxide

In Chapter 4, potential biomass burning plumes are identified using satellite observations of CO from the AIRS (Atmospheric Infra-red Sounder) instrument aboard the Aqua satellite (Texeira 2013). CO is used as a proxy for biomass burning plumes, and used to qualitatively attribute ozone intrusion events (Section 4.3.5). This is a method of detecting fire influence near specific sites through visual analysis.

2.2.1.6 Uncertainties

While satellite data is effective at covering huge areas (the entire earth) it only exists at a particular time of day, is subject to cloud cover, and generally does not have fine

horizontal or vertical resolution. Concentrations retrieved by satellites have large uncertainties, which arise in the process of transforming spectra into total column measurements, as well as instrument degradation (satellite instruments are hard to tinker with once they are launched). Uncertainty in transforming satellite spectra comes from a range of things, including measurement difficulties introduced by clouds, and instrument sensitivity to particular aerosols (Millet et al. 2006). Many products require analysis of cloud and aerosol properties in order to estimate concentration or total column amounts (Palmer et al. 2001; Palmer et al. 2003; Marais et al. 2012; Vasilkov et al. 2017). The main source of error in satellite retrievals of HCHO are due to instrument detection sensitivities, and calculation of the air mass factor (AMF) which converts slanted light path concentrations into a vertical profile (Millet et al. 2006). Calculations of the AMF performed by different groups tend to agree fairly well, as long as all the a priori and ancillary data is similar. Large differences can occur depending on the a priori vertical profile, trace gas concentrations, and cloud properties (Lorente et al. 2017). Choice of radiative transfer model and interpolation operations have a relatively small affect compared to the assumed state of the atmosphere, with high structural uncertainty introduced at this stage of AMF calculation (Lorente et al. 2017).

A common way of reducing satellite uncertainty is through oversampling or temporal averaging. This is done frequently for trace gases (which are often near to the detection limit over much of the globe). For example: Vigouroux et al. (2009) reduce the measurement uncertainty (in SCIAMACHY HCHO columns) by at least a factor of 4 through averaging daily over roughly 500km around Saint-Denis, and only using days with at least 20 good measurements. Another example of this can be seen in Dufour et al. (2008), where monthly averaging is used to decrease the measurements uncertainty at the cost of temporal resolution.

In cloudy, hazy or polluted areas measurements are more difficult to analyse (e.g., Palmer et al. 2003; Marais et al. 2014). Recent work by Vasilkov et al. (2017) showed that updating how the surface reflectivity is incorporated into satellite measurements can change the retrievals by 50% in polluted areas.

2.2.2 Model datasets

2.2.2.1 GEOS-Chem output

The GEOS-Chem model is used extensively in this thesis and is discussed in more detail in Section 2.4. GEOS-Chem model outputs are described in Section 2.4.7.1. These are generally resolved to 47 vertical levels from the ground up to 0.01 hPa, at $2^\circ \times 2.5^\circ$ horizontal resolution.

2.2.2.2 Meteorological reanalysis

Synoptic scale weather patterns are taken from the European Centre for Medium-range Weather Forecasts (ECMWF) Interim Reanalysis (ERA-I) (Dee et al. 2011). These are used in Chapter 4 to determine typical weather systems for stratospheric ozone intrusions. The ERA-I output was the most up to date at the time (2016) but has since been superseded by ERA5.

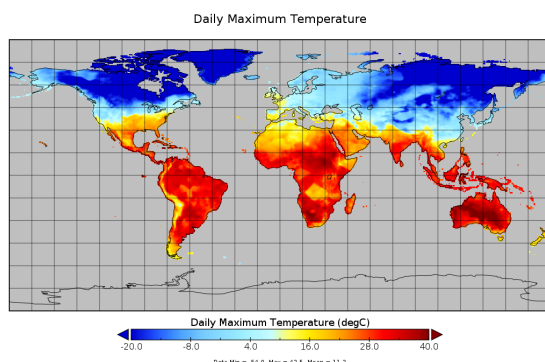


FIGURE 2.3: CPC daily maximum temperature dataset output for 1, Jan, 2005.

2.2.2.3 Surface temperatures

The Climate Prediction Center (CPC) provides a product with maximum daily land-surface temperature at $0.5 \times 0.5^\circ$ horizontal resolution. This data is used to check the correlation between HCHO and temperature at a higher resolution than is provided by GEOS-Chem output. A full description of the data can be found at <https://www.esrl.noaa.gov/psd/data/gridded/data.cpc.globaltemp.html>. CPC Global Temperature data is provided by NOAA/OAR/ESRL PSD, Boulder, Colorado, USA, from their web site at <https://www.esrl.noaa.gov/psd/>. An example of one day of land temperature output is shown in Figure 2.3.

2.2.3 Campaign datasets

Data from several measurement campaigns are used to examine the accuracy of modelled data at specific sites. Figure 2.4 shows the locations of BVOC measurement sites in the top panel, and release sites for ozonesondes in the bottom panel. These took place over disparate times, and are in situ measurements which are hard to directly compare against GEOS-Chem output which is averaged over a large horizontal space.

The campaign datasets provide three separate time series for brief periods of both isoprene and formaldehyde. Figure 2.5 shows these along with the detection limits and also shows isoprene measurements superimposed over a single year. It is apparent that more measurements are required to see more than the daily cycles.

2.2.3.1 Measurements of Urban, Marine and Biogenic Air (MUMBA)

The MUMBA campaign (Paton-Walsh et al. 2017) measured various compound abundances including isoprene, formaldehyde, and ozone from 21 December 2012 to 15 February 2013. These measurements took place in Wollongong, 10 m above ground level (40 m above sea level). Ozone was measured by Thermo UV absorption with 1-minute time resolution averaged into hourly outputs. Isoprene and HCHO were measured by Ionicon Proton-Transfer-Reaction Mass spectrometer (PTR-MS), with a

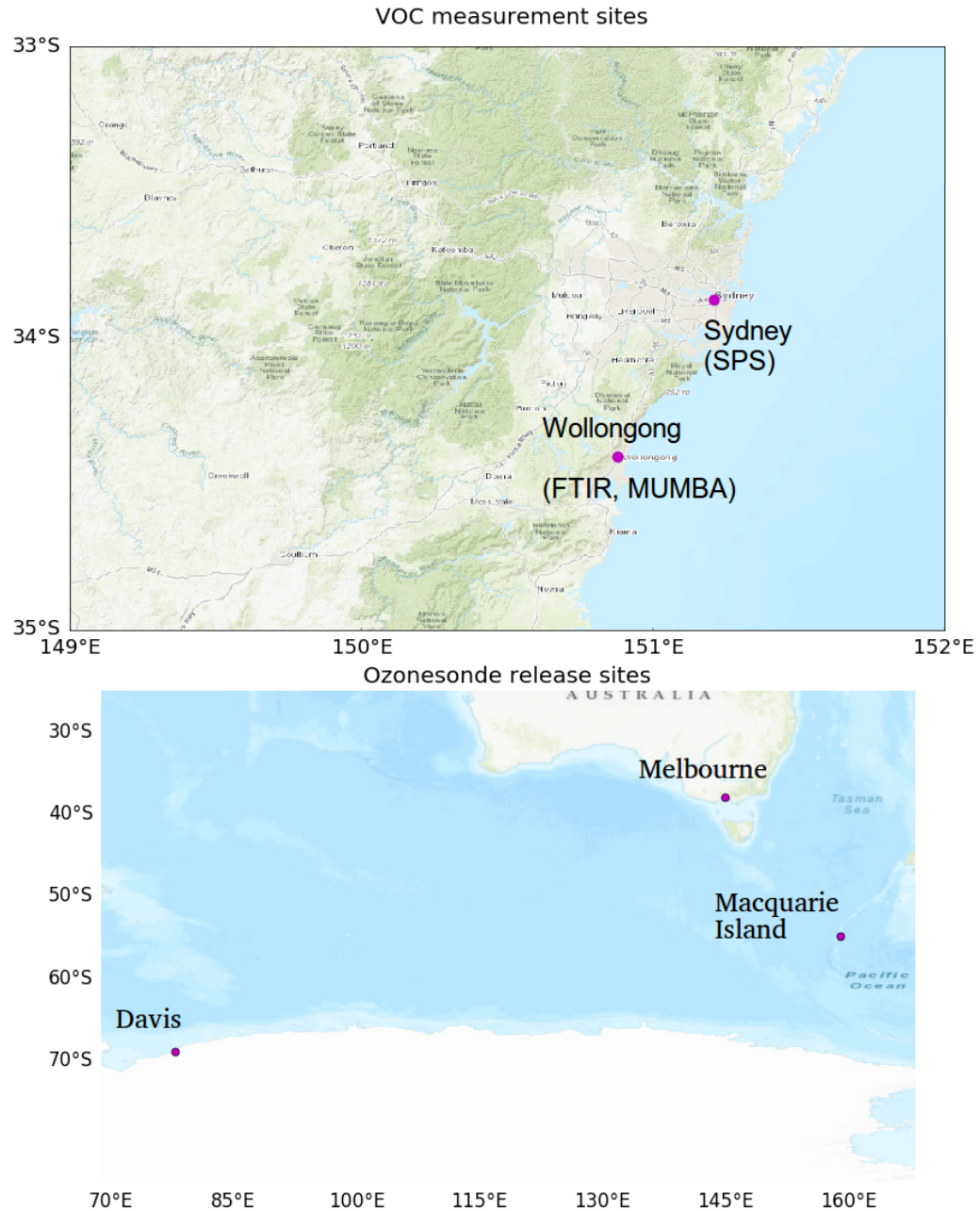


FIGURE 2.4: Locations of VOC measurements (top panel) and ozonesonde release sites (bottom panel). Inlaid in top panel is the flight paths over Australia of the HIPPO campaign.

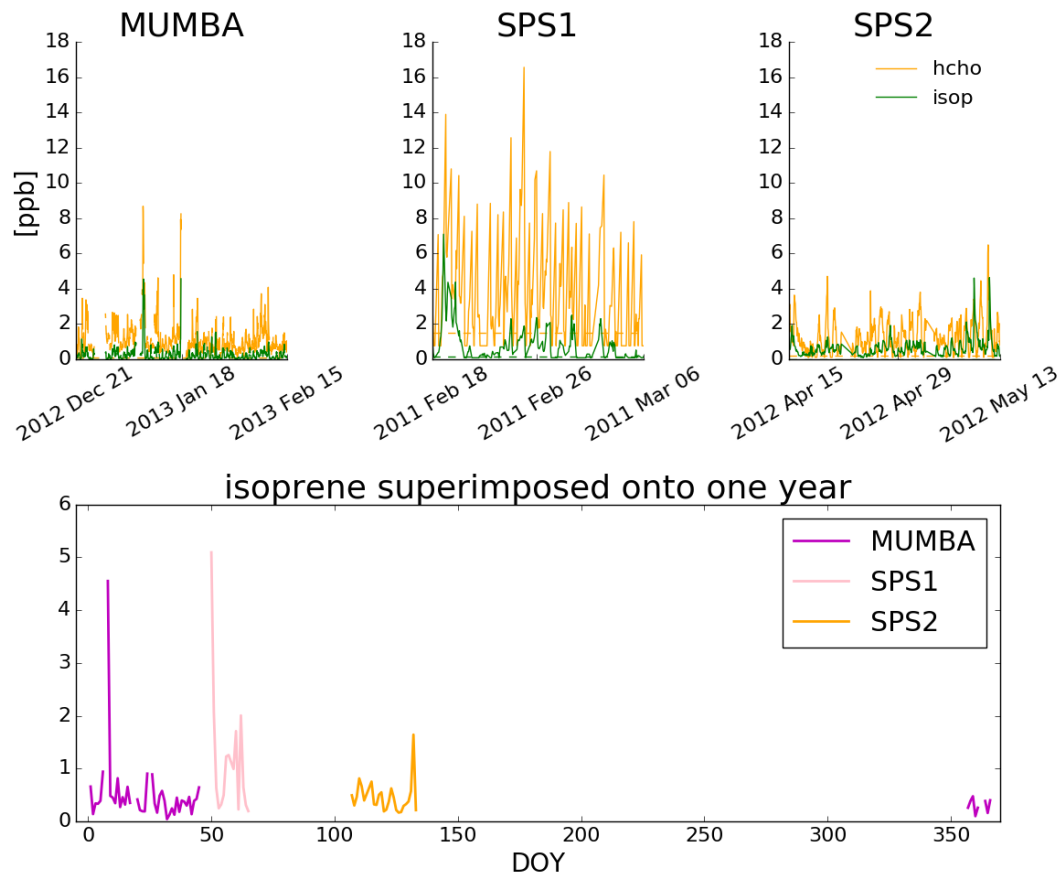


FIGURE 2.5: Top: MUMBA, SPS1, and SPS2 time-series for HCHO (orange) and isoprene (magenta), along with detection limits (dashed). Bottom: isoprene measurements superimposed onto a single year.

TABLE 2.1: Detection limits for MUMBA

Dates	HCHO (ppb)	Isoprene (ppb)	Ozone (ppb)
21/Dec/2012 - 29/Dec/2012	0.205	0.003	0.5
29/Dec/2012 - 18/Jan/2013	0.105	0.005	0.5
19/Jan/2013 - 15/Feb/2013	0.186	0.003	0.5

time resolution of 3-minutes, averaged each hour. Detection limits varied due to instrument conditions, and are listed in Table 2.1. The full dataset has been published on PANGAEA (DOI:10.1594/PANGAEA.871982) (Guérette et al. 2018).

Uncertainty in this product is estimated by Dunne et al. (2018) to be 50%. Although the uncertainty determined through calibration measurements was only 15% (Guérette et al. 2018), this does not account for competing trace gas interference (such as furan). When used in this thesis, readings are re-sampled to hourly averages, and measurements below the detection limit are set to half of the detection limit.

2.2.3.2 Sydney Particle Studies (SPS1, SPS2)

Two trace gas measurement campaigns took place at the Westmead air quality station. Stage 1 (SPS1) from 5 February to 7 March, 2011 and stage 2 (SPS2) from 16 April to 14 May, 2012. Two instruments measured VOC concentrations: a PTR-MS, and a gas chromatograph with a flame ionisation detector (GC-FID). The PTR-MS uses chemical ionisation mass spectrometry and can quantify VOCs at high temporal resolution (< 1 s). It was calibrated several times per day against HCHO, isoprene, α -pinene, and several other VOCs, further measurement specifics can be found in Dunne et al. (2018).

The output lists hourly averaged ppbv concentrations of trace gases based on the mass to charge ratio (m/z), which for isoprene is 69. It is possible that other chemicals (such as furan, with the same m/z) interfered with this value, especially at low ambient isoprene concentrations and towards the end of autumn (SPS2) when wood fires start to become frequent (Guérette et al. 2018). The GC-FID analysed samples collected in multi-absorbent tubes, with lower temporal resolution but no interference. Further details for this method can be found in Cheng et al. (2016). GC-FID data is averaged from 0500-1000 LT, and 1100-1900 LT, while PTR-MS data is averaged hourly. Significant differences occur between measurement devices when detecting isoprene, potentially due to interfering compounds in the PTR-MS (Dunne et al. 2018).

Figure 2.6 shows isoprene and formaldehyde over the course of these two campaigns, as well as the detection limits (dashed lines), as measured by PTR-MS. In order to compare with GEOS-Chem output (see Section 2.4) a daily average and an midday time (13:00-14:00 LT) average are both created from these data. In averaging, any measurements below the machine detection limit are set to half of the detection limit, as done in Lawson et al. (2015). This is performed to minimise any introduced bias.

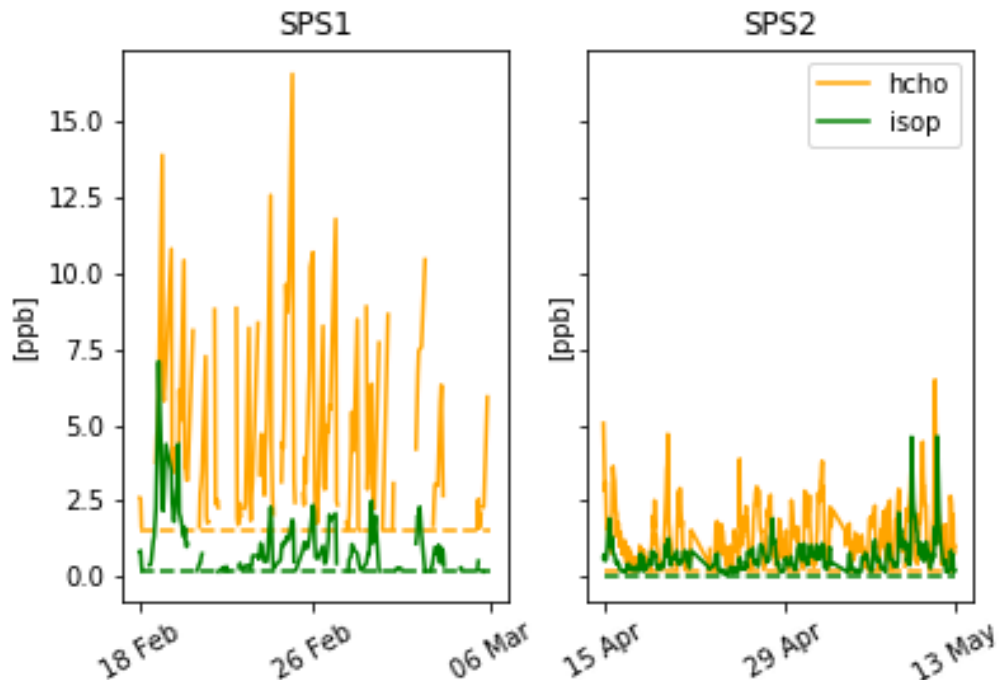


FIGURE 2.6: SPS HCHO (yellow) and isoprene (green) time series, along with detection limits (dashed). SPS 1 (left) took place in late summer 2011, while SPS 2 (right) occurred during autumn 2012.

2.2.3.3 Ozonesondes

Ozonesonde data come from the World Ozone and Ultraviolet Data Centre (WOUDC). Ozonesondes are weather balloons that measure ozone concentrations using an electrochemical concentration cell (<http://www.ndsc.ncep.noaa.gov/organize/protocols/appendix5/>). Ozonesondes provide a high vertical resolution profile of ozone, temperature, pressure, and humidity. Generally the instrument will perform 150-300 measurements ranging from the surface to around 35km.

Ozonesondes are launched approximately weekly from Melbourne (38° S, 145° E), Macquarie Island (55° S, 159° E) and Davis (69° S, 78° E). Melbourne, a major city with more than 4 million residents (ABS 2013), may be affected by anthropogenic pollution in the lower troposphere. Macquarie Island is in the remote Southern Ocean and unlikely to be affected by any local pollution events. Davis (on the coast of Antarctica) is also unlikely to experience the effects of anthropogenic pollution. More information on this dataset is given in Section 4.3.

2.2.3.4 Wollongong

Upon the roof of the Chemistry building at the University of Wollongong lies a solar Fourier transform infra-red spectrometer (FTIR) which measures HCHO (amongst other gases) in the path of light between the instrument and the sun. The instrument is part of the Network for the Detection of Atmospheric Composition Change (NDACC) and data can be retrieved from the NDACC database (<http://www.ndaccdemo.org/stations/wollongong-australia>). The current principle investigator producing and quality assuring the data set is Dr. Nicholas Jones.

Measurements of vertical profiles are affected by the instruments sensitivity to HCHO at all vertical levels. Vertical mixing ratios resolved to 42 vertical levels are created with the help of a priori assumed vertical profiles (x_{apri}). The averaging kernel (A) essentially represents how the retrieval technique is sensitive to HCHO concentrations. Figure 2.7 shows averaged retrievals x_{ret} and the a priori side by side. Most of the HCHO is close to the surface, and generally the a priori lies within the inter-quartile range of the retrievals, just below the mean. Figure 2.8 shows how the instrument based retrievals of total vertical column HCHO (Ω) in molec cm⁻² is sensitive to HCHO between 0 km and 60 km altitude. The panel on the right shows how each retrieved vertical level is sensitive to HCHO at all levels. This shows how there is not much sensitivity at higher altitudes, and how HCHO at lower altitudes can affect retrieved values for concentrations at higher altitudes. When comparing FTIR measurements to modelled data, vertical columns are used rather than profiles as the degree of freedom in each measurement is low (~ 1.3 in summer to ~ 1.7 in winter). Degrees of freedom signify how many pieces of information can be retrieved from a measurement, and profiles resolved to N vertical levels would require at least N-1 degrees of freedom.

The retrieved vertical profile (x_{ret}) can be expressed as a linear function of the true vertical profile (x_{true}) and the a priori vertical profile (x_{pri}):

$$x_{ret} = x_a + A(x_{true} - x_a) \quad (2.2)$$

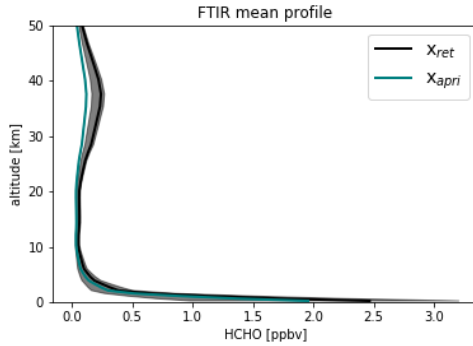


FIGURE 2.7: Mean midday FTIR profile (x_{ret}) and a priori profile (x_{apri}). Shaded area shows the inter-quartile range over the same time period. Profile is averaged between November 2007 to April 2013.

One way of looking at this is to consider if the device was perfectly sensitive to HCHO concentrations at all vertical levels (making $A = I$ the identity matrix), then the retrieval would be equal to the true profile. If the instrument was perfectly useless (making $A = 0$), then the retrieval would completely ignore the true profile and simply equal the a priori. To compare modelled vertical profiles (x_{GC}) with the FTIR, the modelled profiles are *convolved* with the instrument averaging kernel and a priori to create a pseudo retrieval (x'_{GC}) which shows what the instrument would retrieve if the model were the truth:

$$x'_{GC} = x_a + A(x_{GC} - x_a) \quad (2.3)$$

x'_{GC} can be compared against x_{ret} to determine if measurements and modelled vertical profiles or columns show significant differences. This convolution is required so as to avoid seeing a bias between the instrument and the model which is due to the instrument a priori. In this thesis the vertical profiles are transformed into vertical columns (Ω) using the hydrostatic relationship and an assumed dry air profile (see Deeter (2002)):

$$\Omega = x \times 2.12 \times 10^{13} \times \Delta p \quad (2.4)$$

where Ω is in molec cm⁻², x is in ppbv, and p is the pressure in hPa between pressure midpoints for each vertical level in x .

2.2.3.5 Uncertainties

In situ measurements contain errors, and depending on the device used and chemical being measured this error can be significant. The major sources of uncertainty in measurement techniques included interference from non-target compounds and under-reporting (e.g., Dunne et al. 2018; Guérette et al. 2018). Overall isoprene uncertainty in measurements analysed by Dunne et al. (2018) was 50 – 100%. This can feed into uncertainties in modelling and satellite retrievals, as verification and correlations are affected.

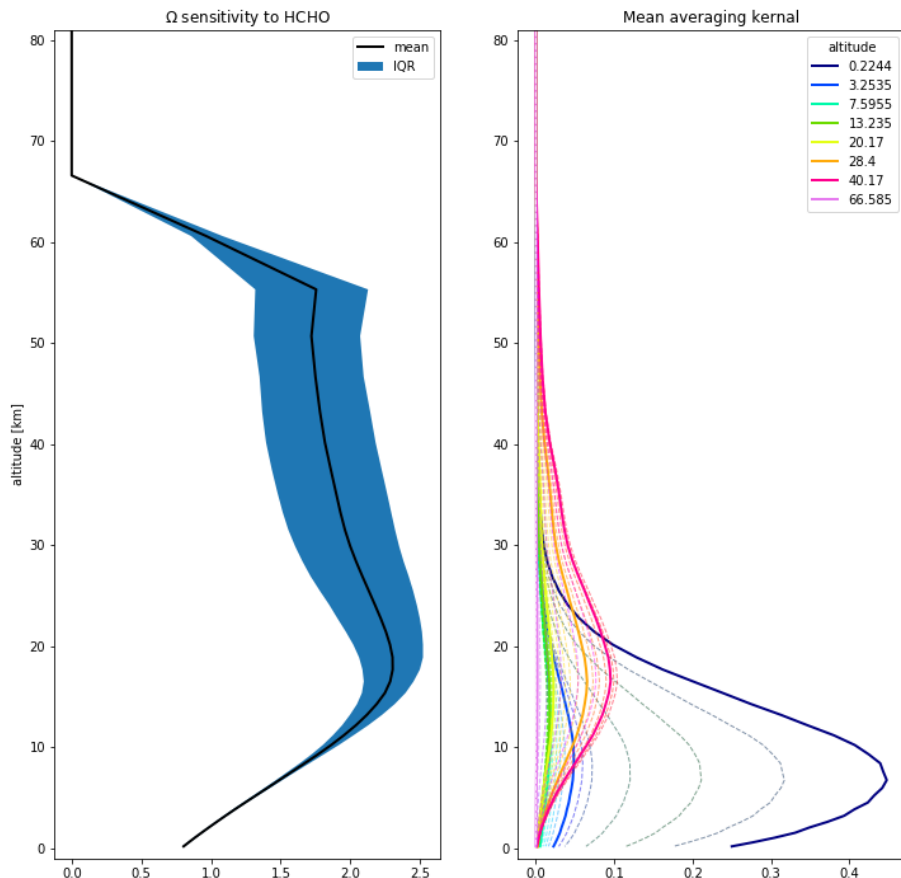


FIGURE 2.8: Left panel shows the mean midday (13:00 - 14:00 local time) total column averaging kernel, along with the inter-quartile range (IQR) between November 2007 and April 2013. Right panel shows the mean averaging kernel for the vertical profile over the same time period, coloured by vertical level. One in six vertical levels are labelled and plotted with a solid line, the rest are shown with dashed lines. The x-axes are unitless in the two plots shown here.

2.3 Satellite formaldehyde

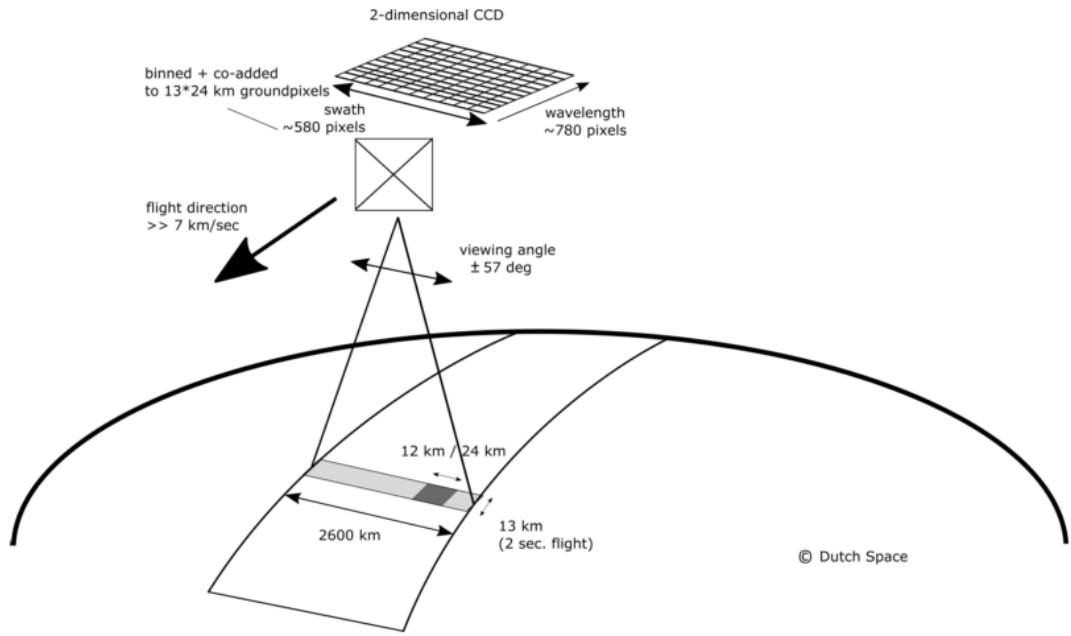
One satellite product used extensively in this thesis is named OMHCHO: from NASA's Earth Observing System's "Aura", which provides several other useful datasets (products). Aura orbits the earth in a polar sun-synchronous pattern, circling the earth on a (geometric) plane coincident with the sun and the poles. Aura houses the Ozone Monitoring Instrument (OMI), a near-UV/Visible Charged Coupled Device (CCD) spectrometer. The OMI instrument onboard Aura has been active since July 2005, it records spectra from 264-504 nm using an array of 60 detectors with mid-resolution (0.4-0.6 nm). This band of wavelengths allows measurements of trace gases (among other quantities) and the formaldehyde product is detailed here.

From here on the word pixel is used to describe one data point retrieved by OMI, each pixel includes a latitude and longitude within OMI's data product. Figure 2.9 shows the details of OMI's detector array and measurement resolutions. OMI measures atmospheric trace gases including NO₂, SO₂, BrO, HCHO, O₃, and aerosols. OMI measurements occur from right to left on a band covering 115°, resulting in swaths of around 2600 km, with pixel sizes from 13x24 km² at nadir to 26x135 km² at the swath edges (Gonzalez Abad et al. 2015). The swaths cover Earth daily, both on the light and dark side of the planet, only daytime measurements provide useful near-UV/Visible information. While satellite measurements can only be used during daytime hours, HCHO lifetimes are sufficiently short that any night-time chemistry will not affect midday observations (Wolfe et al. 2016).

The latest OMHCHO algorithm uses a shape factor determined from GEOS-Chem (V9) using 47 vertical levels at monthly temporal resolution and 2° × 2.5° latitude by longitude horizontal resolution (Gonzalez Abad et al. 2015). The GEOS-Chem model has been substantially updated since then. In this thesis a more recent version V10.01 is used to recalculate the vertical column HCHO (details are shown in Section 2.6).

OMI uses a Differential Optical Absorption Spectroscopy (DOAS) based technique to read HCHO along the path of light which reaches the satellite instrument. The first step is to determine how much HCHO is in the path of light between the sun and detector. Measurements done using DOAS often apply a forward radiative transfer model (RTM) such as LIDORT (see Section 2.3.4) in order to determine the radiative properties of a trace gas at various altitudes. The forward RTM used for satellite data products also involve functions representing extinction from Mie and Rayleigh scattering, and the effect of these on spectra. These RTM are also required to account for (often estimated) atmospheric parameters such as albedo. The next step is to transform the calculated amounts along the non-vertical light path into vertical column amounts. This is done by applying an AMF. In the absence of atmospheric scattering a simple geometric AMF can be defined as a function of the solar zenith angle. The solar zenith angle (θ_s) and the satellite viewing angle (θ_v) are shown in image 2.10. However, in the UV-VIS region of the spectrum, Rayleigh and Mie scattering (see Section 2.3.2) must be accounted for.

A DOAS fit determines the total column amount of a trace gas along the path that the instrument views. This uses the Beer-Lambert law where radiance is reduced as light travels through a medium. I use the NASA OMHCHOv003 data product (Gonzalez Abad et al. 2015), with HCHO determined using the spectral window 328.5 nm–356.5 nm. The algorithm used is based on direct fitting of radiances, and



Channel	Wavelength range	Spectral resolution	Spectral sampling	Ground pixel size
UV1	264–311 nm	0.63 nm = 1.9 px	0.33 nm px ⁻¹	13 × 48 km
UV2	307–383 nm	0.42 nm = 3.0 px	0.14 nm px ⁻¹	13 × 24 km
VIS	349–504 nm	0.63 nm = 3.0 px	0.21 nm px ⁻¹	13 × 24 km

FIGURE 2.9: Figure 1 and Table 1 from Schenkeveld et al. (2017), with the following caption “An impression of OMI flying over the Earth. The spectrum of a ground pixel is projected on the wavelength dimension of the charge-coupled device (CCD; the columns). The cross-track ground pixels are projected on the swath dimension of the CCD (the rows). The forward speed of 7 kms^{-1} and an exposure time of 2 s lead to a ground pixel size of 13 km in the flight direction. The viewing angle of 114° leads to a swath width on the ground of 2600 km.” The table shows the optical properties for OMIs three channels.

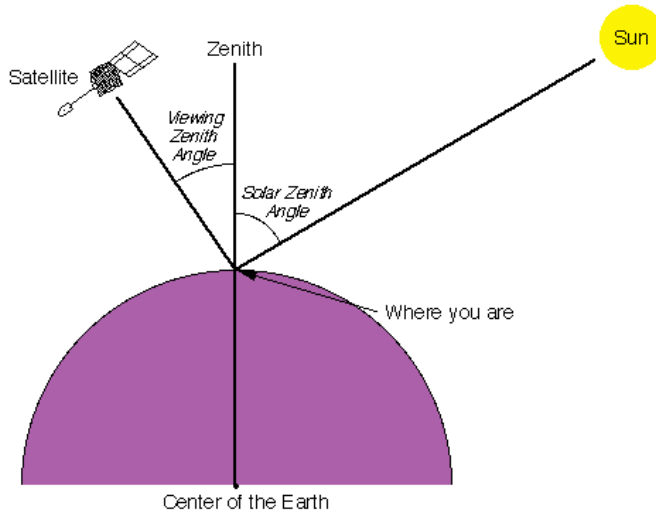


FIGURE 2.10: Solar and viewing zenith angles, image copied from Wikipedia (2016), originally from a NASA website.

accounts for competing absorbers, under-sampling, and Ring effects. An OMI radiance measurement over the remote Pacific ocean is used instead of an irradiance measurement. This means that the slant columns (Ω_S) are formed from the spectra differential with respect to the radiance reference column over the Pacific. The full method details for slant column retrieval by OMI are outlined in the technical document (DOI: 10.5067/Aura/OMI/DATA2015). Slant columns range from $\sim 4 \times 10^{15}$ to $\sim 6 \times 10^{16}$ molec cm^{-2} , with uncertainties from 30% (larger columns) to over 100% (smaller columns) (Gonzalez Abad et al. 2015).

2.3.1 Pixel filtering

This thesis uses the level 2 product swath output from the NASA earth data web portal. OMHCHO level two data includes 14-15 daily swaths of measurements. Each swath contains roughly 9×10^4 pixels, each of which includes latitude, longitude vertical column HCHO, along with all the ancillary data required to make the vertical column and several data quality metrics. The OMHCHO dataset has a quality flag which can be used to remove unlikely or poor satellite measurements. The states represented by this quality flag are shown in Table 2.2 which is reproduced here (originally from Kurosu and Chance (2014)). First all good pixels (those with QA flag equal to 0) are read into a long list (roughly 1 million per day). Filtering bad or missing measurement pixels is performed prior to any other filtering, this includes the datapoints affected by the row anomaly through a particular flag (see https://www.cfa.harvard.edu/atmosphere/Instruments/OMI/PGEReleases/READMEs/OMHCHO_README_v3.0.pdf). This anomaly affects radiance data at particular viewing angles, corresponding to a row on the CCD detectors, and is dynamic over time (Huang et al. 2018). The slant columns affected are flagged and removed before any further processing.

Each ~ 90 minutes the Aura satellite sweeps over the sunny side of the planet of which around 50 k – 80 k of the roughly 90 k pixels are classified as good. Each pixel

TABLE 2.2: OMI quality flag values table from Kurosu and Chance (2014)

Value	Classification	Rational
0	Good	Column value present and passes all quality checks; data may be used with confidence.
1	Suspect	Caution advised because one or more of the following conditions are present: <ul style="list-style-type: none"> • Fit convergence flag is < 300 but > 0: Convergence at noise level • Column $+2\sigma$ uncertainty $< 0 <$ Column $+3\sigma$ uncertainty • Absolute column value $>$ Maximum column amount ($1e19$ molec cm^{-2})
2	Bad	Avoid using as one of the following conditions are present: <ul style="list-style-type: none"> • Fit convergence flag is < 0 : No convergence, abnormal termination • Column $+3\sigma$ uncertainty < 0
< 0	Missing	No column values have been computed; entries are missing

contains several important pieces of data which are needed for recalculation of the HCHO vertical column: the total column of HCHO (Ω ; molec cm $^{-2}$), cloud fraction, associated shape factor, AMF, geometric AMF, scattering weights and their vertical altitudes (hPa), viewing zenith angle, solar zenith angle, latitude, longitude, OMI sensor track, main data quality flag, cross track flag, and total column uncertainty. All of these data are needed in order to reconstruct the total vertical column using a modelled a priori shape factor rather than NASA's included a priori shape factor. Each pixel includes an estimate of the cloud fraction created using the OMI cloud product OMCLDO2.

After being read, pixels are filtered by solar zenith angle (SZA) and latitude, similarly to other works (e.g., Marais et al. 2012; Barkley et al. 2013; Bauwens et al. 2016; Zhu et al. 2016). Satellite measurements pole-wards of 60° north or south are removed as well as measurements with SZA greater than 60°. Measurements taken with high SZA are unlikely to have much information from closer to the ground, and often have high uncertainty. Pixels with cloud fraction greater than 40% are removed after being used in determining the reference sector correction, as is performed in Gonzalez Abad et al. (2015) and De Smedt et al. (2015). This removes around 30% of the pixels which remain after filtering out the bad or missing data.

Due to noise and the differential measurement technique, small negative columns are present in the satellite product which are not removed so as not to introduce a bias. However, some very large negative values which represent an unflagged error in the retrieval process are removed. Unlikely high positive measurements are also removed, leaving only measurements within the density range -0.5×10^{16} to 1×10^{17} molec cm $^{-2}$, as is performed by Zhu et al. (2016). This filter is required due to currently unexplained large negative values which occur in the OMI HCHO product increasingly over time. Figure 2.11 shows how unfiltered HCHO columns are affected by a small set of highly negative values which heavily affect the mean column amount over any region. The highly negative values can be seen around the -10^{19} molecules cm $^{-2}$ region.

2.3.2 DOAS

The DOAS technique uses solar radiation absorption spectra to measure trace gases through paths of light. Beer's law states

$$T = I / I_0 = e^{-\tau} \quad (2.5)$$

with T being transmittance, τ being optical depth, and I, I_0 being radiant flux received at instrument and emitted at source respectively. The Beer-Lambert law of extinction allows spectroscopic measurement of absorbing chemical species (absorbers) in the atmosphere:

$$I_B = I_{B_0} e^{-\tau_s} \quad (2.6)$$

where I_B , I_{B_0} is backscattered intensity with and without the absorber respectively, and τ_s is the optical thickness of the absorber along the measured path between source and instrument.

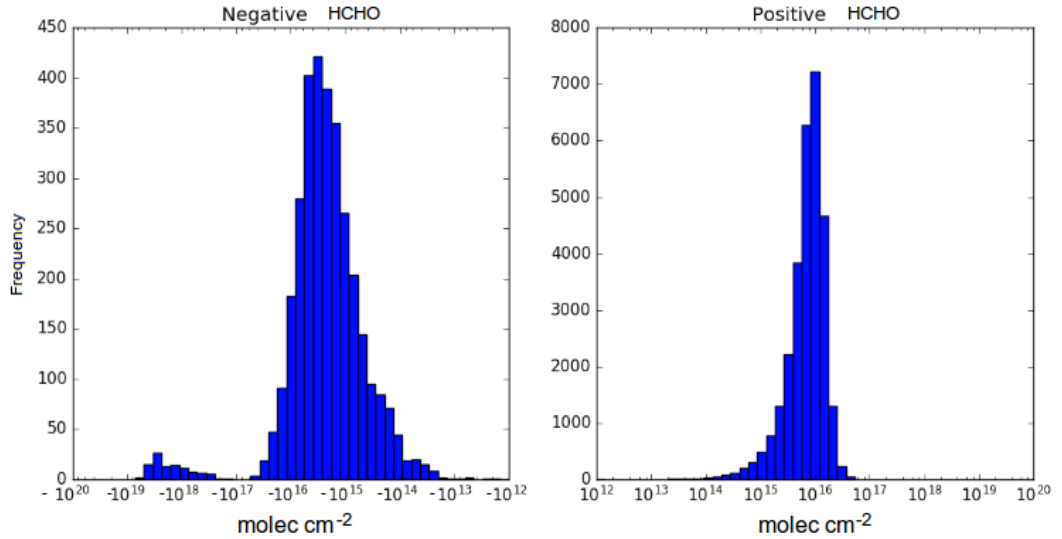


FIGURE 2.11: HCHO Column amount histograms for a subset of OMI swaths over Australia on the 18th of March 2013. Negative entries are shown in the left panel, positive in the right. Note the different scale between negative and positive panels.

τ can be described using the scattering and absorption cross section area (α , cm^2) and density (η , molec cm^{-3}) of an absorber as follows:

$$\tau = \int \alpha(s) \eta(s) ds \quad (2.7)$$

Here τ represents the sum of optical thicknesses of each absorber within the measured path (s) through a medium. substituting Equation 2.7 into Equation 2.6 leads to

$$I = I_0 \exp \left(\sum_i \int \eta_i \alpha_i ds \right) \quad (2.8)$$

Where i represents a chemical species index, and the integral over ds represents integration over the path from light source to instrument.

Another way of describing optical depth (also called optical thickness) is the natural logarithm of the ratio of incident radiant power to transmitted radiant power through a material (from Equation 2.6). In the atmosphere we are interested in the optical depth of various chemical species, and we use incoming solar radiation to determine this. The difference between solar radiation at the top of the atmosphere and the earth's surface defines the atmospheric optical depth along the path of observation.

$$\tau = \ln \frac{\phi_e^i}{\phi_e^t} \quad (2.9)$$

where ϕ_e^i is radiant flux seen at the earth surface, ϕ_e^t is the solar radiant flux which arrives at the top of the atmosphere. In the atmosphere, optical depth can be due to several factors including scattering, chemical absorbance, and aerosols.

2.3.3 Air mass factor (AMF)

To convert the trace gas profile from a reflected solar radiance column (slanted along the light path) into a purely vertical column requires calculations of an air mass factor (AMF). In satellite data, the AMF is typically a scalar value for each horizontal grid point which will equal the ratio of the total vertical column density to the total slant column density. This value requires calculations to account for instrument sensitivities to various wavelengths over resolved altitudes, and is unique for each trace gas under consideration. An AMF characterises measurement sensitivity to a trace gas at various altitudes Palmer et al. 2001, e.g., Lorente et al. (2017) show that AMF calculations can be the largest source of uncertainty in satellite measurements. Another way of describing AMFs are as measures of how radiance at the top of the atmosphere (TOA) changes with trace gas optical depths at specific altitudes (Lorente et al. 2017). Calculation of the AMF is important as it is multiplied against the estimated slant columns in order to give vertical column amounts.

DOAS column retrievals are an integration of a trace gas over the instruments viewing path, in order to convert this total to a vertically distributed column a few assumptions and estimates are required. The vertical profile of a trace gas is assumed or estimated via a CTM, while its scattering and radiative properties are calculated at prescribed altitudes using an RTM. These properties are combined into a single array called the AMF. Two examples of this are GOME-2 (on the MetOp-A satellite) products, which use the LIDORT RTM with IMAGESv2 CTM, and OMI products, which use LIDORT combined with GEOS-Chem (Instrument 2002; Gonzalez Abad et al. 2015). AMFs are unique to each trace gas and due to their complexity and the influence of cloud cover they remain one of the largest error sources in remote sensing of BVOCs (Palmer et al. 2001; Millet et al. 2006)). Lamsal et al. (2014) recommends that when comparing satellite data to models, the AMF should first be recalculated using the model as an a priori. This is in order to remove any a priori bias between model and satellite columns.

Related to the AMF is the averaging kernel (AK), which is used to handle instrument measurements which are sensitive to gas concentrations at different altitudes through the atmosphere. DOAS methods can be heavily influenced by the initial estimates of a trace gas profile (the a priori) which is often produced by modelling, so when comparing models of these trace gases to satellite measurements extra care needs to be taken to avoid introducing bias from differing a priori assumptions. One way to remove these a priori influences is through the satellite AK (or AMF), which takes into account the vertical profile of the modelled trace gas and instrument sensitivity to the trace gas (Eskes and Boersma 2003; Palmer et al. 2001). This process is called deconvolution ($\Omega = AK \times VC_{satellite} + (I - AK) \times VC_{apriori}$) of the AK of the satellite instrument. The AK represents sensitivities to each species at multiple altitudes through the atmosphere and in the case of OMI, can be approximated from the scattering weights ($\omega(z)$) function as follows:

$$AK(z) = \frac{\omega(z)}{AMF} \quad (2.10)$$

(Gonzalez Abad et al. 2015).

2.3.4 LIDORT

LIDORT is a model of LInearized Discrete Ordinate Radiative Transfer, used to determine backscatter intensities and weighting functions at arbitrary elevation angles (Spurr, Kurosu, and Chance 2001). The model solves radiative transfer equations and can be used to determine various atmospheric column measurement attributes such as optical depth, ring effects, and scattering. These radiative properties (or at least estimates thereof) are required when measuring trace gases in the atmosphere through a long path such as seen by satellites (e.g., Palmer et al. 2001; Martin et al. 2002a; De Smedt et al. 2015; Gonzalez Abad et al. 2015).

2.3.5 Uncertainty

Uncertainty in the OMI satellite instrument is calculated by the Smithsonian Astrophysical Observatory (SAO) group using the uncertainty in backscattered radiation retrievals (Gonzalez Abad et al. 2015; Abad et al. 2016). Uncertainty in a single pixel for OMHCHO is roughly the same magnitude as HCHO background levels. Each pixel has $\sim 2 \times 10^{14}$ molec cm $^{-2}$ uncertainty, which is 5 \times higher than GOME. However, there are $\sim 100 - 200\times$ as many measurements allowing a greater reduction of uncertainty with averaging. This is due to the smaller footprint and better temporal resolution of OMI (Instrument 2002; Millet et al. 2008). The finer nadir resolution of OMI (13 by 24 km 2) compared to other satellites also reduces cloud influence (Millet et al. 2006; Millet et al. 2008). The top row in Figure 2.12 shows OMI HCHO columns binned to at 0.25° \times 0.3125° longitude by latitude averaged over one day and one month (with and without filtering). Row two shows uncertainty of the satellite data after averaging. It is clear that one day of satellite data is too uncertain when binned at 0.25° \times 0.3125° horizontal resolution; however, after a month (with or without filtering) the uncertainties become manageable. If we assume the uncertainty is random error, and not bias introduced through calculation techniques, then we are able to reduce the uncertainty through averaging. High resolution low detection limit estimates can be built up using “oversampling”, which averages satellite measurements over time (e.g., Zhu et al. 2014). Uncertainty in satellite recalculations related to estimating isoprene emissions is analysed in Section 3.4.3.

Recently Schenkeveld et al. (2017) analysed the performance over time of OMI and found irradiance degradation of 3-8%, changed radiances of 1-2%, and a stable wavelength calibration within 0.005-0.020 nm. These changes are measured excluding the row anomaly (RA) effect, which is relatively stable since 2011, although it is still growing and remains the most serious concern. Their analysis concludes that data is still of high quality and will deliver useful information for 5-10 more years, with radiance only changing by 1 – 2% outside of RA impacted areas. An analysis of the row anomaly by Huang et al. (2018) state that measurements remain suitable for scientific use, with recommendation for further evaluation. The RA began in June 2007, with some cross-track rows seemingly blocked. The most likely cause is some instrument insulation partially obscuring the radiance port (Schenkeveld et al. 2017). In this thesis pixels potentially affected by the row anomaly are removed prior to calculation or analysis.

OMI HCHO and uncertainty for 200501

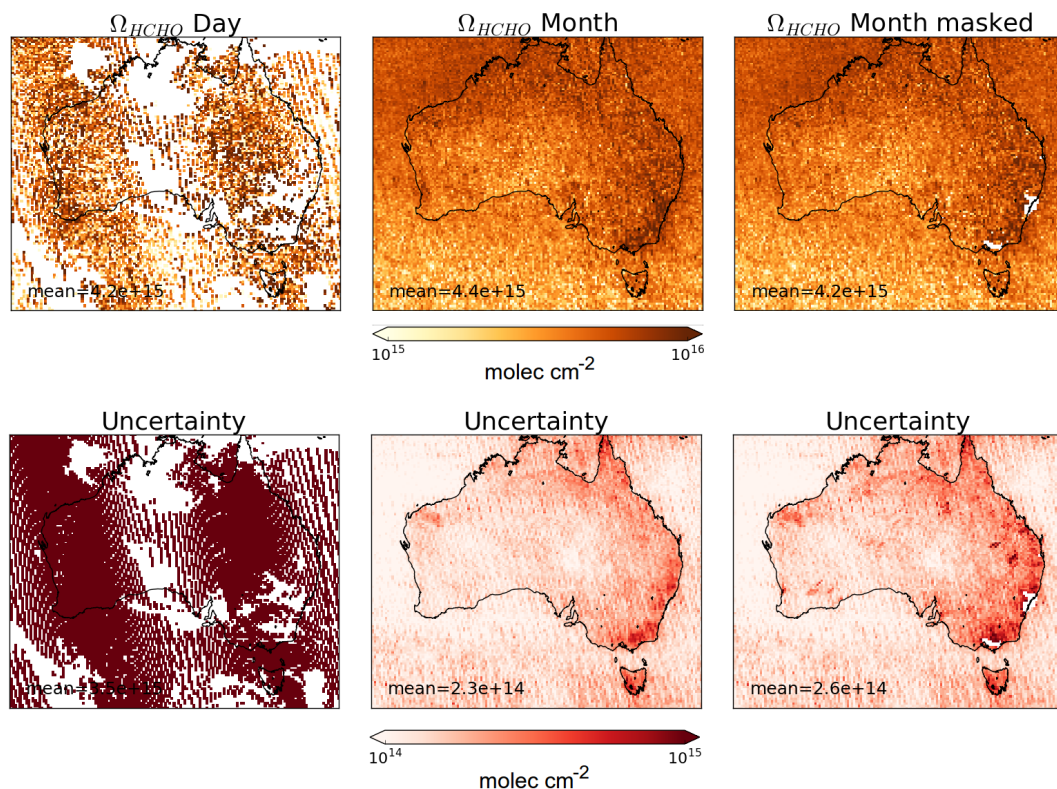


FIGURE 2.12: Top row shows $0.25^\circ \times 0.3125^\circ$ binned OMHCHO columns with one day, one month, and one month with non-biogenic masking applied from left to right respectively. Bottom row shows the uncertainty for each grid square after averaging.

In satellite HCHO products, concentrations over the remote Pacific ocean are sometimes used to analyse faulty instrument readings. This is due to the expected invariance of HCHO over this region. For instance GOME (an instrument which measures trace gases onboard the ERS-2) corrects for an instrument artefact using modelled HCHO over the remote Pacific (Shim et al. 2005). OMI HCHO products use a similar technique to account for sensor plate drift and changing bromine sensitivity (Gonzalez Abad et al. 2015). In this thesis a background uncertainty estimation is performed based on differences between satellite measurements and monthly averaged modelled HCHO over the remote Pacific ocean (see Section 3.4.3).

The OMI dataset may suffer from bias; however, in order to determine any bias an independent dataset is required, and this does not exist over Australia. In this thesis, HCHO columns (pixels) with cloud fractions over 40% are filtered as done in Palmer et al. (2001), which may introduce a clear-sky bias to any monthly averages. This is due to HCHO being lower on unrecorded cloudy days. This bias has been measured as a 13% positive monthly mean bias (Palmer et al. 2001; Surl, Palmer, and Abad 2018). For many places the tropospheric column HCHO measured by satellite is biased low, Zhu et al. (2016) examine six available datasets and show a bias of 20 - 51% over south east USA when compared against a campaign of aircraft observations (SEAC⁴RS). De Smedt et al. (2015) also found OMI and GOME2 observations were 20 - 40% lower than ground based vertical profiles, and Barkley et al. (2013) determine OMI to be 37% low compared with aircraft measurements over Guyana. These bias can be corrected by improving the assumed a priori HCHO profiles which are used to calculate the AMFs of the satellite columns. Millet et al. (2006) examine OMI HCHO columns over North America and determine overall uncertainty to be 40%, with most of this coming from cloud interference. Millet et al. (2008) shows that there also exists some latitude based bias, as well as a systematic offset between the OMI and GOME instruments. This does not appear to be due to the different overpass times of the two instruments.

AMF calculation often dominates the total uncertainty in satellite retrievals, especially in polluted regions (Lorente et al. 2017). In scenarios where the gas is enhanced in the lower troposphere, AMF calculation is the largest uncertainty in satellite measurements. In polluted environments the structural uncertainty is estimated at 42 %, or 31 % over unpolluted environments (Lorente et al. 2017). Another impact often not included in uncertainty calculations is the structural uncertainty of retrieval methods. The structural uncertainty of AMF calculation approaches used by different retrieval groups comes from how the AMF is calculated, rather than uncertainty in the calculation components. The importance of a priori and ancillary data (such as surface albedo and cloud top height) sharply affects the structural uncertainty (Lorente et al. 2017). In this thesis the AMF uncertainty is assumed to be 30%, as concentrations of HCHO and pollution are relatively low over Australia.

2.4 GEOS-Chem

2.4.1 Overview

GEOS-Chem is a well supported global, Eulerian CTM (see Section 1.5.2) with a state of the science chemical mechanism, and transport driven by meteorological input from

the Goddard Earth Observing System (GEOS) of the NASA Global Modeling and Assimilation Office (GMAO). Chemistry, transport, and meteorology are simulated at 15 minute time steps within a global set of 3-D boxes. Emissions are either prescribed by inventories (e.g., fire emissions are pulled from the global fire emissions database GFED4) or modelled (e.g., biogenic emissions are modelled using MEGAN).

GEOS-Chem simulates more than 100 chemical species within the atmosphere, from the earth's surface up to the edge of space (0.01 hPa). Modelled concentrations can be used in combination with measurements to give a verifiable estimate of atmospheric gases and aerosols in places and times where no measurements exist. It was developed, and is maintained, by Harvard University staff as well as users and researchers worldwide. In this thesis I use version 10.01 of GEOS-Chem, which outputs up to 66 chemical species (tracers) in the standard run, at $2^\circ \times 2.5^\circ$ horizontal resolution, with 47 levels up to the top of the atmosphere (TOA at 0.01 hPa).

Global CTMs are often run using one or several emission models (or the output from them) to determine boundary conditions. Some of the inventories used by GEOS-Chem are described here. Meteorological fields are taken from NASA's GEOS-5 dataset ($0.5^\circ \times 0.666^\circ$) (Chen et al. 2009), which exists up to April 2013. GEOS-5 meteorological fields are used as the boundary conditions driving transport. Fire emissions come from the global fire emissions database (GFED4) product (Giglio, Randerson, and Van Der Werf 2013). Anthropogenic VOC emissions come from the Emission Database for Global Atmospheric Research (EDGAR) inventory, while biogenic VOC emissions are simulated using the MEGAN model (see Section 2.4.5). MEGAN is used to determine biogenic emissions for our default GEOS-Chem simulation.

2.4.2 Installing and running GEOS-Chem

GEOS-Chem instructions for download, compilation, and running can be found in the user guide provided by Harvard: <http://acmg.seas.harvard.edu/geos/doc/man/>. In order to build and run GEOS-Chem a high-speed computing system is optimal, as globally gridded chemical calculations can take a long time to perform (for us ~ 70 computation hours per month). I installed GEOS-Chem onto a suitably configured workspace on the Raijin supercomputer at the National Computational Infrastructure (NCI, <http://nci.org.au/>). This workspace included access to compilers and libraries which are needed to build the Fortran based GEOS-Chem source code, and IDL, Python, and various editors and scripting languages to read, run, edit, and analyse both GEOS-Chem and its output.

2.4.3 Chemical Mechanism

A chemical mechanism is a closed system of chemical reactions and their associated rate constants. Chemical reactions are represented by systems of differential equations to be solved for each gridbox in GEOS-Chem. Simplifications are required due to the large number of reactions which occur in the atmosphere, and the coupled and stiff nature of these reactions which slow down computation of the solutions (Brasseur and Jacob 2017). Stiffness in chemical systems of differential equations is due to the massively differing reaction time scales - for instance hydroxyl radicals react within

seconds while methane has an atmospheric lifetime of 8-10 years (Wuebbles and Hayhoe 2002).

Some of the important reactions involving isoprene are reproduced here, including reaction rates (k) in the form $k = A \exp -E/RT$, where T is temperature, E is activation energy, and R is the gas constant, A, E, and R are predefined for each reaction. The following set of equations (2.11) lists the main isoprene and sundry reactions, with terms defined earlier in Table 2.3. LISOPOH is added in order to allow the model to keep track of how much isoprene is oxidised by OH. The mechanisms used in version 10.01 (and its history) are described online at http://wiki.seas.harvard.edu/geos-chem/index.php/NOx-Ox-HC-Aer-Br_chemistry_mechanism.

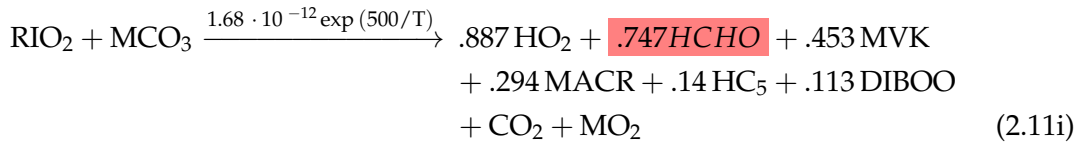
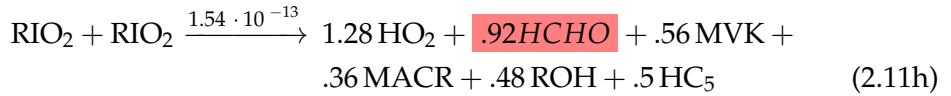
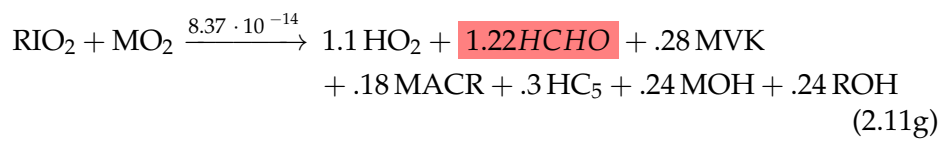
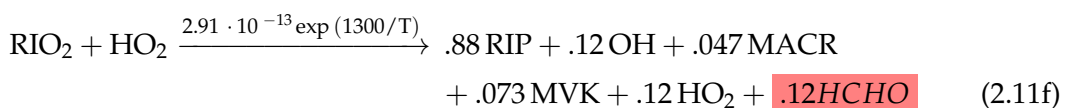
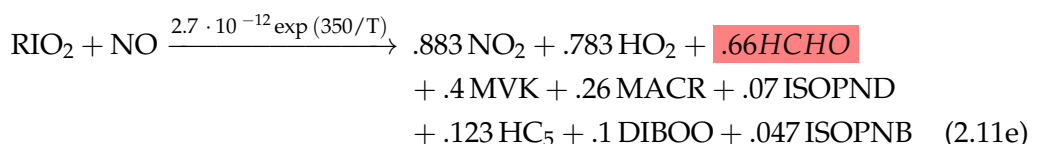
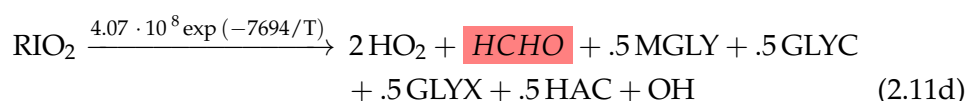
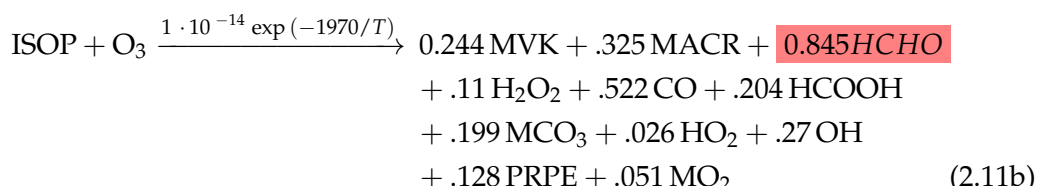
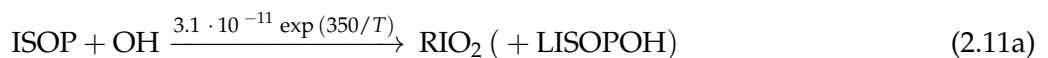


TABLE 2.3: Species or classes from the GEOS-Chem mechanism.

Name	Definition
ACTA	Acetic acid: CH ₃ C(O)OH
DIBOO	Dibble peroxy radical
GLYC	Glycoaldehyde: HOCH ₂ CHO
GLYX	Glyoxal: CHOCHO
HAC	Hydroxyacetone: HOCH ₂ C(O)CH ₃
INO2	RO ₂ from ISOP+NO ₃
ISNP	an isoprene nitrate
ISOPNB	β isoprene nitrates
ISOPND	δ isoprene nitrates
MACR	Methacrolein: CH ₂ =C(CH ₃)CHO
MCO3	Peroxyacetyl radical: CH ₃ C(O)OO
MEK	Methyl ethyl ketone: RC(O)R
MGLY	Methylglyoxal: CH ₃ COCHO
MO2	Methylperoxy radical: CH ₃ O ₂
MOH	Methanol: CH ₃ OH
MVK	Methylvinylketone: CH ₂ =CHC(=O)CH ₃
PRPE	>C ₃ alkenes: C ₃ H ₆ , ...
RIO2	isoprene peroxy radical: ROO [·]
ROH	>C ₂ alcohols

2.4.4 GEOS-Chem isoprene

The isoprene reactions simulated by GEOS-Chem were originally based on Horowitz et al. (1998). The mechanism was subsequently updated by Mao et al. (2013), who changed the isoprene nitrate yields and added products based on Paulot et al. (2009a) and Paulot et al. (2009b). They used the yields and reactions of various positional isomers of isoprene nitrates, and their oxidation products. Further mechanistic properties, like isomerisation rates, are based on results from four publications: Peeters, Nguyen, and Vereecken (2009), Peeters and Muller (2010), Crounse et al. (2011), and Crounse et al. (2012).

In a chamber with clean air and high NO concentrations, isoprene photooxidation is initially driven by OH addition, followed by NO_x chemistry (150 min - 600 min), and finally HO_x dominated chemistry. Formation of isoprene nitrates (ISOPN) affect ozone levels through NO_x sequestration, the yields and fate of these nitrates was analysed in Paulot et al. (2009a). Prior to 2012, oxidation chamber studies were performed in high NO or HO₂ concentrations, giving peroxy lifetimes of less than 0.1 s (Crounse et al. 2012; Wolfe et al. 2012). In most environments NO and HO₂ concentrations are not so high, GEOS-Chem uses production rates for different NO concentrations and peroxy radical lifetimes determined by Crounse et al. (2012).

2.4.4.1 Oxidation

Crounse et al. (2011) examined the isomerisations associated with the oxidation of isoprene to six different isomers of ROO formed in the presence of oxygen. The primary oxidation pathway of isoprene is reaction with the OH radical ($ISOP + OH \rightarrow RIO_2$) shown in Equation 2.11a. Isoprene undergoes OH addition at the 1 and 4 positions, becoming β (71%) or δ (29%) ROO[·], although these are not distinguished in the GEOS-Chem mechanism. Secondary oxidative pathways are from ozonolysis (Equation 2.11b and reaction with NO₃ (Equation 2.11c). These pathways are much slower but can be important in particular scenarios such as inside a pollution plume or at night when NO₃ radicals can build up.

Following isoprene oxidation, seven potential ROO reactions (RIO₂ in Equation 2.11) can occur depending on reactant concentrations and local temperature. Crounse et al. (2011) determined rates and uncertainties involved in these reactions, and studied the rate of formation of C₅-hydroperoxyenals (C₅-HPALD) by isomerisation. Reactions 2.11d - 2.11j compete to determine the fate of ROO[·], which is often grouped into high or low NO_x concentration pathways.

2.4.4.2 Nitrogen oxide impacts

GEOS-Chem reactions account for high and low NO_x scenarios as determined in Mao et al. (2013), based on Paulot et al. (2009a). High NO_x has been defined as conditions where NO reactions are the main cause of losses for ROO[·] (Reaction 2.11e) (Palmer et al. 2003). High NO_x concentrations are roughly 1 ppb, while low NO_x concentrations are around 0.1 ppb.

In low NO_x ROO[·] losses occur from isomerisation or reaction with several potential compounds. NO_x + HO₂ (Reaction 2.11f) produces mostly hydroxy hydroperoxides (ISOPOOH), and some HCHO. ISOPOOH can be oxidised (by OH) to produce epoxydiols, recycling OH (Paulot et al. 2009b). Isomerisation of ROO[·] (Reaction 2.11d) largely produces HCHO, while recycling OH and producing HO₂. This isomerisation accounts for 1,5-H shifts producing MACR, MVK, HCHO, or 1,6-H shifts producing HPALDs. HPALDs can photolyse to regenerate OH and small VOCs (Crounse et al. 2011; Wolfe et al. 2012; Jozef et al. 2014). Under low NO_x conditions the expected production of HCHO, MVK, and MACR is 4.7%, 7.3%, and 12% respectively. Refer to Section 1.3.3 for more information. Less frequently, ROO[·] reacts with itself, MO₂, or MCO₃.

Under high NO_x conditions, the fate of ROO[·] differs depending on how it was formed. The β -hydroxyl reacts with NO_x and produces HCHO (66%), methylvinylketone (40%) (MVK), methacrolein (26%), and β -hydroxyl nitrates (6.7%) (ISOPNB). The δ -hydroxyl reacts with NO to form δ -hydroxyl nitrates (24%) (ISOPND), and ISOPNB (6.7%). These two pathways are combined in Reaction 2.11e, which shows the production from ROO[·] and NO.

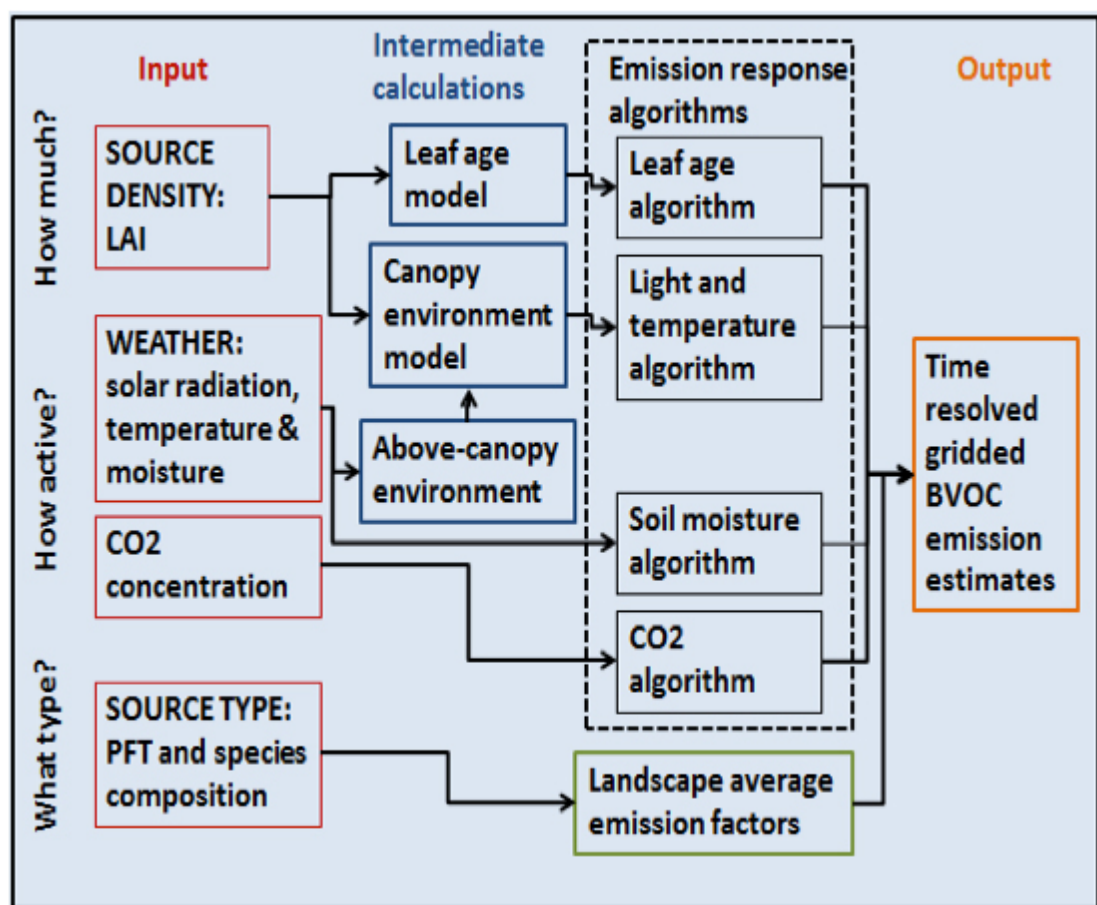
2.4.4.3 OH

Until recently, models struggled to represent OH in the atmosphere, due to missing chemistry and issues in measurement techniques. Prior to Mao et al. (2012), measurements of OH in high VOC regions may have been up to double the real atmospheric OH levels, due to formation of OH inside measuring instruments. OH regeneration through photolysis of HPALDs in areas with high isoprene emissions are included from Peeters and Muller (2010). Photolysis of photolabile peroxy-acid-aldehydes generates OH, improving model agreement with continental observations. OH and HPALD interactions are central to maintaining the OH levels in pristine and moderately polluted environments, which makes isoprene both a source and sink of OH (Peeters and Muller 2010; Taraborrelli et al. 2012). Isoprene chemistry in GEOS-Chem includes OH regeneration from oxidation of epoxydiols (not shown in Equation 2.11) and slow isomerisation of ROO (Equation 2.11d) (Mao et al. 2013). This regeneration dealt with the problem seen in older models where ISOPOOH production titrated OH, which was not backed up by measurements (Paulot et al. 2009b; Mao et al. 2013). Mao et al. (2013) showed that drastically lowering (by a factor of 50) the rate constant for ROO isomerisation lead to better organic nitrate agreements with measurements. These chemical updates led to more accurate modelling of OH concentrations, especially in low NO_x conditions common in remote forests. The updates to isoprene chemistry by Mao et al. (2013), and those shown in Crounse et al. (2011) and Crounse et al. (2012) are the last before GEOS-Chem version 11.

2.4.5 Emissions from MEGAN

GEOS-Chem runs the Model of Emissions of Gases and Aerosols from Nature (MEGAN) to determine biogenic emissions globally. GEOS-Chem V10.01 uses MEGAN V2.1 with biogenic emissions from Guenther et al. (2012). MEGAN is itself a global model with resolution of around 1 km, which uses globally estimated or measured inventories of parameters to estimate emissions. MEGAN uses leaf area index (LAI), global meteorological data, plant functional types (PFT), and photosynthetic photon flux density to simulate terrestrial isoprene emissions (Kefauver, Filella, and Peñuelas 2014). The schematic for MEGAN, from <http://lar.wsu.edu/megan/>, is shown in Figure 2.13.

MEGAN was developed as a replacement for two earlier canopy-environment emission models (the biogenic emission inventory system, and the global emissions initiative), initially including a simple canopy radiative transfer model which parameterised sun-lit and shaded conditions through a canopy. Early models did not account for abiotic stresses, such as drought, prior rainfall and land use changes. These stresses influence species-specific emissions by more than an order of magnitude (Nininemets et al. 1999). Isoprene emissions were based on temperature, leaf area, and light, but have since been updated to include leaf age activity (Guenther et al. 2000), and a leaf energy balance model (Guenther et al. 2006) in MEGANv2.0. This update included a parameter for soil moisture, to account for drought conditions; however, this parameter is currently (as of version 2.1) not applied to isoprene (Sindelarova et al. 2014). Instructions to run version 2.1 are available at http://lar.wsu.edu/megan/docs/MEGAN2.1_User_GuideWSU.pdf. Version 2.1 (updated from 2.0 (Guenther et al.

FIGURE 2.13: MEGAN schematic, from <http://lar.wsu.edu/megan/>

2006)) includes 147 species, in 19 BVOC classes, which can be lumped together to provide appropriate output for mechanisms in various chemical models. GEOS-Chem uses an embedded version of MEGAN 2.1.

GEOS-Chem computes some emissions using predefined emission factor (ϵ) maps from MEGAN source code, and others using PFT maps and associated emission factors. For isoprene (the focus in this thesis) MEGAN calculates emissions online, using local meteorological conditions. Emissions E of species i are calculated using these EF for classes of plant types j and associated grid-box coverage ξ and an activity factor γ which accounts for response to environmental conditions. The following equation is reproduced from Guenther et al. (2012) showing how E_i are determined in MEGAN:

$$E_i = \gamma_i \sum_j \epsilon_{i,j} \chi_j \quad (2.12)$$

For example: isoprene emissions are tied to sunshine, temperature, plant emission strength (ϵ), emitting species coverage, etc., for each grid box.

2.4.6 Nitrogen oxides

NO_x concentrations affect atmospheric oxidative capacity, which changes many factors important in estimating isoprene emissions including isoprene to HCHO yield, isoprene lifetime, and isoprene oxidation pathways. In GEOS-Chem, NO_x concentrations are regulated by O_3 , VOC, HO_x , Bromine and aerosols reactions. NO_x emissions from nearby agriculture, power generation, and combustion transport drive enhancements in populated areas. The largest source (70%) of NO_x emissions comes from agriculture where nitrogenous fertilisers are in use (*World Bank Nitrogen Oxide Emissions*). In GEOS-Chem, anthropogenic emissions are taken from the Emissions Database for Global Atmospheric Research (EDGAR), for more details visit http://wiki.seas.harvard.edu/geos-chem/index.php/EDGAR_v4.2_anthropogenic_emissions. Other NO_x emissions arise from sources including soil emissions ($\sim 10 \text{ Tg N a}^{-1}$), and lightning. Soil emissions are layed out in **Hudson2012** parameterised using biome specific emission factors, and an explicit fertiliser dataset. Lightning based NO_x production is created based on inventories of lightning flash rates scaled within GEOS-Chem. Conversion to nitric acid (HNO_3) followed by deposition is the primary NO_x removal mechanism (Delmas, Serca, and Jambert 1997; Ayers and Simpson 2006).

If GEOS-Chem is misrepresenting NO_x then yields and the effects of transport may be incorrectly accounted for. In order to determine the accuracy of GEOS-Chem simulated NO_x over Australia, modelled NO_2 amounts are compared to satellite data (where available) for 2005. Figure 2.14 shows tropospheric NO_2 columns from GEOS-Chem, OMNO2d, and their differences over four seasons in 2005. Simulated GEOS-Chem tropospheric NO_2 columns averaged from 13:00-14:00 local time (LT) are compared against OMNO2d data which are averaged into seasonal $2^\circ \times 2.5^\circ$ bins. Both data sets show Sydney and Melbourne as NO_2 hotspots; however, Sydney itself is underestimated by GEOS-Chem throughout the year, likely due to low or poorly aligned emission maps (shown in Figure 2.15). Over much of the country GEOS-Chem overestimates NO_2 by 10-60%, except in the northern areas where up to 50% underestimation occurs in Summer. An underestimation in southern NSW can also be seen in the later

half of the year. Notably GEOS-Chem anthropogenic NO does not have any seasonality (Figure 2.15), while soil shows clear differences in emission hotspots between summer and winter.

Figure 2.16 shows scatter plots with one data point for each land square over Australia, for each season, coloured by total NO emissions. The correlation between model and satellite NO₂ columns is reasonable throughout the year over Australia, with a general positive bias throughout the year in modelled amounts. A comparison between the bias (GEOS-Chem - OMNO2d) with anthropogenic or soil emissions (columns 2 and 3 respectively) shows no real correlation, suggesting the bias is not driven by either anthropogenic or soil NO emissions in any season. Without a clear link between emissions and biases, alterations would be too subjective, and a change to NO_x chemistry is beyond the scope of this thesis. Additionally, high satellite NO₂ columns are filtered in later calculations which assume biogenic air masses as they suggest anthropogenic influence. The conclusion drawn is that modelled anthropogenic and soil NO emissions do not show sufficient evidence of biasing GEOS-Chem NO₂ columns away from satellite measurements over Australia. For this reason modelled NO emissions are not modified in model runs in this thesis.

2.4.7 GEOS-Chem simulations

GEOS-Chem is run five times independently in this thesis, with different outputs from each simulation used to determine specific information. The different output types are first described in Section 2.4.7.1. Following this is the list of model runs, including a summary of the run, outputs created, and a summary of how they are used (Section 2.4.7.2). Finally a brief comparison between a subset of the runs is performed (Section 2.4.7.3).

2.4.7.1 GEOS-Chem outputs

GEOS-Chem in this thesis is run with a 15 minute time step for transport and 30 minutes for chemistry, at $2^\circ \times 2.5^\circ$ horizontal resolution over 47 vertical levels. Output is the average of these time steps. Optionally one to many columns can be output at high temporally resolution. This has been used here to compare modelled ozone with ozonesonde profiles at three sonde release sites discussed in Chapter 4.

Midday output is output from averaging over a window of local time for each grid-box. Output averaged between 13:00-14:00 local time is saved to match with Aura satellite measurements, as Aura overpasses at \sim 1330 local time each day. Midday output is saved both for comparison with, and recalculation of, satellite measurements.

HEMCO diagnostics :the Harvard-NASA Emissions Component (HEMCO) deals with emissions inventories used in GEOS-Chem. When working with globally gridded data, handling local time offsets becomes more important. The hourly averaged emissions of isoprene are saved using GMT, and an offset based on the longitude is used to retrieve values at local time. This offset is determined as one hour per 15° (as 360° is 24 hours).

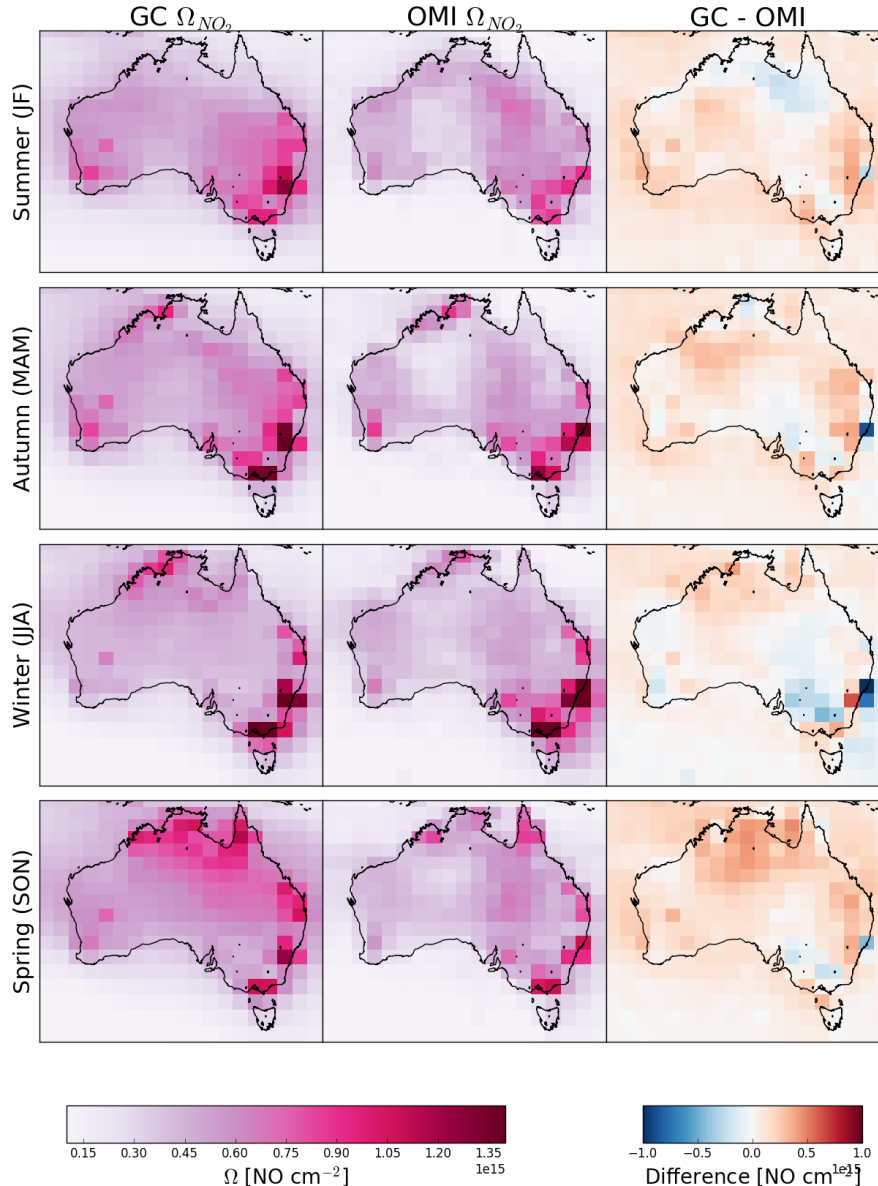


FIGURE 2.14: Left to right columns show tropospheric NO_2 columns (Ω_{NO_2} ; molec cm^{-2}) from GEOS-Chem (GC), OMNO2d (OMI), and the differences. Each row shows one season from 2005, the left two columns use the left colour scale, while the third column uses the right colour scale.

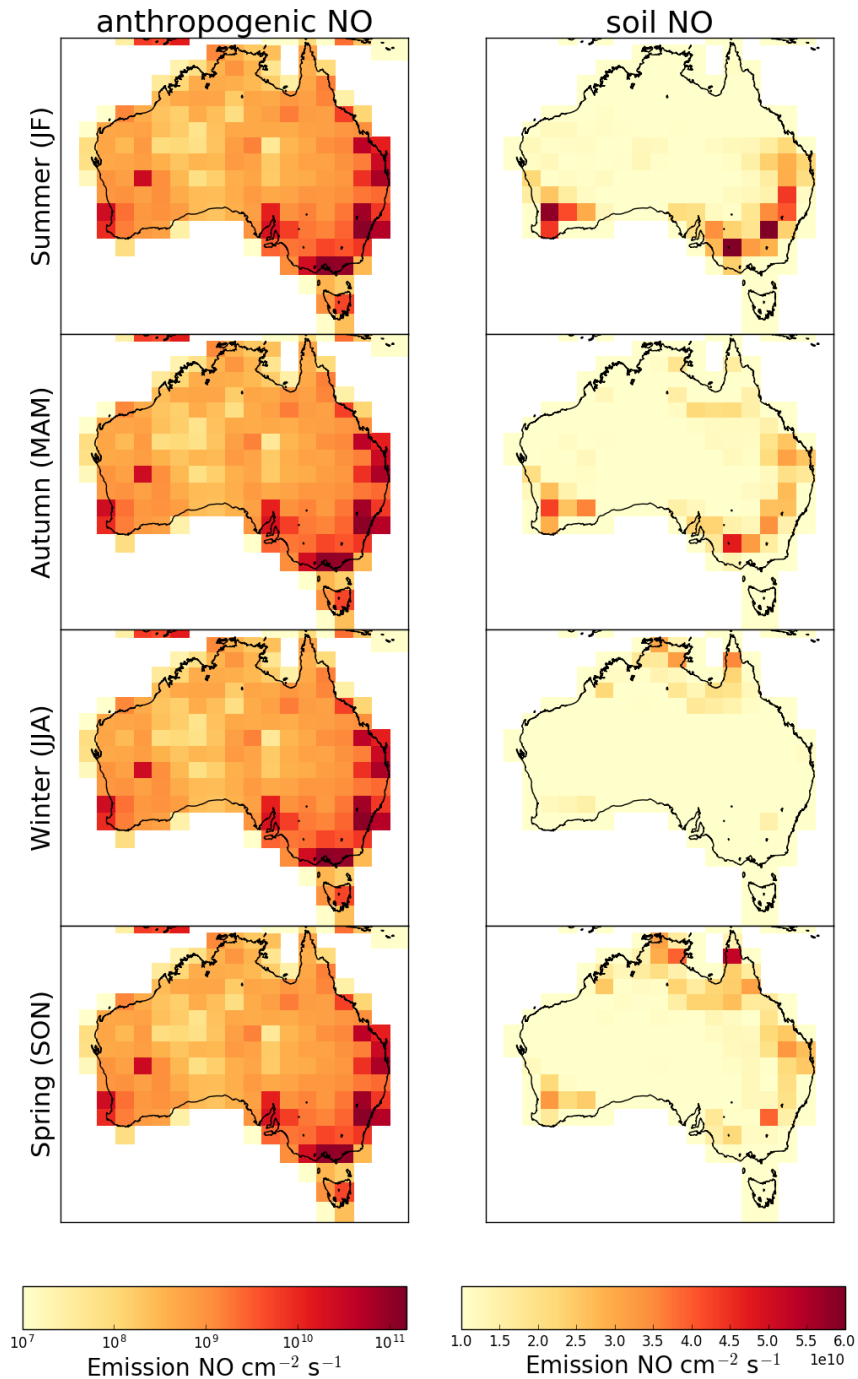


FIGURE 2.15: Left and right columns show anthropogenic and soil emissions of NO respectively from GEOS-Chem in molec $\text{cm}^{-2} \text{s}^{-1}$. Each row shows one season from 2005. Anthropogenic and soil emissions use a logarithmic and linear colour scale respectively.

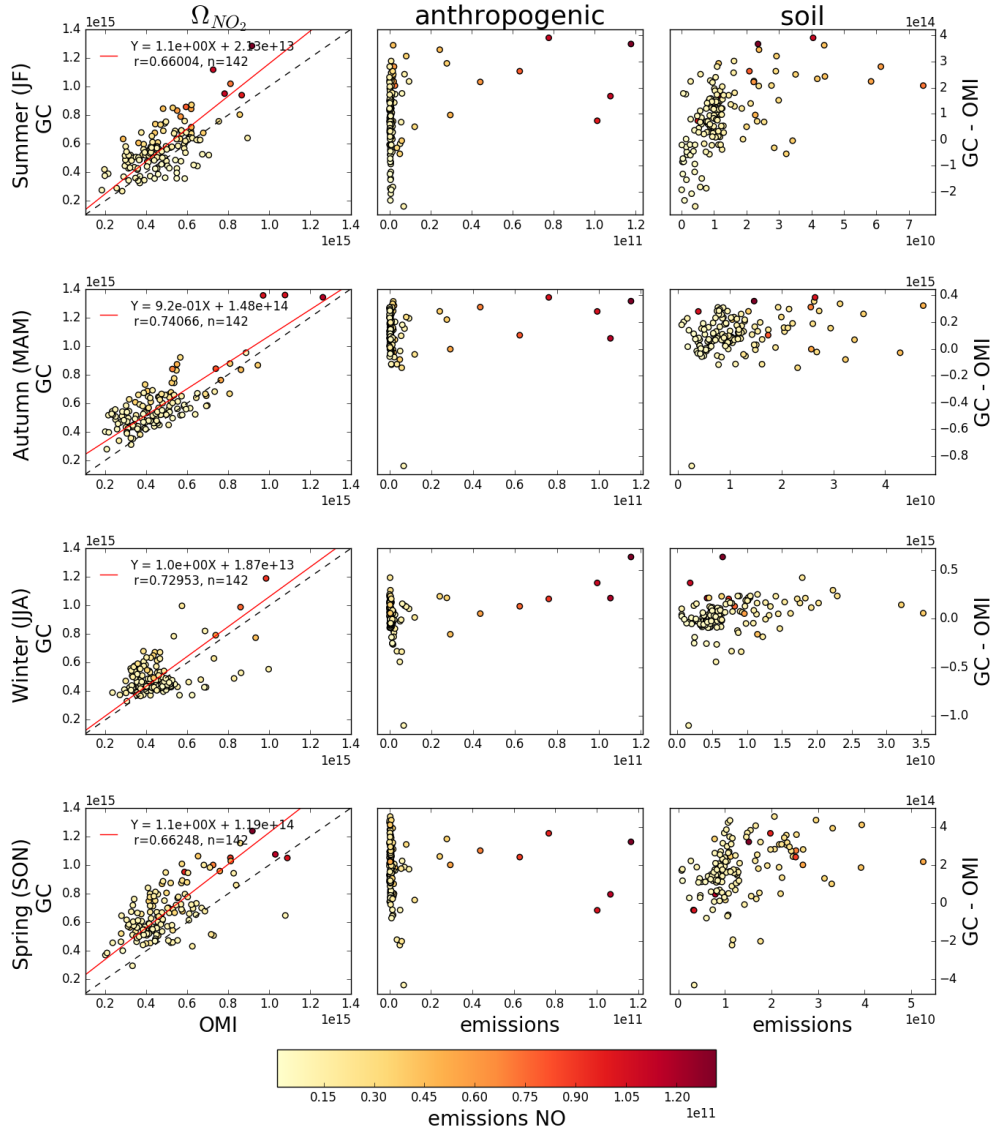


FIGURE 2.16: The first column shows the scatter plots of tropospheric NO_2 columns between GEOS-Chem (y-axis) and OMNO2d (x-axis) at $2^\circ \times 2.5^\circ$. The reduced major axis linear regression is drawn in red, and the equation, regression coefficient (r), and number of grid squares (n) used is inlaid as a legend. The second and third columns show the scatter between emissions and the bias between GEOS-Chem and OMNO2d (GC-OMI), for anthropogenic and soil emissions respectively. These two columns share the far right axis; however, emissions are from anthropogenic and soil sources respectively. All scatter points are coloured by the sum of anthropogenic and soil NO emissions (from GEOS-chem), as per the colour bar shown at the bottom.

Tracer averages are daily or monthly averaged gridbox concentrations.

Time series are vertical profiles of ozone and other species and meteorological diagnostics saved at a temporal resolution of up to 15 minutes.

2.4.7.2 GEOS-Chem runs

The following list summarises each model run as well as enumerating the outputs (described above), and how the run is used in the thesis.

UCX The model was run using the Universal tropospheric-stratospheric Chemistry eXtension (UCX) mechanism with 72 vertical levels from the surface to the top of the atmosphere (TOA ~ 0.1 hPa). UCX runs a chemistry mechanism with combined tropospheric and stratospheric reactions, with an increased number of stratospheric calculations performed online (Eastham, Weisenstein, and Barrett 2014).

1. Outputs: Midday output, daily tracer averages, and time series over three stations.
2. This run shows what influence the stratospheric chemistry additions have over tropospheric isoprene, HCHO, and ozone concentrations.
3. The daily tracer averages are used to determine ozone intrusion quantification (Section 4.6.1), and ozone concentration seasonality (Section 4.5).
4. Time series outputs are compared against ozonesonde releases (Section 4.5) both over time and vertically.

Tropchem (standard) default settings for GEOS-Chem 10.01, using 47 vertical levels at $2^\circ \times 2.5^\circ$ horizontal resolution. Additional midday output is created to allow AMF recalculation code to run on OMI satellite measurements (Section 2.6.3.2).

1. Outputs: Midday output, daily tracer averages, and HEMCO diagnostics
2. These are used in recalculation of the satellite AMF (Section 2.5), and the modelled background HCHO over the remote Pacific which is used in the reference sector correction for OMI column retrievals (Section 2.6.5). Additional diagnostic outputs are used hard coded to allow AMF recalculation.
3. Midday output is combined from two different runs in order to determine smearing (Section 2.7.3)
4. Total yearly ozone concentrations are compared before and after scaling isoprene emissions using the top-down estimate.

Tropchem (isoprene emissions halved) identical to standard tropchem except isoprene emissions are halved.

1. Outputs: Midday output, and monthly tracer averages
2. Check modelled ozone sensitivity to isoprene emissions (following section Figure 2.21).
3. Combined with standard run to determine model sensitivity transport (Section 2.7.3)

Tropchem (biogenic emissions only) identical to standard tropchem except all non-biogenic emissions inventories are disabled.

1. Outputs: Midday output, and hourly biogenic emissions from MEGAN
2. Midday and HEMCO outputs are used to determine isoprene to HCHO yield, after removing days with high smearing (Section 3.2.4)
3. HEMCO diagnostics are compared against top-down estimations of isoprene emissions (Section 3.3.1)

Tropchem (altered MEGAN scaling factor) Identical to standard tropchem except isoprene emissions are scaled to match multi-year monthly averaged top-down estimates.

1. Midday output, time series, daily averaged tracers
2. Compare to campaign datasets after altering isoprene emissions (see Chapter 3)
3. Compare against satellite column HCHO as a sanity check on improving isoprene emissions

2.4.7.3 UCX vs tropchem

Here we compare the model output with and without enabling the Universal tropospheric-stratospheric Chemistry eXtension (UCX). Both runs use $2^\circ \times 2.5^\circ$ latitude by longitude; however, the UCX mechanism is run with 72 vertical levels from the surface to the top of the atmosphere (TOA ~ 0.1 hPa), while the standard (tropchem) run uses 47 levels. The reduced vertical levels are created by lumping together sets of the higher resolved levels from around 70 hPa to the top of the atmosphere. For both runs the input parameters such as MEGAN emissions and GEOS-5 meteorological fields are identical.

Figure 2.17 shows an example of surface HCHO amounts, averaged over Jan and Feb, 2007, with and without the UCX mechanism enabled. Surface HCHO (first model level; up to ~ 100 m) does not differ much between runs. The differences do not exceed 3% over Australia, and absolute differences are minor (note the scale in A-B). The major notable difference occurs over northern Africa, where HCHO is around 20% lower in the UCX run. Additionally a slight ($< 8\%$) decrease in HCHO over the oceans can be seen. The comparison is repeated using total columns (instead of surface values) in Figure 2.18, showing that differences affecting HCHO between the model run are spread over the entire vertical column.

Figure 2.19 shows the differences in surface isoprene concentrations over Australia, averaged over 1, Jan to 28, Feb, 2007. Here we start to see a higher relative difference in concentrations, although this is generally over the areas with less absolute concentrations. Very little isoprene is seen away from the continents (4-5 orders of magnitude less), due to its short lifetime and lack of oceanic sources. Generally isoprene is 0-30% higher over mid to western Australia when the UCX mechanism is turned on; however, this increase is lower in the regions with high isoprene emissions (north-east to south-east coastline). This enhancement can be seen throughout the entire tropospheric column as shown by Figure 2.19. There is a greater effect in Africa

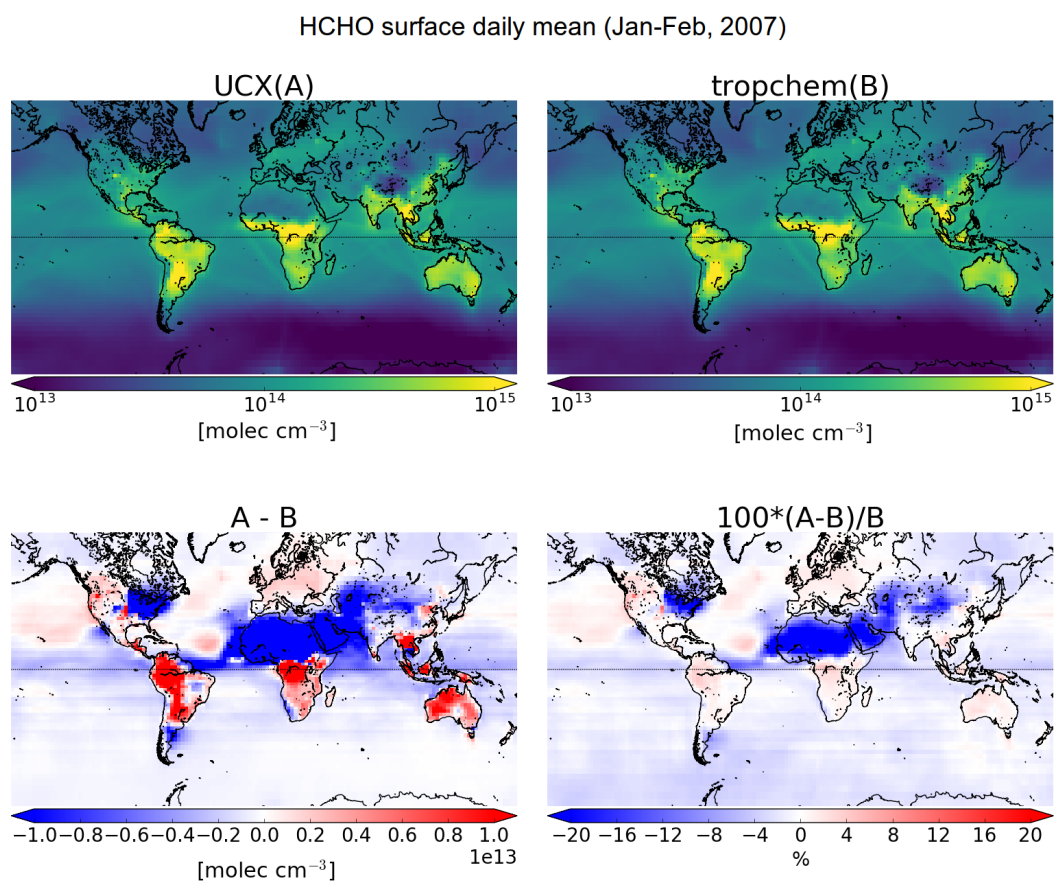


FIGURE 2.17: Surface HCHO simulated by GEOS-Chem with UCX (A: top left), and without UCX (B: top right), along with their absolute and relative differences (bottom left, right respectively). Amounts are the average of all times between 1 Jan and 28 Feb 2007.

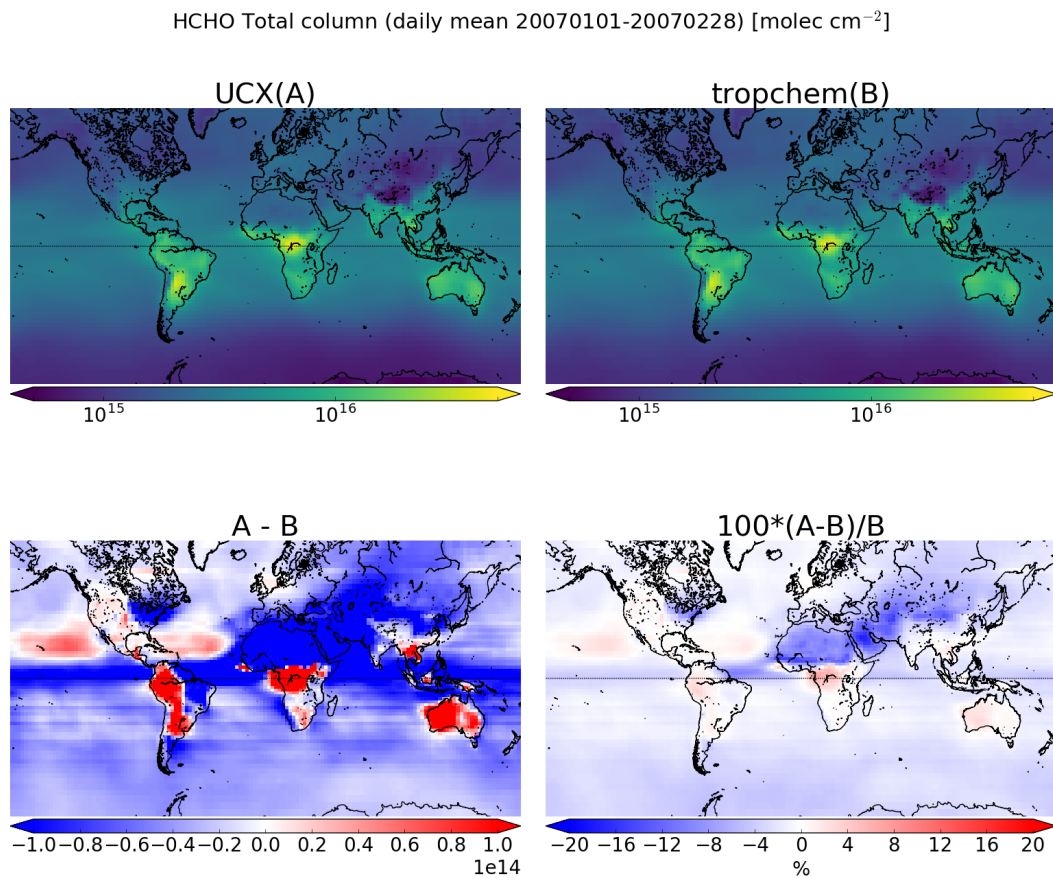


FIGURE 2.18: As Figure 2.17 using total column amounts instead of surface concentrations.

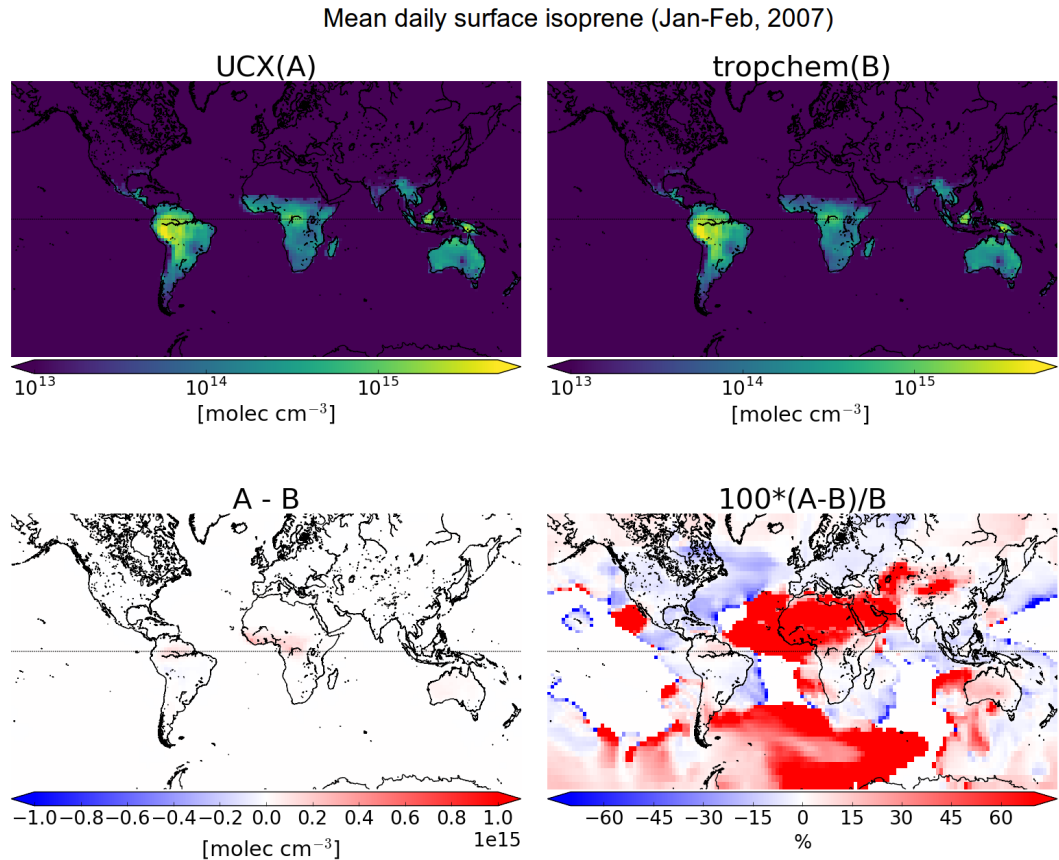


FIGURE 2.19: As Figure 2.17, except showing isoprene surface concentrations.

and South America in the tropics, with high relative differences in many regions with low absolute amounts.

The difference in isoprene between UCX and tropchem is likely caused by differences in the modelled radiation reaching the troposphere due to differences in simulated ozone in the stratosphere. Figure 2.21 shows the total column ozone between UCX and non-UCX run. This shows that UCX ozone is lower everywhere except for a thin band just north and south of the equator. With higher stratospheric ozone levels, less radiation would reach the troposphere. This would slow photolysis limited reactions, such as the splitting of ozone which leads to OH production in the troposphere, in turn slowing the isoprene loss to OH reactions.

Overall the UCX mechanism and increased vertical resolution lead to slightly higher isoprene and HCHO, and slightly lower ozone over Australia. These differences are on the order of 0-10% and as shown later (see Section 3.4) are minimal compared to other uncertainties in both AMF calculation and emissions estimation. Running UCX requires roughly twice the computation (and real) hours, and outside of Chapter 4 the normal tropchem runs are used.

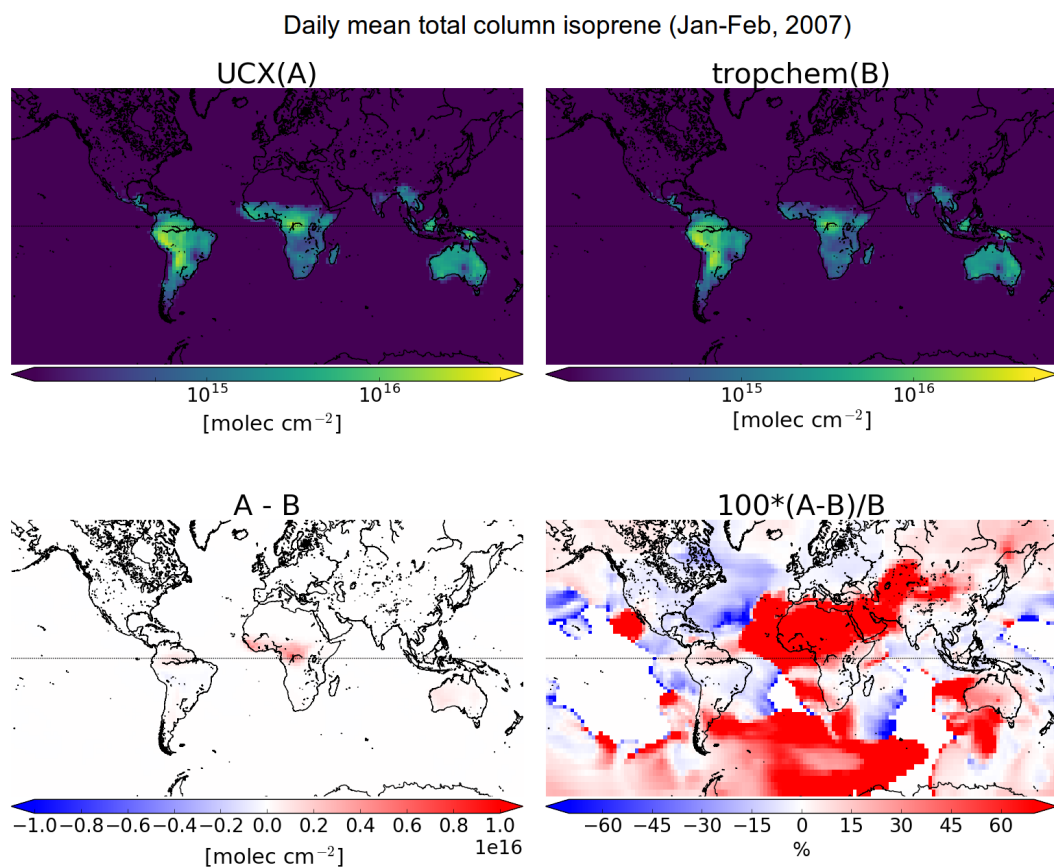


FIGURE 2.20: As Figure 2.19, except showing isoprene total column amounts.

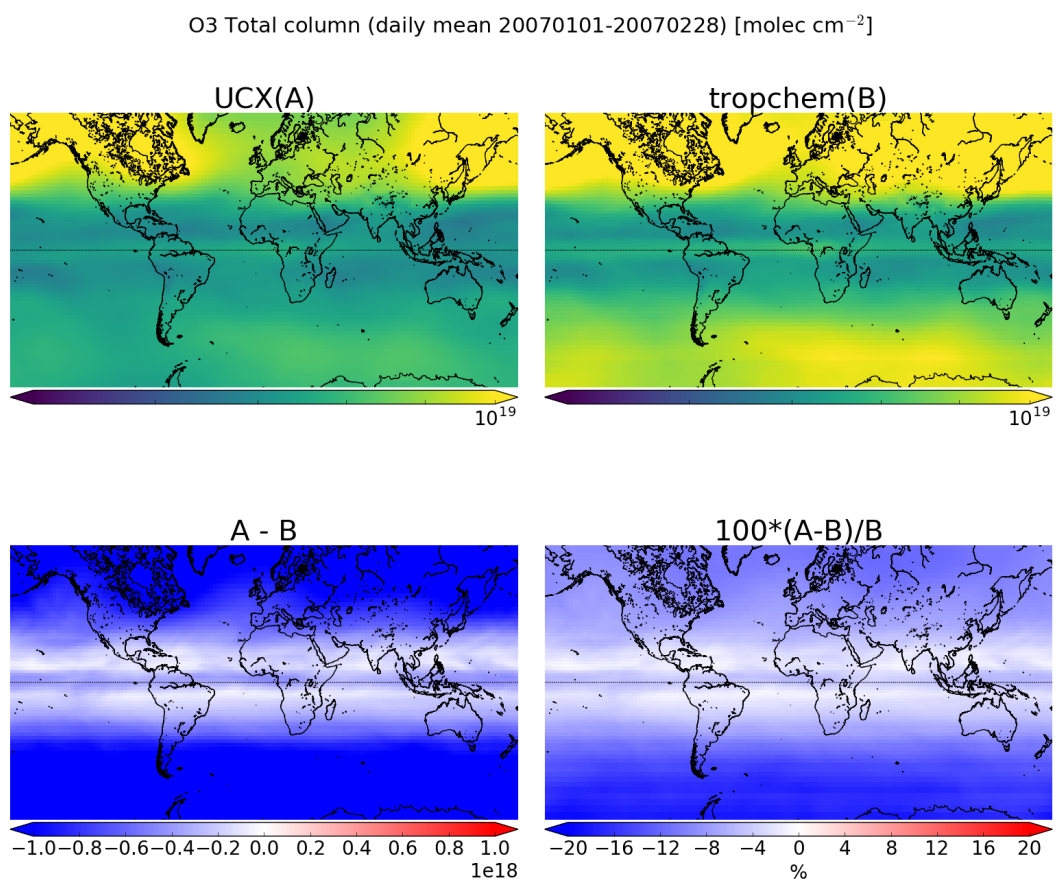


FIGURE 2.21: Total column ozone simulated by GEOS-Chem with UCX (A: top left), and without UCX (B: top right), along with their absolute and relative differences (bottom left, right respectively). Amounts are the average of all times between 1 Jan and 28 Feb 2007.

2.5 Calculating new AMF

One of the uses of GEOS-Chem in this thesis is to update the a priori HCHO column used in satellite measurements. The a priori is used when deriving the air mass factor (*AMF*), which is needed to transform satellite slant columns (*SC*) into vertical columns (Ω in molecules cm^{-2}): The AMF is the ratio of *SC* to the vertical column

$$AMF = \frac{SC}{\Omega} = \frac{\tau_s}{\tau_v} \quad (2.13)$$

with τ being the optical depth or thickness of the absorber through the slant (*s*) or vertical (*v*) path of light.

The OMI instrument records spectra of light which enters the viewing lens on the Aura satellite. The spectra provide backscattered intensity (I_B) at various wavelengths (see Section 2.3), with the light source (I_{B_0}) being the sun. Using the log of Beers law (Equation 2.5) we get

$$\tau_s = \ln I_{B_0} - \ln I_B$$

which can be subbed into Equation 2.13 to give an expression for the AMF which includes scattering:

$$AMF = \frac{\ln I_{B_0} - \ln I_B}{\tau_v} \quad (2.14)$$

We use $\nabla I = I_B - I_{B_0}$ to represent the change in intensity due to the absorber. For optically thin absorption, $\nabla I/I_B \ll 1$, and we can use:

$$AMF = \frac{\ln \left(1 - \frac{\nabla I}{I_B} \right)}{\tau_v} \approx \frac{-\frac{\nabla I}{I_B}}{\tau_v} \quad (2.15)$$

This is due to the logarithmic property $\ln(1 - x) \approx -x$ for $x \ll 1$. ∇I can also be expressed as the integral of the absorption slices over optical depth increments:

$$\nabla I = \int_0^{\tau_v} \frac{\partial I_B}{\partial \tau} d\tau \frac{\nabla I}{I_B} = \int_0^{\tau_v} \frac{\partial \ln I_B}{\partial \tau} d\tau$$

which can be placed into Equation 2.15 leading to

$$AMF \approx \frac{-1}{\tau_v} \int_0^{\tau_v} \frac{\partial \ln I_B}{\partial \tau} d\tau$$

We can then convert $d\tau$ to our path using Equation 2.7 leading to

$$AMF = \frac{-1}{\tau_v} \int_0^{\infty} \frac{\partial \ln I_B}{\partial \tau} \alpha(z) \eta(z) dz \quad (2.16)$$

where $\alpha(z)$ and $\eta(z)$ represent absorption cross section in $\text{m}^2 \text{ molecule}^{-1}$, and number density in molecules m^{-3} respectively. This uses the attenuation cross section relationship to optical depth (see Section 2.3.2).

To represent an average cross section weighted by the absorbing species' vertical distribution, the effective cross section (α_e) is used. This is to account for temperature

and pressure dependence of $\alpha(z)$, and is defined as:

$$\begin{aligned}\alpha_e &= \frac{1}{\Omega_v} \int_0^\infty \alpha(z) \eta(z) dz \\ &= \frac{\tau_v}{\Omega_v}\end{aligned}$$

Then replacing the τ_v in Equation 2.16 we obtain:

$$AMF = - \int_0^\infty \frac{\partial \ln I_B}{\partial \tau} \frac{\alpha(z)}{\alpha_e} \frac{\eta(z)}{\Omega_v} dz \quad (2.17)$$

Often the integrand of this AMF formula (Equation 2.17) is broken apart into two defining terms: the scattering weights $\omega(z)$ and the shape factor $S(z)$, described here:

- ω The scattering weights describing sensitivity of the backscattered spectrum to the abundance of an absorber at altitude z:

$$\omega(z) = - \frac{1}{AMF_G} \frac{\alpha(z)}{\alpha_e} \frac{\partial \ln I_B}{\partial \tau} \quad (2.18)$$

It is worth noting that in the OMI satellite product, the provided $\omega(z)$ term does not include the $\frac{1}{AMF_G}$ term and the calculations which follow therefor do not include this term when utilising the provided ω . This is not noted in any of the papers which recalculate the AMF from the OMI product, due to them recalculating the ω term themselves with a radiative transfer model such as LIDORT.

- ω the shape factor describes the profile of an absorber ($\eta(z)$) normalised by its total vertical column amount (Ω_v):

$$S(z) = \frac{\eta(z)}{\Omega_v} \quad (2.19)$$

Plugging Equations 2.18 and 2.19 into Equation 2.17 gives us:

$$AMF = AMF_G \int_0^\infty \omega(z) S(z) dz \quad (2.20)$$

Since we are using the ω provided by OMI, the AMF_G term is removed from this calculation as it is not part Equation 2.18 leading to

$$AMF = \int_0^\infty \omega(z) S(z) dz \quad (2.21)$$

Additionally the AMF can be determined using the sigma (σ) coordinate system, which denotes altitude as going from 1 (ground level) to 0 (TOA) (see Section 2.2). A conversion to the σ vertical coordinate is performed using $p = \sigma(p_S - p_T) + p_T$, where p_T is pressure at the top of the atmosphere and p_S is surface pressure. S_σ is a dimensionless normalised shape factor on the σ coordinate system. In the sigma

coordinate system we calculated the shape factor as defined in Palmer et al. (2001):

$$S_\sigma(\sigma) = \frac{\Omega_a}{\Omega_v} C_{HCHO}(\sigma) \quad (2.22)$$

where Ω_a is the vertical column of air from the surface to the top of the atmosphere and $C_{HCHO}(\sigma)$ is the mixing ratio of HCHO. We can integrate over the sigma coordinates using the hydrostatic relation $p = -\rho_a g z$, with ρ_a being air density, and g the gravitational acceleration:

$$\begin{aligned} \rho_a g z &= \sigma (p_S - p_T) + p_T \\ d\sigma &= -\frac{\rho_a g}{p_S - p_T} dz \end{aligned}$$

Substitution into 2.21 gives AMF using the sigma coordinates:

$$AMF = \int_0^1 w(\sigma) S_\sigma(\sigma) d\sigma \quad (2.23)$$

2.6 Recalculation of OMI HCHO

OMI HCHO vertical columns are calculated using modelled a priori HCHO profiles (see Section 2.3). When comparing satellite measurements against models it is important to recognise the impact of this a priori on the total column values. This is complicated by how OMI is differently sensitive to HCHO (and other trace gases) vertically throughout the atmosphere. When comparing OMI vertical columns (Ω_{OMI}) to GEOS-Chem (Ω_{GC}), the satellite AMF needs to be recalculated using GEOS-Chem modelled vertical gas profiles as the a prioris. Without performing this step a bias between modelled and measured total column values may be due to the a priori rather than chemistry or measurements (Palmer et al. 2001; Lamsal et al. 2014).

To recalculate vertical columns two components are calculated: and AMF and a reference sector correction. Here, two new AMFs are calculated, both using GEOS-Chem HCHO profiles as the new a priori. The first (AMF_{GC}) recalculates the satellite shape factor, but uses the original satellite scattering weights. The second (AMF_{PP}) recalculates both the satellite shape factor and the scattering weights. AMF_{PP} is created using code initially written by Professor P. Palmer.

In addition to a new AMF, a reference sector correction is determined using the method described in Abad et al. (2016). This correction has also been applied to the original vertical column in the OMHCHO product, so the column is available with and without this correction. The reference sector correction is unique for each of the 60 measurement tracks used by OMI. The correction is calculated for each of the two new vertical columns, and applied to each pixel to create the corrected vertical columns. The end product is three sets of corrected vertical columns: the original, one based on new shape factors, and one from with new shape factors and scattering weights.

2.6.1 Outline

An outline in computational order of what takes place when recalculating the Ω from OMI follows:

1. Section 2.6.2 describes how GEOS-Chem satellite overpass output is used to create new shape factors (S_z and S_σ).
 - (a) Vertical pressure edges and geometric midpoints are determined, along with altitudes (z), and box heights H .
 - (b) Number density and mixing ratio of HCHO (n_{HCHO} , C_{HCHO} respectively) are taken or created from model outputs HCHO (ppb), air density (molec cm⁻³), and box heights (m).
 - (c) Total column HCHO from GEOS-Chem (Ω_{GC}) is calculated

$$\Omega_{GC} = \sum_z (n_{HCHO}(z) \times H(z))$$

along with total column air (Ω_A , calculated similarly).

- (d) The shape factor $S_z(z)$ is calculated for each altitude

$$S_z(z) = n_{HCHO}/\Omega_{HCHO}$$

- (e) Sigma coordinates are created from pressures (see Section 2.2, Equation 2.1).
- (f) $S_\sigma(z)$ is calculated on each altitude:

$$S_\sigma(z) = C_{HCHO}(z) \times \frac{\Omega_A}{\Omega_{HCHO}}$$

2. For each pixel, new AMF (AMF_{GC} and AMF_{PP}) is created using the GEOS-Chem shape factors and satellite scattering weights in Section 2.6.3:

- (a) Satellite pixels (SC, scattering weights ($\omega(z)$)), pressure levels, latitude and longitude) are read from the OMHCHO dataset.
- (b) scattering weights (ω) are interpolated onto the same vertical dimensions (z and σ) as the shape factors.
- (c) Integration (approximated using rectangular method) is performed along the vertical dimension to calculate the new AMF on both coordinate systems:

$$AMF_z = \sum_z (\omega(z) \times S_z(z) \times H(z)) \quad (2.24)$$

$$AMF_\sigma = \sum_\sigma (\omega(\sigma) \times S_\sigma(\sigma) \times d\sigma) \quad (2.25)$$

These two AMFs represent the same thing using different coordinates, and either one can be used as the AMF_{GC} .

- (d) Code from Dr. Surl and Professor Palmer is used to recalculate both the shape factor and scattering weights to produce AMF_{PP} .

3. Section 2.6.4 describes how the original AMF, AMF_{PP} , and AMF_{GC} are used to determine the new vertical columns: $\Omega = SC/AMF$.

4. A reference sector correction (RSC) is defined each day using these AMFs along with modelled HCHO over the remote Pacific in Section 2.6.5:
 - (a) GEOS-Chem midday output ($\Omega_{GEOS-Chem}$ from 140°W to 160°W) are averaged monthly and longitudinally to provide modelled vertical columns over the reference sector.
 - (b) These vertical columns ($\Omega_{GEOS-Chem}$) are turned into modelled slant columns by multiplication with the AMF over the reference sector:
$$SC_{GEOS-Chem} = \Omega_{GEOS-Chem} \times AMF$$
 - (c) For each satellite pixel in the reference sector, a correction (*corr*) is calculated as the measured *SC* minus the modelled slant column at the nearest latitude:

$$corr[lat, track] = SC[lat, track] - VC_{GEOS-Chem}[lat] \times AMF$$
 - (d) These corrections are binned by satellite detector (track: 1-60), and latitude (0.36°; 500 latitudes from 90°S to 90°N).
 - (e) The median entry of each bin is determined and this forms the RSC[lat,track] (e.g., Figure 2.24).
5. VCC are determined using $VCC = (SC - RSC[lat, track]) / AMF$ for each measured SC and using each AMF, with the RSC linearly interpolated to the latitude of the satellite pixel (see Section 2.6.6).
 6. The VCC (along with most of the pixel and GEOS-Chem data) are binned onto a $0.25^\circ \times 0.3125^\circ$ grid along with other information (see Section 2.6.7).

2.6.2 Creating new shape factors

To visualise and analyse OMI HCHO columns, slant columns are transformed into vertical columns using the AMF. The shape factor (*S*) is one of the key components in creation of the AMF (see Section 2.5, Equation 2.21). The shape factor is calculated using GEOS-Chem midday output (see Section 2.4.7.1) which provide simulated HCHO concentration profiles ($\eta(z)$) and total columns (Ω) at $2^\circ \times 2.5^\circ$ horizontal resolution. Using Equation 2.19 to determine the shape factor is straightforward $S(z) = \frac{\eta(z)}{\Omega}$. The associated OMI per-pixel scattering weights are not changed in this calculation (unlike in Section 2.6.3.2).

Model output is provided as mixing ratios (C in ppbv), and is converted before being used in the shape factor calculation. The following equation converts model profile output from ppbv into number density (η) in molecules cm^{-3} :

$$\eta_{HCHO} = C_{HCHO} \times \eta_a \times 10^{-9} \quad (2.26)$$

where η_{HCHO} is the number density of HCHO, η_a is the number density of air (from model output), and C_{HCHO} is the mixing ratio of HCHO. The modelled total vertical

column Ω_{HCHO} is determined by:

$$\Omega_{HCHO} = \Sigma_z (\eta_{HCHO} \times H(z))$$

where $H(z)$ is the box height for altitude z . In effect this equation sums over the molecules per cm² in each altitude level.

As a sanity check S_σ is calculated (through Equation 2.22) to confirm that these shape factors are equivalent. Comparing the resulting AMFs created by Equations 2.23 and 2.21 for each pixel provides confidence in the unit conversions (and other factors) applied. These AMF values are nearly identical in practice (correlation coefficient > 0.99).

2.6.3 Creating new AMF using GEOS-Chem

2.6.3.1 Updating shape factors

From Equation 2.21 we have:

$$AMF = \int_0^{\infty} \omega(z) S(z) dz$$

Using the $\omega(z)$ from satellite data, along with our calculated S_z interpolated linearly onto the same vertical grid as $\omega(z)$, the AMF can be determined through integration. The integration is performed using a simple rectangular method, which multiplies the integrand midpoints by the change in height, and then takes the sum for each vertical box. This assumes that the provided scattering weights and shape factors are linear between the 47 resolved values.

2.6.3.2 Recalculating the AMF using PP code

The major limitation of vertical columns which implement AMF_{GC} is that the scattering weights also depend on the model atmosphere, which is not updated when only the shape factor is recalculated. This is addressed using Fortran code written by Paul Palmer and Randal Martin, subsequently updated by Luke Surl. This Fortran code (PP code) is computationally expensive, and is run on a subset of the globe (50-10° S, 160° W-160° E) covering Australia and the Pacific ocean. This allows both vertical column recalculations and reference sector correction.. The instrument sensitivity (or scattering weights; ω) and shape factors for each pixel are calculated within the PP code.

The code uses a combination of GEOS-Chem a priori profile information and satellite measurement data to calculate the AMF_{PP} by using LIDORT radiative transfer calculations to determine scattering.

Code for recalculating AMF using satellite swaths and modelled aerosol optical depths and gas profiles can be found at http://fizz.phys.dal.ca/~atmos/martin/?page_id=129. The coded method is detailed in Palmer et al. (2001), with modifications for clouds and use of the LIDORT radiative transfer model (Spurr 2002) as described by Martin et al. (2003). Modifications performed by Luke Surl at University of Edinburgh enabled the PP code to utilise OMI satellite data. Additionally, required

tropopause heights averaged within satellite overpass times are created by modifying the GEOS-Chem diagnostic output. The calculation of $\omega(z)$ is simplified by using large “look up tables” of values based on many parameters such as cloud top heights and optical depths. These AMF look up tables can be found in the source code at <https://github.com/LukeSur1/amf581g>. The PP code uses HCHO concentration profiles averaged between 1300 and 1400 LT, including optical depths at 550 nm, and dust concentrations from GEOS-Chem, along with a subset of the OMI pixel information. The required information is taken from OMHCHO daily swath files, and sorted into csv files (one per day) which are then read by the PP code in conjunction with the GEOS-Chem outputs for each day. The PP code then produces a list of recalculated AMF which are read by python code and associated with the corresponding satellite pixel.

2.6.3.3 Saving the AMF with satellite pixels

OMI satellite pixels are read and filtered for quality (see Section 2.3.1) and have their AMFs calculated as shown above. The process is outlined in figure 2.43 for a single day. This filtering removes highly uncertain pixels, including row anomaly affected pixels. Additional information is added to each pixel, including the new AMFs. Each pixel and its relevant data are saved in a long list for subsequent processing.

2.6.4 Vertical columns from AMF

All that remains for recalculating the total vertical column using our new a priori shape factor is to apply the new AMF to the slant columns and grid them onto our chosen resolution. Each satellite pixel at this stage has an associated SC along with three AMFs: the original (AMF_{OMI}), one with recalculated shape factors (AMF_{GC}), and one completely recalculated using PP code (AMF_{PP}). These are used to create vertical columns (Ω) through Equation 2.13: $\Omega = SC / AMF$.

Figure 2.22 shows a comparison between the three satellite Ω over Australia for 2005. Fully recalculated AMF_{PP} show a distinct bi-modal distribution compared against the approximately Gaussian distributions of the AMF_{GC} and the original AMF_{OMI} . Additionally there is a steep decline in mean AMF_{PP} after February which is not seen in the other AMF, and for the rest of the year the three AMF follow the same pattern with AMF_{PP} around 10% lower on average. While the explanation for this is beyond the scope of this thesis, it does show that a complete recalculation of both the shape factor and the scattering weights makes a large difference in the AMF calculation when compared to just recalculating the shape factor.

2.6.5 Reference sector correction

On a medium to long time scale, OMI degradation needs to be accounted for. To remove effects from the deterioration of the satellite instrument, measurements over the remote pacific (our reference sector) are combined with GEOS-Chem simulations to create a reference sector correction (RSC). In this thesis we use OMI HCHO columns to estimate isoprene emissions, and correcting background HCHO does not affect this

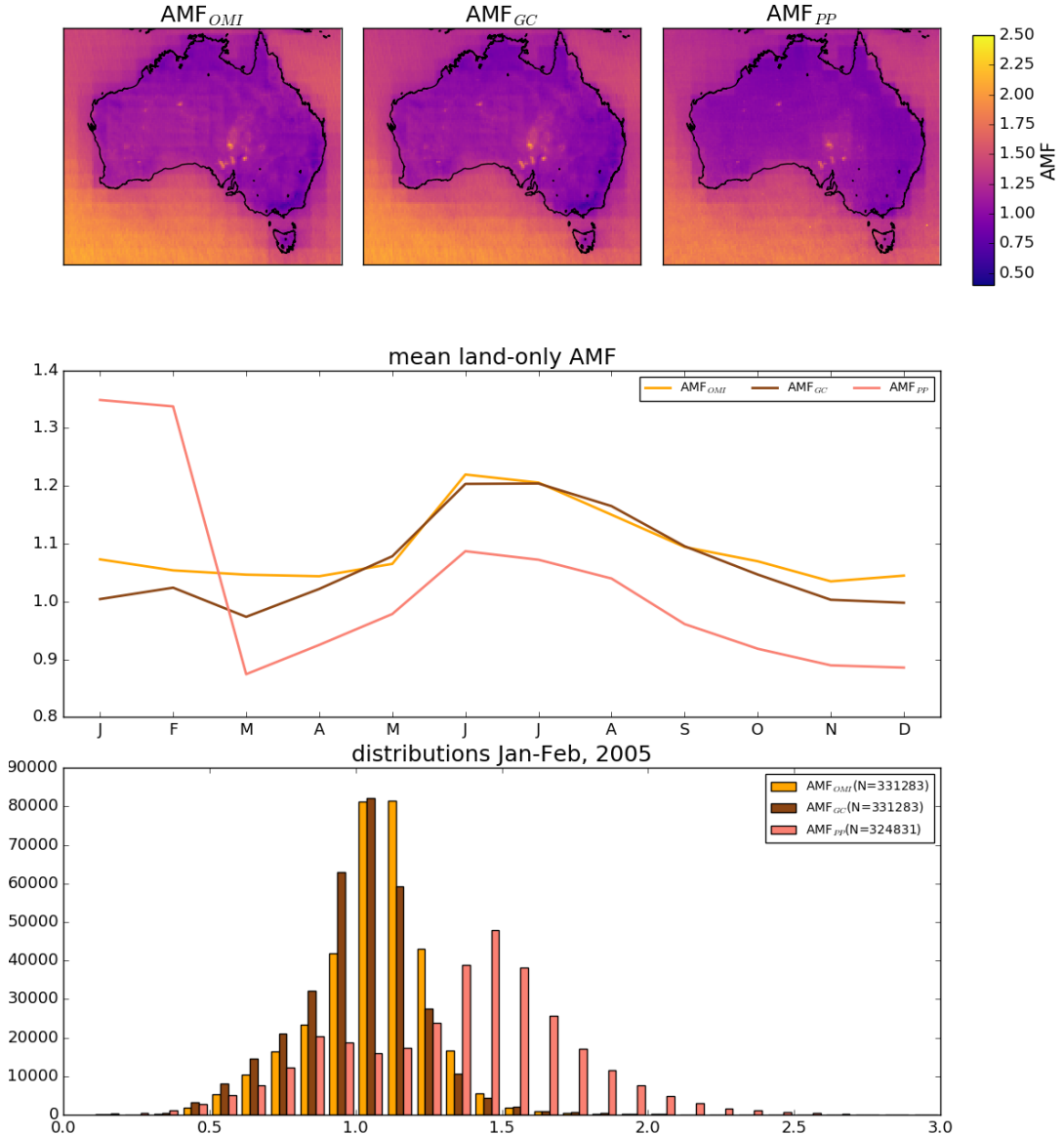


FIGURE 2.22: Top row: averaged OMI Satellite AMF for 2005, from the OMHCHO data set (left, AMF_{OMI}), recalculated using GEOS-Chem shape factors (middle, AMF_{GC}), and recalculated using GEOS-Chem shape factors and scattering weights (right, AMF_{PP}). Middle row: AMF time series over 2005 for each recalculation. Bottom row: AMF frequency distributions over January and February. Oceanic pixels are filtered out, only land pixels are included in this figure.

calculation. The correction should reduce bias caused by satellite degradation, without impacting isoprene emissions estimation. The RSC corrects for several problems; however, it introduces some a priori model influence. One corrected problem is the potential influence of varying dead/hot pixel masks across the OMI 2-D detector array (De Smedt et al. 2015). This method also corrects for the errors introduced through correlations between BrO and HCHO absorption cross sections, which are especially significant at high latitudes (Gonzalez Abad et al. 2015).

HCHO products from OMI and SCIAMACHY both use a median daily remote Pacific ocean radiance reference spectrum, over 15°S-15°N, 140°-160°W where it is assumed that the only significant source of HCHO is methane oxidation (De Smedt et al. 2008; Barkley et al. 2013; Kurosu and Chance 2014). Here a new reference sector correction is created using modelled and measured HCHO columns over the remote Pacific to produce corrected vertical columns (VCC). This follows Abad et al. (2016), and defines the remote Pacific as the band between 140°W to 160°W. Each satellite slant column measurement is corrected by how much the satellite reference sector measurements at that latitude diverge from modelled amounts over the reference sector.

Modelled slant columns over the reference sector ($SC_{GEOS-Chem}$) are calculated by multiplying modelled vertical columns with the AMF calculated in prior sections using Equation 2.13:

$$SC_{GEOS-Chem} = \Omega_{GEOS-Chem} \times AMF$$

The longitudinal average is taken within the remote Pacific, as corrections are (assumed to be) longitudinally invariant. These modelled slant columns are averaged over the month and interpolated latitudinally to 500 equidistant bins. Figure 2.23 shows the simulated reference sector vertical columns as an example, calculated for January 1st 2005. In this figure the latitudinal resolution is increased from 2° to 0.36°, through linear interpolation, in order to form 500 vertical bins which are used in correcting the satellite data. This resolution is chosen to match that of Abad et al. (2016).

For OMI swaths, each row of measured data contains 60 “Across track” (track) measurements. The track index i relates the measurement to one of the 60 columns of data. Corrections (molecules cm⁻²) for each measurement are calculated by taking the difference between the measured slant column and the a priori slant column as follows:

$$Correction(i, j) = SC(i, j) - \Omega_{GEOS-Chem}(lat(j)) \times AMF(i, j) \quad (2.27)$$

where j represents a latitude index. The RSC is this list of *Correction* values binned by latitude using medians, and used per pixel based on the linear interpolation to that pixels latitude. The RSC is independently calculated for each of the 60 tracks, at each latitude in the 500 0.36° bins. This provides a different RSC for each of the three AMFs. Due to incomplete latitudinal coverage, the correction for each track is interpolated linearly between measurements, with corrections outside of the highest measured latitudes being equal to the corrections at the highest measured latitudes.

Figure 2.24 shows an example of the 60 track corrections for January 1st 2005. The points are satellite measurements longitudinally averaged over the remote Pacific, coloured by track number. Another way to look at this correction is given in the OMI corrections panel of Figure 2.23, which has tracks along the x axis and latitude on the y

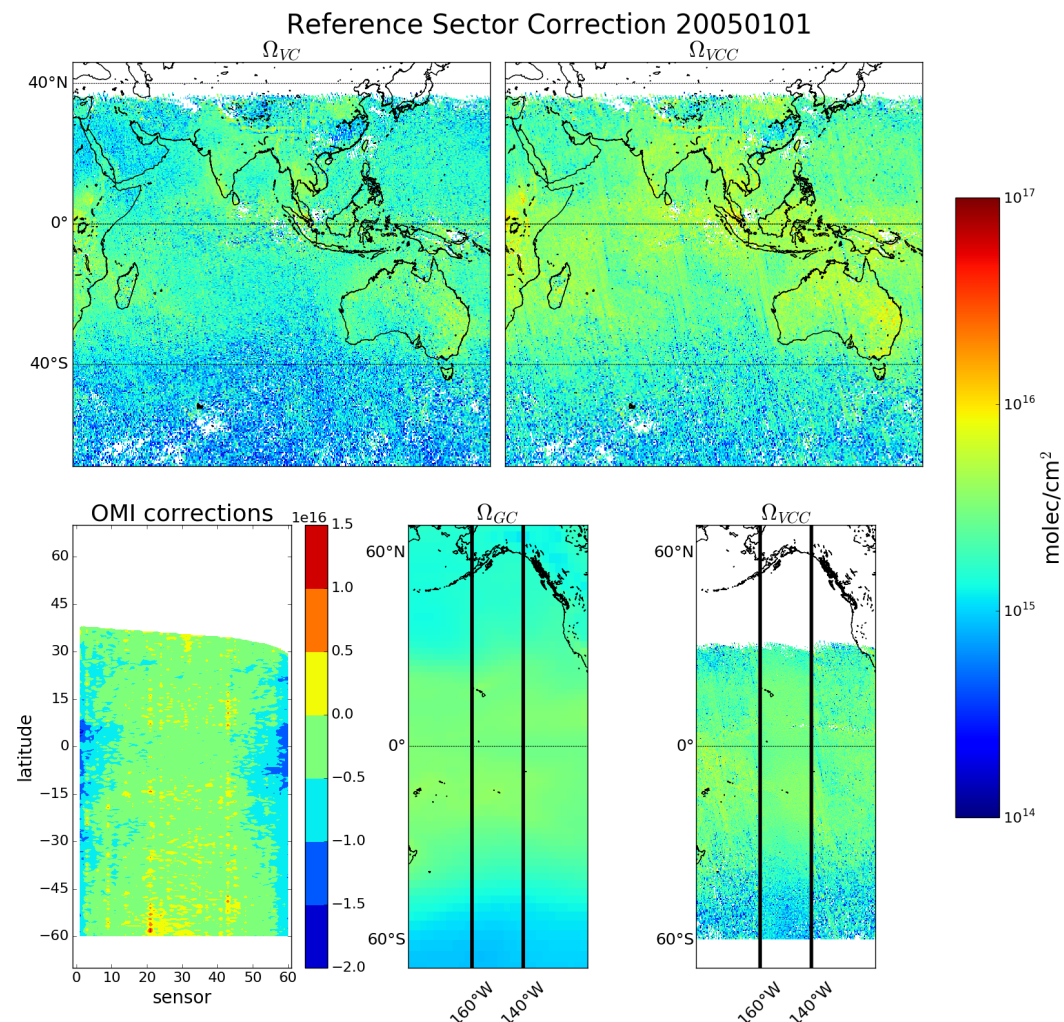


FIGURE 2.23: Example of remote Pacific RSC using 8-day average measurements and one month modelled data. OMIVC shows the uncorrected vertical columns, while *Corrected* shows the corrected vertical columns. OMI corrections shows the correction applied globally based on latitude and OMI track number(sensor). Ω_{GC} shows the GEOS-Chem modelled HCHO VC over the reference sector (region within black vertical lines), with Ω_{VCC} showing the corrected VC over the same area.

axis. This figure shows how corrections are distributed (over this 8-day sample) with more negative values towards the outside tracks, especially in the tropics.

2.6.6 Corrected vertical columns

Corrected vertical columns, or VCC, are created using the difference between slant columns (SC) and reference sector corrections (RSC, detailed in prior section) divided by the AMF.

$$VCC = \frac{(SC - RSC)}{AMF} \quad (2.28)$$

This is equivalent to taking the difference between the slant column and its measured reference sector equivalent (SC_0), and then adding the modelled reference sector column ($\Omega_{GC,0}$):

$$VCC = \frac{(SC - SC_0)}{AMF} + \Omega_{GC,0} \quad (2.29)$$

This method is used in several works, including De Smedt et al. (e.g., 2008), De Smedt et al. (2012), De Smedt et al. (2015), Barkley et al. (2013), and Bauwens et al. (2016). Recently this correction was expanded (for OMI data) to include latitudinal and instrument track influence by Gonzalez Abad et al. (2015).

One *correction* (Equation 2.27) is associated with every good satellite measurement. This is used to create a reference sector corrected measurement (VCC) through the following equation:

$$VCC(i,j) = \frac{SC_{HCHO}(i,j) - correction(i, lat(j))}{AMF(i,j)} \quad (2.30)$$

For each good satellite measurement the corrected vertical column is calculated two times, once using each new AMF.

2.6.7 Binning the results daily

Finally the pixels are binned into a gridded dataset named OMHCHORP, as shown in Figure 2.43. The resolution is chosen to match the native resolution of the GEOS meteorological fields ($0.25^\circ \times 0.3125^\circ$). A bin entry count is used to allow easy re-binning, and can be used to check for sparse data days due to filtering. Data averaged into this dataset:

1. OMI slant column
2. OMI air mass factor
3. OMI vertical column
4. OMI corrected vertical column
5. GEOS-Chem recalculated air mass factor
6. GEOS-Chem recalculated vertical column
7. GEOS-Chem recalculated corrected vertical column

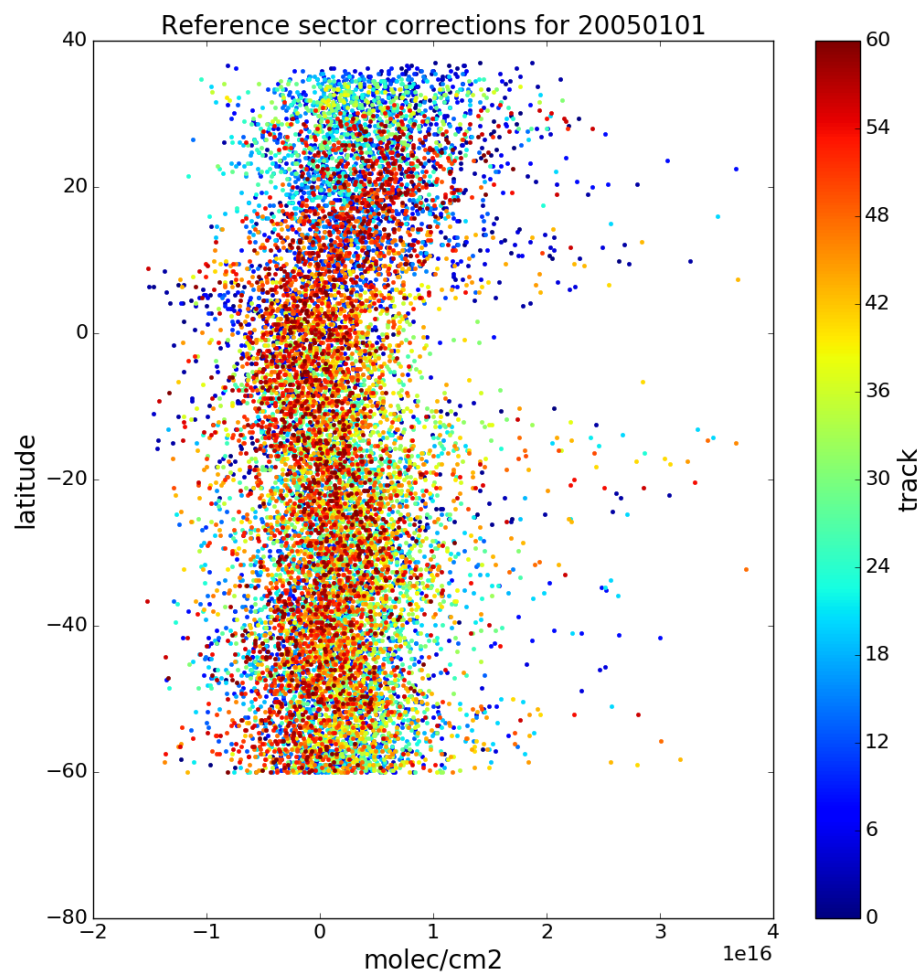


FIGURE 2.24: Example of track correction interpolations for January 1st 2005, points represent the difference between satellite slant column measurements and modelled slant columns over the remote Pacific.

8. GEOS-Chem air mass factor recalculated using PP code (AMF_{PP})
9. GEOS-Chem corrected vertical column based on PP code
10. satellite pixel counts (summed into bins)
11. OMI vertical column fitting uncertainty

This process requires processing time and storage space, and is performed on the National Computing Infrastructure (NCI) supercomputer. In order to reprocess one year of swath files (~ 162 GB = $142 + 16 + 4$ GB OMHCHO, MOD14A1, and OMNO2d respectively per year) of daily data was downloaded and then transformed into ~ 8 GB (per year) of daily gridded data. This takes around 90 minutes per day; however, each day is completely independent and can be run in parallel once model output is available. Initially parallelism was built into the python code; however, simply running python code independently for each date was simpler and more scalable. As much as possible this work uses HDF-5 or NetCDF-4 formats, although GEOS-Chem output is in bitpunch format. The scripts to regrid and reprocess the swath data set are available from github at https://github.com/jibbals/OMI_regridding.

2.6.8 Difference between original and corrected OMI HCHO columns

Corrected vertical columns (VCC) of HCHO are created at $0.25^\circ \times 0.3125^\circ$ horizontal resolution. Three VCC are created based on OMI and the new AMFs (from section 2.6.4) and RSCs. Figure 2.25 shows how the recalculated columns compare to the original (OMI, left). VCC_{OMI} are the lowest overall for the depicted month, and recalculating just the shape factor increases the column amounts (VCC_{GC}); however, recalculating both the shape factor and the scattering weights leads to a broader spread of values. Both sets of recalculated columns (GC , PP) show more high concentration (> 1.5 molec cm^{-2}) columns and lower background concentrations over the ocean. Together this may lead to a slightly steeper continental enhancement which may be expected since elsewhere OMI HCHO is seen to be up to 40% underestimated (e.g., Zhu et al. 2016; De Smedt et al. 2015; Barkley et al. 2013).

Potential TODO: Worth looking at regressions between the three AMF and VCC techniques? Plot and discussion paragraph would go here.

When reading AMF_{PP} , missing and near zero ($AMF_{PP} < 0.0001$) values are removed, which leads to fewer overall pixels used to recalculate VCC_{PP} than the original VCC_{OMI} . Figure 2.26 shows how many pixels go into the column recalculation over Australia each month. The filtered pixel counts refers to how many pixels are removed through applied filters, which are described in the following section (Section 2.7). A decrease in pixel counts is apparent starting in April and lasting until August, which is caused by the reduction in good pixels recorded at increased solar zenith angles which occur during winter at higher latitudes. There is a consistent bias of 1 – 10% between the techniques, caused by the extra filtering applied to unreasonable AMFs calculated by the PP code.

Figure 2.27 shows global and Australian HCHO averaged total column maps for 2005, along with time series and distributions. The completely recalculated VCC_{PP} has a higher number of high HCHO amounts compared to both the original and partially

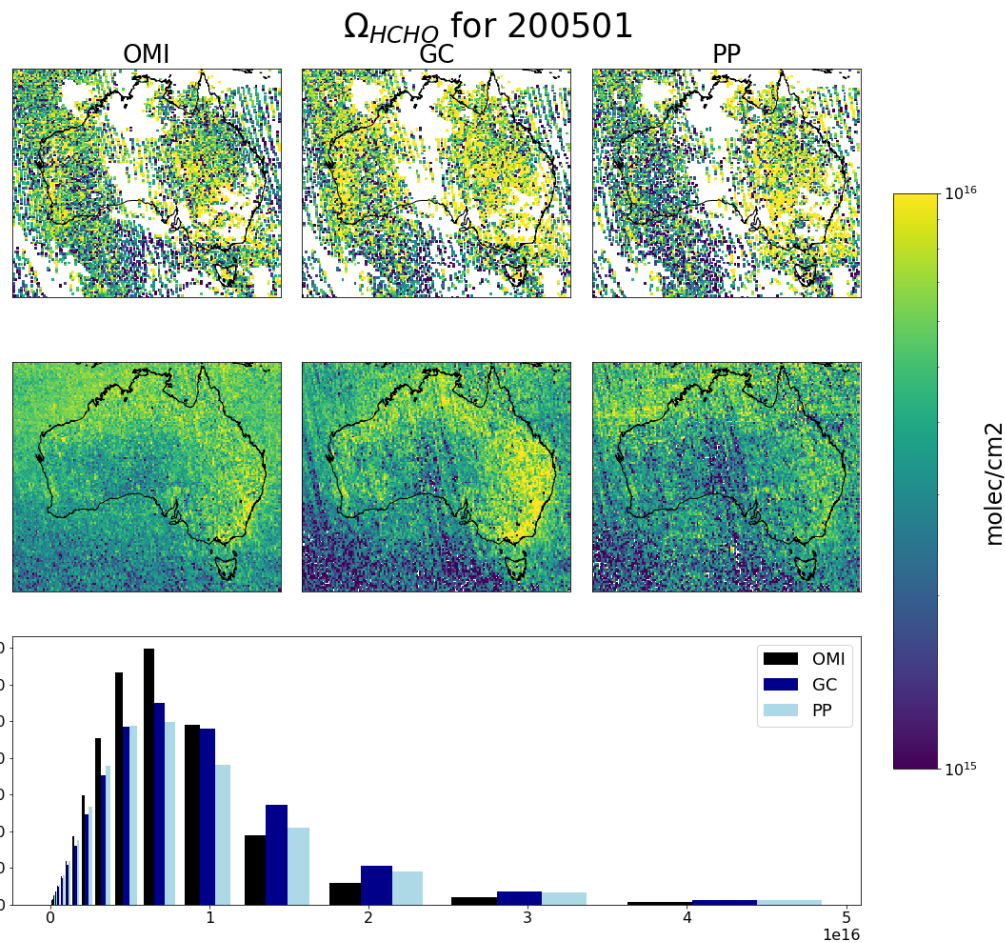


FIGURE 2.25: Row 1: regredded corrected Ω_{HCHO} from OMHCHO on January 1, 2005: original (left), recalculated using new shape factors (middle), and additionally using updated scattering weights (right). Row 2: shows the monthly average for January 2005. Row 3: shows the distribution over the month for each of the three column amounts. Distribution bins are logarithmic, resulting in wider bins for higher column amounts.

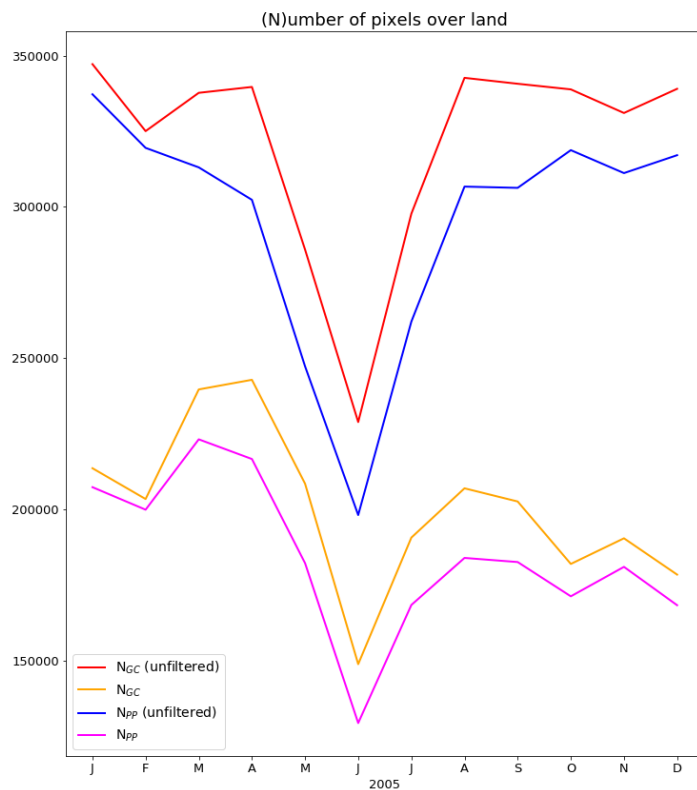


FIGURE 2.26: Monthly pixel counts over Australia (non-oceanic) used in recalculations of vertical columns. N_{GC} refers to the number of pixels used in AMF recalculation without running code from Paul Palmer, N_{Pp} refers to those which have been recalculated using their code. Filters applied are described in Section 2.7,

recalculated VCCs. Both recalculated VCCs appear to have lower average background amounts, seen over the ocean and parts of southern Australia, and also increased average amounts in the HCHO hot spots around the north and eastern coastal regions. This comparison shows how reprocessing with an updated model can have a systematic influence on the total column.

2.7 Filtering Data

A major goal in this work is to infer biogenic isoprene emissions from HCHO columns. Isoprene is the dominant source of HCHO over continental land masses; however, other precursor NVMOCs can contribute to observed HCHO. The main interference in the biogenic isoprene signal in HCHO comes from fire smoke plumes and major anthropogenic source regions. Biomass burning can be a large local or transported (via smoke plumes) source of HCHO, glyoxal (CHOCHO), and other compounds which influence HCHO levels. Anthropogenic emissions from power generation, transport, and agriculture can influence these levels as well. So to infer biogenic isoprene emissions, pyrogenic and anthropogenic influences should be removed (where possible) from modelled and measured data. In GEOS-Chem we simply turn off pyrogenic and anthropogenic emissions; however, in the OMI HCHO satellite product we mask potentially affected pixels.

In this work anthropogenic and pyrogenic influences on the OMHCHO satellite HCHO columns are removed by masking active fires, high AAOD, and high NO₂ levels measured by satellite. Active fires and suspected smoke plumes are masked, and together termed the pyrogenic filter. NO₂ measurements are used to mask potential anthropogenic influence. A summary of yearly filtering over Australian land squares at $0.25^\circ \times 0.3125^\circ$ resolution is provided in Table 2.4. Figure 2.28 shows an example year of anthropogenic and pyrogenic filtering, highlighting how many days and pixels are removed across Australia. The anthropogenic filter completely removes grid squares over Brisbane, Melbourne, and Sydney. Other major cities in Australia either do not emit enough NO₂ or are too dispersed and do not breach the threshold to be filtered as anthropogenic. The anthropogenic filter removes from $\sim .25\% - \sim 5\%$ of grid squares each day. Pyrogenic filtering removes from $\sim 5\% - \sim 20\%$ of the available grid square measurements per day. This filter tends to cover forested areas (as they are more prone to burning) as well as some hot spots that are likely due gas flaring or burning.

2.7.1 Pyrogenic filter

MODIS fire counts are used in conjunction with smoke AAOD enhancements from OMI to remove data points which may be affected by fires or fire smoke plumes. The MODIS fire counts come from a combination of measurements from the Terra and Aqua satellites (Terra overpasses at 10:30, 22:30 LT; Aqua at 13:30, 01:30 LT). satellite AAOD from product OMAERUVd (described in Section 2.2.1.3) is analysed over Australia to determine a suitable filter threshold. AAOD is used instead of an alternative product AOD as it is less sensitive to the presence of clouds (Ahn, Torres, and Bhartia 2008).

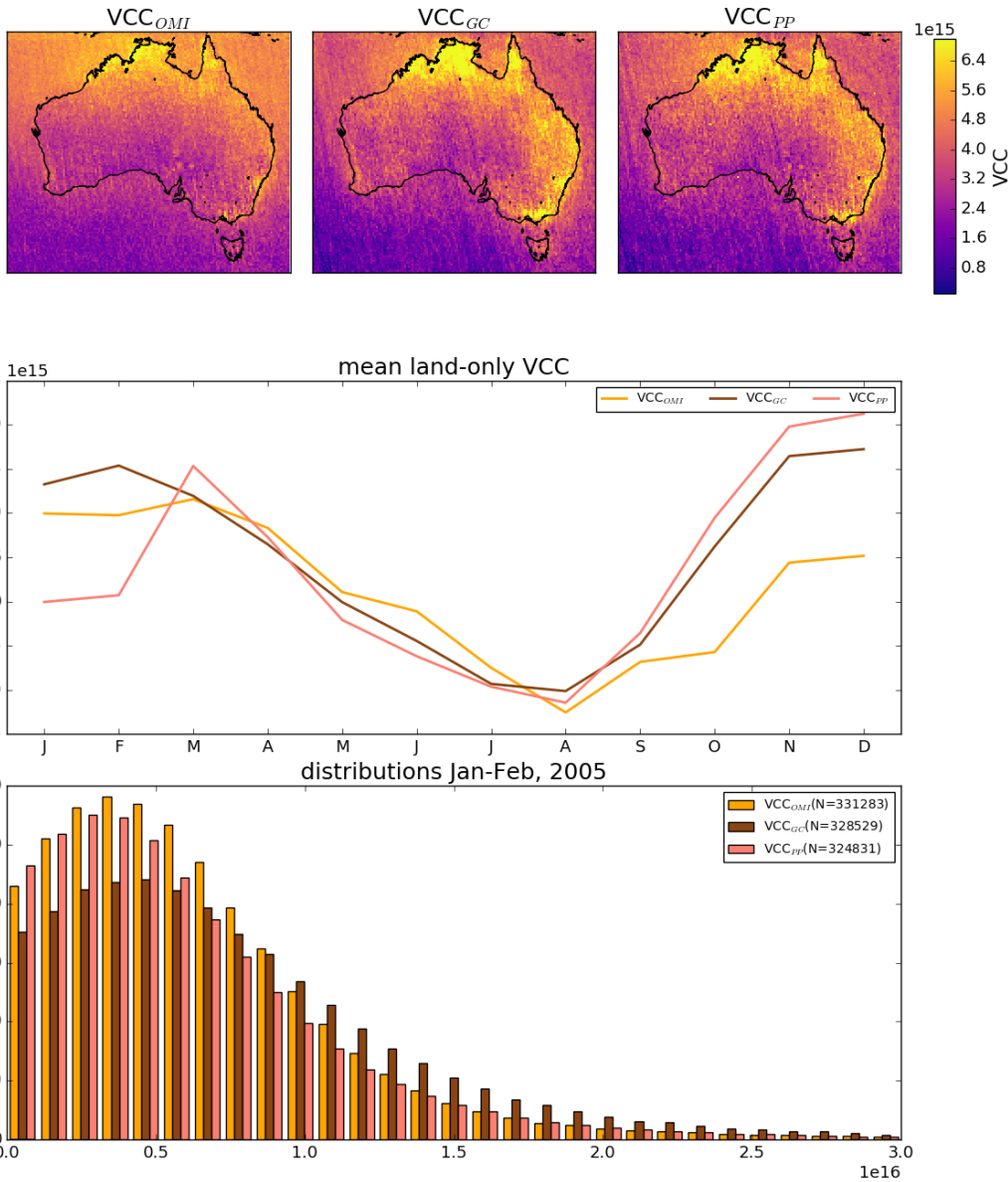


FIGURE 2.27: Top row: averaged OMI Satellite VCC for 2005, from the OMHCCHO data set (left, VCC_{OMI}), recalculated using GEOS-Chem shape factors (middle, VCC_{GC}), and recalculated using GEOS-Chem shape factors and scattering weights (right, VCC_{PP}). Middle row: VCC time series over 2005 for each recalculation. Bottom row: VCC frequency distributions over January and February. Oceanic pixels are filtered out, only land pixels are included in this figure.

TABLE 2.4: Satellite pixels remaining after filtering by active fires, smoke, and anthropogenic masking. In parenthesis are the portion of pixels filtered.

Year	Pixels	Active fires	Anthropogenic	Smoke	Total
2005	3.9e+06	3.5e+06(9.2%)	3.8e+06(1.3%)	3.8e+06(1.7%)	3.4e+06(11.5%)
2006	3.8e+06	3.4e+06(11.2%)	3.7e+06(2.4%)	3.7e+06(3.2%)	3.2e+06(14.8%)
2007	3.7e+06	3.4e+06(9.9%)	3.7e+06(2.0%)	3.7e+06(2.6%)	3.3e+06(13.0%)
2008	3.5e+06	3.3e+06(8.1%)	3.5e+06(1.4%)	3.5e+06(1.1%)	3.2e+06(10.0%)
2009	2.7e+06	2.4e+06(9.1%)	2.6e+06(1.8%)	2.6e+06(1.7%)	2.4e+06(11.6%)
2010	2.0e+06	1.9e+06(6.5%)	2.0e+06(1.4%)	2.0e+06(0.5%)	1.9e+06(8.1%)
2011	1.9e+06	1.7e+06(12.5%)	1.9e+06(1.9%)	1.9e+06(2.7%)	1.6e+06(15.2%)
2012	2.5e+06	2.2e+06(14.3%)	2.5e+06(1.8%)	2.5e+06(3.3%)	2.1e+06(17.4%)

Pixels: how many land pixels are read over Australia, after cloud fraction filtering.
Total removed pixels accounts for overlap between filters.

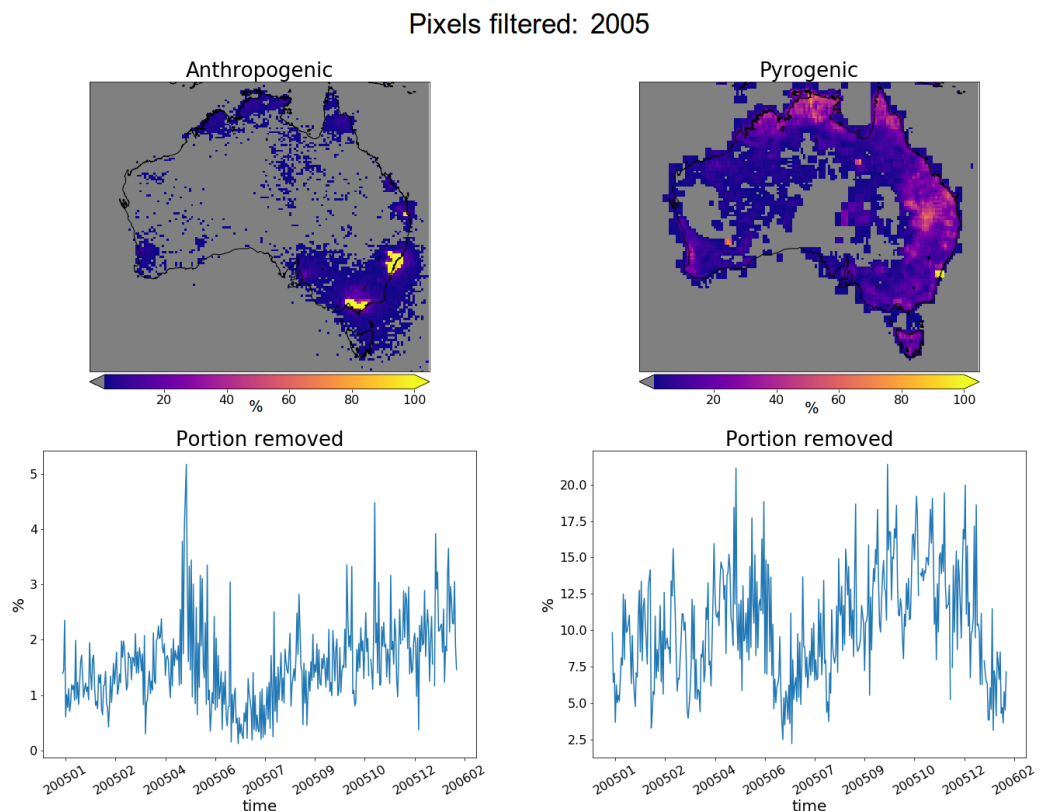


FIGURE 2.28: Top row shows grid squares filtered out by anthropogenic (left) and pyrogenic (right) influence masks over 2005. Bottom row shows portion of Australian grid squares filtered out each day.

OMHCHO total column HCHO Ω is processed into a $0.25^\circ \times 0.3125^\circ$ horizontal daily grid. Pyrogenic filters are interpolated to the same horizontal resolution as Ω to simplify application. The following steps are performed to create the pyrogenic influence mask:

1. MOD14A1 daily gridded Aqua/Terra combined fire counts ($1 \times 1 \text{ km}^2$) are binned into $0.25^\circ \times 0.3125^\circ$ bins (matching the resolution of binned Ω).
2. A rolling mask is formed which removes Ω if one or more fires are detected in a grid square, or in the adjacent grid square, up to 2 days previously. This includes the current day, making 3 days of fires in total being filtered out on each day.
3. AAOD at 500 nm is mapped from OMAERUVd ($1 \times 1^\circ$ resolution) onto the $0.25^\circ \times 0.3125^\circ$ resolution.
4. An AAOD threshold of 0.03 is determined through visual analysis of AAOD distributions over several days, including days with and without influence from active fires, dust, and transported smoke plumes. Grid squares with AAOD over this threshold are considered potentially affected by transported fire smoke.

This method of masking fires can be compared to Marais et al. (2012) and Barkley et al. (2013): Marais et al. (2012) removed pixels colocated with non zero fire counts in any of the prior eight days, within grid squares with $1^\circ \times 1^\circ$ resolution, and Barkley et al. (2013) used fires from the preceding and current day, within local or adjacent grid squares, at $0.25^\circ \times 0.3125^\circ$ resolution.

Figure 2.29 shows the effects from filtering HCHO vertical columns with different fire filtering. Vertical column amounts averaged over January, 2005, and the pixel counts are shown side by side. The figure shows the effects of applying an increasingly strict fire filter. Each row has a stricter fire filter applied from top to bottom, with no fire filter on the first row up to filtering pixels from squares with fires up to 8 days prior. Increasing prior days used when creating the fire filter leads to a serious reduction in available pixels, with a wider range of areas dropping to near zero pixel counts. The overall decrease in vertical column HCHO is minor, dropping from ~ 4 to $\sim 3.9 \text{ molec cm}^{-2}$ between applying no filter and the strictest filter. In this month the highest the fires are most prominent across Queensland and northern NSW, and a large section of the north eastern coast becomes largely filtered out. Increasing the strength of the active fire filter increases the regional impacts on HCHO columns. In this work two prior days of active fires are masked.

Determining the AAOD due to smoke can be difficult since both smoke and dust absorb UV radiation (Ahn, Torres, and Bhartia 2008; Marais et al. 2012). AAOD filtering is designed to remove pixels affected by smoke; however, it may occasionally remove pixels affected by dust. Dust in Australia is highly episodic and false positives in the smoke filter should not affect more than a few days per month, especially over regions with high tree coverage (Shao et al. 2007). The threshold is determined through analysing AAOD over Australia in 4 scenarios: normal conditions, active local fires, transported fire smoke, and large scale dust storms. An example of these scenarios and the AAOD distributions is shown in Figure 2.30. This figure shows AAOD maps and distributions, along with satellite imagery on the same day in column 4 (from <https://worldview.earthdata.nasa.gov/>).

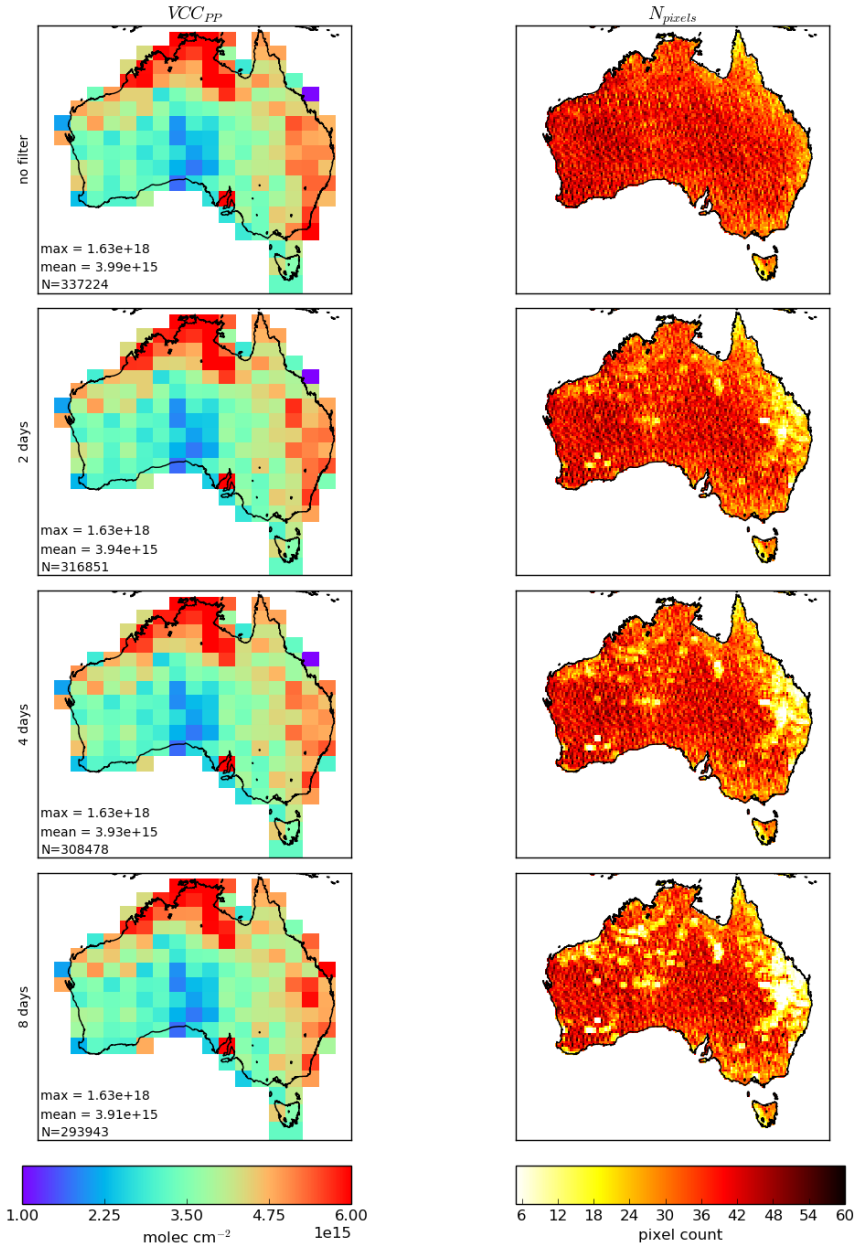


FIGURE 2.29: Recalculated OMI vertical HCHO columns and pixel counts for January 2005. Column 1: VCC_{PP} amounts after applying the active fire filter. The filter is applied at $0.25^\circ \times 0.3125^\circ$ resolution, before output is averaged into $2^\circ \times 2.5^\circ$ bins. Column 2: Pixel counts after applying the active fire filter (summed into $0.25^\circ \times 0.3125^\circ$ bins). Row 1-4: increasing number of prior days which have active fires are included when masking fire influence. The first row shows the values without applying any active fire filter. The average and maximum VCC column amount (at $0.25^\circ \times 0.3125^\circ$ resolution), and number of pixels, is inset as text in column 1 of each row.

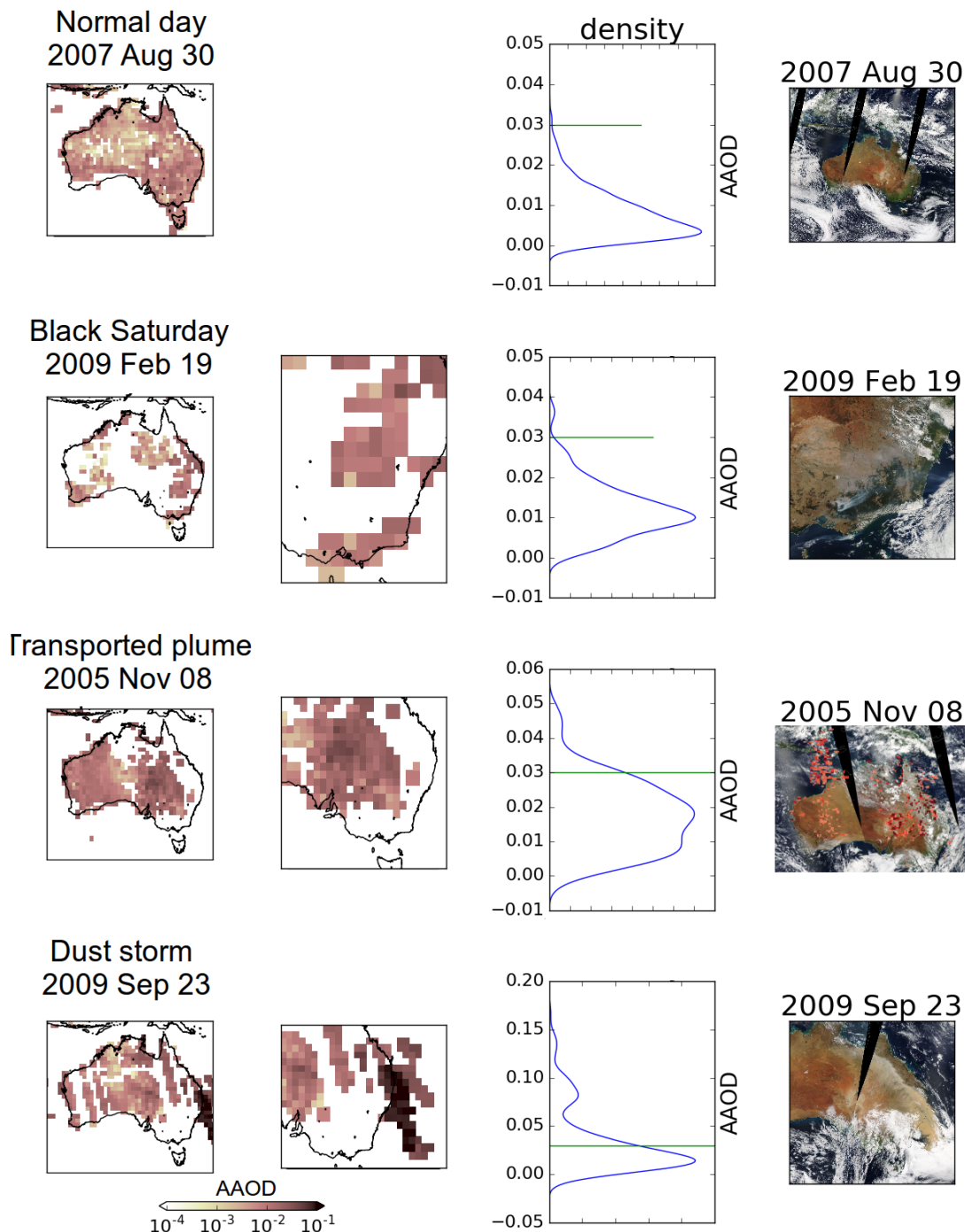


FIGURE 2.30: AAOD from OMAERUVd (columns 1, 2, 3) over Australia for four different scenarios (rows 1-4). Black Saturday (row 2) demarks the occurrence of widespread bush fires across Victoria. The transported plume in row three can be seen in the overlaid AOD shown in the last column, Indonesia (northwards from Darwin) suffered from wide-spread forest fires around this time. Scenes in the final column are created using the EOS Worldview website <https://worldview.earthdata.nasa.gov/> from satellite products provided therein. AAOD = 0.03 is demarcated by a horizontal line in the density plots in column 3. Density plots show normalised AAOD frequencies (scale not shown).

Figure 2.31 shows the extent of pixels filtered out by the pyrogenic filter over 2005 and 2012. One clear hot spot is located over Port Kembla (south of Sydney), most likely due to the flame which burns over the blast furnace stack throughout the year (<https://www.bluescopeillawarra.com.au/community/skylineimages/>). Another hot spot can be seen in Western Australia over Kalgoorlie, where a large open cut gold mine is always open and blasting daily (<https://superpit.com.au/wp-content/uploads/2015/01/Blasting-Information-Sheet.pdf>). In Western Queensland over Mount Isa there is again a mining hotspot, with a blast furnace and several smoke stacks (<http://www.mountisamines.com.au/en/about-mim/Pages/home.aspx>). A large area in southern Queensland/northern NSW is also heavily filtered, potentially due to gas flaring in the Surat Basin, which has thousands of petrol and gas wells (<http://www.ga.gov.au/scientific-topics/energy/resources/petroleum-resources/gas>). The highest concentrations of removed pixels lie along the northern and eastern coastlines, and correspond with forested areas (see Figure 2.33), which suggests that forest fires are being masked properly. Central Australia is largely unmasked, which could be due to a lack of sufficient vegetation to create fires and smoke visible by satellite. The proliferation of petrol or gas wells (see Figure 2.32) may also lead to AAOD enhancement wherever activity stirs up dust, and could be mistaken as active fires wherever gas flaring occurs. In 2005, 388 gas wells existed in Queensland; however, more than 2000 wells (cumulative) were approved by 2013 (Carlisle 2012). The comparison between fire filtering in 2005 and 2012 does not indicate that the proliferation of gas wells in the intervening years had any strong effect on data filtering.

2.7.2 Anthropogenic filter

Enhanced NO₂ concentrations indicate anthropogenic influence over Australia. We use NO₂ as a proxy for potential anthropogenic NMVOC emissions, as these could bias the inversion performed in Chapter 3. A filter is designed using the tropospheric NO₂ columns in the OMNO2d product.

NO₂ columns near several major cities in south eastern Australia over 2005 are used to determine a suitable threshold for anthropogenic influence. The mean, standard deviation, and time series over Australia of tropospheric NO₂ measured by satellite is shown in Figure 2.34. Tropospheric NO₂ columns averaged within all of Australia and each region is shown in Figure 2.34. Anthropogenic influences are clearly visible near major cities in Australia, and some influence can be seen along nearly every coastline.

The anthropogenic filter is created for each year from in two steps:

1. Daily grid squares with NO₂ greater than 1.5×10^{15} molec cm⁻² are flagged as anthropogenic.
2. After taking the yearly average for each grid square, any tropospheric NO₂ columns greater than 2×10^{15} molec cm⁻² are flagged for the whole year.

These thresholds are chosen subjectively through trial and error so as to ensure the removal of definite anthropogenic influence while not removing too many data points over near uninhabited portions of Australia. These thresholds completely remove grid squares over major cities which are likely emitting NMVOCs year round, and also

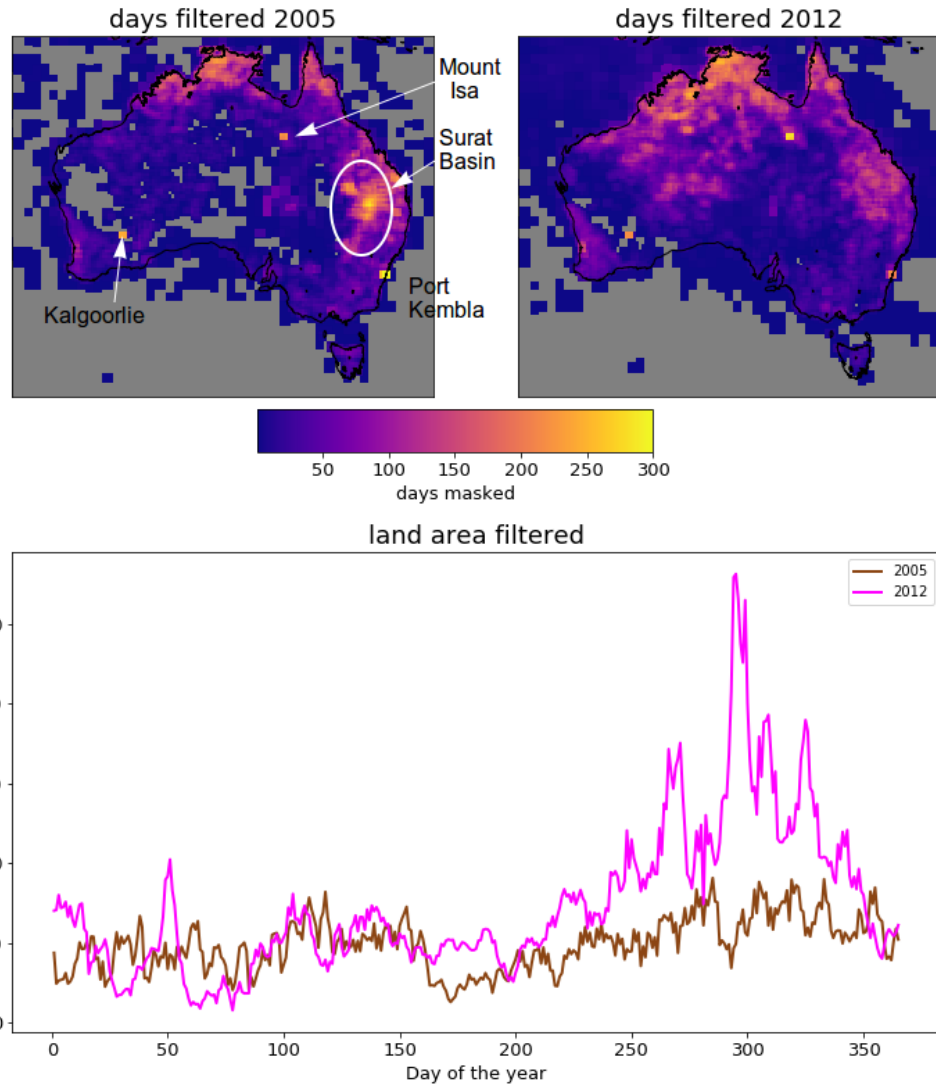


FIGURE 2.31: Top: percentage of pixels filtered out by fire and smoke masks in 2005 (left) and 2012 (right). Bottom: percentage filtered out each day from land squares in Australia for the two years shown.

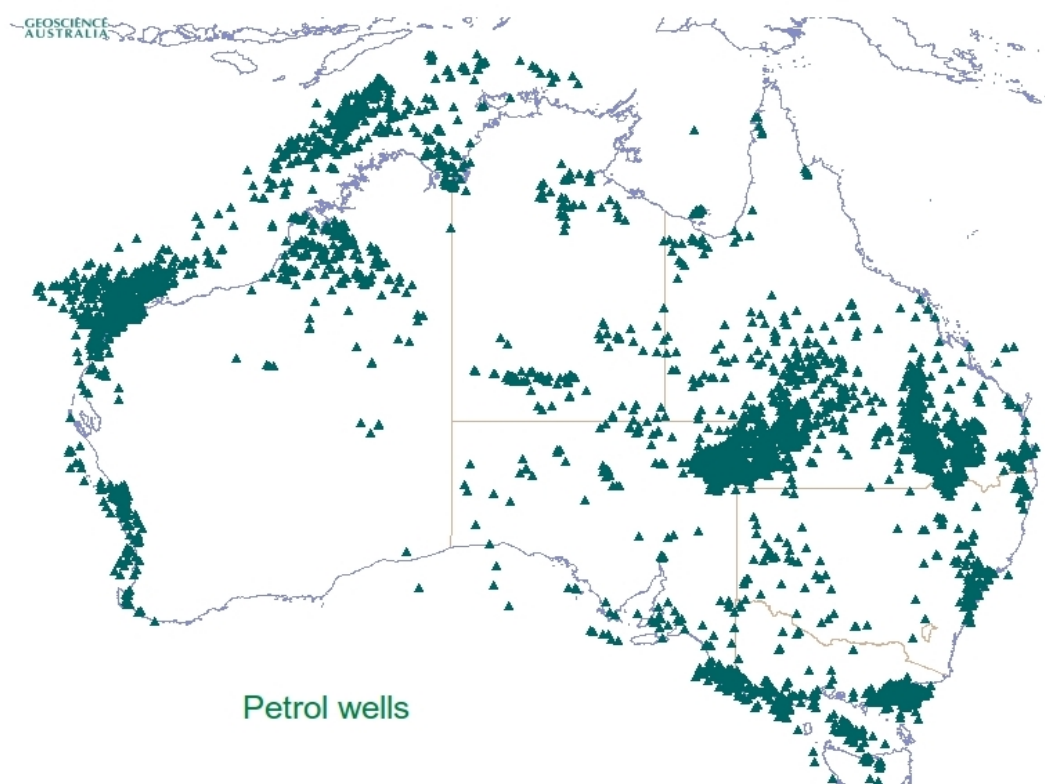
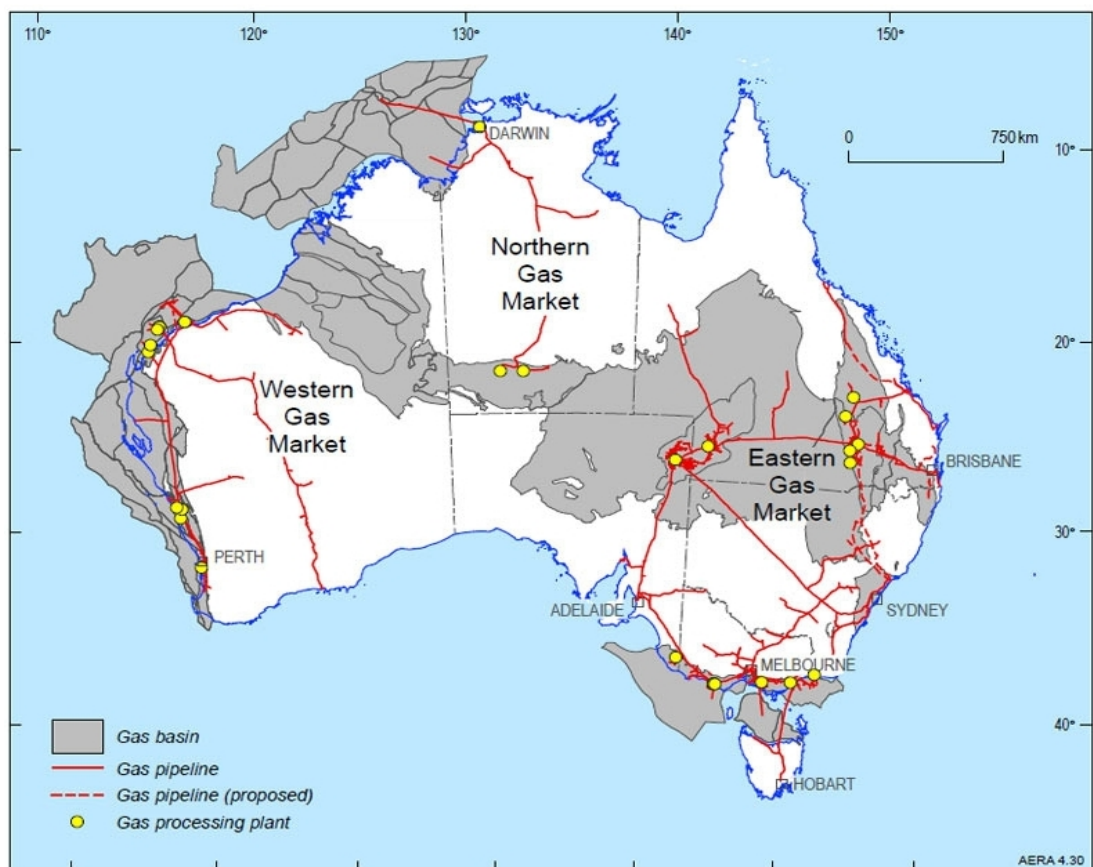


FIGURE 2.32: Top: gas fields and pipelines (2018) for Australia (<http://www.ga.gov.au/scientific-topics/energy/resources/petroleum-resources/gas>). Bottom: petrol Well locations over Australia (as of 2018) (<http://dbforms.ga.gov.au/www/npm.well.search>).

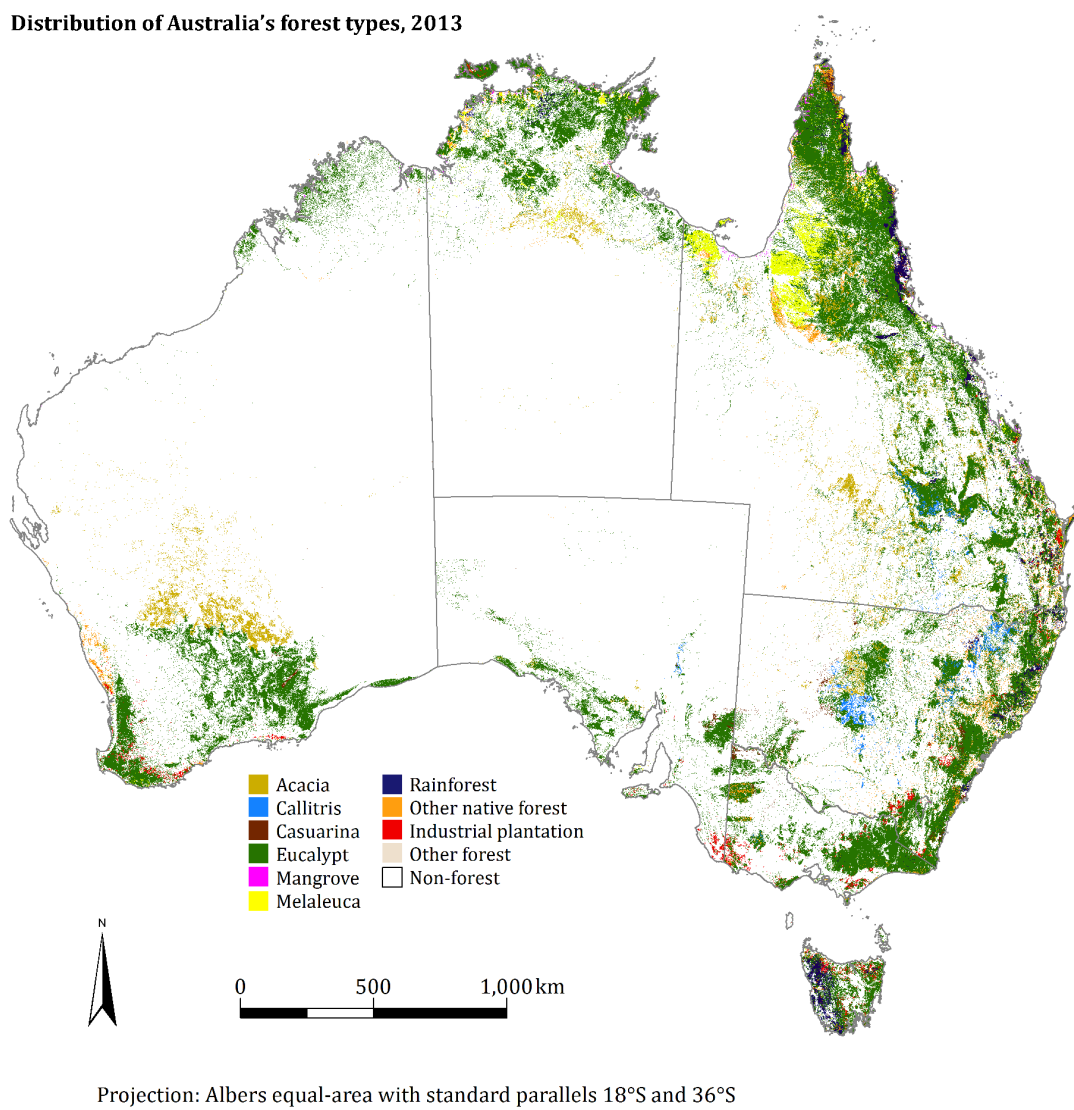


FIGURE 2.33: Forest coverage, coloured by predominant tree species.

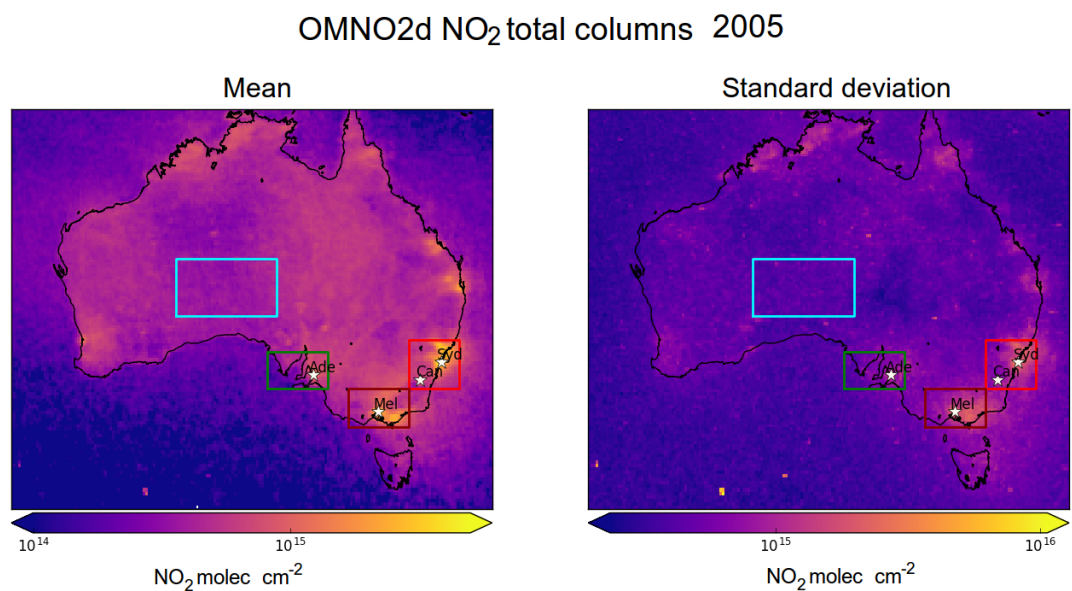


FIGURE 2.34: Mean (top left) and standard deviation (top right) of OMNO2d daily $0.25^\circ \times 0.25^\circ$ tropospheric cloud filtered NO₂ columns. Time series for Australia, and each region (by colour) shown in the bottom panel, with mean for that region shown on the right. The grey shaded area depicts the 25th to 75th percentiles of Australia averaged NO₂ columns for each day in the time series, with a thicker black line showing the Australia-wide mean value.

TABLE 2.5: NO₂ averages (molec cm⁻² × 10¹⁴) by region before and after filtering for anthropogenic emissions using 2005 data from the OMNO2d product.

Region	NO ₂	NO ₂ after filtering	% Data lost
Aus	4.9	4.5	2.1%
Sydney	10.4	5.9	25.3%
Adelaide	6.2	5.4	4.0%
Middle	3.8	3.7	0.5%
Melbourne	9.6	5.3	25.4%

frequently remove grid squares down wind. The affects of applying this filter to the OMNO2d product itself can be seen in Figure 2.35. Areas over Sydney and Melbourne tend to oscillate around the upper quartile of Australian NO₂ tropospheric columns once the filter is applied. Many coastal regions show some effect from the filtering, and Sydney, Melbourne, and east of Melbourne are completely removed.

The same regions as in Figure 2.34 are shown again in Figure 2.36, with NO₂ pixel densities for each region shown, along with the threshold of 2×10^{15} molec cm⁻². The reduction in NO₂ columns along with the portion of available data removed over Australia and each subset region is listed in Table 2.5. Roughly a quarter of the available data-points are removed over Sydney and Melbourne, decreasing the mean NO₂ amounts by ~ 50%, while not too much information is lost overall.

2.7.3 Smearing filter

Smearing is a measure of how much HCHO in a given grid box was produced from isoprene emitted in a different (upwind) grid box. Smearing affects emissions estimates as HCHO enhancements downwind of where precursor emissions occurred lead to misinterpretation of local emissions. In high NO_x ($>\sim 1$ ppb) environments, isoprene has a lifetime on the order of 30 minutes, and HCHO can be used to map isoprene emissions with spatial resolution from 10-100 km (Palmer et al. 2003). In low NO_x conditions, isoprene has a longer lifetime (hours) and may form HCHO further from the source area (Fan and Zhang 2004; Liu et al. 2016b; Liu et al. 2017b). Over Australia, NO_x levels are generally low and smearing is therefore expected to be important. Smearing limits the horizontal resolution of the linear top-down inversion process, as a finer resolution increases sensitivity to transport. Horizontal transport *smears* the HCHO signal so that its source location would need to be calculated using wind speeds and loss rates (Palmer et al. 2001; Palmer et al. 2003). In this chapter smearing affected grid squares are filtered out prior to application of Equation 3.7.

2.7.3.1 Calculation of smearing

Smearing has been analysed in several publications (e.g., Martin et al. 2003; Palmer et al. 2003; Millet et al. 2006; Stavrakou et al. 2009; Marais et al. 2012; Barkley et al. 2013; Zhu et al. 2014; Wolfe et al. 2016; Surl, Palmer, and Abad 2018) and is often calculated using the method used in this thesis, as first described by Palmer et al. (2003). This involves using two model runs, one of which has isoprene emissions scaled globally

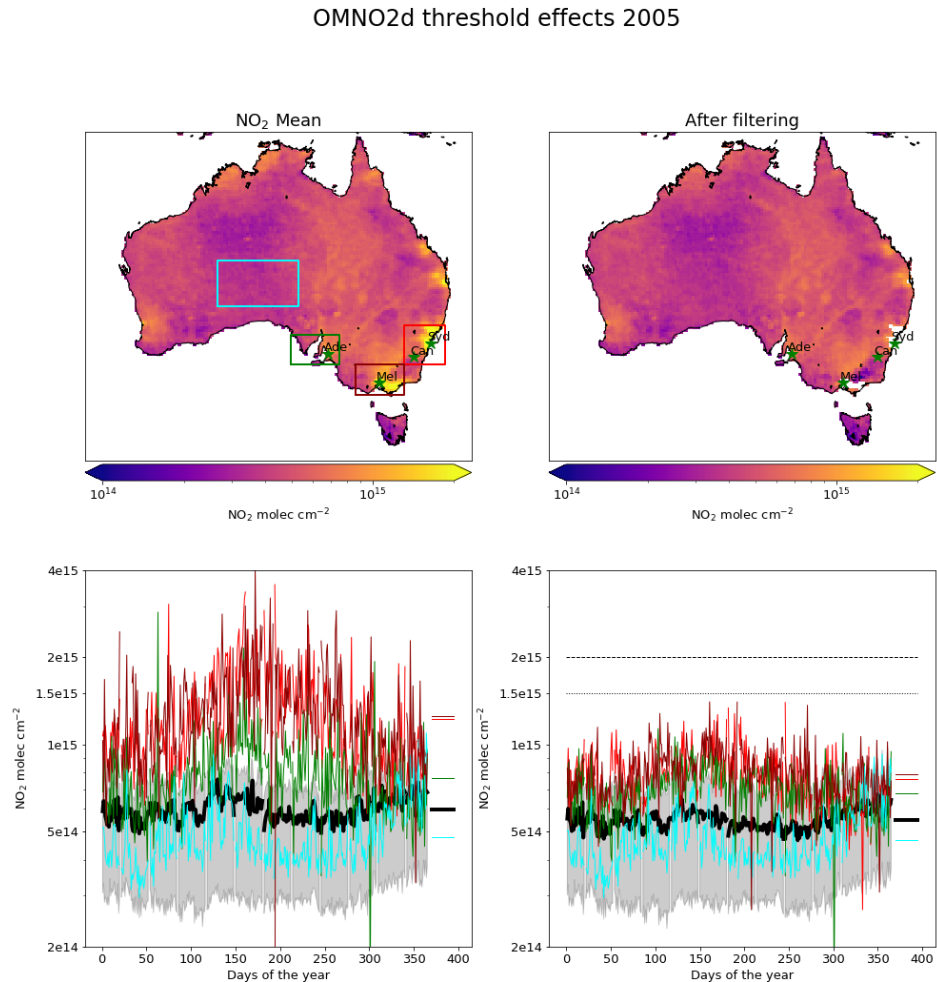


FIGURE 2.35: Top row: 2005 OMNO2d NO₂ column mean before (left) and after (right) applying the threshold filters as described in the text. Bottom row: time series for Australia, and each region (by colour) shown in the bottom panel, with mean for that region shown on the right. The time series before (left) and after (right) applying the anthropogenic filter are shown, the dashed and dotted horizontal lines show daily and yearly mean thresholds respectively.

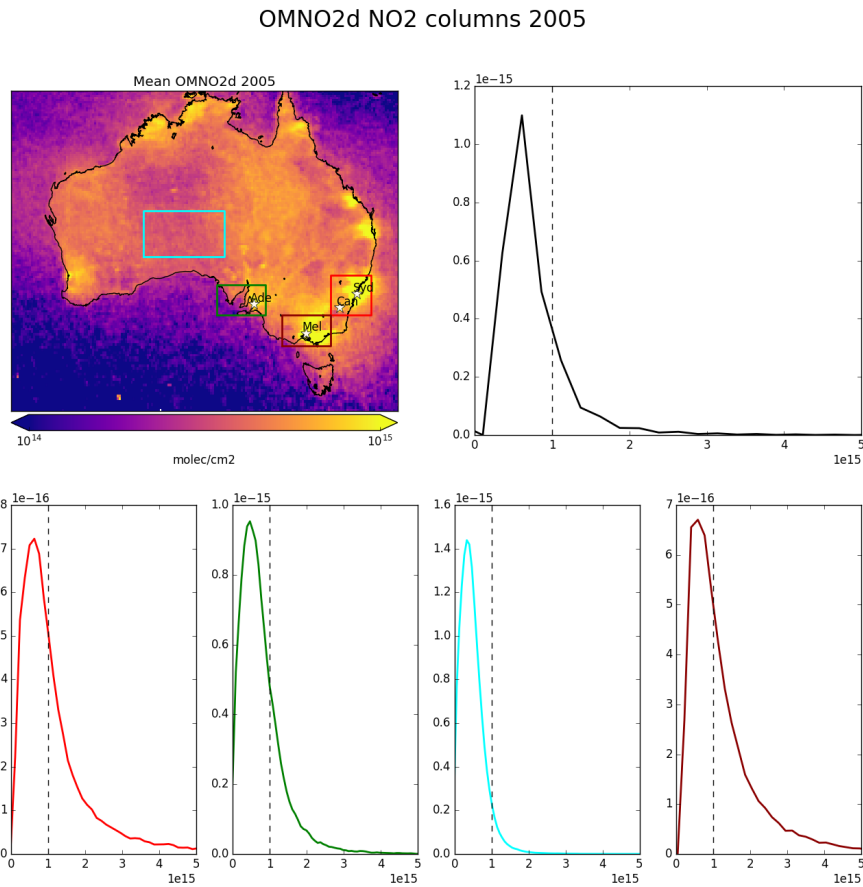


FIGURE 2.36: 2005 OMNO2d NO₂ column means (top left) and distributions (top right) for Australia, and each region shown in the area map (by colour). Vertical dashed lines show the threshold for anthropogenic influence, any columns above this value are filtered out. The vertical axis is normalised so that area under the curve adds up to unity, and as such is not important except as a visual measure of the relative width between the distributions.

by a constant (generally from 0.5 to 2). From Section 3.2.4, Equation 3.7 states that the modelled slope (S) is the yield of HCHO per C of emitted isoprene divided by the HCHO loss rate ($S = \frac{Y_{isop}}{k_{HCHO}}$). Using two runs of GEOS-Chem with differing isoprene emissions but otherwise identical we have:

$$\begin{aligned} Run_1 : \Omega_{HCHO} &= SE_{isop} + \Omega_0 \\ Run_2 : \Omega'_{HCHO} &= S'E'_{isop} + \Omega'_0 \end{aligned} \quad (2.31)$$

There are several assumptions that need to be understood, as these are what is tested by the smearing calculation. The initial assumption is that the system is at steady state, with no transport of isoprene affecting HCHO columns. This is the basis for equation 2.31. It is also assumed that background values (Ω_0) are from oxidation of methane and other long-lived VOCs, so that $\Omega_0 = \Omega'_0$. Between these two runs we are only changing the E term. Chemistry is unchanged so that the yield and loss rate should not change between the two runs:

$$S = S' = \frac{Y_{isop}}{k_{HCHO}} \quad (2.32)$$

Equations 2.31 may then be combined as follows:

$$\begin{aligned} Run_1 - Run_2 : \Omega_{HCHO} - \Omega'_{HCHO} &= SE_{isop} - S'E'_{isop} + \Omega_0 - \Omega'_0 \\ \Omega_{HCHO} - \Omega'_{HCHO} &= S(E_{isop} - E'_{isop}) \\ \Delta\Omega_{HCHO} &= S\Delta E_{isop} \\ \hat{S} \equiv & \frac{\Delta\Omega_{HCHO}}{\Delta E_{isop}} \approx \frac{Y_{isop}}{k_{HCHO}} \end{aligned} \quad (2.33)$$

This allows the combination of outputs from the two runs to determine where \hat{S} diverges from expected values for S .

Potential smearing is masked by checking a daily modelled value for $\hat{S} \approx Y_{isop}/k_{HCHO}$ against thresholds. By assuming that midday HCHO lifetime ($\tau = 1/k_{HCHO}$) typically falls within 1.5 to 4 hrs (as seen in the USA; Palmer et al. (e.g., 2006) and Wolfe et al. (2016)) and isoprene-to-HCHO yield (HCHO per isoprene carbon emitted) lies within the range 0.2 to 0.4 (scenarios estimated in Palmer et al. (2003)), one can set a simple bound on \hat{S} of $[0.2 \times 1.5, 0.4 \times 4]$ hrs or 1080 to 5760 seconds. As NO_x levels across Australia are relatively low, and lower NO_x levels reduce the prompt yield (Palmer et al. 2003; Wolfe et al. 2016), I reduce the threshold range by 20% and round to the nearest hundred leading to a bounding range of 800 to 4600 for \hat{S} . This range strikes a balance between unlikely modelled yields and how much data is lost to filtering. Table 2.6 compares the smearing filter for Australia used in this thesis to typical slopes used in previous work for other regions.

GEOS-Chem is run with normal isoprene emissions and with isoprene emissions halved, then Equation 2.33 ($\hat{S} = \frac{\Delta\Omega_{HCHO}}{\Delta E_{isop}}$) provides \hat{S} . Here Δ represents the difference (daily 1300-1400 LT) between default and scaled runs. If \hat{S} sits outside the 800-4600 range then we remove that grid square day from both S and subsequent a posteriori calculations. A relatively large change in Ω_{HCHO} compared to local emissions ($\hat{S} >$

TABLE 2.6: Smearing filters or typical slopes (S) from literature.

Source	min. (s)	max. (s)	type ^a	Region
Palmer et al. (2003)	1270	2090	Range	North America ^b
Marais et al. (2012)		4000	Limits	Africa
Barkley et al. (2013) ^c	1300	1800	Limits	South America
Surl, Palmer, and Abad (2018)	2200	4900	Range	India
This Thesis	800	4600	Limits	Australia

a: Slope *ranges* are observed or modelled S , while smearing *limits* are the applied acceptable limits for S .

b: Slope range for summer only.

c: Assumed HCHO lifetime of 2.5 hours implies yields from 0.14 to 0.2 per C, consistent with box modelling.

4600) suggests HCHO production is from non-local isoprene emissions. Alternatively, a relatively low value of \hat{S} ($\hat{S} < 800$) suggests emissions from the local grid square are being exported before they form HCHO.

2.7.3.2 NO_x dependence

NO_x concentration directly affects the fate of VOCs in the atmosphere, influencing HCHO production by isoprene. In low NO_x environments, reported HCHO yields from isoprene are around 0.2 - 0.3 C per C (or 100-150 molar %), while in high NO_x environments this value becomes two to three times higher (Palmer et al. 2003; Wolfe et al. 2016). Some values for HCHO yield from prior literature are shown in Table 2.7.

The effect of NO₂ on smearing can be seen in Figure 2.37. This plot shows how smearing over Australia compares to satellite NO₂, with smearing distributions binned by NO₂ both with and without filtering for smearing. At lower NO₂ levels smearing is more frequently below the lower threshold. These low values decrease in frequency, and have less affect on the mean \hat{S} at around 5×10^{14} molec cm⁻² NO₂.

2.8 Relationship between temperature and HCHO

Biogenic HCHO concentrations are correlated with temperature, as isoprene emissions are strongly correlated with temperature (Palmer et al. 2006; Zhu et al. 2013; Surl, Palmer, and Abad 2018). Fires emit HCHO precursors and increase HCHO concentrations independently of the relationship between temperature and HCHO, and should be revealed as outliers when comparing HCHO to temperature. Figures 2.38 - 2.40 show the relationship between modelled temperature, and satellite HCHO for January 2005 within subsets of Australia. A reduced major axis regression is used to determine the correlation between surface temperature (X axis) and HCHO (Y axis). Using the natural log of HCHO we can take the linear regression and then exponentiate each side in the equation $\ln Y = mX + b$ to get $Y = \exp mX + b$. This gives us the exponential fit as shown, with the correlation coefficient between $\ln HCHO$ and temperature. The distributions of exponential correlation coefficient and m terms is shown

TABLE 2.7: Isoprene to HCHO yields and lifetime.

HCHO Yield (molar %)	Lifetime	NO _x background	Source
315±50		High	a
285±30		High	a
225	35 min	High	b
450		High	c
235		1 ppbv	d
150		Low	b
150		Low	c
150		0.1 ppbv	d

a Atkinson and Arey (2003): Table 2, Yield from Isoprene reaction with OH, two values are from two referenced papers therein.

b Palmer et al. (2003): lifetimes assume [OH] is 1e15 mol cm⁻³.

c Wolfe et al. (2016): “prompt yield”: change in HCHO per change in isop₀. $[isop]_0 = [isop] \exp(k_1[OH]t)$; where k_1 is first order loss rate. Effectively relates HCHO abundance with isoprene emission strength.

d Dufour et al. (2008): One-day yields from oxidation modelled by CHIMERE, using MCM reference scheme.

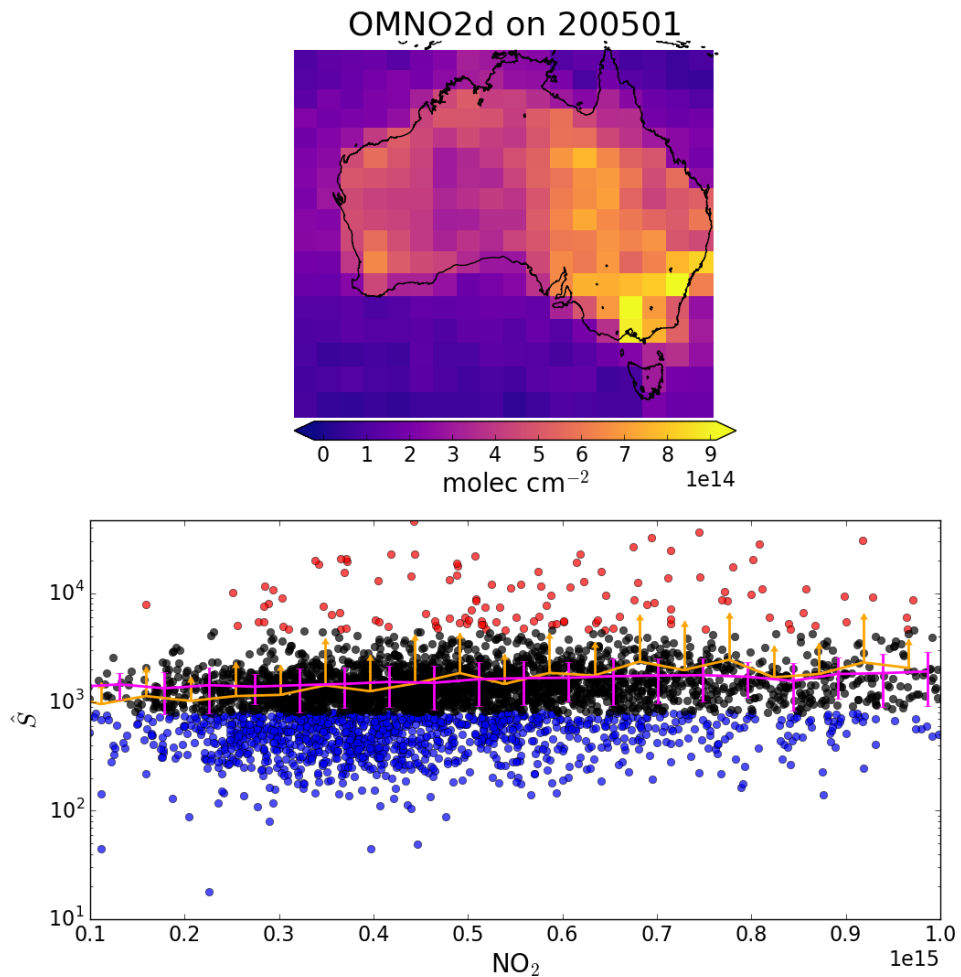


FIGURE 2.37: Top: OMNO2d tropospheric NO₂ columns averaged into 2° × 2.5° horizontal bins for Jan, 2005. Bottom: Scatter plot of NO₂ against smearing calculations from GEOS-Chem (\hat{S}), with points above and below the smearing threshold range of 800–4600 s coloured red and blue respectively. Points are binned by NO₂ with and without the smearing filter applied (orange and magenta respectively). Overplotted is the mean and standard deviation (error bars) within each bin. Due to the logarithmic Y scale we only show the positive direction of standard deviations for unfiltered data.

in the embedded plot, with one data point available for each grid square where the regression is performed. These figures show that the modelled temperature is not well correlated with corrected recalculated OMI vertical columns (r ranges from -0.24 to 0.47), but is with modelled columns (r ranges from 0.49 to 0.84). Correlations between modelled temperatures and HCHO are further improved when using the spatial average within each region. Furthermore the relationship is improved in individual grid squares over south Eastern Australia by removing non-biogenic emissions from the model (r increased from 0.58 to 0.75). This improvement is not seen in Northern Australia, nor south Western Australia. Overall this suggests that modelled correlations between temperature and HCHO are spatially dependent, and generally well reflected in satellite measurements over Australia.

One problem with detecting outliers in the temperature and enhanced HCHO relationship is that days when fires occur are likely to be hot. Another problem with correlating heat and HCHO is that increased temperature accelerates HCHO destruction (Zheng et al. 2015). We test the fire mask (see prior Section 2.7.1) by examining the relationship between modelled temperature and satellite HCHO with and without applying the filters for smoke and active fires. Figure 2.41 show the regressions between midday surface HCHO and temperature, where two independent data sets are used for the temperature: one from GEOS-Chem output and the other from CPC daily maxima. Regressions over both the grid square containing Sydney and averaged over a wider area are reduced in quality when after applying the pyrogenic filter. This could be due to the low resolution of available GEOS-Chem midday output, which greatly increases the strictness of the fire filter, which originally is created at $0.25^\circ \times 0.3125^\circ$ horizontal resolution but here is widened out to $2^\circ \times 2.5^\circ$. While the modelled correlation between surface HCHO and temperature is quite strong ($r > 0.8$) the correlation coefficient is reduced while the slope (temperature coefficient) is changed by more than 30% when applying the pyrogenic filter at the model resolution. If we use recalculated satellite HCHO columns instead of modelled midday outputs, then higher horizontal resolution can be achieved; however, this is at the cost of vertical resolution. Figure 2.42 shows the relationship between total column HCHO and temperature, which is not as strong as that shown between surface HCHO and temperature. At this resolution the application of the pyrogenic filter is shown to slightly strengthen the correlation over the wider south eastern Australian region, with r increasing from ~ 0.31 to ~ 0.38 . In this thesis the pyrogenic filter is applied at the higher horizontal resolution ($0.25^\circ \times 0.3125^\circ$), and this analysis suggests that the filter should strengthen the relationship between total column HCHO and its biogenic precursors over Australia.

2.9 Process schematic

Figure 2.43 shows an overview of how vertical columns (modelled and measured) along with filters and sundry data are created in this thesis. As described in this chapter, satellite and modelled data is combined combined to form recalculated corrected vertical columns (VCC), with masks created for potential anthropogenic, pyrogenic, and smearing influence. The end product is a gridded data file which contains new

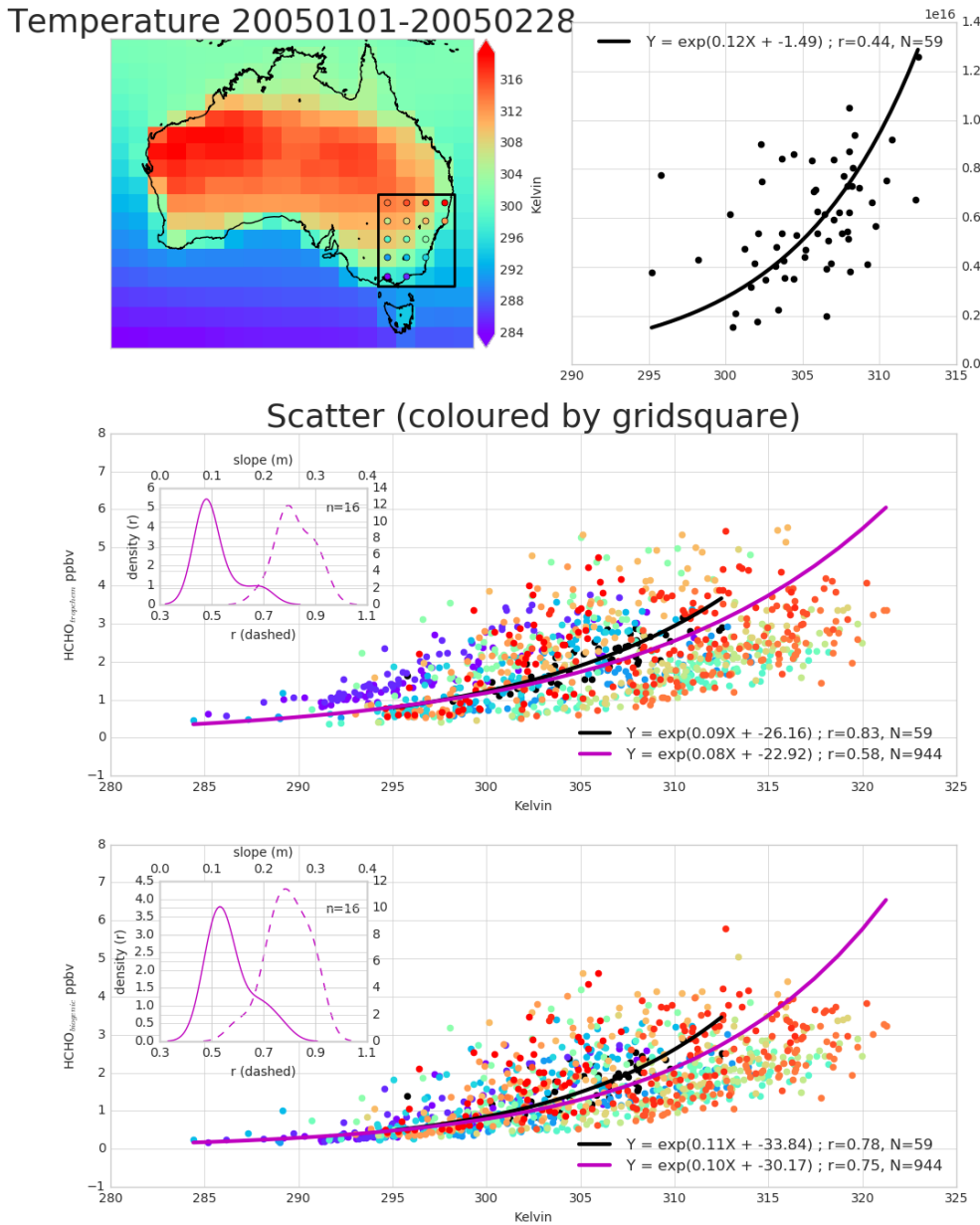


FIGURE 2.38: Top row (left): surface temperature averaged over January and February 2005. Top row (right): correlation between spatially averaged GEOS-Chem temperatures and recalculated satellite vertical columns. Second row: GEOS-Chem surface temperatures correlated against GEOS-Chem HCHO, with different colours for each grid box, and black showing the spatially averaged correlation over time. Third row: as second row, except GEOS-Chem HCHO comes from the bio-genic emissions only simulation. A reduced major axis regression is used within each gridbox using daily overpass time surface temperature and HCHO. The distribution of slopes (solid) and regression correlation coefficients (dashed) for the exponential regressions is shown in the inset panels in rows 2 and 3.

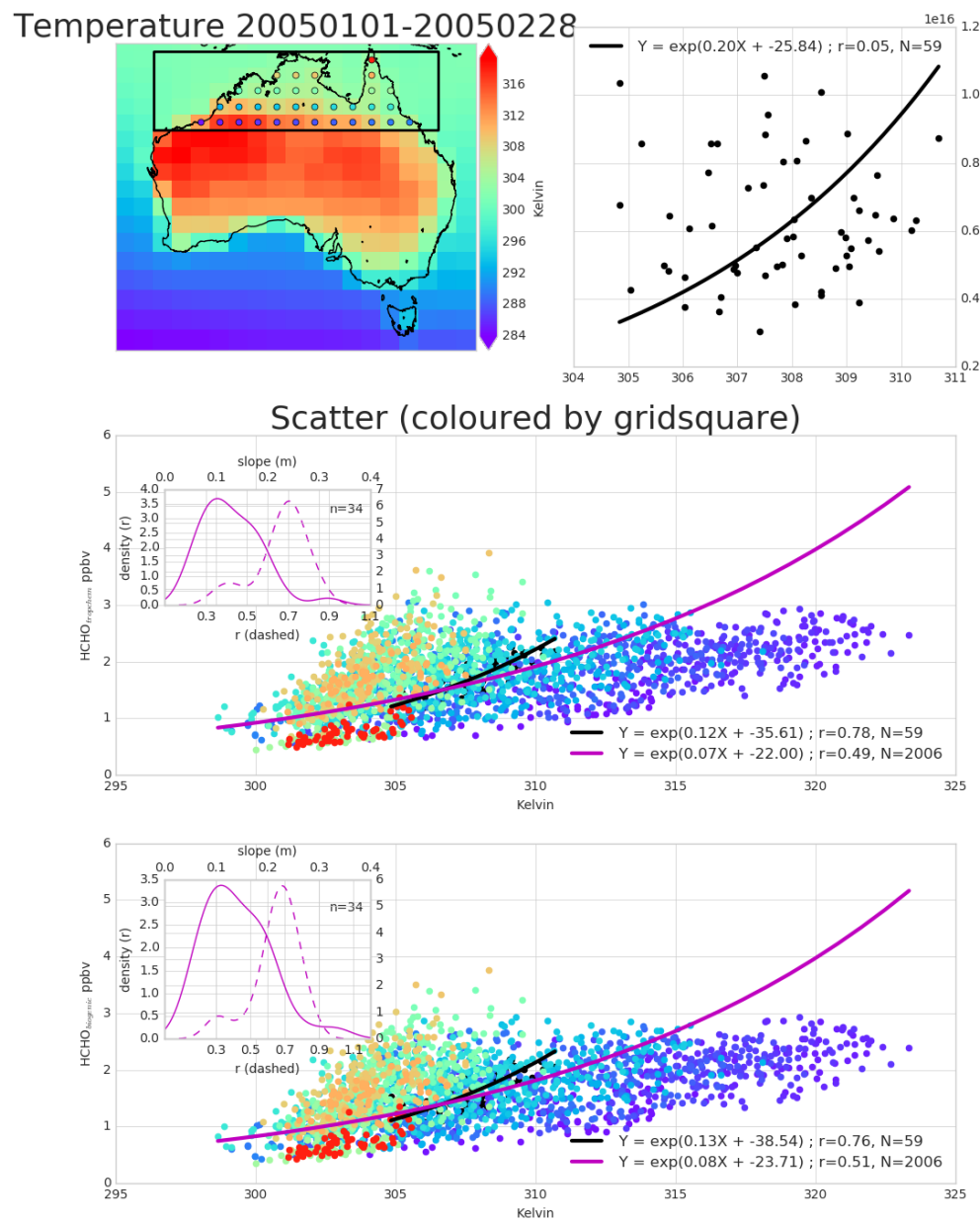


FIGURE 2.39: As Figure 2.38 but for northern Australia.

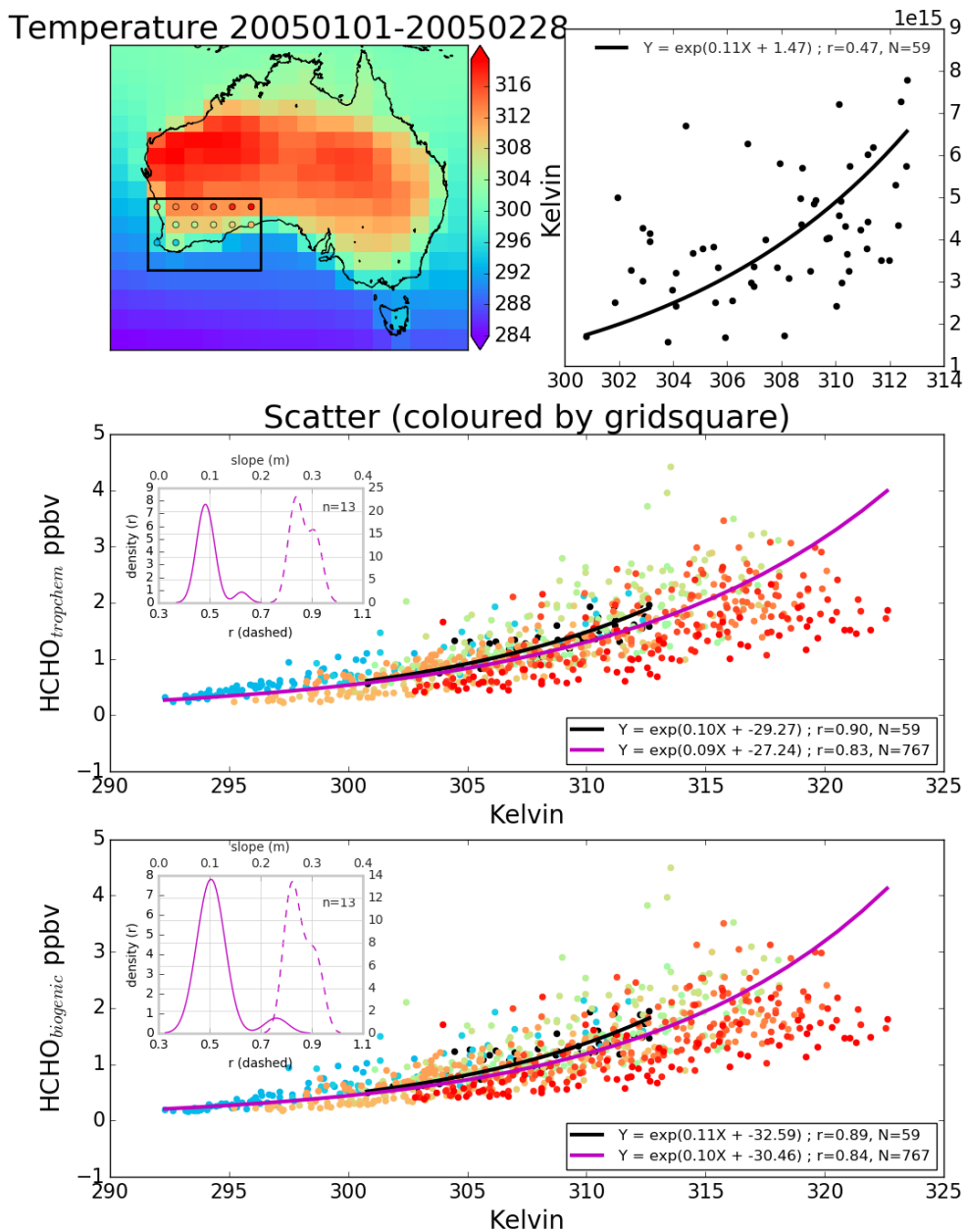


FIGURE 2.40: As Figure 2.38 but for south-western Australia. TODO:
Fix y axis in subplot 322

Temperature vs surface HCHO [ppbv] 20051201-20060228

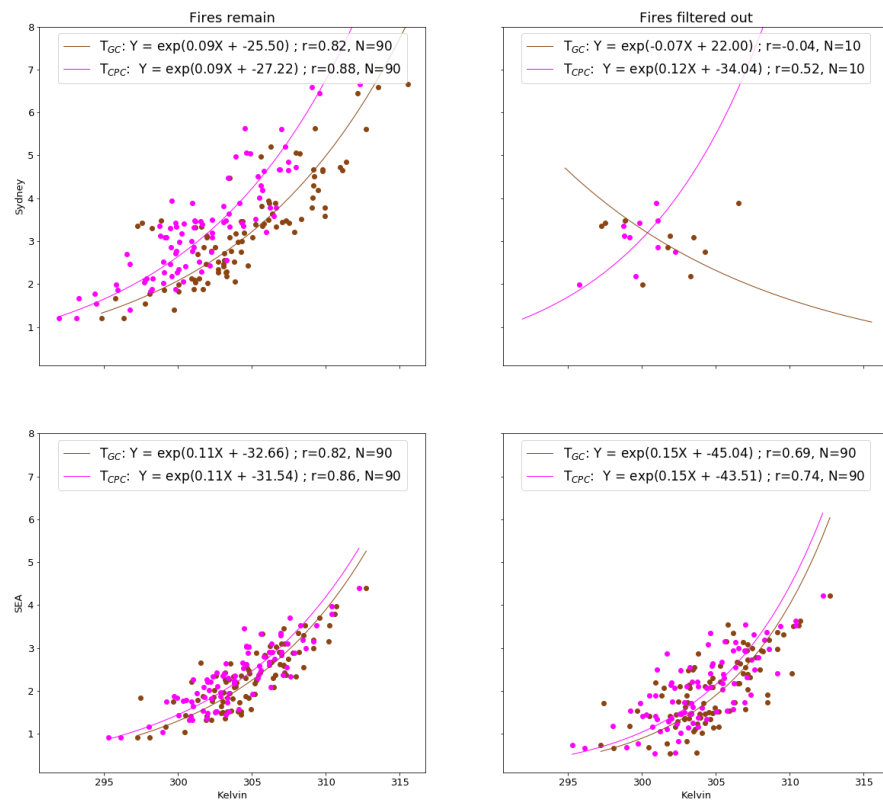


FIGURE 2.41: Surface HCHO from GEOS-Chem overpass output (midday) on the Y axis vs surface temperatures at midday (T_{GC}) and vs maximum daily temperatures from the CPC data set (T_{CPC}). Top row: Sydney grid square scatter plot and regression with one data point for each day in the summer of 2005-2006. Bottom row: as top row except averaging over several grid boxes covering south eastern Australia (SEA: 37°S to 29°S, 146°E to 153.5°W). Grid squares with pyrogenic influence detected are removed (prior to any averaging) in the right column.

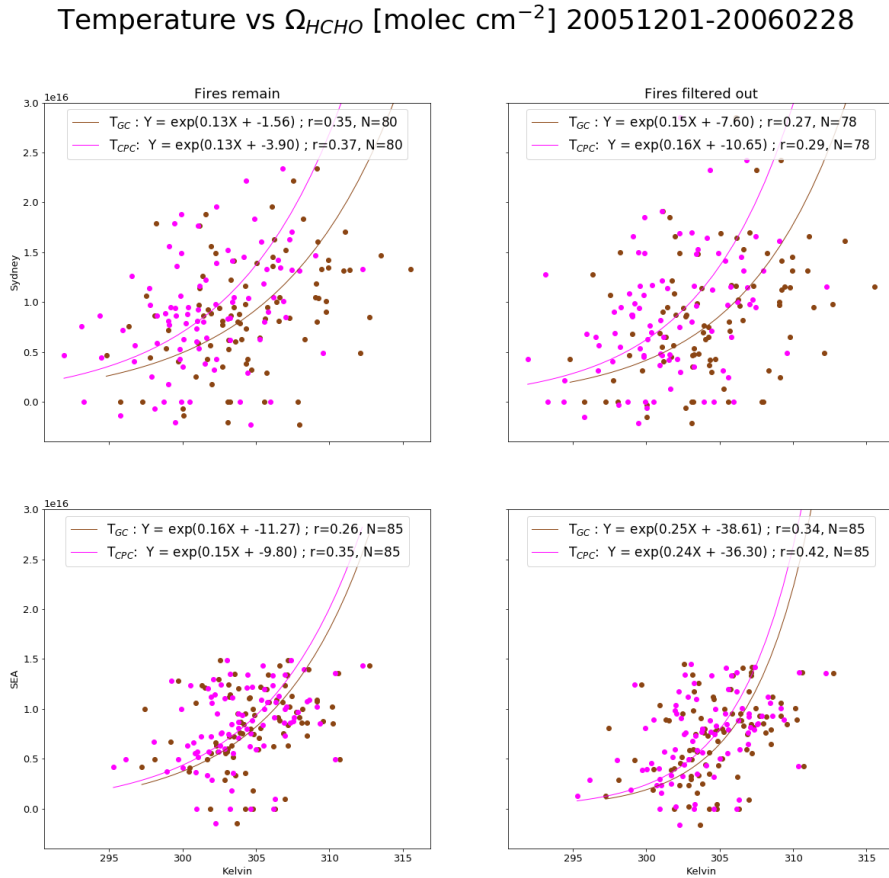


FIGURE 2.42: OMI recalculated vertical columns of HCHO on the Y axis vs surface temperatures at midday (T_{GC}) and vs maximum daily temperatures from the CPC data set (T_{CPC}). Top row: Sydney grid square scatter plot and regression with one data point for each day in the summer of 2005-2006. Bottom row: as top row except averaging over several grid boxes covering south eastern Australia (SEA: 37°S to 29°S, 146°E to 153.5°W). Grid squares with pyrogenic influence detected are removed (prior to any averaging) in the right column.

and old satellite and modelled vertical columns, along with sundry data to allow uncertainty calculation and other analyses. The original and recalculated AMF are also binned and stored.

2.10 Data Access

- AIRS** Atmospheric Infra-red Sounder instrument aboard the Aqua satellite (Texeira 2013). Satellite measurements of carbon monoxide downloaded from <https://search.earthdata.nasa.gov> with the product name AIRS3STD. Data from this product is used in Chapter 4, and briefly described in Section 2.2.1.5.
- CPC** Climate Prediction Center global temperature data provided by the NOAA/OAR/ESRL PSD, Boulder, Colorado, USA, from their website at <https://www.esrl.noaa.gov/psd/>. Surface temperatures from this data set used in Section 2.6.8, and described in Section 2.2.2.3.
- ERA1** European Centre for Medium-range Weather Forecasts (ECMWF) Interim Re-analysis (ERA-I) (Dee et al. 2011). Downloaded using the online portal: <https://apps.ecmwf.int/datasets/data/interim-full-daily/>. This data set is used in Chapter 4
- MUMBA** Measurements of Urban, Marine and Biogenic Air campaign (Paton-Walsh et al. 2017). Several trace gases from this campaign are examined here in Section 3.3.3, the data set is described in more detail in Section 2.2.3.1.
- OMHCHO** Satellite swaths of HCHO slant columns downloaded from <https://search.earthdata.nasa.gov>, with DOI 10.5067/Aura/OMI/DATA2015. More information can be found in Section 2.3.
- OMNO2d** Daily satellite NO₂ product downloaded from <https://search.earthdata.nasa.gov/search>, DOI:10.5067/Aura/OMI/DATA3007. For more information in refer to section 2.2.1.2.
- OMAERUVd** Gridded satellite based AAOD measurements downloaded from the NASA earth data portal <https://search.earthdata.nasa.gov>. A summary can be found at https://disc.gsfc.nasa.gov/datasets/OMAERUVd_V003/summary, Omar O. Torres (2008). *OMI/Aura Near UV Aerosol Optical Depth and Single Scattering Albedo L3*. DOI: 10.5067/Aura/OMI/DATA3003. URL: https://disc.gsfc.nasa.gov/datasets/OMAERUVd__V003/summary (visited on 05/30/2019). This dataset is described in detail in Section 2.2.1.3.
- SPS** Measurements of trace gases relevant to air quality in Western Sydney, Australia, from May 2016 to September 2017 as part of the Western Air Shed and Particulate Study for Sydney (Phillips et al. 2017). Available from PANGAEA, <https://doi.org/10.1594/PANGAEA.884317>. Some trace gas measurements are examined here in Section 3.3.3. Relevant measurements described in detail in Section 2.2.3.2.

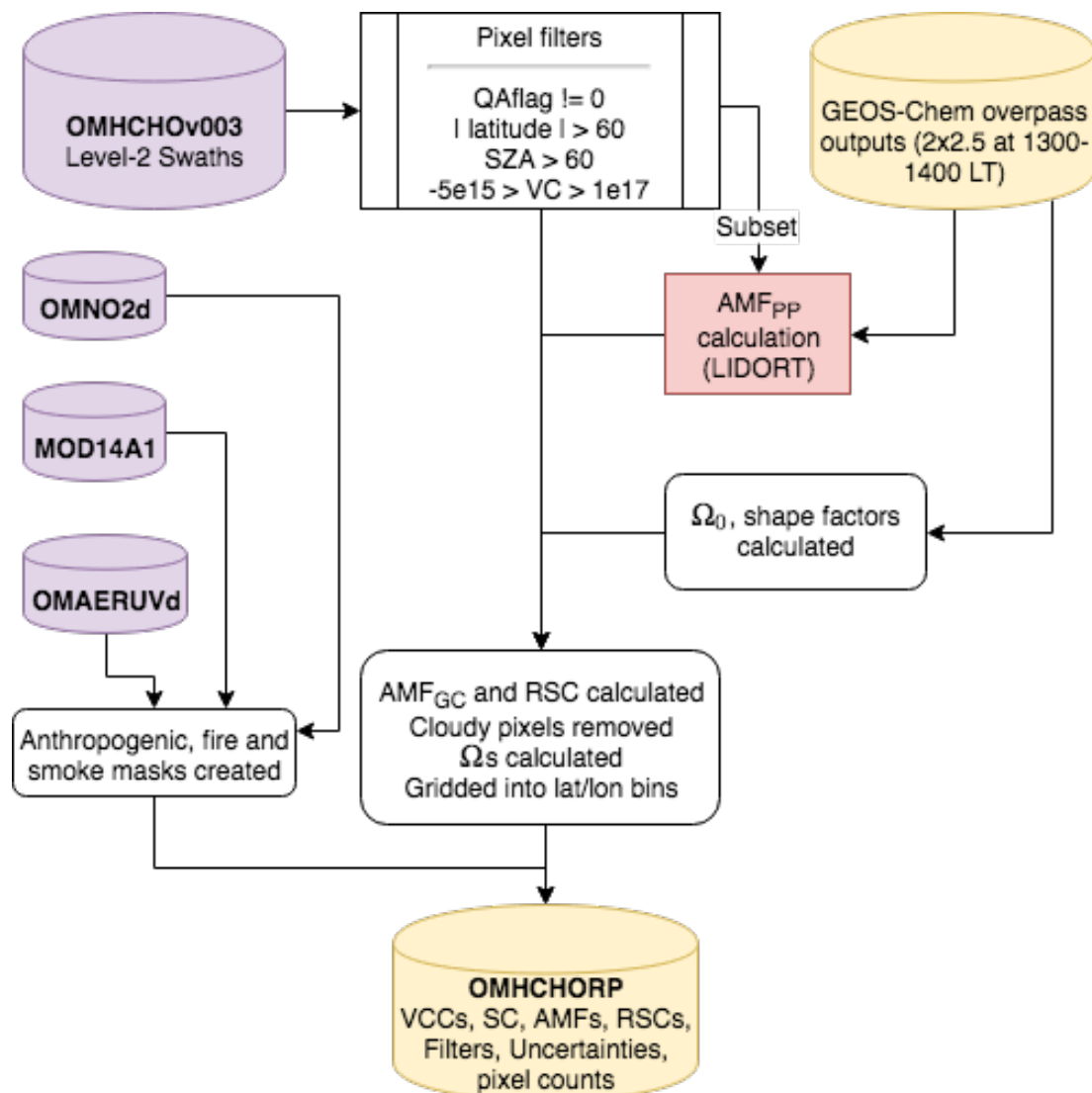


FIGURE 2.43: Flow diagram showing how OMHCHO level two swath data is read, processed, and gridded in this thesis.

Wollongong FTIR The instrument is part of the Network for the Detection of Atmospheric Composition Change (NDACC) and data can be retrieved from the NDACC database (<http://www.ndaccdemo.org/stations/wollongong-australia>). The current principle investigator producing and quality assuring the data set is Dr. Nicholas Jones.

Ozone sondes Ozonesonde data was retrieved from the World Ozone and Ultraviolet Data Centre (WOUDC) <http://woudc.org/data/explore.php>.

Chapter 3

Biogenic Isoprene emissions in Australia

3.1 Introduction

Biogenic volatile organic compounds (BVOC) affect the oxidative capacity of the atmosphere and are largely driven by what type of vegetation is in the area (Kefauver, Filella, and Peñuelas 2014). In the troposphere, BVOC emissions affect hydroxyl radical (OH) cycling, ozone (O_3) production, secondary organic aerosol (SOA) production, and methane lifetime. Australian forests are strong emitters of isoprene, the primary BVOC emitted globally (Guenther et al. 2006; Messina et al. 2016). Poor measurement coverage of isoprene, isoprene products, and isoprene emissions within Australia means that emissions are poorly understood. The lack of measurements makes it difficult to estimate the subsequent atmospheric processes. Isoprene (C_5H_8) is relatively difficult to measure due to its high reactivity and short lifetime.

Emission models used to derive estimates of isoprene fluxes are based on understanding the emissions from different plant species (phenotypes) in varying conditions. Guenther et al. (2012) estimated global biogenic isoprene emissions at roughly 535 Tg yr^{-1} , while Sindelarova et al. (2014) estimated around 411 Tg yr^{-1} . Reactions following emissions are complex, and are sensitive to other trace gases in the atmosphere. Uncertainties in several important products such as ozone and SOA are increased due to both isoprene measurement difficulties and its complicated subsequent chemical mechanisms. Isoprene emissions may be overestimated in Australia since they are based on measurements taken from a few young trees (Winters et al. 2009) that may emit more than older trees (Emmerson et al. 2016). The sample of trees include 4 types of Eucalyptus, which are not representative of the hundreds of species that make up Australian forests. Additionally, how these species depend on biological and meteorological stresses is unclear (Winters et al. 2009; Fortems-Cheiney et al. 2012). Emissions estimates are often used as boundary conditions for atmospheric chemistry models and improving these estimates for Australia is one goal of this thesis.

In this chapter I describe and implement a *top down* technique using satellite measurements of HCHO to calculate surface isoprene emissions. HCHO is a primary product of most BVOC (including isoprene) reactions, and is measured by satellites via remote sensing. In situ isoprene concentration measurements are costly and sparse within Australia, while satellite HCHO data are plentiful and freely available, making

this technique very attractive. Top down techniques have informed isoprene emission inventories in North America (Abbot 2003; Palmer et al. 2003; Palmer et al. 2006; Millet et al. 2006; Millet et al. 2008), South America (Barkley et al. 2013), Europe (Dufour et al. 2008; Curci et al. 2010), Africa (Marais et al. 2012), Asia (Fu et al. 2007; Stavrakou et al. 2014), India (Surl, Palmer, and Abad 2018), and even globally (Shim et al. 2005; Fortems-Cheiney et al. 2012; Bauwens et al. 2016). In this thesis I apply the technique solely focusing on Australia for the first time.

3.1.1 Aims

Recent work suggests that modelled emissions may be overestimated in southeast Australia (Emmerson et al. 2016). This chapter aims to improve the understanding of isoprene emissions over the whole of Australia, clarifying the spatial distribution of bias and how these biases impact modelled chemistry. I estimate isoprene emissions in Australia using a top-down technique based on OMI HCHO measurements and GEOS-Chem modelled yields. This a posteriori top-down estimate is evaluated against bottom-up a priori estimates and also briefly compared against available ground-based measurements. The GEOS-Chem model is modified to run with the a posteriori isoprene emissions to determine potential impact on modelled chemistry. Goodness of fit between in situ, satellite, and modelled HCHO is determined before and after scaling emissions estimates.

In this section I outline why current isoprene emissions estimates are inadequate and how they can be improved. I discuss literature that shows how the estimates may be too high, and describe how emissions may be calculated using satellite datasets. Section 3.2 lays out how new isoprene emissions are estimated, with results examined in Section 3.3. Section 3.3 includes a comparison of updated satellite HCHO columns (Chapter 2) to available measurements, and an examination of how these changes in emissions would affect ozone concentrations in Australia. Uncertainties for each step along the way are quantified in Section 3.4.

3.1.2 Existing emissions estimates

The Model of Emissions of Gases and Aerosols from Nature (MEGAN) is one of the most widely used sources for estimating biogenic isoprene emissions. However, along with other models that rely on measured plant emission rates, it is poorly calibrated for Australian conditions. Emissions of isoprene (C_5H_8) appear to be overestimated within Australia (Sindelarova et al. 2014; Stavrakou et al. 2014; Emmerson et al. 2016), although the lack of measurements of isoprene emission rates in Australia makes this overestimation difficult to characterise. Bauwens et al. (2016) showed that isoprene emissions were overestimated by up to a factor of 3 over Australia. Emmerson et al. (2016) suggest isoprene emissions are estimated 2-6 times too high compared against available measurements of isoprene concentrations. They also show that no blanket increase or decrease in emission factors is appropriate for the entire southeast of Australia. They compared modelled data to campaign measurements from multiple sites over different seasons and found that scaling emissions did not universally improve model outputs.

Recently Bauwens et al. (2016) estimated isoprene emissions with a top-down technique using the IMAGESv2 global CTM. They calculated emissions that create the closest match between model and satellite vertical columns, and compared these a posteriori data with their a priori (model) data and independent data sets. For Australia they found emissions ranging from $26\text{--}94 \text{ Tg C yr}^{-1}$, with MEGAN based estimates ranging from 38 Tg C yr^{-1} – 94 Tg C yr^{-1} , and a posteriori emissions of 36 Tg C yr^{-1} . In this thesis I focus on the analysis of a top-down emissions estimate compared against MEGAN, along with how changed emissions affect modelled ozone levels.

3.1.3 Top-down isoprene emissions estimates

In the remote troposphere HCHO production is dominated by methane oxidation, while in the continental boundary layer production is largely due to non-methane VOCs (NMVOCs) (Abbot 2003; Kefauver, Filella, and Peñuelas 2014). This leads to a causal relationship between enhanced HCHO concentrations and NMVOC emissions at low ($< 1 \text{ km}$) altitudes. NMVOCs are generally short lived ($< 1 \text{ hr}$), and the most prominent of these is isoprene. Isoprene is emitted and enters the atmosphere in the gas phase, where it begins a complex series of reactions. HCHO is produced with high yield in many reactions beginning with isoprene oxidation (discussed in more detail in Section 1.3.3) and it has a lifetime of a few hours (Kefauver, Filella, and Peñuelas 2014).

Top-down estimates determine emissions of a particular species through careful analysis of the measurable products of that species. This generally takes advantage of longer-lived products that may reach an equilibrium in the atmosphere. Continental tropospheric HCHO enhancement can be directly linked to biogenic isoprene emissions. Since 1997, when the Global Ozone Monitoring Experiment (GOME) satellite measurements were first used to measure HCHO over Asia, satellites have been used to provided a total column measurement of HCHO, enabling isoprene emissions estimation by top-down methods (Thomas et al. 1998; Palmer et al. 2001; Bauwens et al. 2016). Using satellite information to improve estimates of biogenic emissions has been highlighted as a valuable use of satellite derived datasets (Streets et al. 2013). Here NASA’s OMHCHO product based on measurements from the OMI instrument onboard the Aura satellite (see Section 2.3) is the basis for a top down biogenic isoprene emission estimate over Australia.

There are two top-down isoprene emission estimation techniques, Bayesian and linear, which are discussed briefly here. Both the linear and Bayesian techniques assume that modelled chemistry is accurate and only try to correct precursor emissions. This is an additional source of uncertainty given existing uncertainties in chemical mechanisms.

3.1.3.1 Bayesian inversion

Bayesian inversion optimises model parameters in order to minimise the difference between model output and an (ideally) independent dataset such as satellite measurements. Emissions of isoprene (and other precursors to HCHO) will form part of the set of model parameters that are adjusted to make the model HCHO output most closely match satellite measurements. These inversions can be set up to account for effects

from transport and allow source attribution (e.g., Curci et al. 2010; Fortems-Cheiney et al. 2012).

In general, a model (the forward model) is used to determine the relationship between HCHO (y) and the state variable x , which represents isoprene emissions (and other variable parameters of interest):

$$y = \mathbf{Kx} + b + \epsilon \quad (3.1)$$

where ϵ are the (assumed) independent errors in measurements. K is the Jacobian matrix determined from the forward model representing the sensitivity of y to the state variable x . Essentially the K matrix is the modelled estimation of how y responds to each of the driving parameters represented by elements of x . This K matrix is used in conjunction with error covariance in x to determine the most likely solution to x , given what is known about y .

This method was used by Shim et al. (2005) to optimise isoprene emissions in areas with high HCHO concentrations. They showed model underestimation of isoprene emissions by 14-46%, which was reduced to 3-25% after applying satellite based improvements. More recently Kaiser et al. (2018) showed a 40% bias in MEGAN isoprene emissions over the southeast US using a Bayesian inversion based on OMI HCHO.

An advantage (over the linear method described below) of the Bayesian method is that it can account for pyrogenic and anthropogenic emissions, as these form part of the state variable x . However, biases may still arise due to errors in modelled emission estimation (Curci et al. 2010). More limiting is the fact that the Bayesian method is computationally expensive due to the requirement that model runs take place using many permutations of changed input parameters. In this work I do not use the Bayesian method due to the computational costs surpassing the resources available.

3.1.3.2 Linear inversion

The linear technique is the less complicated of the two, and is performed in this thesis. Vertical columns of HCHO from satellite and modelled yield from isoprene allow the inference of local (grid space) isoprene emissions (Palmer et al. 2003; Millet et al. 2006; Marais et al. 2012; Bauwens et al. 2016). The primary assumption of the linear inversion technique is that HCHO and its precursors (primarily isoprene) are in a linear steady state relationship. This allows one to link isoprene emissions to HCHO measurements using production and loss rates. Essentially a linear relationship between total column HCHO (Ω) enhancement above a background level (Ω_0) and isoprene emissions (E_{isop}) is determined:

$$\Omega = S \times E_{isop} + \Omega_0$$

This uses modelled vertical columns and emissions to estimate the slope (S). Then this modelled S is applied to satellite measurements of Ω (Ω_{sat} and $\Omega_{sat,0}$) to determine \hat{E}_{isop} :

$$\hat{E}_{isop} = \frac{\Omega_{sat} - \Omega_{sat,0}}{S}$$

This is described further in Section 3.2, with an outline in Section 3.2.1.

The calculation requires reaction rates and yields from isoprene to HCHO, which can be determined most readily using chemical modelling. The method for calculating isoprene emissions from HCHO is laid out in Palmer et al. (2003), taking into account the expected lifetime and reaction rates of the precursor VOCs and HCHO. In their work, isoprene emissions fluxes over the US were derived using the GOME satellite instrument. The method has since been applied to many regions using OMI, GOME, GOME-2, and SCIAMACHY satellite data (e.g., Abbot 2003; Barkley et al. 2013; Stavrakou et al. 2014; Surl, Palmer, and Abad 2018). In this thesis I apply the technique solely focusing on Australia for the first time.

The linear inversion assumes fast HCHO yield from isoprene and no precursor transport, which is unrealistic in certain scenarios. For example, high wind speeds can transport precursors, or low NO_x concentrations can slow HCHO production (Palmer et al. 2006; Surl, Palmer, and Abad 2018). Filtering out data that do not match assumptions is required but can limit the utility of this technique, and leads to some dependence on environmental factors. Uncertainties in the technique are discussed in more detail in Section 3.4.1. Nonetheless, a major benefit is that the simple nature of the inversion requires very little computational power after acquiring satellite and model datasets, even over large amounts of gridded data. This allows an inversion using more than 8 years of satellite and model data, capturing inter-annual variability over all of Australia. With the computational resources available this would not have been possible using the Bayesian inversion.

3.2 Methods

I broadly follow the method of Palmer et al. (2001) to create a biogenic isoprene emissions estimate over Australia. A relationship is modelled between biogenic-only midday tropospheric columns of HCHO and GEOS-Chem midday biogenic isoprene emission rates, and then this relationship is applied to satellite measured HCHO total columns to derive a new isoprene emissions estimate. Daily modelled values averaged between 13:00-14:00 LT are used to match the overpass time of the Aura satellite. Then the slope is calculated using the reduced major axis (RMA) regression between the a priori isoprene emissions (those from GEOS-Chem, E_{GC}) and tropospheric HCHO columns in each model grid box each month. There is very little HCHO above the tropopause, so differences between total and tropospheric column are negligible. In this work total and tropospheric column HCHO are used interchangeably and referred to using Ω .

3.2.1 Outline

This section provides an overview of the steps involved in creating a top-down emissions estimate. This process is summarised in Figure 3.1.

1. Corrected vertical columns (Ω_{OMI} ; saved in the OMHCHORP dataset) are calculated (see Section 2.6) using level two OMI HCHO satellite data (see Section 2.3), along with GEOS-Chem model runs (see Section 2.4.7). Satellite columns are binned into both $0.25^\circ \times 0.3125^\circ$ and $2^\circ \times 2.5^\circ$ horizontal resolutions. In this

step model background values (columns over the remote Pacific) are used to correct the vertical columns, which is explained in Section 2.6.5.

2. Level three satellite data are used to make anthropogenic, fire, and smoke influence masks (see Section 2.7). These are applied to remove Ω_{OMI} that may be influenced by pyrogenic or anthropogenic sources.
3. A mask is created showing where the HCHO production is not dominated by local isoprene emissions. This is determined by calculating smearing over Australia using two model runs with differing isoprene emissions. The smearing value is determined as $\hat{S} = \Delta\Omega_{GC}/\Delta E_{OMI}$: the ratio of the differences between model runs of HCHO columns and isoprene emissions. A full description of the creation of this smearing filter is given in Section 2.7.3.
4. GEOS-Chem modelled biogenic emissions of isoprene (E_{GC}) along with biogenic columns of HCHO (Ω_{GC}), both averaged over $2^\circ \times 2.5^\circ$ horizontally and 13:00-14:00 LT temporally, are used to calculate a reduced major axis linear regression slope S ($\Omega_{GC} = S \times E_{GC} + \Omega_{GC,0}$). Calculation of this modelled slope is explained in Section 3.2.4.
5. Satellite HCHO Ω_{OMI} and S then form the basis for the top-down estimate of biogenic isoprene emissions (E_{OMI} atoms C cm $^{-2}$ s $^{-1}$). This product is our a posteriori, and calculation details are given in Section 3.2.7.
6. A posteriori top-down emissions E_{OMI} are compared against a priori emissions, and analysed in conjunction with independent observations from in-situ measurements (MUMBA and SPS). Results are examined in Section 3.3.
7. GEOS-Chem is run using the a posteriori emissions (see Section 3.2.9), and HCHO, O₃, isoprene, and NO_x outputs are compared to a priori values and to campaign and satellite measurements where possible (Sections 3.3.3).

3.2.2 Masks and reprocessed satellite HCHO

Satellite data pixels are read from OMHCHO, the level 2 OMI HCHO dataset, AMFs are recalculated, and then pixels are gridded daily into $0.25^\circ \times 0.3125^\circ$ horizontal bins. This forms the intermediate product OMHCHORP, which is fully described in Section 2.6.1. This dataset includes gridded satellite HCHO columns (Ω_{OMI}), along with pixel counts (how many satellite datapoints were used for each grid box) to allow averaging, re-binning, and uncertainty analysis. In this thesis I use the OMI product as it has better temporal coverage and increased pixel counts over Australia when compared to GOME or GOME-2 (on board the ERS-2 and METOP-A satellites respectively).

In order to determine biogenic HCHO enhancements from Ω_{OMI} , we require filters for non-biogenic sources. These masks are described in Section 2.7, and a brief recap is provided here. Methane oxidation is a major part of the formation of background HCHO; however, the linear regression used to estimate isoprene emissions effectively ignores this source, which means a methane filter is not required. Anthropogenic, pyrogenic, and smoke influence masks are created from three satellite products: NO₂

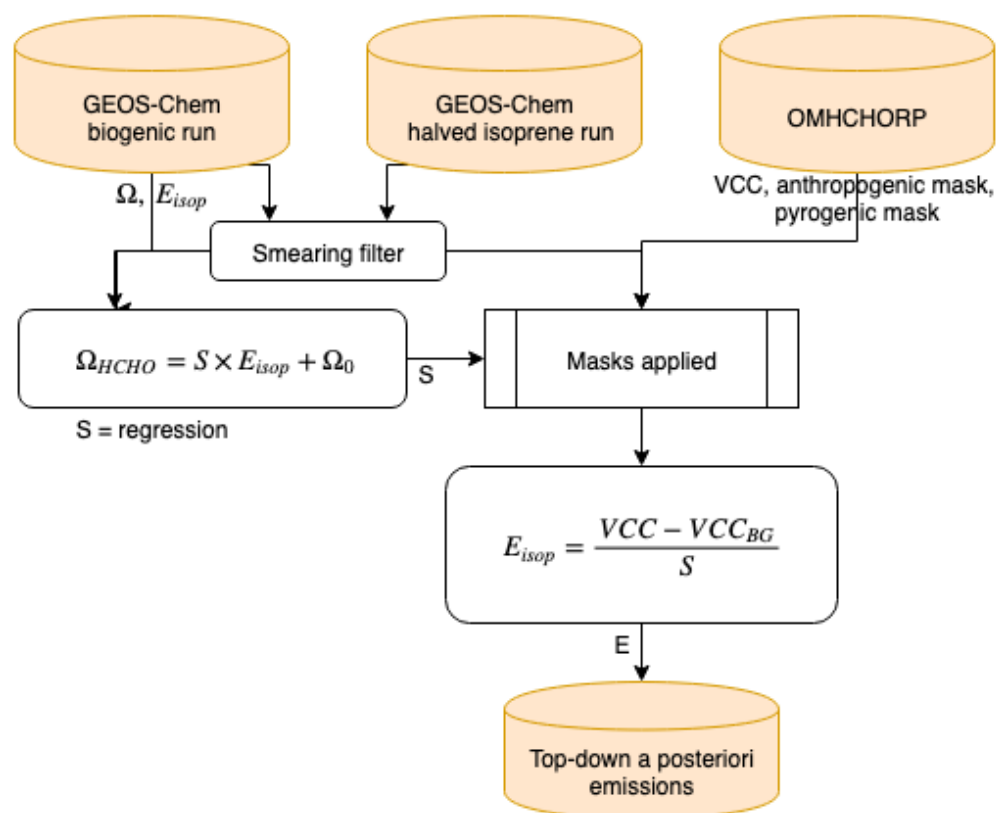


FIGURE 3.1: Top-down isoprene emissions estimate formation using OMHCHORP and GEOS-Chem outputs.

from OMNO2d, fire counts from MOD14A1, and AAOD from OMAERUVd, respectively.

1. The fire mask is created daily using non-zero MODIS fire counts over the prior 2 days that occur in local or adjacent grid squares at $0.25^\circ \times 0.3125^\circ$ horizontal resolution.
2. Influence from transported smoke plumes is removed by flagging grid squares where OMI aerosol absorption optical depth (AAOD, from OMAERUVd) is greater than 0.03.
3. A filter for anthropogenic influence is created daily using OMNO2d NO₂ tropospheric column amounts, masking any grid squares with greater than 2×10^{15} molec cm⁻² on any particular day, along with grid squares where the yearly average is above 1.5×10^{15} molec cm⁻².

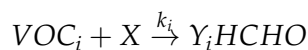
The recalculated corrected vertical columns are saved to OMHCHORP dataset both before and after applying the filters to allow filter analysis.

3.2.3 GEOS-Chem emissions

In this work MEGAN (version 2.1) is run as a module within GEOS-Chem (version 10.01). The chemical model is coupled to a meteorological model driven by GEOS-5 meteorological fields at $0.25^\circ \times 0.3125^\circ$ horizontal resolution. GEOS-Chem output is averaged onto 47 vertical levels (72 for the UCX run) at $2^\circ \times 2.5^\circ$, based on chemistry and transport calculated every 30 and 15 minutes respectively. Isoprene emissions from the default *tropchem* simulation are referred to as the a priori emissions. When shown as part of a formula the a priori are denoted as E_{GC} .

3.2.4 Relationship between isoprene emissions and formaldehyde

Tropospheric HCHO production is primarily due to the oxidation of VOC precursor species (VOC_i). Background concentrations are driven by methane; a longer lived (~ 8 yr) VOC. Over continental land masses, the variability in HCHO is driven by shorter lived precursor emissions (Chance et al. 2000; Palmer et al. 2003). HCHO is then produced quickly from short-lived intermediates:



where X is an oxidant, Y_i is HCHO yield (per C atom in VOC_i), and k_i is the reaction rate constant. In specific conditions described below, HCHO total columns (Ω ; molec cm⁻²) can be linearly related to isoprene emissions. In Australia the effective molar HCHO yield from isoprene has not been extensively studied, while in other continents this value varies from 1-3 depending on local NO_x concentrations (e.g., Palmer et al. 2006; Millet et al. 2006; Bauwens et al. 2016; Surl, Palmer, and Abad 2018).

The isoprene to HCHO relationship is derived using several assumptions that are outlined here. The first assumption is that HCHO is at steady state, which implies

production (P_{HCHO}) and loss (L_{HCHO}) are equivalent:

$$\frac{d\Omega}{dt} = 0 = P_{HCHO} - L_{HCHO} \quad (3.2)$$

This is reasonable during midday when isoprene emissions are steady and Ω has had time to stabilise. The second assumption is that loss (with loss rate constant k_{HCHO}) is only first order, such as from photolysis and oxidation:

$$L_{HCHO} = k_{HCHO}\Omega \quad (3.3)$$

This assumption means that loss due to transport must be negligible as it is not first order. This assumption is reasonable for large enough grid boxes as transport becomes negligible relative to the linear (first order) terms. Production and loss are on the order of minutes, and grid box sizes in this work are rectangular with ~ 200 km edge lengths. Monthly averaged wind speeds rarely exceed 20 km hr $^{-1}$ over Australia, meaning HCHO and precursor transport remain minor. Transport can still be an issue, however, and is handled by applying a smearing filter described in Section 2.7.3.

Another assumption is that Ω production above the background level is due only to precursor emissions (E_i ; atoms C cm $^{-2}$ s $^{-1}$) multiplied by their yields to HCHO (Y_i):

$$P_{HCHO} = \sum_i Y_i E_i \quad (3.4)$$

By combining Equations 3.2, 3.3, and 3.4, we can relate Ω to precursor emissions:

$$\begin{aligned} k_{HCHO}\Omega &= \sum_i Y_i E_i \\ \Omega &= \frac{1}{k_{HCHO}} \sum_i Y_i E_i \end{aligned} \quad (3.5)$$

Finally, we assume isoprene emissions are driving changes in Ω (as assumed elsewhere, e.g., Palmer et al. 2003; Millet et al. 2008; Marais et al. 2014; Stavrakou et al. 2015) and lump other terms together:

$$\sum_i Y_i E_i = Y_{isop} E_{isop} + \sum_{i \neq isop} Y_i VOC_i \quad (3.6)$$

This assumption is reasonable only over continental land masses, and can be false when pyrogenic or anthropogenic emissions influence the HCHO column, however these scenarios are filtered using independent satellite measurements (see Section 2.7). The linear relationship between isoprene emissions and Ω is determined by equating P_{HCHO} and L_{HCHO} from Equations 3.4 and 3.3, substituting Equation 3.6, and assuming that the lumped terms make up the background:

$$\begin{aligned} k_{HCHO}\Omega &= Y_{isop} E_{isop} + \sum_{i \neq isop} Y_i VOC_i \\ \Omega &= \frac{Y_{isop}}{k_{HCHO}} E_{isop} + \Omega_0 \\ &= S \times E_{isop} + \Omega_0 \end{aligned} \quad (3.7)$$

Here S is the slope: $S \equiv \frac{Y_{isop}}{k_{HCHO}}$.

3.2.5 Calculation of modelled slope

To determine S , the link between biogenic isoprene and midday column HCHO, we use GEOS-Chem. The term E_{GC} is used when discussing isoprene emissions estimated within GEOS-Chem and Ω_{GC} is used to represent simulated HCHO. The method to calculate S using GEOS-Chem follows roughly the following three stages:

1. Hourly gridded model output E_{GC} (atoms C cm⁻² s⁻¹) at 13:00 LT daily are extracted, along with Ω_{GC} (molec cm⁻²) output.
2. Filtering removes gridded output on days where grid squares are likely to be affected by smearing (see Section 3.2.8).
3. A reduced major axis regression slope is determined between Ω_{GC} and E_{GC} using a month of modelled output (one value per day) for each grid square (e.g., see Figure 3.2)

Modelled background concentrations can be ignored here as they do not affect slope calculation. This effectively provides monthly gridded slope (S) between biogenic isoprene emissions and HCHO columns, in units of seconds.

Figure 3.2 (top left) shows how S varies spatially over Australia for an example mid-summer month. High S values suggest increased sensitivity to isoprene emissions. Some areas can be seen to be very sensitive to emissions, such as the west coast and Eyre basin, which is likely due to the low isoprene and HCHO levels in those areas. The regression coefficients also vary spatially (top right), and some areas show little correlation. It is likely that this is due to weather, transport, and a lack of local emission sources. The slopes in the bottom panel show a small sample of scatter and regression plots. These can range widely due to differences in emission and yield parameters, which plays a role in the smearing filters described in Section 2.7.3. Due to the 2° × 2.5° horizontal resolution of GEOS-Chem, calculations over coastal grid boxes that are mostly oceanic are often discarded as the change in HCHO is not dominated by emissions of isoprene, as is assumed for equation 3.7.

One issue with slope calculation is potential transport (also known as smearing), either of isoprene transported in from outside the local grid box (before any HCHO is formed), or of HCHO formed by local emissions but transported out of the local grid box. The effects of this are dealt with using a smearing filter (see Section 2.7.3). Days where we expect smearing may be affecting local levels of HCHO are removed before calculating S , and a quick analysis is performed on how the filter affects monthly slope, correlation, and uncertainty. Figure 3.3 shows the calculated slope for 2005–2012, along with its 95% confidence interval over Sydney. The monthly and multi-year monthly averages are shown before and after the smear filter is applied. The filter slightly reduces the amplitude of the seasonal cycle, raising the January minimum and lowering the June and July maximum. Filtering slightly improves the correlation coefficient throughout the year. Surprisingly, more data is filtered in summer, presumably due to higher biogenic isoprene emissions over summer, making transport more noticeable on windy days. Additionally, in winter, the HCHO column is relatively

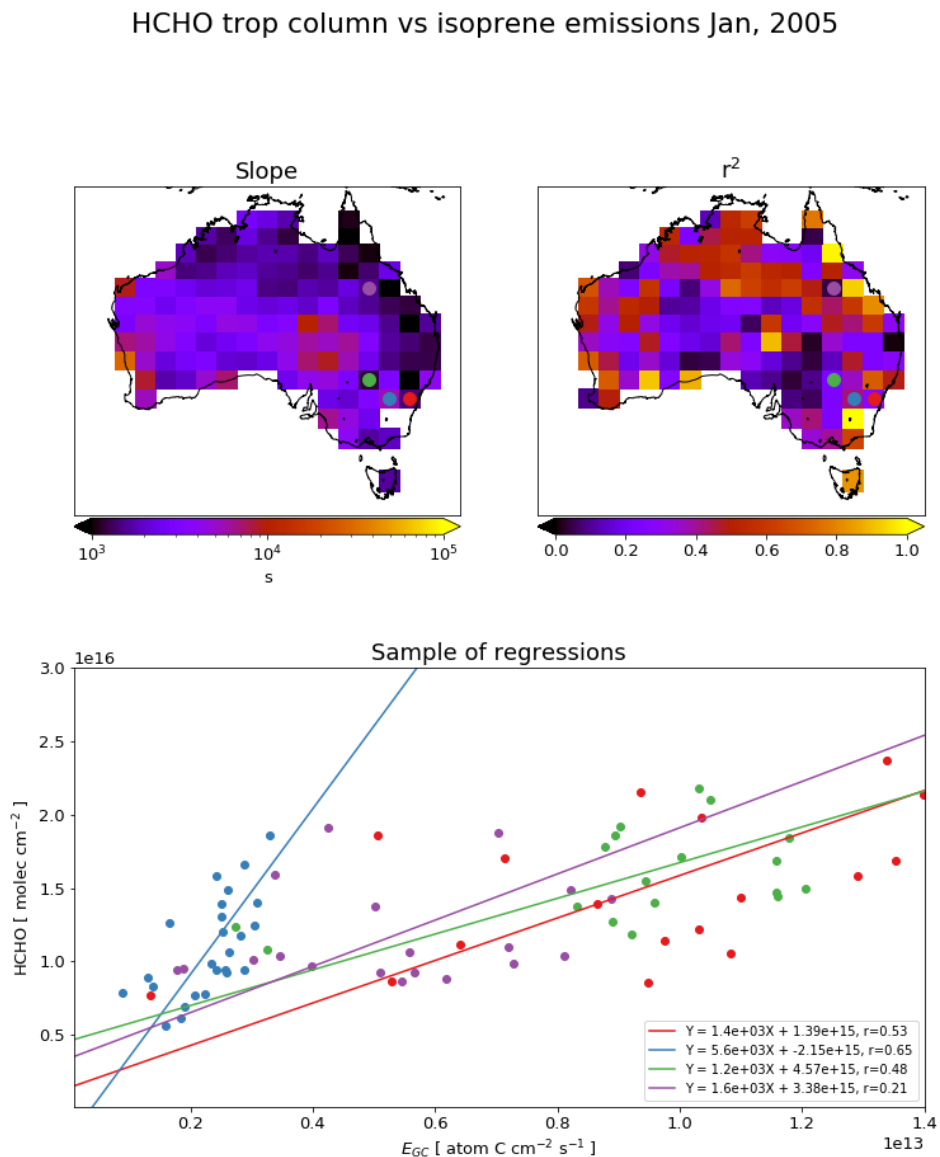


FIGURE 3.2: Top left: RMA slope between modelled tropospheric column HCHO and isoprene emissions (E_{GC}) using midday (13:00-14:00 LT) values over for January 2005, per grid square at $2^\circ \times 2.5^\circ$ horizontal resolution. Top right: Squared RMA correlation coefficient for regression in top left. Bottom: Sample of correlations from four grid squares. Coloured dots in top panels correspond to the colour of the regressions shown in bottom panel.

more affected by anthropogenic precursors, which are not halved between the two runs. This may lower the smearing filter signal over Sydney and other densely populated areas. This plot has been repeated for several grid squares over Australia (not shown). When calculating top-down emissions the smearing-filtered slope (S) is generally used for each grid square month. The multiple year monthly averaged slope is used instead when the regression coefficient (r) is less than 0.4, or the number of data points used in the regression (n) is less than 10. When r for the multiple year slope is also lower than 0.4 (does not happen in the example grid square), no estimation is performed.

3.2.6 Modelled background HCHO

There are two simple ways to determine the modelled background HCHO, one of which involves running the model with no isoprene emissions. Since we have assumed variation in HCHO columns only depends on isoprene emissions, our background term is theoretically identical to the simulated HCHO without isoprene emissions. The other method uses HCHO over the remote Pacific Ocean at matching latitudes and times, which emulates how the background is determined for the satellite measured HCHO. Figure 3.4 shows the background total column HCHO calculated in these two different manners, and how they compare to each other and normal levels for an example month (January, 2005). The difference between these definitions is approximately 15%, and may be due to non-isoprene HCHO precursors such as pyrogenic and anthropogenic emissions. Generally in summer months the continental HCHO levels are over 3 times higher than background levels. For consistency with the satellite data, we determine backgrounds using the remote Pacific. Background HCHO for any latitude in this thesis is calculated by averaging longitudinally (140°W to 160°W) the matching latitudes over the remote Pacific.

3.2.7 Calculation of Emissions

Top-down emissions estimates are calculated using OMHCHO (see Section 2.3) slant columns and an updated AMF calculated using code written by Paul Palmer and Randal Martin, with modifications by Luke Surl (see Section 2.6.3.2). These emissions are referred to as the a posteriori from here onward, or E_{OMI} in formulae.

A posteriori emissions are calculated using the linear relationship described in Section 3.2.4 using the modelled slope S calculated in the prior section and satellite HCHO columns recalculated in 2.6:

$$\begin{aligned}\Omega_{OMI} &= S \times E_{OMI} + \Omega_0 \\ E_{OMI} &= \frac{\Omega_{OMI} - \Omega_0}{S}\end{aligned}\tag{3.8}$$

This is the same as equation 3.7, except now we use the satellite HCHO (Ω_{OMI} and Ω_0). Ω_0 is calculated using Ω_{OMI} in the remote Pacific averaged monthly and longitudinally, for each latitude. This leaves E_{OMI} as the only unknown once the satellite measurements are processed to match the temporal and horizontal resolution of S . Figure 3.5 shows an example of how the a priori compares to the a posteriori, averaged over January 2005. This figure gives a single month of output as an example. The

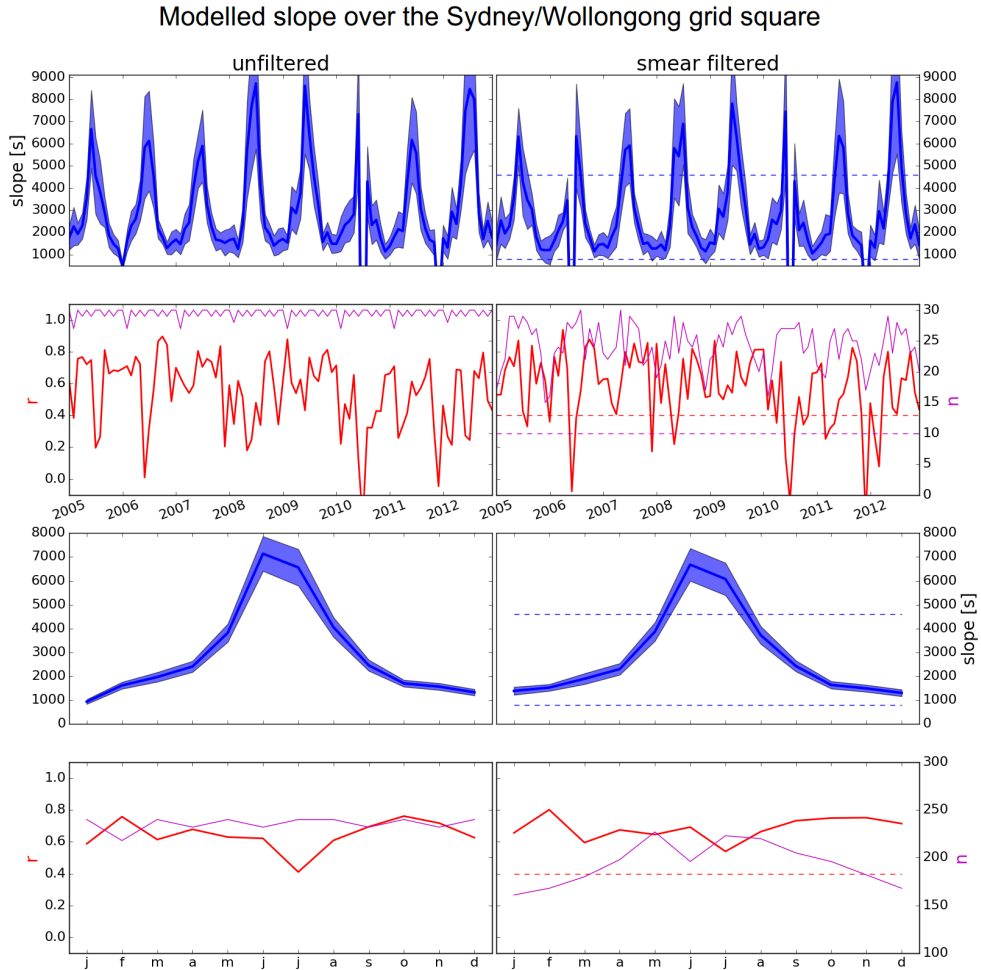


FIGURE 3.3: Row 1: monthly slope along with 95% confidence interval both before (left) and after (right) applying the smear filter for the model grid square containing Sydney over 2005-2012. Limits used in creation of the smear filter are shown with dashed lines. Row 2: regression coefficient and data-point counts for slope shown in row 1. Additionally limits for r and n used in slope utilisation (see text) are shown with dashed lines. Row 3: slope and confidence interval using the multi-year dataset for each month. Row 4: regression coefficient and data-point counts for row 3.

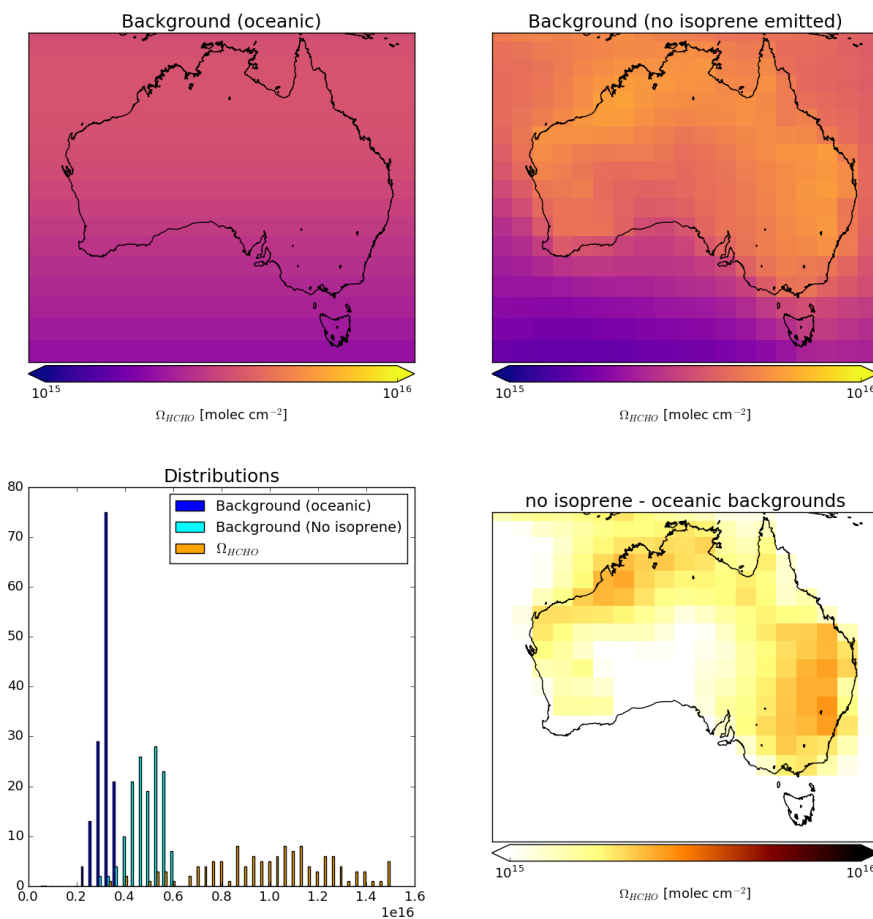


FIGURE 3.4: Top left: Background total column HCHO based on longitudinally averaged values over the remote Pacific Ocean. Top right: Background total column HCHO based on GEOS-Chem output with isoprene emissions set to zero. Bottom left: Distributions of column amounts over land squares in Australia from the two background definitions and the monthly HCHO average from GEOS-Chem (standard tropchem run). Bottom right: Absolute difference between the two background defined value maps.

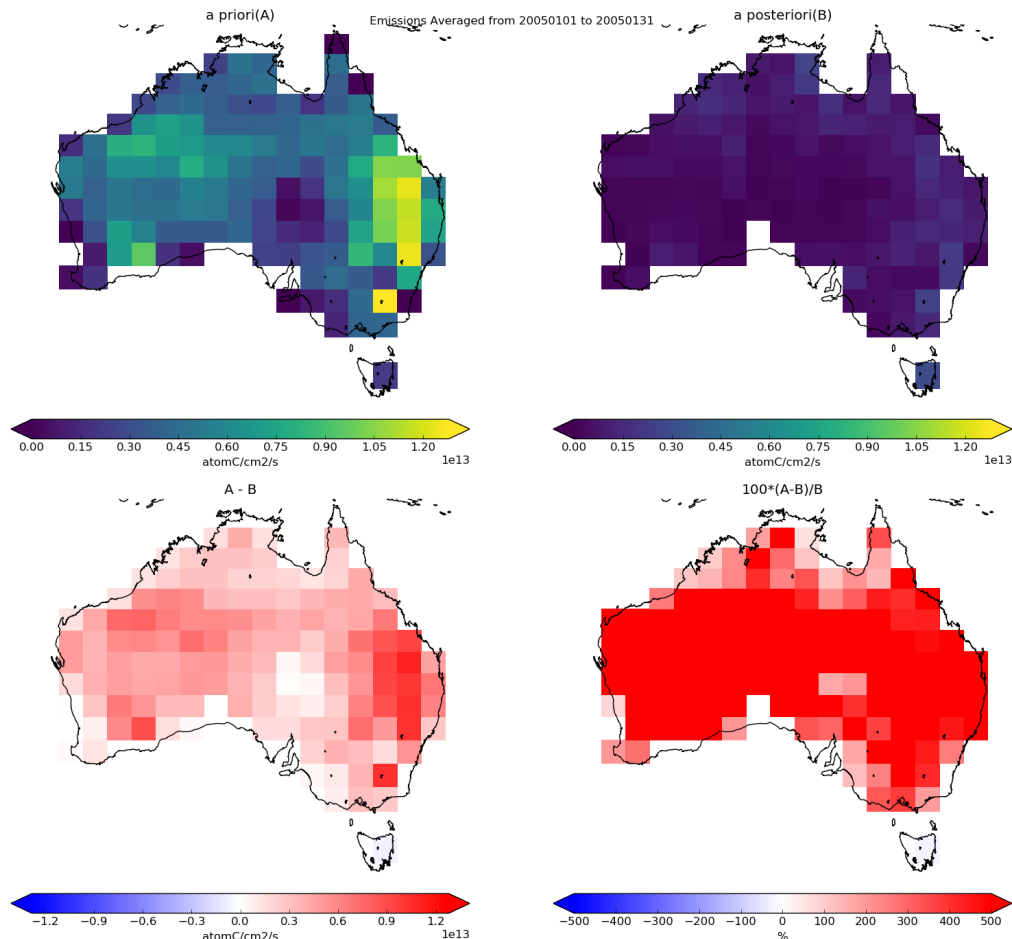


FIGURE 3.5: Top row: isoprene emissions from GEOS-Chem (a priori, left) simulation and top-down (a posteriori, right) calculations averaged over the month of January, 2005. Bottom row: the absolute (left) and relative (right) differences between the two.

a priori exceeds 500% of the a posteriori in many regions; however, the major absolute differences occur in the east between Sydney and Brisbane. Analysis of the full record is discussed in the results (Section 3.3).

One potential issue in this top down estimation technique is the low number of valid satellite measurements that may occur due to the higher solar zenith angles in winter and at higher latitudes. Another issue is that negative emissions are commonly calculated in areas wherever measured HCHO columns are lower than background amounts (as $E_{OMI} = \frac{\Omega_{OMI} - \Omega_0}{S}$). These are set to zero, which increases the overall average emissions from 4.4×10^{11} atom C cm⁻² s⁻¹ to 1.1×10^{12} atom C cm⁻² s⁻¹, due to the frequency of sub-zero column amounts (especially in winter) over low isoprene emission areas.

3.2.8 Sensitivity to smearing

The top-down isoprene emission estimate assumes enhanced HCHO is caused by local emissions, which is not always the case. A *smearing* filter is created (see Section 2.7.3) which filters out grid squares on days when transport is likely, and the effects on the modelled S values are shown here. Smearing can be dependent on local or regional weather patterns, as greater wind speeds will reduce the time any emitted compound stays within the local grid box. As such smearing can vary both spatially and temporally. Smearing is also sensitive to time of day, season, and latitude, as lower insolation results in slower photolysis. Figure 3.6 shows smearing and how frequently grid squares are filtered using the smearing filter. The smearing filter is more active in winter and spring, especially at higher latitudes. Grid squares along the east coast are filtered frequently in all seasons, as well as grid squares in the high smearing lake Eyre region in northeastern South Australia. During summer data loss from smearing is approximately 30% over the entirety of Australia, which increased to 40% over winter. The data loss is generally higher towards the north east and southern coastlines, and at lake Eyre.

When limiting smearing (\hat{S}) to within 800-4600 s, GEOS-Chem correlations between isoprene emissions and HCHO columns improve marginally and not uniformly (Figure 3.3). Where smearing is prevalent, the relationship between a priori emissions and HCHO columns may already be weak due to low emissions or unsuitable meteorological conditions. S and associated regression coefficients (r) are calculated monthly. If $r < 0.4$ then the regression is calculated using multiple years of data for that month. This multiple year regression is discarded completely if it also has a coefficient of $r < 0.4$, leaving no slope for the grid square for the month, and therefore no estimated a posteriori emission. This happens only infrequently, and only in locations with very limited isoprene emissions such as the lake Eyre basin.

3.2.8.1 Modelled HCHO lifetimes

By assuming yield Y_{isop} lies between 0.2 and 0.4, we find a range for midday lifetimes of HCHO using equation 3.7:

$$\begin{aligned} S &= \frac{Y_{isop}}{k_{HCHO}} \\ \tau &\equiv \frac{1}{k_{HCHO}} \\ \tau &= \frac{S}{Y_{isop}} \end{aligned} \tag{3.9}$$

τ is heavily influenced by assumed yield, and improved methods of estimating yield over Australia are required to improve this estimate. Figure 3.7 shows the GEOS-Chem HCHO lifetime estimated throughout the year. There is a clear seasonal cycle with longer lifetimes in winter months. In June (and sometimes March, July and August), HCHO lifetimes increase, which is caused by the reduced winter HCHO concentrations, temperature, and insolation. These factors may limit the utility of any top-down emissions estimation technique using HCHO in the winter months. The

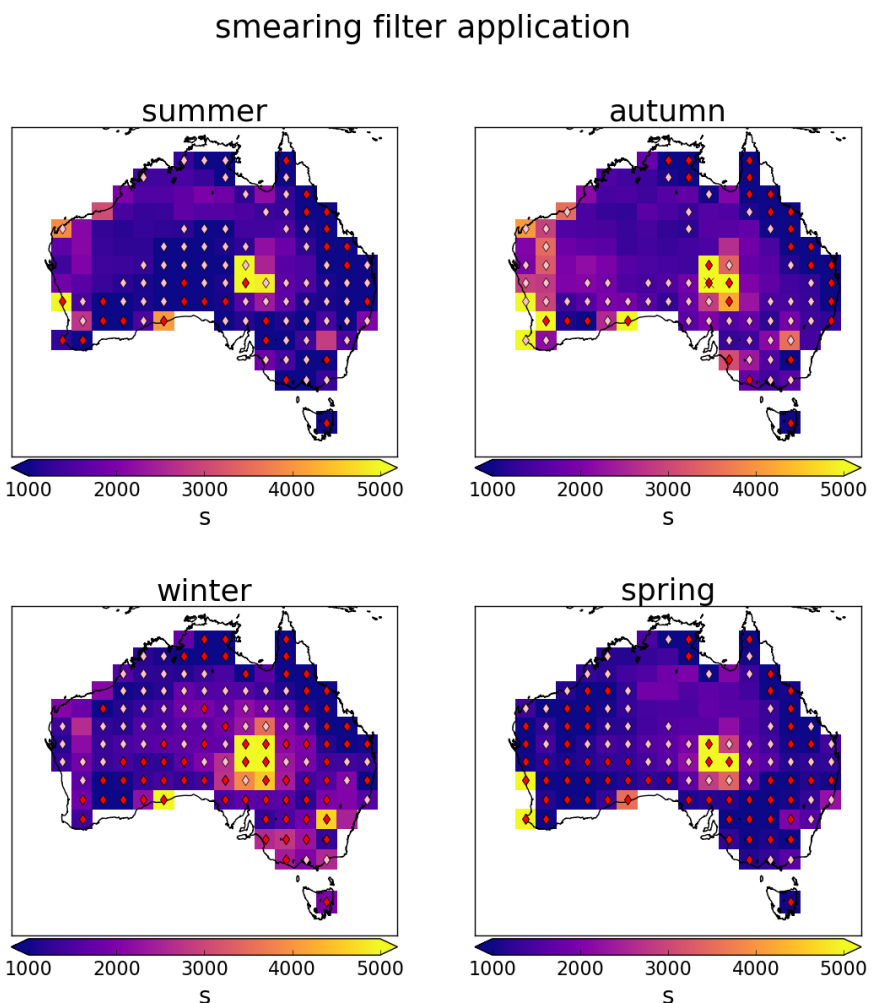


FIGURE 3.6: Seasonally averaged smearing (\hat{S} , see text) over 2005. Diamonds represent grid squares which have had at least 10 (pink) or 30 (red) days removed due to the smearing filter over the season. Red crosses show where the filter has removed all data.

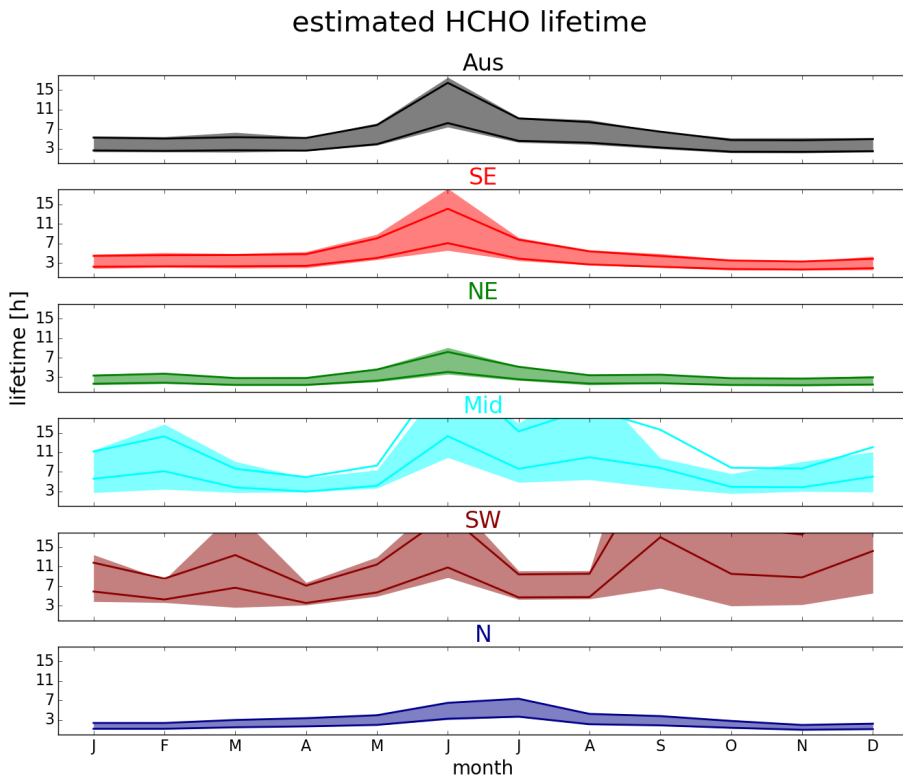


FIGURE 3.7: Monthly area averaged HCHO lifetime (τ in hours), with IQR shaded. Solid lines show lifetime assuming yield is 0.2, and 0.4 (higher and lower lines respectively). Coloured by regions shown in Figure 3.10.

figure is produced using filtered slope information from 2005; however, outliers along with low data availability (in some months) are issues which lead to wide estimate ranges and high uncertainty. Noise in the southwest and middle regions may be indicative of substantial filtering, potentially driven by westerly winds which can bring transported pollution and also lead to smearing.

3.2.9 Running GEOS-Chem using a posteriori emissions

After creating the a posteriori isoprene emissions estimate, GEOS-Chem is re-run with biogenic emissions scaled to match the new estimate. This is performed by applying a seasonal scaling factor α , based on the multi-year monthly average difference between midday a priori and a posteriori emissions at $2^\circ \times 2.5^\circ$ horizontal resolution. α is the ratio between the multi-year averaged monthly emissions from GEOS-Chem E_{GC} and the a posteriori E_{OMI} :

$$\alpha = \frac{E_{OMI}}{E_{GC}} \quad (3.10)$$

This seasonal scaling retains shorter time-scale variability and meteorological dependencies built into the parameterisations of the MEGAN model, while ensuring the

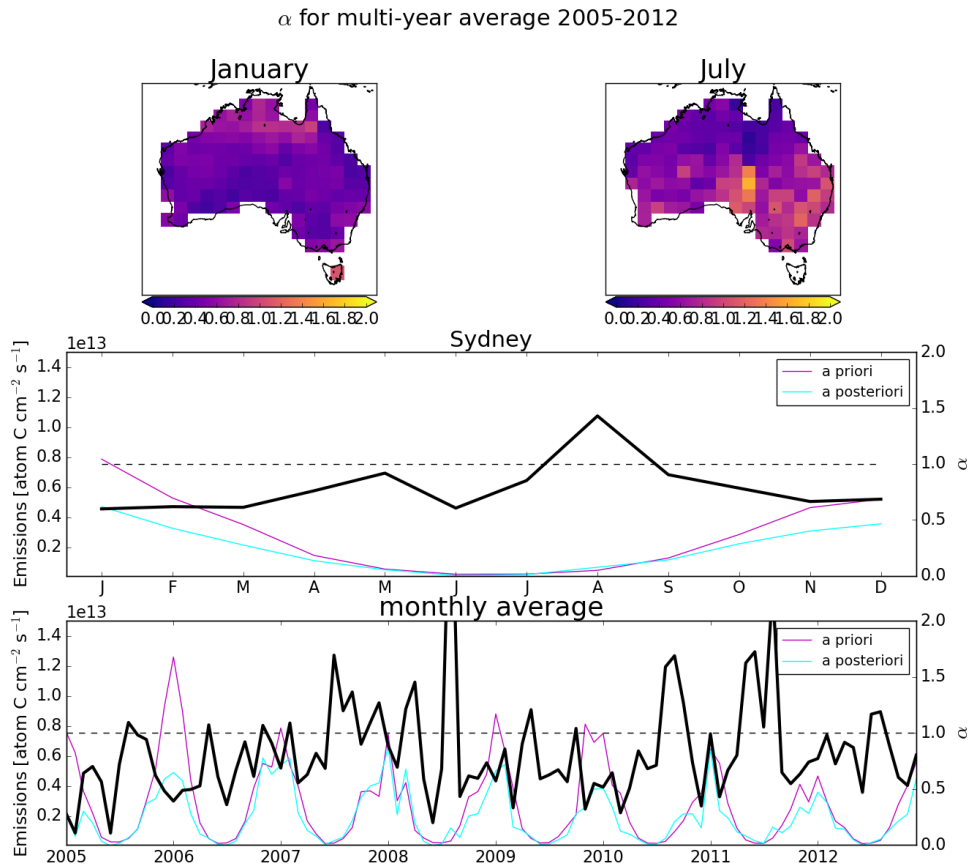


FIGURE 3.8: Row 1: α for the average January (left) and June (right) over 2005-2012. Row 2: a priori (magenta, left axis), a posteriori (cyan, left axis), and α (black, right axis) multi-year monthly averages calculated for Sydney. Row 3: Monthly averages of the same terms in Row 2.

multi-year monthly averaged emissions match. Initially α is uniformly set to 1 globally. Where top down emissions exist and E_{GC} is non-zero, we set α using Equation 3.10. α is applied through the emissions module in GEOS-Chem where isoprene emissions are calculated. First, the new midday (13:00-14:00 LT) emissions (per grid box) are combined forming a multi-year monthly mean, which can be compared to the a priori equivalent. Missing values for α when E_{GC} are zero are a negligible issue since the dominant discrepancies between estimates occur during summer when high emission rates are overestimated. Figure 3.8 shows α for January and June averaged over 2005-2012, along with the time series of E_{GC} and E_{OMI} and α calculated for Sydney and their multi-year seasonal average.

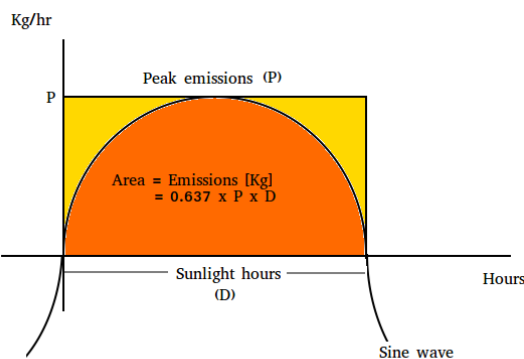


FIGURE 3.9: Total daily isoprene emissions (in kg) is represented by the area under the sine wave.

3.2.10 Conversion to emissions by kg

Top-down emission rates calculated in this work are in units of atom C cm⁻² s⁻¹. In order to calculate the emissions in kg, each grid square is multiplied by its area, and then daily emissions are assumed to follow a sine wave peaking at the midday value. Figure 3.9 shows how the daily approximation of total emitted isoprene per grid square is calculated. Daytime hours are estimated per month, from 14 hrs (Jan) to 10 hr (Jul) (<https://en.wikipedia.org/wiki/Daytime>). This approximation is required since OMI observations occur at midday, when isoprene emissions are at their diurnal peak. GEOS-Chem emissions are similarly multiplied by area, but then integrated over time using hourly output to derive emissions in kg.

3.3 Results

Australia covers roughly 7.7×10^6 km², with heterogeneous environmental conditions. The results presented in this section are therefore frequently split into five regions that are differentiated by colour, as shown in Figure 3.10. These regions are large enough to reduce the uncertainty with at least 10 grid squares in each area, and small enough to be somewhat homogeneous at the national scale.

3.3.1 A posteriori emissions

Figure 3.11 shows a priori emissions over Australia along with a posteriori emissions calculated as described in the prior sections. This figure shows the time series of seasonal area averaged midday emissions, and their absolute differences. Differences between a priori and a posteriori estimates are seasonally and spatially diverse. A seasonal overestimate peaking in summer can be seen in all regions except for the northern region, which is generally overestimated but less so in summer.

Figure 3.12 shows the multi-year seasonal emissions for each region for the a priori and a posteriori emissions side by side. The a priori is approximately twice that of

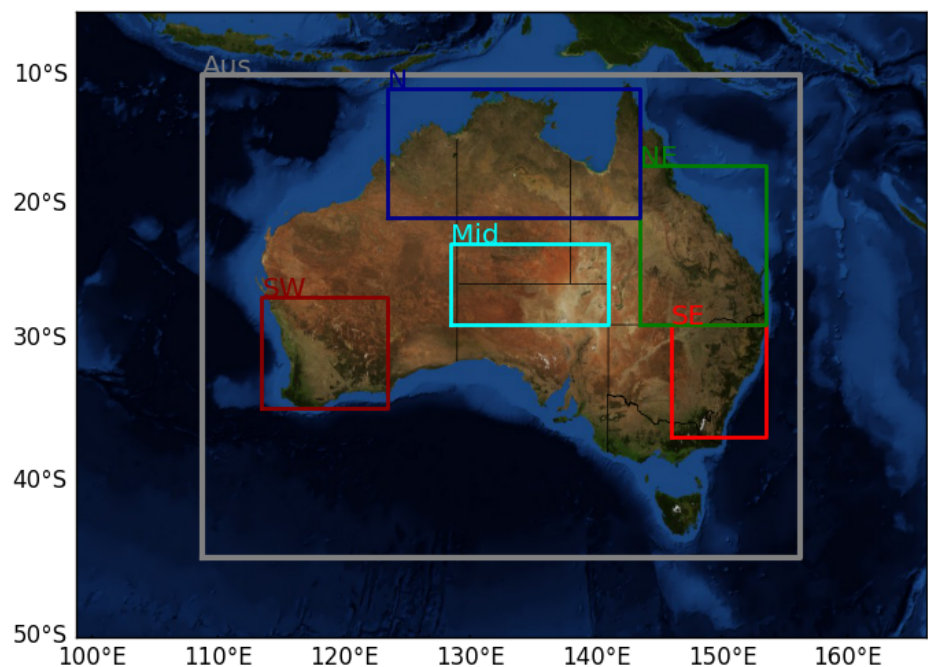


FIGURE 3.10: Sub-regions used in subsequent figures: Northern, North Eastern, South Eastern, South Western, and Middle. Australia-wide averages will be black or grey, while averages from within the coloured rectangles will match the colour shown here.

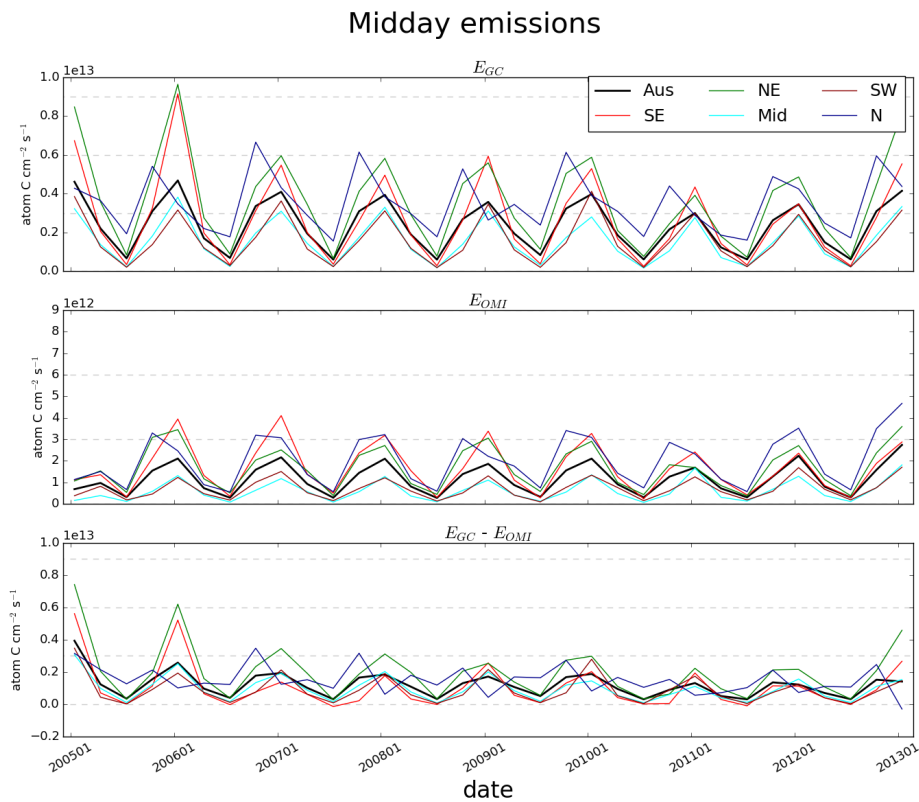


FIGURE 3.11: Row 1: Biogenic emissions of isoprene from GEOS-Chem (a priori, E_{GC}). Row 2: Emissions calculated using the OMI top down inversion (a posteriori, E_{OMI}). Row 3: Absolute differences between the first two rows. Midday emissions are averaged for each season (DJF, MAM, JJA, SON), and colours represent averaged areas from sub-regions shown in Figure 3.10. Grey dashed horizontal bars are added highlighting the scale between rows.

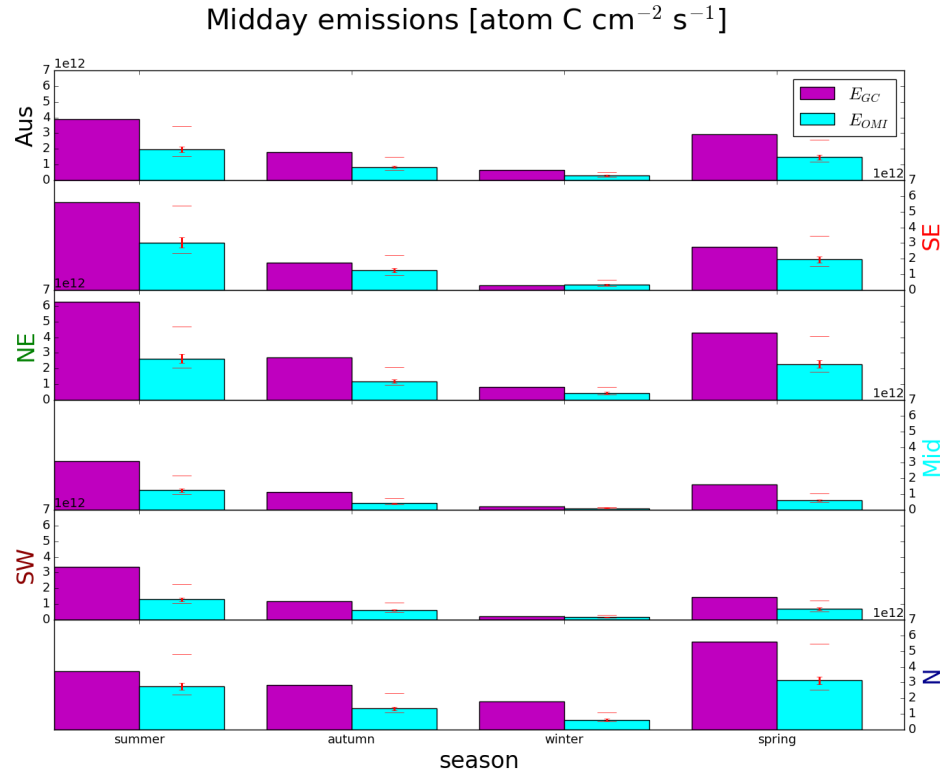


FIGURE 3.12: Regional multi-year seasonal mean a priori emissions (magenta) compared to a posteriori emissions (cyan). Error bars show the regionally averaged uncertainty. Additional horizontal dashes show the uncertainty plus effects from potential HCHO biases (discussed in Section 3.4.1) from satellite underestimation (40%) and monthly clear sky overestimation (13%).

the a posteriori. Absolute differences are highest in spring and summer, when emissions are generally greatest. The exception is the northern region, where the largest overestimates occur in spring, and large differences are seen in all seasons. Uncertainty is summarised for the a posteriori using the mean monthly uncertainty per grid square within each region, divided by the square root of 24 (8 years times 3 months per season). Uncertainty is relatively small since we have 8 years of data combined into the seasonal mean. The potential bias (see Section 3.4.1) is added to the uncertainty and displayed using horizontal red bars. The highest over-estimations (occurring in spring in the Northern region, and summer in all others) lie outside the potential bias caused by satellite underestimations of HCHO. However, many overestimated seasons within each region are within this wide range of potential bias and uncertainty. Some monthly grid squares are very uncertain (> 200%) and these are removed for this plot, causing an increase in a posteriori emissions of < 1%. The cause for these highly uncertain grid squares is not analysed, but may be worth examining in future work.

Figure 3.13 shows the multi-year monthly mean and inter-quartile range of daily

midday isoprene emissions estimates in each region. Months outside of May to August show the most difference between a posteriori and a priori. The most overlap is seen in the south-eastern region, where high summer emissions along with high variance occur in both the a priori and a posteriori. The highest variance is seen in both eastern regions, potentially due to diversity within the regions which include high density cities, large forests, and rural areas. Over the entirety of Australia the seasonal cycle of emissions is shown to be overestimated by the a priori. This overestimate by the a priori may be caused by some mixture of overly high emission factors and high emission sensitivity to temperatures and soil moisture (Emmerson et al. 2016; Emmerson et al. 2019).

While most regions show similar overestimates, the northern region of Australia follows a different cycle of bias. Northern Australian emissions appear to be overestimated throughout the year, with the lowest bias in early summer. One potential reason is that the wet season (November-April) interferes with satellite measurements due to increased cloud coverage, while also changing the ecosystem's response to sunlight and temperature (e.g., Surl, Palmer, and Abad 2018). This is evidenced by the low summer OMI pixel count (before filtering) in this region (see Section 3.4.3). Low measurement counts in summer in the northern region could lead to a low bias in the a posteriori emissions estimate from the drier regions being over-represented. In-situ measurements in both monsoon and non-monsoon seasons are required before robust conclusions can be drawn in this region.

There is only weak correlation between daily estimates of the a priori and a posteriori ($r < 0.2$), and a priori distributions show more variance (figure not shown). This is likely due to the filtering applied to satellite data (e.g., whenever cloud coverage exceeds 40%) which reduces the count and spread of a posteriori emission calculations. Figure 3.14 shows how the distributions of a posteriori emissions compare to a priori emissions in each region during summer months (DJF) with zeros removed from both distributions. This figure also shows the regressions between monthly averages of the same data. In the summer monthly averages, the linear regression coefficient r ranges from 0.2 to 0.81 depending on which region is being compared. The highest correlations between a priori and a posteriori emissions are in the southeast ($r = 0.81$) and southwest ($r = 0.79$) regions, followed by the northeast ($r = 0.61$) region. This is likely due to isoprene emissions in these regions being dominated by the biogenic sources (large forests) that the top down emission estimate is based upon. Although the northern region also contains large areas of forest, the correlation is the worst. In part this is due to misrepresented forest emissions in the model, exacerbated by unrepresented responses to moisture and poorly modelled environmental stresses in this region which lies within the tropics and undergoes monsoonal weather and intense heat and drought seasons (Emmerson et al. 2016; Surl, Palmer, and Abad 2018; Emmerson et al. 2019). If the same analysis is performed over winter months, the regression in the northern region is greatly improved (to $r = 0.66$), while other regions remain approximately the same. If the modelled emissions are correct, this suggests that satellite measurements are not capturing representative samples of monthly grid square averages in summer, likely because of cloud coverage, and the summer inversion in this region may be biased.

When comparing GEOS-Chem (MEGAN) to the a posteriori calculated using our

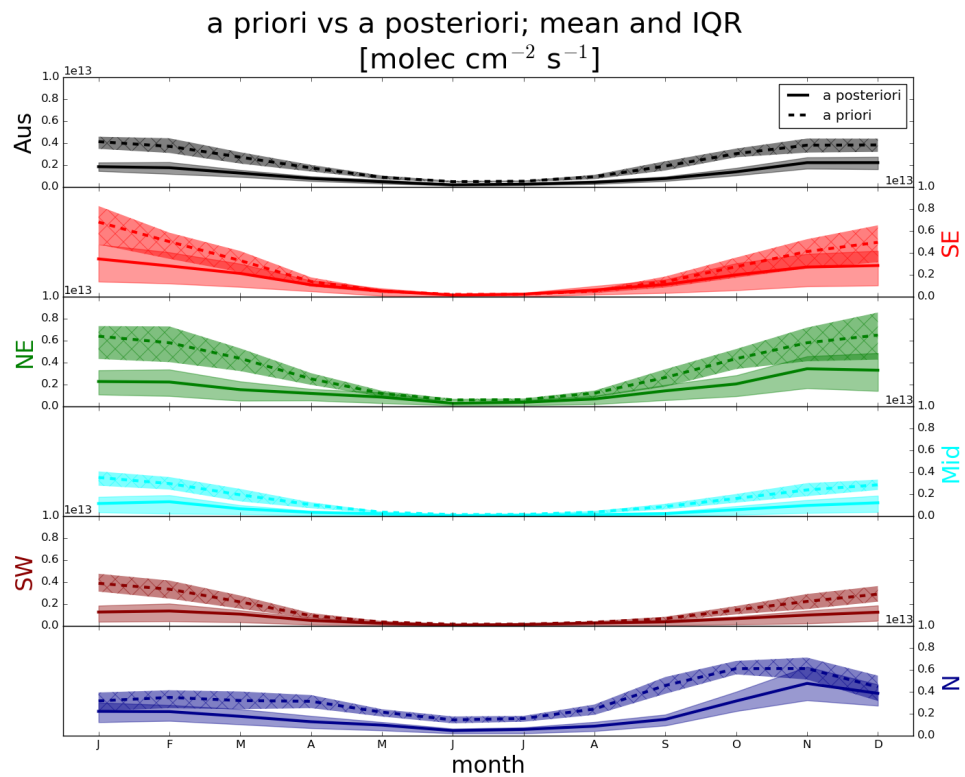


FIGURE 3.13: The multi-year monthly mean (lines) and IQR (shaded) of midday (13:00-14:00 LT) isoprene emissions estimates. A priori emissions are shown by the dashed lines and hatched shaded areas show the IQR. A posteriori emissions are shown using the solid lines, with IQR shown by unhatched shaded areas. Colours denote the region over which the monthly average was taken, as in Figure 3.10.

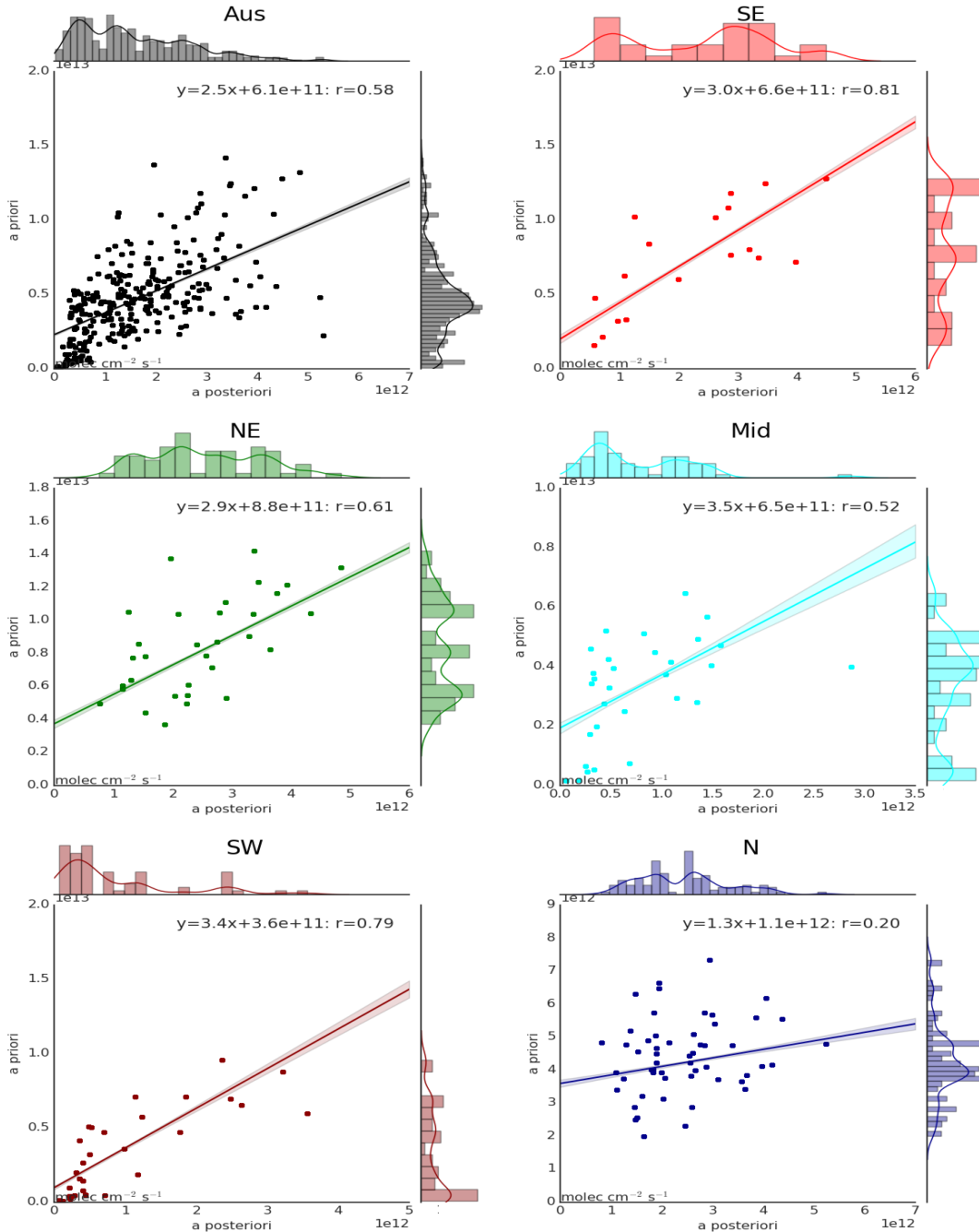


FIGURE 3.14: Scatter plot of a priori emissions against a posteriori using monthly averaged grid squares as regression datapoints. Data points are created using monthly averages (of midday emissions) for each grid box for each month of summer (DJF) within each region shown. Multiple years of data are used, meaning if a region has 10 grid boxes, the 8 years of data will add up to $10 \text{ boxes} \times 3 \text{ months} \times 8 \text{ years} = 240$ data points minus filtered and zero emission squares. Plots are coloured by regions matching those shown in Figure 3.10. The linear best fit regression is inset into each plot along with the line equation and regression coefficient. The normalised distribution of each population is shown at the top and right spine of each subplot, with the right spine (facing the a priori axis) using the a priori axis and scale, and the top spine using the a posteriori axis and scale.

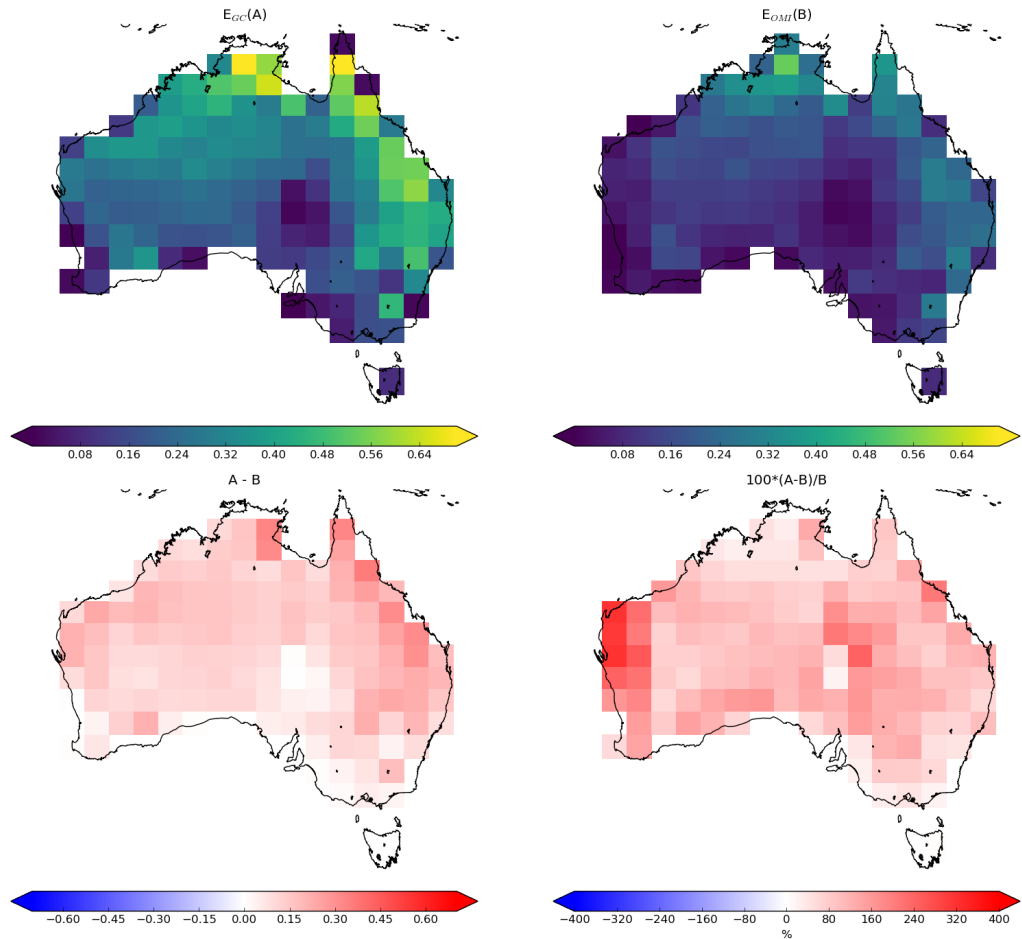


FIGURE 3.15: Top row: multi-year mean a priori emissions in Tg yr^{-1} from E_{GC} (GEOS-Chem; running MEGAN) and E_{OMI} (top-down emissions) respectively. E_{OMI} uses an assumed sinusoidal daily cycle, with daylight hours prescribed for each month: see Section 3.2.10). Bottom left and right show the absolute and relative differences, respectively.

top-down inversion, we find a decrease of $\sim 46\%$ from 39 Tg yr^{-1} to 21 Tg yr^{-1} . Table 3.1 compares annual Australian isoprene emissions from this work to previously published values. Our a posteriori estimate of 19 Tg yr^{-1} suggests isoprene emissions may be lower than any bottom up estimates, and is close to the lowest estimate of Bauwens et al. (2016) of 26 Tg yr^{-1} . Figure 3.15 shows how this decrease is distributed spatially, with E_{GC} and E_{OMI} in Tg yr^{-1} calculated as a multi-year mean. Across all of Australia we see large reductions of total emissions using the new top-down estimate.

3.3.1.1 Diurnal emissions

Figure 3.16 shows the a priori daily emissions cycle for Australia compared to the estimated a posteriori emissions cycle over Australia. The conversion of midday a posteriori emissions ($\text{molec cm}^{-2} \text{ s}^{-1}$) into Tg yr^{-1} involves integration over an assumed

TABLE 3.1: Isoprene emissions (Tg/yr) from Australia

Estimate ^a	Source	Year	Reference
39.2(4.0)	bottom-up	2005-2012	This thesis ^b
20.7(1.6)	top-down	2005-2012	This thesis ^c
~ 80	bottom-up	1980-2010	Sindelarova et al. (2014) ^d
26-94	bottom-up	2005-2013	Bauwens et al. (2016) ^e
36	top-down	2005-2013	Bauwens et al. (2016) ^f

a: Standard deviation shown in parentheses.

b: GEOS-Chem with MEGAN diagnostics based on 3-hourly averages.

c: Based on daily peak emissions integrated over a sinusoidal daily curve.

d: MEGAN run using MERRA meteorology.

e: Range shown here based on three models, two of which implement MEGAN.

f: OMI based top-down inversion.

sinusoidal diurnal emission cycle as described in Section 3.2.10. A priori emissions peak from approximately 11:00 LT to 16:00 LT, while outside these hours there is a non-sinusoidal drop in emissions to below the assumed a posteriori diurnal emission cycle. This means the conversion may be biased by this consistent difference between modelled a priori diurnal emission cycles and the assumed diurnal a posteriori cycle. This potential bias is not analysed further, and should be relatively small compared to other uncertainties as it only affects emissions towards the daily minima.

3.3.1.2 Trends

Figure 3.17 shows monthly deseasonalised a priori and a posteriori midday emission anomalies for each region. First the emissions are spatially averaged within each region to form a daily time series of midday emission rates. They are averaged into monthly data, and then the multiyear monthly mean is subtracted to form the anomaly time series. Any anomaly greater than three standard deviations from the mean is removed (crosses in Figure 3.17). An ordinary least squares linear regression is then performed to look for any significant trend. A trend is considered significant if the p-value from a Wald test (equivalent to a t-test) is less than 0.05. The same process is repeated for surface concentrations of ozone, HCHO, and NO_x (not shown). Trend results for isoprene are summarised in Table 3.2. The a priori midday surface isoprene concentrations show a small decline outside of the southwest region over the 8 year period from 2005-2012. This decline reduces in scale by approximately a factor of 2-3 in the a posteriori emissions. None of the species shows any significant changes in trend due to scaling isoprene emissions. Some trends are no longer significant in surface HCHO, however none of the trends change sign. Since the scaling factor α is applied to each grid square seasonally and not changing each year, changing trends are not expected.

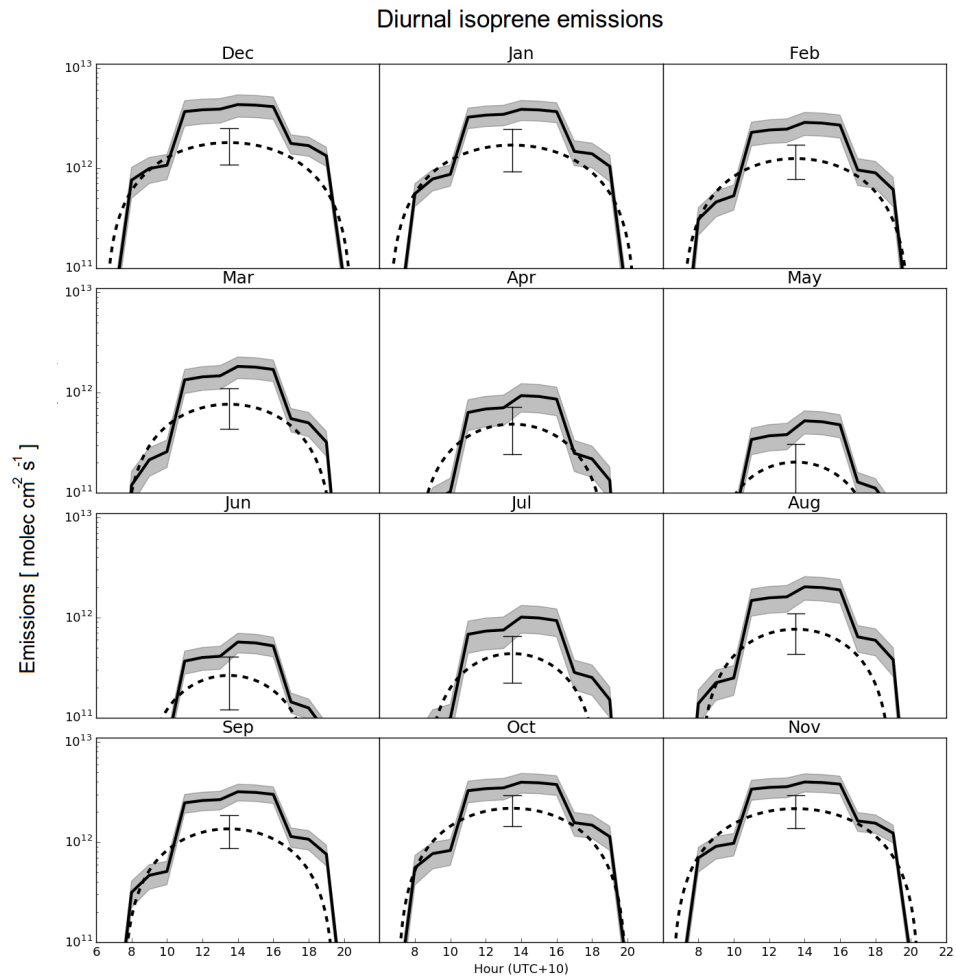


FIGURE 3.16: The diurnal cycle of GEOS-Chem a priori emissions (solid line) averaged by month into hourly bins over from 2005 to 2013 are shown against top-down a posteriori (dashed line) emissions. Standard deviations for the monthly average are shaded for the a priori, and shown with error bars at 13:30 LT for the a posteriori. Top down emissions shown here are based on monthly midday emissions being the peak of a sine wave which drops to zero after and before daylight hours (see Section 3.2.10).

TABLE 3.2: Yearly trend in surface amounts (ppbvC) before and after scaling isoprene emissions.

Region	a priori	a posteriori
Isoprene		
Aus	-.04	-.02
SE	-.15	-.07
NE	-.13	-.04
Mid	-.07	-.02
SW	-.01	-.01
N	-.06	-.02

Statistically significant (two sided test with $\alpha = 0.1$) trends are bolded.

Units are ppbv Carbon rounded to two decimal places.

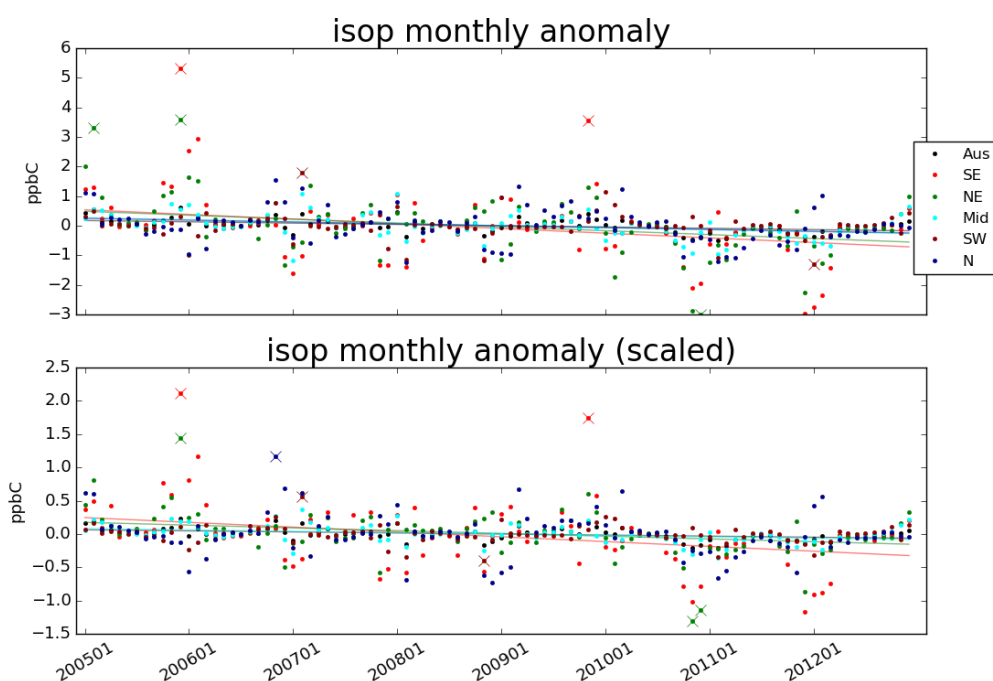


FIGURE 3.17: A priori (row 1) and a posteriori (row 2) emissions anomaly from multiyear monthly mean, split by region (see Figure 3.10).

3.3.2 Modelled impacts of reduced isoprene emissions

This section uses GEOS-Chem to determine how the improvements to biogenic isoprene emissions impact subsequent atmospheric chemistry and composition. A posteriori emissions are implemented in GEOS-Chem as described in Section 3.2.9. Outputs from the scaled GEOS-Chem run using the a posteriori are denoted by superscript α . For example, column HCHO from GEOS-Chem before and after scaling are denoted Ω_{GC} and Ω_{GC}^α respectively.

3.3.2.1 Implications for HCHO

As a preliminary check on the GEOS-Chem output, simulated Ω_{GC} and Ω_{GC}^α is compared to Ω_{OMI} over January and February, 2005 in Figure 3.18. In every region, Ω_{GC}^α is closer to Ω_{OMI} with biases decreasing from $\sim 100\%$ to $\sim 50\%$ everywhere except the northern region, which has biases decreasing from $\sim 50\%$ to $\sim 25\%$. Note that this is not an independent validation as Ω_{OMI} drive the creation of Ω_{GC}^α , and as we expect the relationship is much improved. The remaining differences are most likely driven by filtering and temporal averaging of the applied scaling factor α . When looking over all of Australia from 2005-2012, the summer mean decreases from 9.8×10^{15} to 7.4×10^{15} molec cm $^{-2}$ after scaling isoprene emissions, while the satellite column is 4.9×10^{15} .

Figure 3.19 shows HCHO is most reduced in summer for the majority of Australia. In winter, a reduction is seen along the northern edge of Australia, most likely because emissions in this area are less affected by the seasonal decline. Seasonal means and the standard deviations for each region are summarised in Figure 3.20. Both mean and variance within the vertical column of HCHO are reduced after running GEOS-Chem with scaled isoprene, although the mean is lower still in OMI vertical columns. Model output standard deviations in summer range from $\sim 20 - 30\%$, while OMI standard deviations range from $\sim 32 - 41\%$. The highest OMI standard deviations occur in winter, ranging over $\sim 46 - 73\%$, which is the opposite of model output with standard deviations between $\sim 12 - 27\%$. This could be an effect from the increased winter uncertainty in satellite output, which is amplified by the low column amounts in the season. Overall the standard deviation within model output appears to be too low in all regions, ranging from three quarters (south eastern region) to one fifth (middle region) of the standard deviations within the OMI HCHO column output

Decreasing isoprene emissions in the model lead to reduction in HCHO concentrations as one would expect. Figure 3.21 shows an example (over Wollongong) of the modelled HCHO profile before and after scaling isoprene emissions. This reduction of HCHO is greatest at the surface, and is highly correlated ($r > .8$) in all regions to the reduction in isoprene emissions. The high correlation is effectively a sanity check of the top-down method used in this thesis to estimate isoprene emissions.

3.3.2.2 Implications for ozone

Isoprene oxidation can eventually lead to ozone formation, especially when isoprene-enriched air masses mix with polluted urban air masses that contain high NO_x. Figure

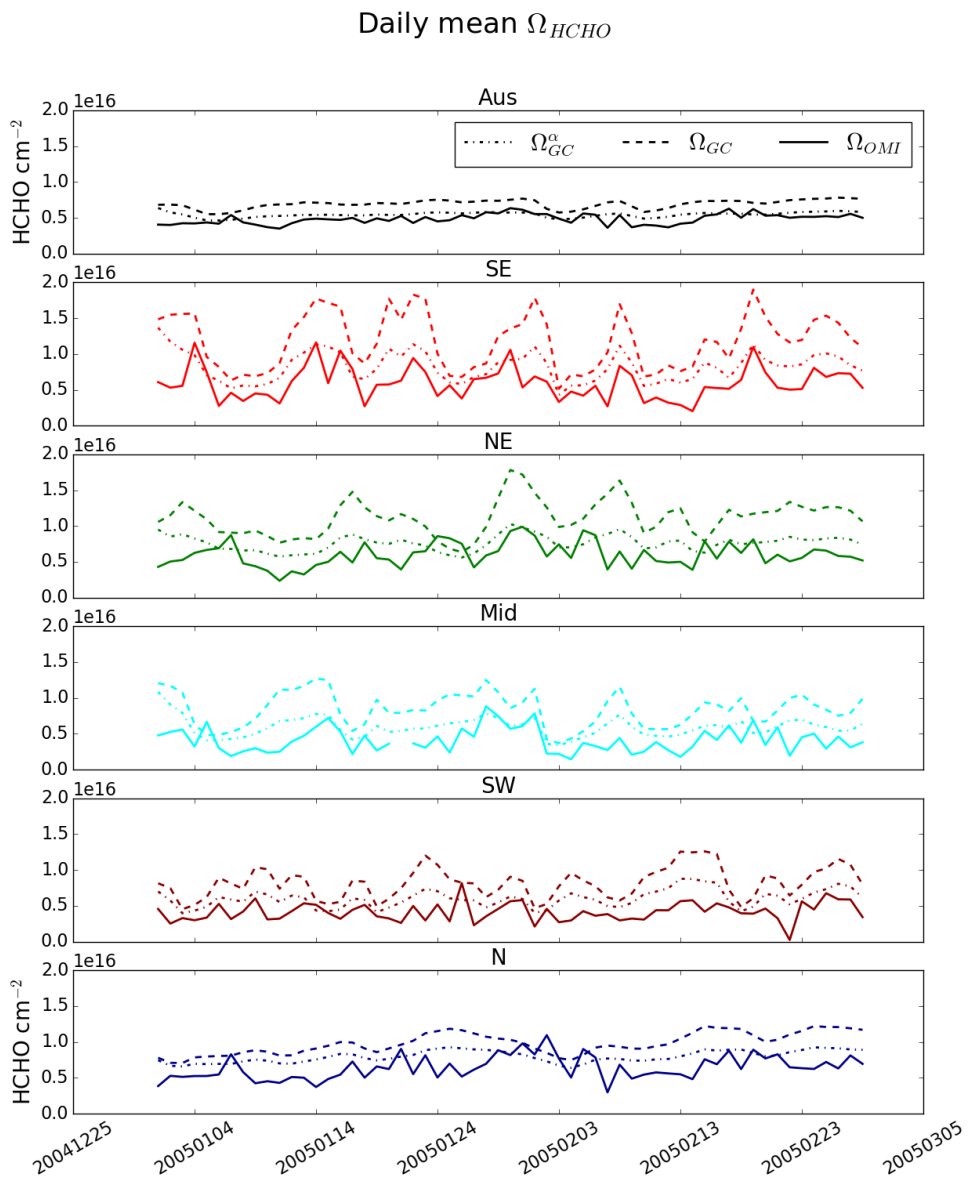


FIGURE 3.18: Daily mean total column HCHO amounts from GEOS-Chem with a priori (new emissions run) and a posteriori (tropchem run) a posteriori scaled isoprene emissions, along with the recalculated OMI HCHO columns. Each row shows the average over regions in Figure 3.10.

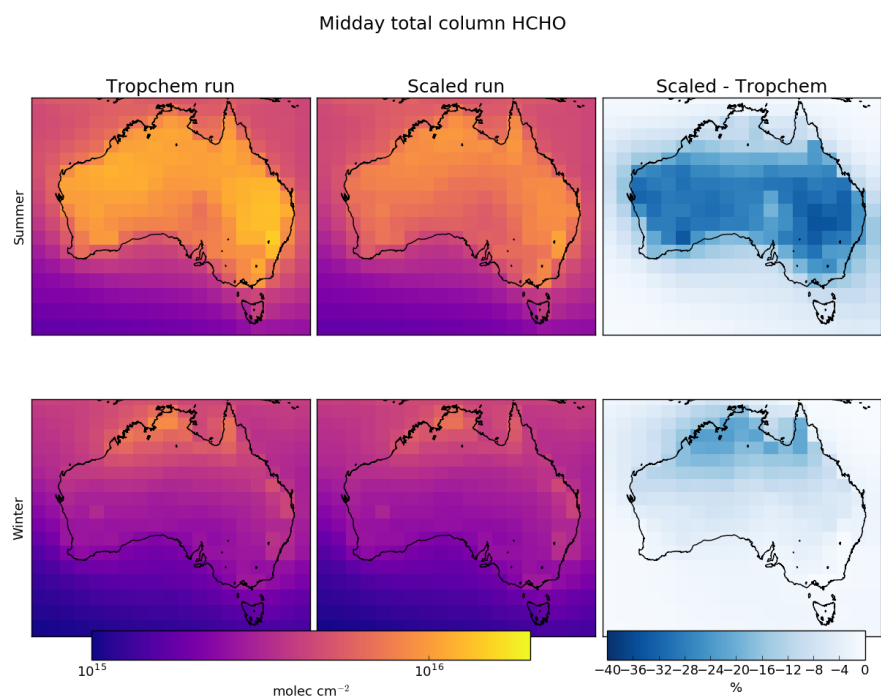


FIGURE 3.19: Total column HCHO before (left) and after (middle) scaling isoprene emissions, and their relative differences (right). Top row shows summer (DJF) averaged total columns, while bottom row shows the winter (JJA).

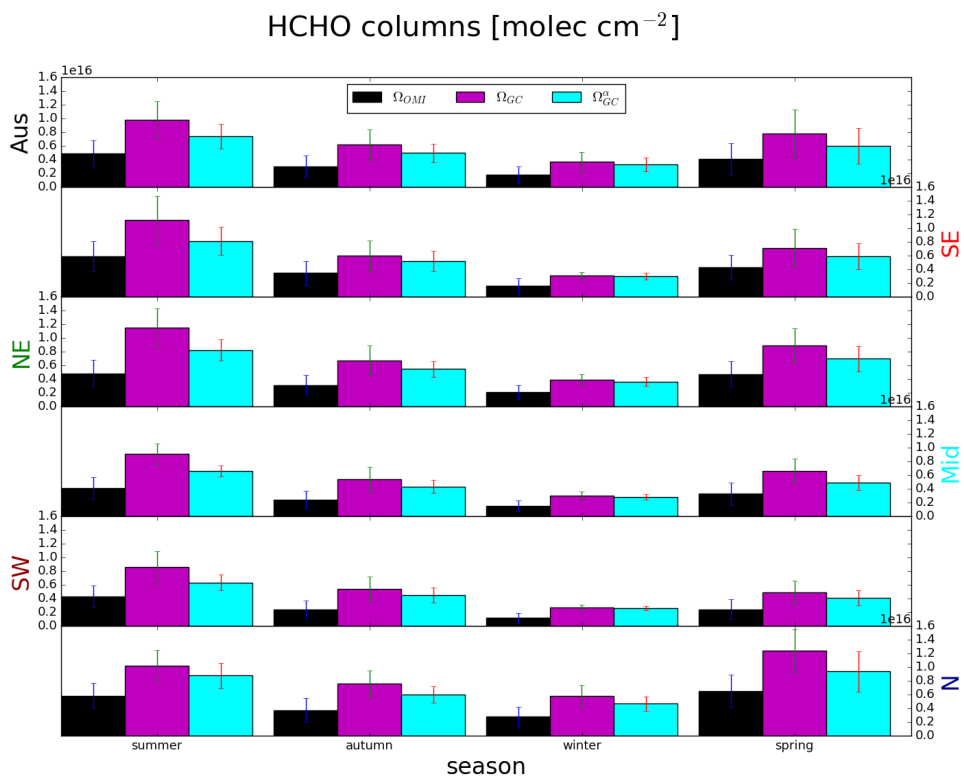


FIGURE 3.20: Regionally and seasonally averaged HCHO total columns from GEOS-Chem and recalculated OMI measurements side by side. Each row represents one region within Australia, while each column represents from left to right: summer, autumn, winter, spring.

Standard deviations are shown with error bars.

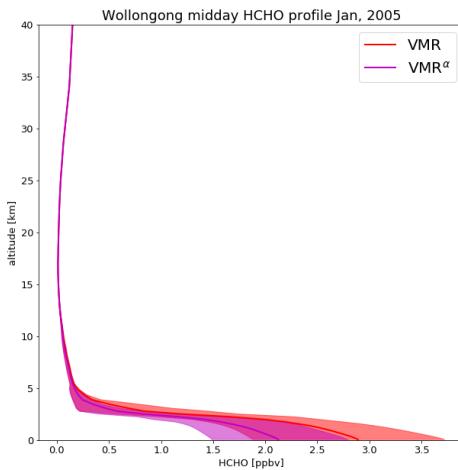


FIGURE 3.21: Monthly averaged HCHO profile over Wollongong modelled by GEOS-Chem before (VMR) and after (VMR^α) scaling isoprene emissions. Shaded areas represent the inter-quartile range over the month.

3.22 shows surface level (up to ~ 150 m altitude) ozone concentrations over 2005 before and after scaling modelled isoprene emissions. Reducing isoprene emissions lowers surface ozone concentrations by ~ 1 ppbv in all regions in all seasons. The largest reductions (~ 3 ppbv) occur in the northern region in spring. A regression between the change in isoprene emissions, and the change in surface ozone was performed (as in the prior section with HCHO); however, only very weak correlations between reductions are apparent. While the overall decrease in surface ozone is clear, there is no direct correlation between monthly grid square averaged reductions in isoprene emission and surface ozone concentrations. This suggests that changes in isoprene emissions affect ozone in grid squares where absolute emission reductions are not as strong.

Ozone and fine particulate concentrations in Australian cities have not reduced over the last 10 years, unlike other atmospheric pollutants such as CO, NO₂, and SO₂ (Keywood, Emmerson, and Hibberd 2016). This could be in part due to the downwind effects of isoprene emission, which are most likely to affect suburban fringes (e.g. western Sydney) of Australian cities which are surrounded by vegetation (Millet et al. 2016). Outside of densely populated regions, Australia is likely to be NO_x-limited and changes in VOC emissions will have less of an impact on ozone production. Here the modelled ozone output is averaged over large areas that are mostly non-urban, which means detected ozone sensitivity to isoprene emissions is likely understated for cities. Figure 3.23 shows how ozone is reduced in summer and winter after scaling isoprene emissions. In summer, reductions are strongest in Sydney and Melbourne, but can also be seen in the west coast and central Australia. Winter reductions are more uncertain (relatively); however, they are strongest in the coastal and oceanic regions around Darwin. In the future the estimated emissions will be downscaled to

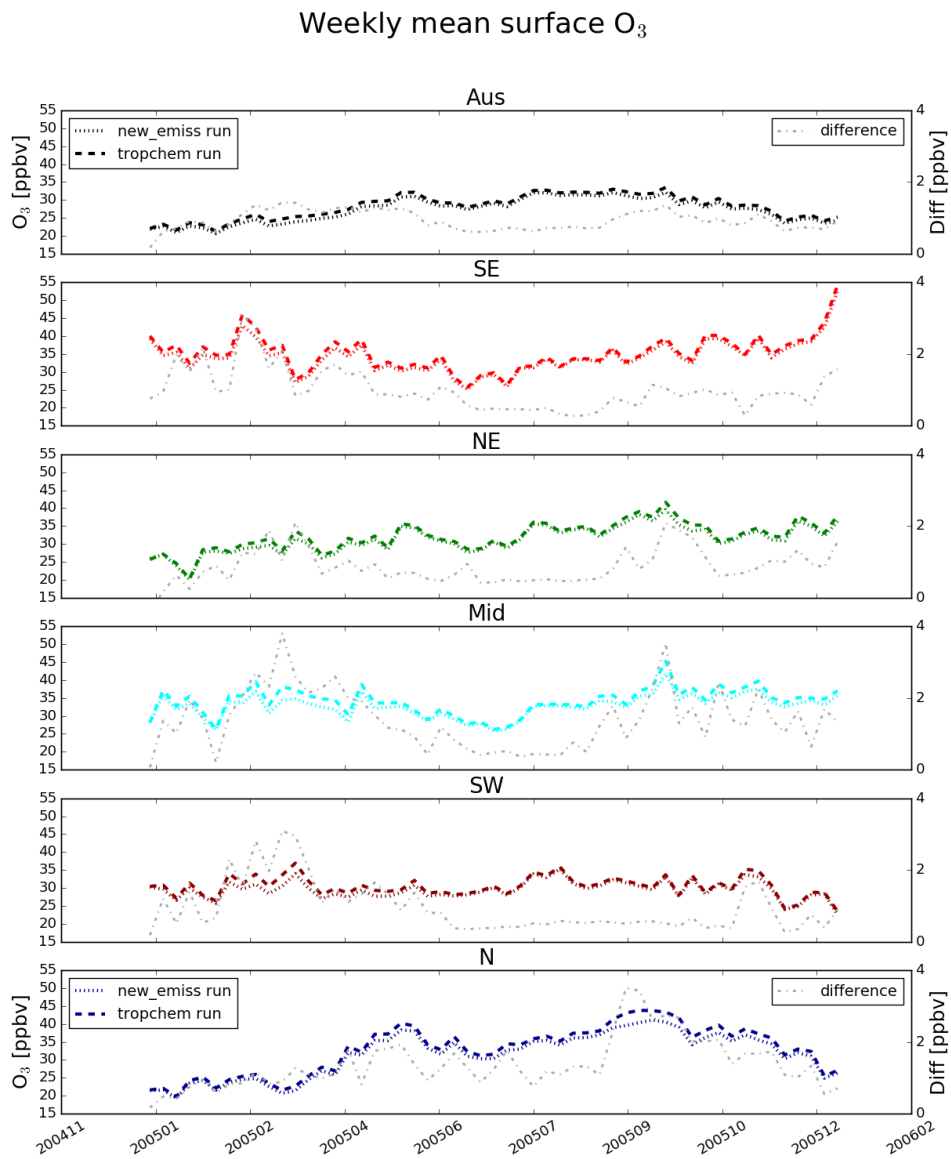


FIGURE 3.22: Surface ozone concentrations (ppb) per region over 2005. Concentrations are shown using the left axis, and absolute differences (tropchem run - scaled run) shown in grey using the right axis.

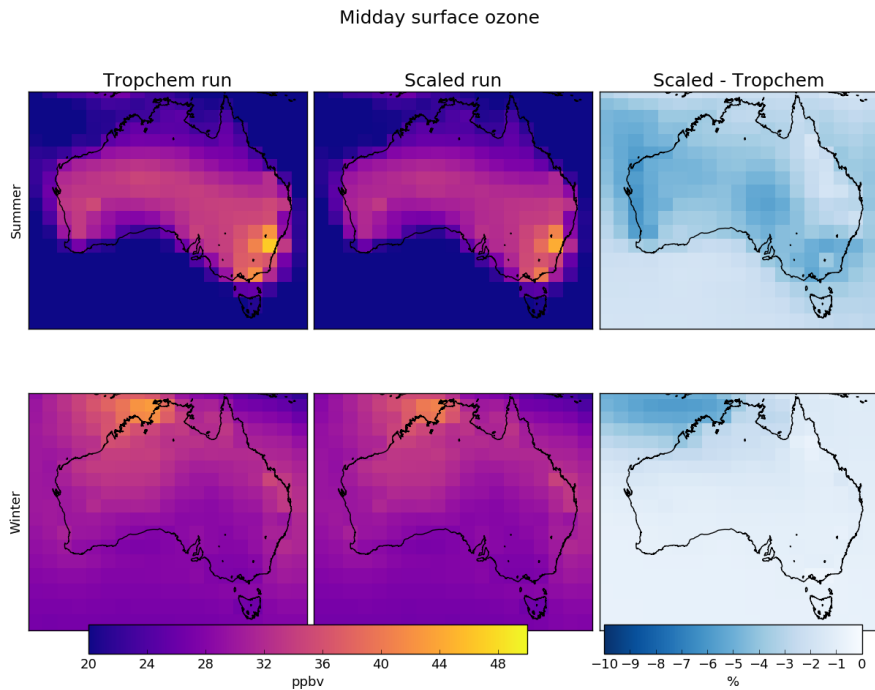


FIGURE 3.23: Surface (up to ~ 150 m) ozone before (left) and after (middle) scaling isoprene emissions, and their relative differences (right). Top row shows summer (DJF) averaged total columns, while bottom row shows the winter (JJA).

properly evaluate their impacts on ozone in different NO_x regimes (for instance over cities).

3.3.3 Comparison with in situ measurements

Comparison between ground-based measurements and large ($2^\circ \times 2.5^\circ$) averaged model output suffers from representation error. Figure 3.24 shows the SPS and MUMBA measurement sites, along with the extent of the relevant $2^\circ \times 2.5^\circ$ GEOS-Chem grid box, a rectangle with edge lengths of roughly 200 km^2 . The urban footprint of Sydney and Wollongong can be seen, along with ocean, forest, and rural regions, which will all affect the model output as it is based on the average of inputs within the grid box. Due to high uncertainty in components of the top-down emissions estimate, temporal resolution is also limited. MUMBA (Section 2.2.3.1), SPS1 and SPS2 (Section 2.2.3.2) each provide on the order of one month of hourly or daily data, which are compared in this section against surface level concentrations from GEOS-Chem (midday output) before and after scaling the biogenic emissions.

Figure 3.25 shows GEOS-Chem output in the grid square containing Sydney and Wollongong campaign measurements. The measurements are subset to those taken between 13:00 and 14:00, which are averaged on days when more than one data point in this time window exists. Midday measurements from MUMBA (summer, Wollongong) compared against SPS (summer, autumn, Sydney) show lower isoprene and

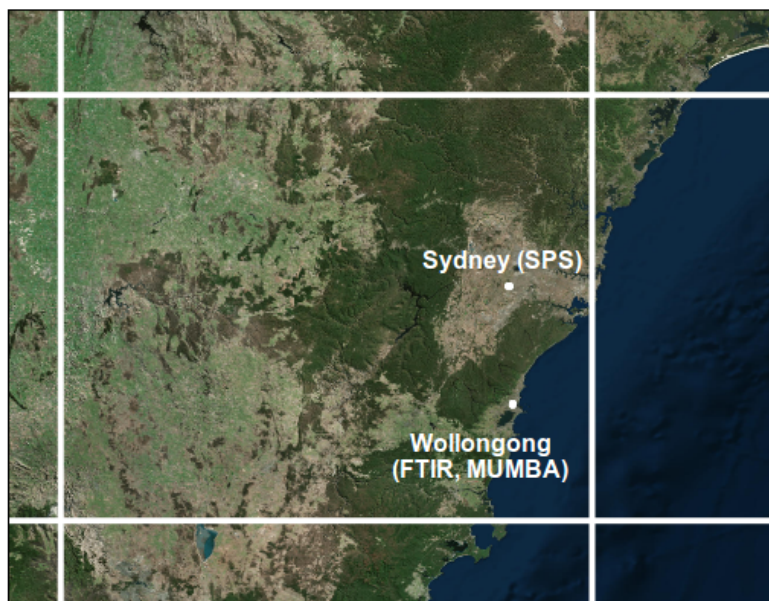


FIGURE 3.24: GEOS-Chem grid box ($2^\circ \times 2.5^\circ$) containing Wollongong FTIR, SPS, and MUMBA campaign data.

TABLE 3.3: Campaign measurements compared to model output [ppb].

	MUMBA			SPS1			SPS2		
	mean	RMSE	r	mean	RMSE	r	mean	RMSE	r
Isoprene	Meas	1.16		0.46			0.47		
	GC	1.34	0.89	0.83	0.24	0.36	0.44	1.87	1.66
	GC ^a	0.67	1.15	0.84	0.18	0.39	0.43	0.93	0.73
	HCHO	mean	RMSE	r	mean	RMSE	r	mean	RMSE
HCHO	Meas	3.92			2.02			1.41	
	GC	2.38	2.63	0.47	1.28	1.28	0.77	3.00	1.97
	GC ^a	1.83	3.01	0.54	1.19	1.35	0.78	2.21	1.17
	Ozone	mean	RMSE	r	mean	RMSE	r	mean	RMSE
Ozone	Meas	30.14			22.71			24.59	
	GC	40.91	15.46	0.52	33.75	13.59	0.35	49.97	28.01
	GC ^a	39.20	14.23	0.54	32.81	12.69	0.36	47.14	24.91
									0.36

Meas: Measurements (midday means)

GC: GEOS-Chem (tropchem run)

GC^a: (GEOS-Chem scaled run)

HCHO levels, and similar ozone levels, and also lower variance across all three species. Variation in SPS data is higher than modelled, which is likely due to a dependence on local meteorology, as plumes of HCHO or isoprene enriched air can be detected as they pass by while the modelled grid square averages these out. Although, this higher variance is not seen in the MUMBA midday concentrations.

The mean of each campaign, and how the measurements compare to coincident modelled values of isoprene, HCHO, and ozone are summarised in Table 3.3. Isoprene correlations are greatest during the MUMBA campaign at $r = 0.83, 0.84$, nearly double that of SPS1 and SPS2. This may suggest that isoprene in the large grid square may be more representative of a Wollongong-like environment, with somewhat more forest and less urban influence when compared to Sydney. However, the root mean square error (RMSE) is approximately 100% in summer, and more than 300% in autumn (SPS2) before isoprene scaling is applied. In this case the reduced isoprene emissions improves the model drastically, bringing the RMSE down to $\sim 50\%$. Similarly for HCHO, the SPS2 RMSE is reduced from $\sim 130\%$ to $\sim 80\%$ by bringing down the mean modelled amounts. In summer (MUMBA and SPS1), modelled HCHO is too low, and is further reduced through scaling. Without improved model resolution or further measurements, this is assumed to be due to local influences which are measured but not captured by the model. Modelled ozone concentrations are slightly reduced (3 – 8%) when scaling isoprene emissions, however the concentrations remain 30 – 50% too high in summer and nearly 100% too high in autumn. This is likely due to the reduced ozone concentrations in cities compared to regional areas, as the modelled ozone concentrations are averages over the larger area which is mostly non-city.

A spectrometer (FTIR) on the roof of the Chemistry building at the University of Wollongong measures total column HCHO in the atmosphere during clear sky conditions. This is the only non-satellite long-term measurement record of total column

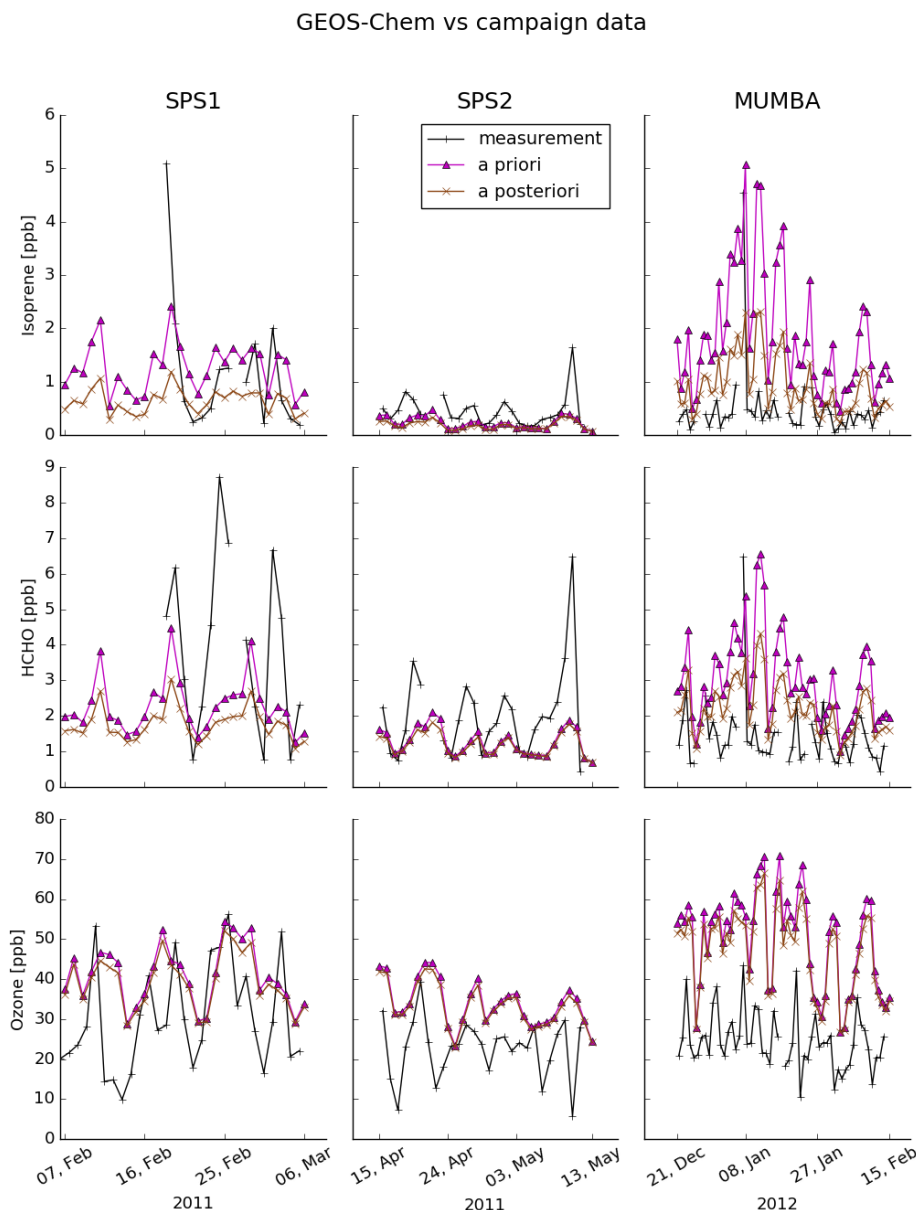


FIGURE 3.25: SPS1, SPS2, and MUMBA (left to right columns respectively) midday (13:00-14:00 local time) measurements of isoprene, HCHO, and ozone (top to bottom rows respectively). Shown in magenta and brown are the a priori and a posteriori GEOS-Chem surface outputs for the matching grid square at midday for days containing measurements.

TABLE 3.4: Mean total column HCHO amounts in 10^{15} molec cm $^{-2}$.

Season	Ω_{FTIR}	Ω_{GC}	Ω_{GC}^{α}
summer	15.4	17.7	13.6
winter	3.68	4.41	4.49

HCHO available in Australia. In order to compare modelled profiles against retrievals from the FTIR, modelled profiles are first convolved with the instrument averaging kernel and a priori as shown in Section 2.2.3.4. FTIR output is resampled to only include measurements taken at midday (13:00-14:00) and GEOS-Chem overpass outputs are interpolated onto matching vertical levels for days where FTIR output exists. Figure 3.26 shows total column HCHO from FTIR, and GEOS-Chem before and after scaling isoprene. While the comparison suffers from representational error between FTIR measurements and GEOS-Chem output, one can see that the summer overestimation of HCHO from GEOS-Chem is removed by isoprene scaling. The mean summer underestimation of HCHO shown after scaling makes more sense due to the relatively dense forested areas around Wollongong, which would raise local HCHO concentrations above the average for the large grid square represented by GEOS-Chem. Another feature is the January and December dip in all three data sets. FTIR has a lower data count and higher variance in these (holiday) months as measurements involve manual processes, increasing uncertainty for the measurements. Analysis of this dip could be performed in future work; however, it would require an in depth examination of local and synoptic HCHO patterns, and higher resolution model data. Seasonal mean HCHO from the FTIR measurements and co-located, convolved, and resampled model output is summarised in Table 3.4. The original modelled summer vertical column is higher than the FTIR measurements by $\sim 15\%$, which decreases with isoprene scaling to $\sim -12\%$. In winter the column is modelled high by $\sim 20\%$, which increases to $\sim 22\%$ after scaling.

3.4 Uncertainty

This section identifies and quantifies the overall uncertainties of calculating isoprene emissions using OMI HCHO observations and the GEOS-Chem model in the top-down method used in this chapter. However, these uncertainties lack verification against measurements. Even as the top-down inversion performed in this chapter attempts to work around the lack of measurements over Australia, it suffers from the lack of independent observations against which it can be verified.

The major source of uncertainty throughout the year comes from uncertainty in the modelled yield slope S (see Section 3.4.2); however, in winter, uncertainty from satellite column calculations become dominant (see Section 3.4.3). Monthly calculated slope uncertainty mostly lies within 30% to 50%, and since output is averaged to form monthly values, the slope uncertainty is not reduced by the averaging. Uncertainty from each OMI satellite measurement is relatively large ($> 100\%$); however, averaging thousands of pixels in each grid square greatly reduces the monthly uncertainty.

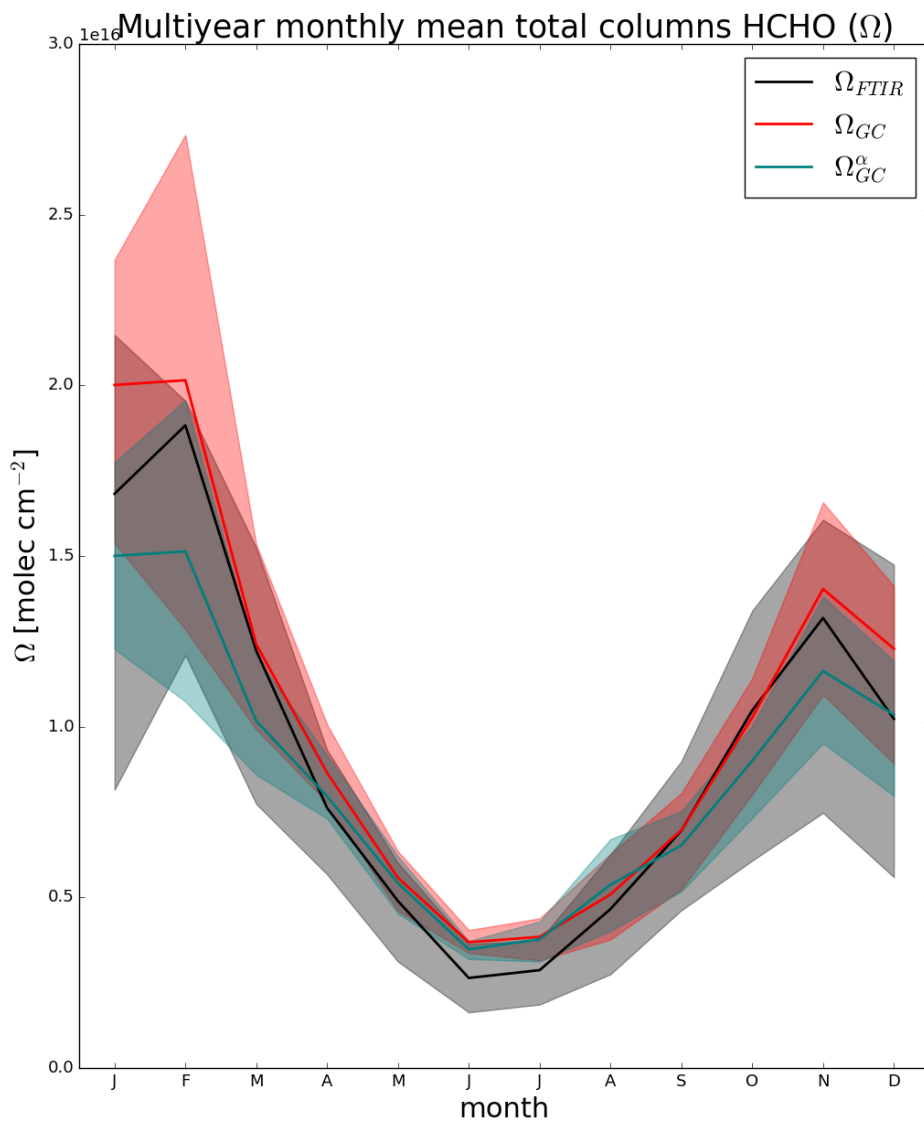


FIGURE 3.26: Multi-year (from all days where both measurements and model data exist) monthly mean total column (Ω) HCHO from the FTIR instrument, and the colocated convolved GEOS-Chem equivalent before (Ω_{GC}) and after (Ω_{GC}^α) scaling isoprene emissions. Shaded areas show inter quartile range.

TABLE 3.5: Relative uncertainty estimates.

Region	Summer			Winter		
	$\frac{\Delta E_{OMI}}{E_{OMI}}$	$\frac{\Delta \Omega_{OMI}}{\Omega_{OMI}}$	$\frac{\Delta S}{S}$	$\frac{\Delta E_{OMI}}{E_{OMI}}$	$\frac{\Delta \Omega_{OMI}}{\Omega_{OMI}}$	$\frac{\Delta S}{S}$
Aus	46%	21%	36%	51%	258%	35%
SE	54%	14%	37%	66%	141%	38%
NE	53%	18%	35%	51%	40%	37%
Mid	45%	38%	38%	47%	41%	35%
SW	43%	27%	32%	61%	96%	36%
N	39%	16%	33%	38%	22%	30%

a: Grid squares with monthly uncertainty over 200% are removed when calculating the mean uncertainty, which has small $< 1\%$ impacts on E_{OMI} overall, but removes many data points in winter.

Uncertainty in satellite HCHO is seasonally dependent, with better signal during the summer. Reliable OMI measurements are less frequent (leading to higher uncertainty) at high solar zenith angles, which worsen with latitudes and during winter. Table 3.5 shows the estimated uncertainty calculated in this work in summer and winter over each region described by Figure 3.10. The assumptions and calculations made to determine uncertainties in the top-down estimate (ΔE_{OMI}), the satellite column ($\Delta \Omega_{OMI}$) and the slope (ΔS) are described in the following subsections.

3.4.1 Top down emissions

Important factors in the calculation of isoprene emissions using OMI HCHO include the modelled relationship between HCHO and isoprene, and satellite HCHO measurements. Uncertainty in each of these terms is quantified before being combined in quadrature to give the uncertainty estimate of the a posteriori. Additional biases may arise due to the filters applied to satellite data and model output, and where possible these are assessed.

The final determination of top-down emissions comes from Equation 3.8, repeated here:

$$E_{OMI} = \frac{\Omega_{OMI} - \Omega_{OMI,0}}{S}$$

Assuming each term is independent, we use the following quadrature rules to estimate random error in E_{OMI} :

$$z = x + y : \Delta z = \sqrt{(\Delta x)^2 + (\Delta y)^2} \quad (3.11)$$

$$z = x/y : \Delta z = z \sqrt{\left(\frac{\Delta x}{x}\right)^2 + \left(\frac{\Delta y}{y}\right)^2} \quad (3.12)$$

Which leads to the uncertainty estimation for our a posteriori emissions as follows

$$\Phi \equiv \Omega_{OMI} - \Omega_{OMI,0}$$

$$\Delta\Phi = \sqrt{(\Delta\Omega_{OMI})^2 + (\Delta\Omega_{OMI,0})^2} \quad (3.13)$$

$$\Delta E_{OMI} = E_{OMI} \times \sqrt{\left(\frac{\Delta\Phi}{\Phi}\right)^2 + \left(\frac{\Delta S}{S}\right)^2} \quad (3.14)$$

ΔE_{OMI} is calculated using the uncertainty in underlying terms: ΔS , $\Delta\Omega_{OMI}$, and $\Delta\Omega_{OMI,0}$. For ΔS ($\Omega_{GC} = S \times E_{GC} + \Omega_{OMI,0}$ from equation 3.7) I use variance in the monthly linear regression of modelled isoprene emissions and column HCHO, shown in Section 3.4.2. For $\Delta\Omega_{OMI}$ and $\Delta\Omega_{OMI,0}$, uncertainty comes from instrument fitting uncertainty, modelled AMF uncertainty, and uncertainty in the background correction terms, which are described and calculated in Section 3.4.3.

Figure 3.27 shows relative uncertainty over each region of Australia in monthly bins. Uncertainty in the southern regions increases between May and July due to increased error in the satellite measurements. Northern regions are impacted less by the seasonal satellite error, which generally is 10 – 20 % lower than the error from S . Figure 3.28 shows the spatial distribution of relative uncertainty in the a posteriori in summer and winter. Here the effects of satellite uncertainty at higher latitudes (especially in winter) can be seen, through the increase in uncertainty with increasing latitude.

3.4.2 Model Uncertainty

E_{OMI} depends partly on the product it is trying to improve, as modelled yield is based on GEOS-Chem run with MEGAN emissions. The uncertainty in the RMA regression slope between model HCHO (Ω_{GC}) and emissions (E_{GC}) is used to estimate ΔS in Equation 3.14. Here I use the ratio of the upper bound of the 95% confidence interval (CI_{UB}) over S to represent the relative uncertainty.

$$\frac{\Delta S}{S} = \frac{CI_{UB}}{S} - 1 \quad (3.15)$$

For example, if the interval upper bound is 30% higher than the slope, relative uncertainty is set to 0.3 (or 30%). The confidence interval for each month is based on the covariance matrix between Ω_{GC} and E_{GC} , and the critical t-statistic considering n to be the days in the month and α to be 0.025.

This is a simple method of approximating the uncertainty of this term, only accounting for monthly uncertainty of the slope calculation. It does not take into account uncertainty in the underlying model, nor uncertainties arising from temporal or spatial resolution, which would be difficult to quantify. Figure 3.29 shows the relative uncertainty in S over Australia and for each region. There is little discernible seasonality to the relative error in S , which generally ranges from 0.3 – 0.4 (30 – 40%). For comparison, Palmer et al. (2006) found $\frac{\Delta S}{S}$ to be 30% after comparing with another chemical transport model and in situ measurements. To improve understanding of uncertainty in S would require further analysis of GEOS-Chem yield over Australia,

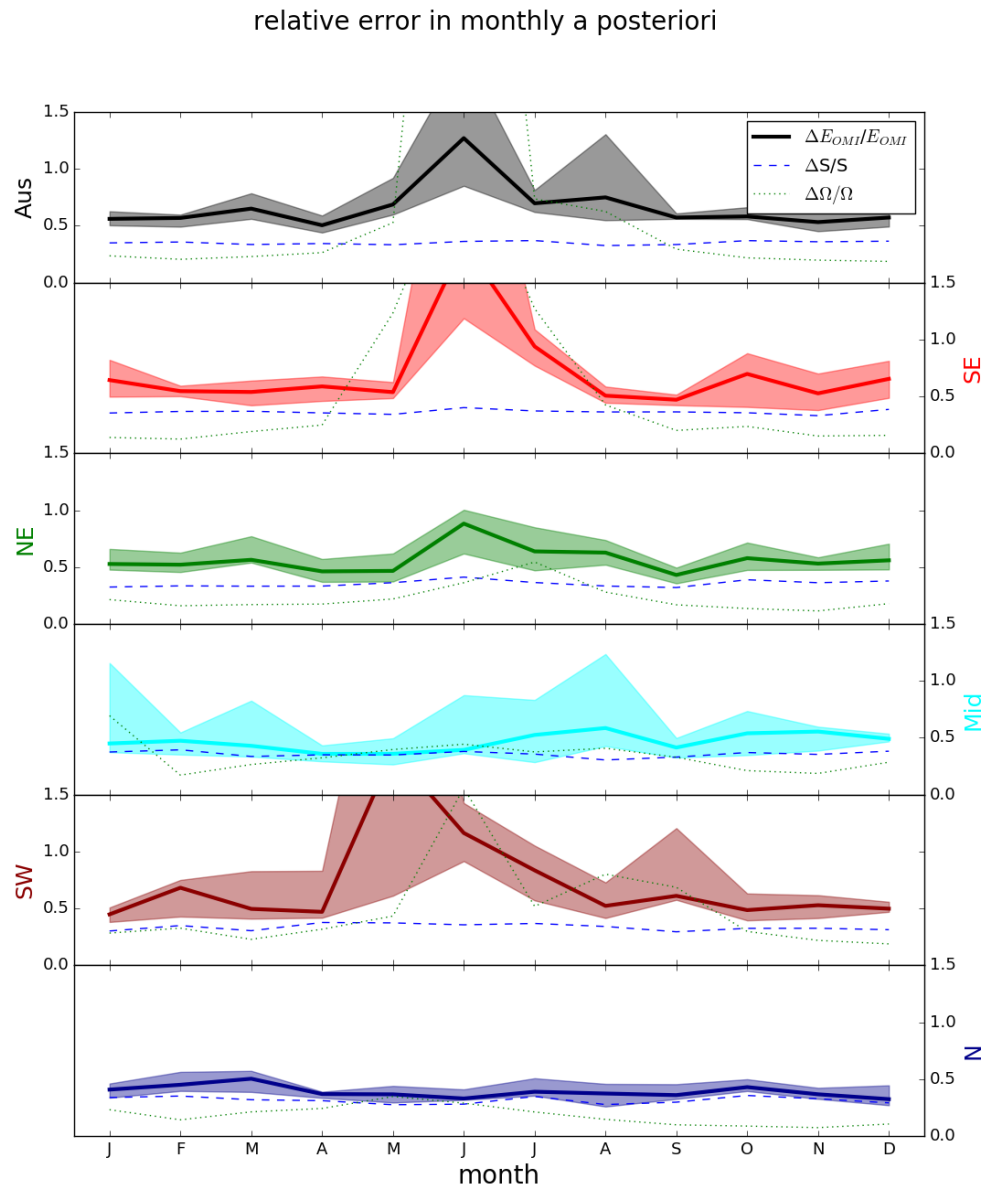


FIGURE 3.27: Median and inter-quartile range of multi-year monthly relative uncertainty in the a posteriori. Median relative uncertainty in S and Ω are added as dashed and dotted lines respectively.

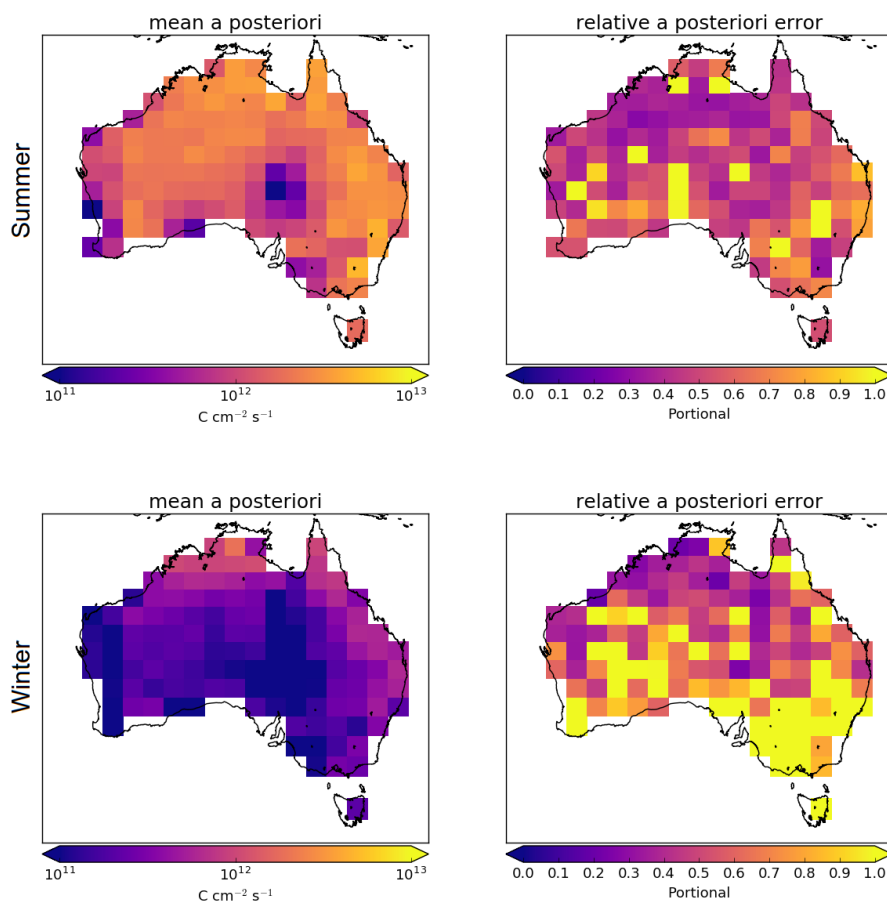


FIGURE 3.28: Summer (DJF, top row) and winter (JJA, bottom row) a posteriori emissions (left column) and relative error (right column).

including how it responds to environmental and meteorological parameters, and how representative this modelled quantity is when compared to measurements.

Filtering for spatial smearing (see Section 3.2.8) reduces the number of data points making up the regression slope S . The process generally improves the linear relationship, which suggests it is working as intended to remove days when local biogenic emissions are not driving HCHO enhancement. Where S regressions have a correlation coefficient (r) of less than 0.4, a multi-year average (or in the worst cases no value at all) is used in lieu of monthly S data. The thresholds for the smearing filter are based on literature values from other countries, which may prove to be unsuitable within Australia. To improve the understanding of smearing in Australia, a better approximation of HCHO lifetimes and yields, and NO_x seasonality and regional concentrations, is required. The filtering process is accounted for in the calculation of ΔS , and the effect is a small reduction of the overall uncertainty from S .

Model biases are not analysed in this thesis, except to note that they would impact both preliminary OMI calculations and the modelled slope. Insufficient independent measurements in Australia make it impossible to quantify uncertainty at a national scale.

3.4.3 Satellite Uncertainty

Corrected vertical columns of HCHO from the OMI product are calculated using Equation 2.28: $\Omega = \frac{SC - RSC}{AMF}$. Error in satellite HCHO columns is determined by error in the three terms SC , RSC , and AMF :

Fitting error from the OMI retrieval

Fitting error represents the uncertainty in the DOAS technique used to estimate HCHO concentrations. Fitting error is provided in the OMHCHO product. This error is ascribed to the SC term.

Provided with the OMI product is the measurement of uncertainty in each pixel, calculated by the Smithsonian Astrophysical Observatory from the back scattered solar radiation fit (Gonzalez Abad et al. 2015; Abad et al. 2016). This is used as the ΔSC in Equation 3.16. The relative fitting error per pixel ($\frac{\Delta SC}{SC}$) ranges from around 20% to 150%, and is higher where low amounts of HCHO are detected, and at higher solar zenith angles (i.e. at high latitudes).

Uncertainty in AMF calculations

Air mass factors model vertical sensitivity to slant path measurements in the satellite instruments, and uncertainties arise predominantly from uncertain cloud parameters (Palmer et al. 2006). Vertical columns from OMI are recalculated using AMFs derived from GEOS-Chem (Section 2.6.3). AMF uncertainty can be determined through comparison of GEOS-Chem output to independently measured HCHO columns. Here we use 30% as a rough estimate of error in this term (Palmer et al. 2006), since measurements over Australia are lacking. For comparison, Wollongong FTIR is over-predicted by GEOS-Chem modelled vertical columns by $\sim 15 - 20\%$. Here the assumed error of 30% is ascribed to the AMF term.

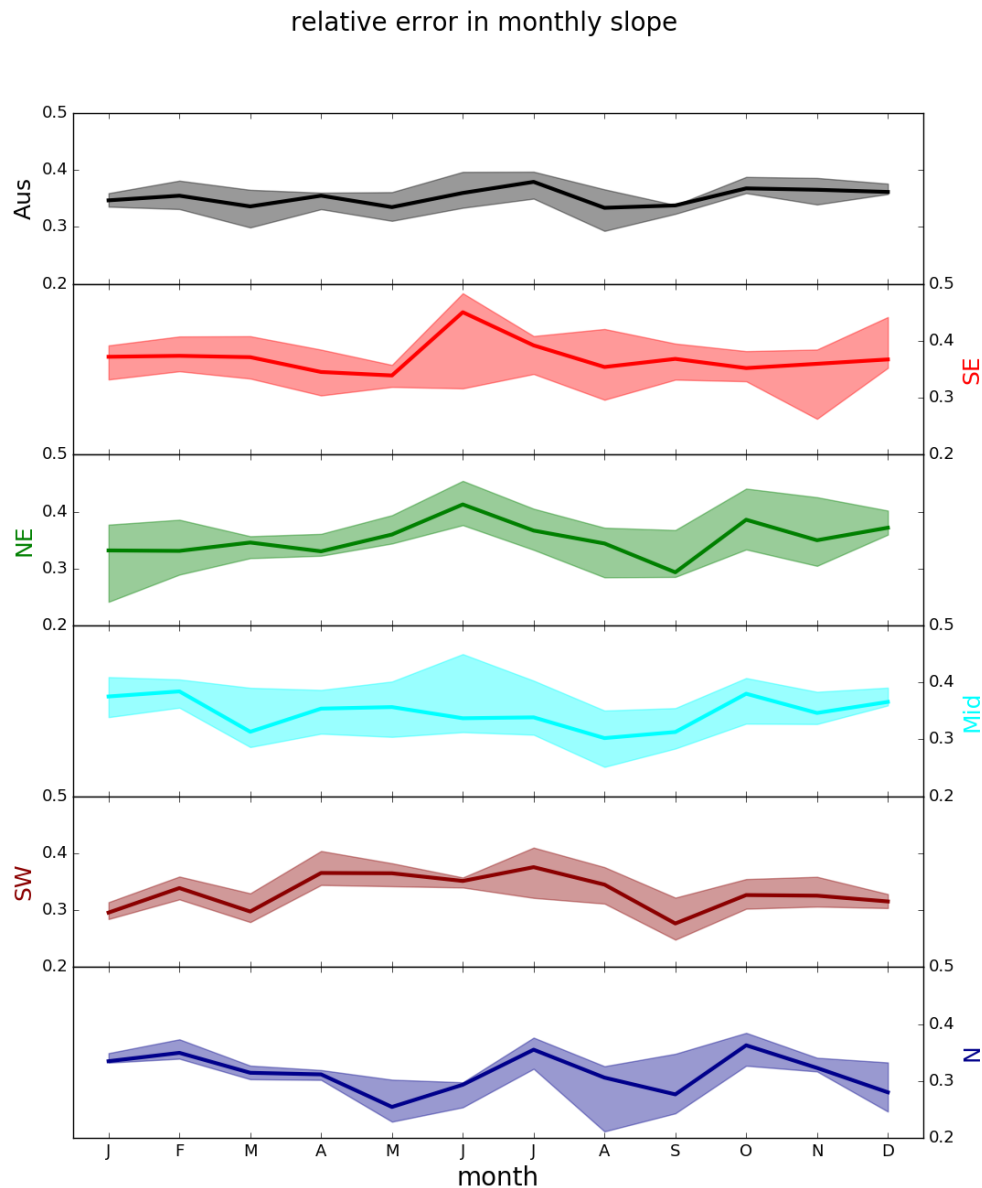


FIGURE 3.29: Median and inter-quartile range of monthly binned uncertainty in S .

Palmer et al. (2006) calculate the error in AMF through combining estimates of error in the UV albedo database ($\sim 8\%$), model error based on in situ measurements, cloud error (20 – 30% (Martin et al. 2003)), and aerosol errors (< 20%), totalling AMF error of around $\sim 30\%$ (calculated in quadrature). Compare this error estimate with that of Curci et al. (2010), where the error in AMF calculations and background columns are respectively found to be 30% and 15% based on their analysis of CHIMERE. Millet et al. (2008) also examine this uncertainty and determine an overall uncertainty (1σ) of 25 – 27% in HCHO vertical columns with calculated AMFs where cloud fraction < 0.2.

Uncertainty of HCHO background

OMI vertical columns are corrected using background (or reference sector) measurements. This is to account for instrument degradation, and adds some uncertainty to the column. In this work vertical columns are corrected using reference sector measurements combined with modelled HCHO, which is described in Chapter 2 (Section 2.6.5). Error from background uncertainty is ascribed to the *RSC* term.

The *RSC*, or background correction, is based on differences in the remote Pacific between daily HCHO slant columns measured by OMI and monthly averages from GEOS-Chem. The correction for each pixel is determined per latitude and OMI track; however, here we use a couple of conservative simplifications to estimate the error in this term. For each SC, the *RSC* is set to the mean correction matching the *SC* latitude over all tracks. For each day, the ΔRSC is set to the standard deviation of the *RSC* over Australian latitudes (45°S to 10°S) in all tracks. These terms are used in Equation 3.16. Background error calculated in this way is on the order of 5%-10% after monthly averaging, however this error increases in the higher southern latitudes during autumn and winter to $\sim 15\%$. For comparison, the background error is assumed to be 15% in Curci et al. (2010) following (Dufour et al. 2008).

These sources of error can be reduced through spatial and temporal averaging, as they are assumed to be unbiased. Uncertainty is reduced by the square root of the number of pixels averaged over each $2^\circ \times 2.5^\circ$ grid square for each day or month. For example, daily averaging reduces pixel uncertainty by a factor of 2-4. Figure 3.30 shows the pixel counts in each region before and after applying filters. Winter has lower pixel count for southern regions, with approximately 50-60% fewer good pixels through May, June, and July. The lowest pixel counts occur in the southeast in winter, likely due to a mix of relatively high solar zenith angles and filtering of anthropogenic emissions. Northern regions have lower pixel counts in the summer, most likely due to increased cloud coverage which limits satellite measurement capabilities as discussed previously.

Calculation of uncertainty in the OMI vertical column HCHO ($\Omega = \frac{SC - RSC}{AMF}$) is performed using quadrature equations 3.11 and 3.12. Error in the slant column (ΔSC) is combined with our assumed relative AMF error ($\frac{\Delta AMF}{AMF}$) of 30%, and background

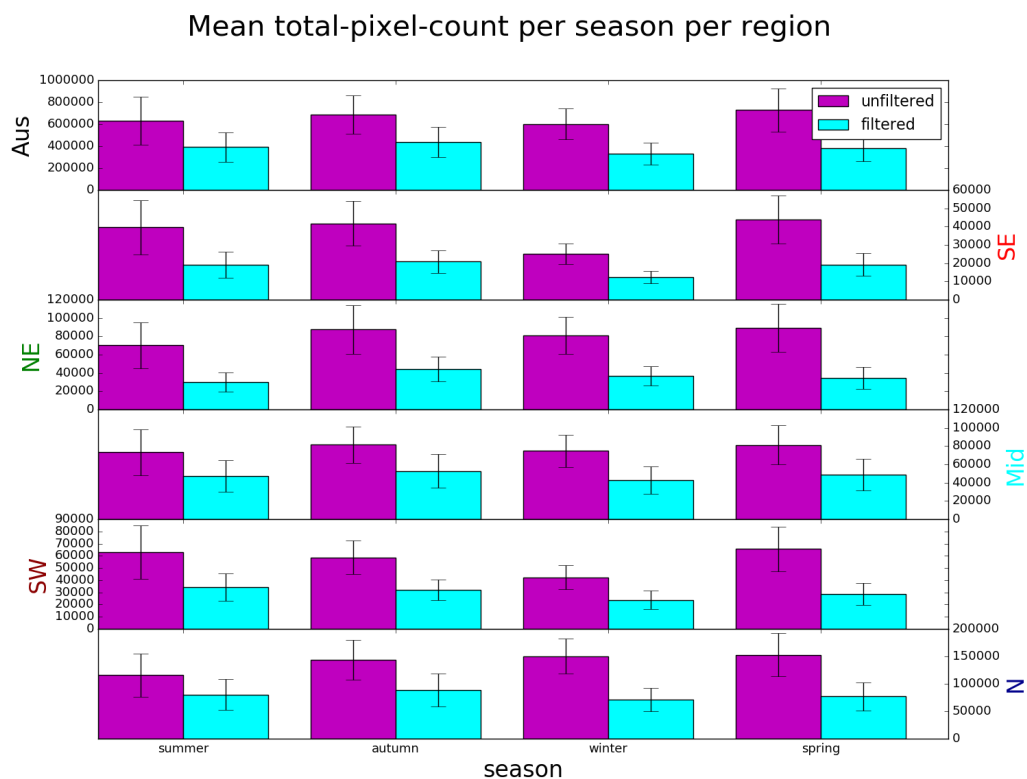


FIGURE 3.30: Mean and standard deviation (vertical error bars) of total pixel counts per region per season, before (magenta) and after (cyan) applying smearing, pyrogenic, and anthropogenic filters.

TABLE 3.6: Uncertainties in satellite total column HCHO.

uncertainty	location	notes
40%	North America	GOME, mostly due to cloud interference ^a
26%	North America	GOME, OMI, with cloud fraction less than 20% ^b
30%-40%	global	GOME-2 ^c
> 60%	Mid-latitude	GOME-2 in winters ^c
1%-10%	Australia	OMI, monthly uncertainty at $2^\circ \times 2.5^\circ$ ^d
50%-100+%	Australia	OMI, in winter at higher latitudes ^d

a: Millet et al. (2006) and Palmer et al. (2006)

b: Millet et al. (2008)

c: De Smedt et al. (2008) and De Smedt et al. (2012)

d: This work

error to calculate $\Delta\Omega_{OMI}$ (and $\Delta\Omega_{OMI,0}$) as follows:

$$\begin{aligned} \Delta(SC - RSC) &= \sqrt{(\Delta SC)^2 + (\Delta RSC)^2} \\ \Delta\Omega &= \Omega \sqrt{\left(\frac{\Delta(SC - RSC)}{(SC - RSC)} \right)^2 + \left(\frac{\Delta AMF}{AMF} \right)^2} \\ \frac{\Delta\Omega}{\Omega} &= \sqrt{\frac{(\Delta SC)^2 + (\Delta RSC)^2}{(SC - RSC)^2} + \left(\frac{\Delta AMF}{AMF} \right)^2} \end{aligned} \quad (3.16)$$

The RSC term is described in Chapter 2 Section 2.6.6 ΔRSC for each latitude is based on the standard deviation of corrections over the remote Pacific. Negative columns can occur where column amounts are lower than RSC , and these are not removed so as not to introduce a bias. When monthly averages are less than zero, relative error is set to 100%. This only impacts the uncertainty calculations in winter for the non-northern regions, where occasional highly negative absolute uncertainty was seen when Ω approached 0.

Figure 3.31 shows the relative uncertainty in monthly satellite columns for each sub-region and all of Australia. Uncertainty in winter at higher latitudes is greatly increased due to lower pixel counts, lower absolute column amounts, and higher fitting error.

Uncertainty in satellite HCHO ($\Delta\Omega$) from literature and calculated here is listed in Table 3.6. De Smedt et al. (2012) found satellite HCHO uncertainty to be 30 – 40% for the GOME-2 instrument by combining slant column systematic and random errors. For mid latitude winters they found an excess of 60% uncertainty. OMI measurements will have similar uncertainty; however, the array of detectors provide more pixels which can be averaged to reduce this uncertainty.

In order to calculate the bias or systematic error, an understanding of biases in the underlying terms is required, since there is little in the way of comparable measurements. OMI has been shown to underestimate observed HCHO by up to $\sim 40\%$. For example OMI underestimated aircraft measurements by 37% in Guyana (Barkley et al. 2013). OMI underestimates range from 20-37% when compared against aircraft

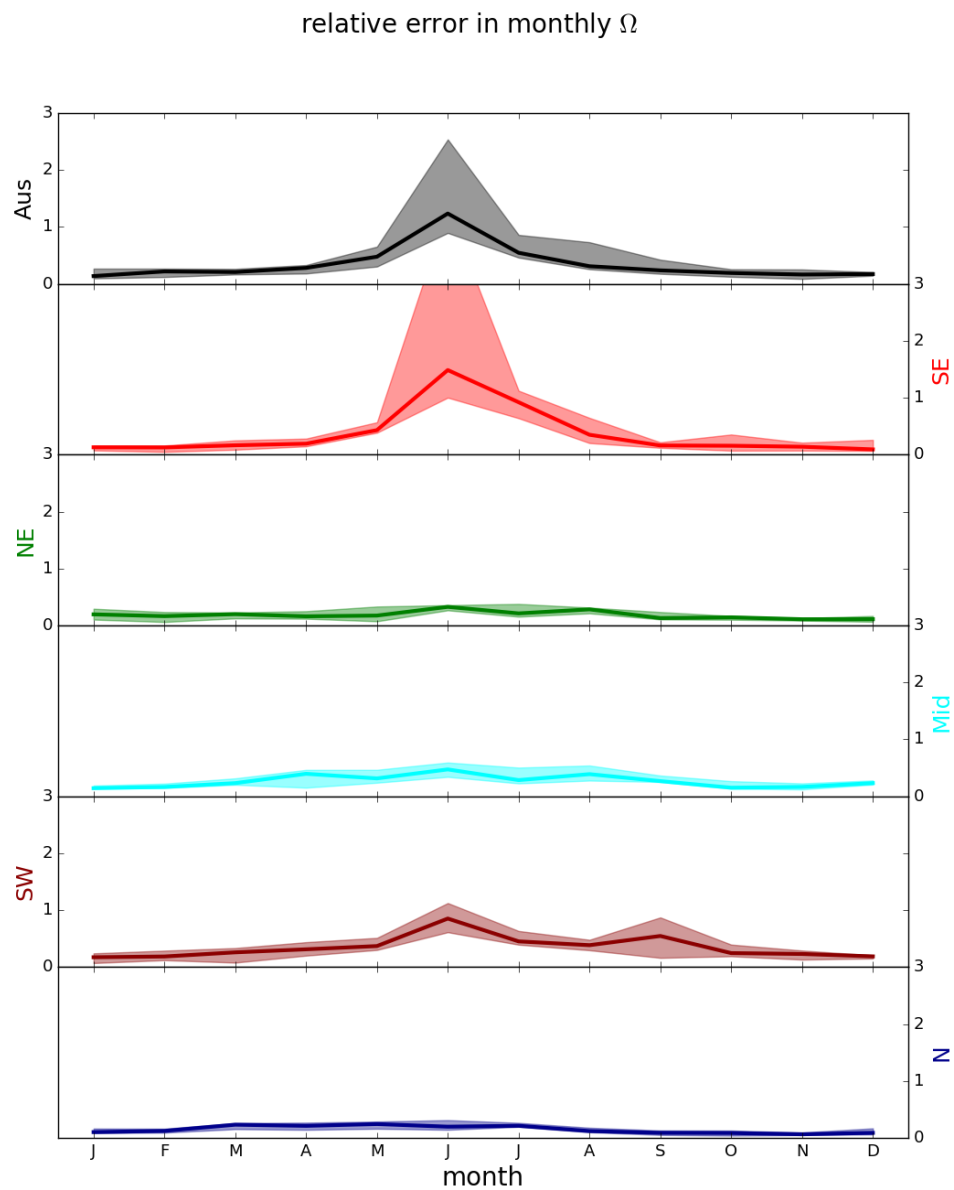


FIGURE 3.31: Median and inter-quartile range for monthly binned relative uncertainty in satellite vertical columns.

data over the southeast United States (Zhu et al. 2016)). OMI validation against 7 sites (the most southern site being Reunion Island at 20.9°S) using MAX-DOAS or FTIR retrievals showed up to 50% underestimation by satellite HCHO retrievals (De Smedt et al. 2015). The highest underestimate occurred during periods of high concentration; however, there was less underestimation when compared with the FTIR instrument which was at the southernmost site (Vigouroux et al. 2009; De Smedt et al. 2015). Satellite HCHO may also suffer from $\sim 13\%$ overestimation when taking monthly averages due to only measuring on relatively cloud-free days (Surl, Palmer, and Abad 2018). Since our *a posteriori* is linearly related to the satellite HCHO, any bias is directly transferred. The conclusion drawn here is that the isoprene emissions product in this work may be affected by satellite HCHO underestimation of up to 40%, and also by monthly HCHO overestimation of 13%, which gives a potential bias of 1/0.6 to 1/1.13. This may be complicated further if the satellite bias over Australia does not match the bias over the remote Pacific at corresponding latitudes. However we can not quantify bias over Australia due to insufficient measurements. GEOS-Chem biases would affect the recalculation of HCHO, but they cannot be quantified and so are not included in this thesis. Lacking suitable measurements to estimate satellite bias over Australia, the potential bias range is applied to the mean emissions in each month when calculating the uncertainty range shown in the results (see Figure 3.12).

3.4.4 Sensitivity to AMF recalculation

This section examines the sensitivity of the top-down isoprene emission estimations (E_{OMI}) to the AMF recalculation method. The *a posteriori* emissions change linearly with recalculated vertical columns, which are calculated in three different ways: using the AMF provided in the OMHCHO product (AMF_{OMI}), recalculating AMF shape factors but keeping the original scattering weights (AMF_{GC}), or recalculating both shape factors and scattering weights (AMF_{PP}).

Figure 3.32 shows AMFs and emissions recalculated differently over 2005. This figure only depicts grid squares with non-zero emissions, since we are interested in regions where emissions are stronger. The fully recalculated AMF_{PP} is higher in summer, but lower in other seasons compared against the other recalculations. The direct affect of a lower AMF is an increased vertical column, which should lead to higher emission estimates, and vice versa. This can be seen in all seasons except for summer, although even here the emissions estimates are higher than if they are calculated using the original AMF_{OMI} . Emission estimates vary widely over Australia, but the sensitivity to AMF recalculation technique is proportional and potentially non-linear. Changes in AMF of 5 – 30% cause changes in emission estimates of 5 – 50%. Further analysis is warranted and may be a focus in future work.

3.4.5 Sensitivity to filtering

Figure 3.33 shows emissions estimates with and without filtering for smearing, anthropogenic, and pyrogenic influences. The overall effect of filtering is to slightly raise emissions in all non-summer months, with relatively little change to the mean in winter months. This is true in all regions except for northern Australia, which shows a slight decrease in summer. Eastern regions are most frequently filtered, with more

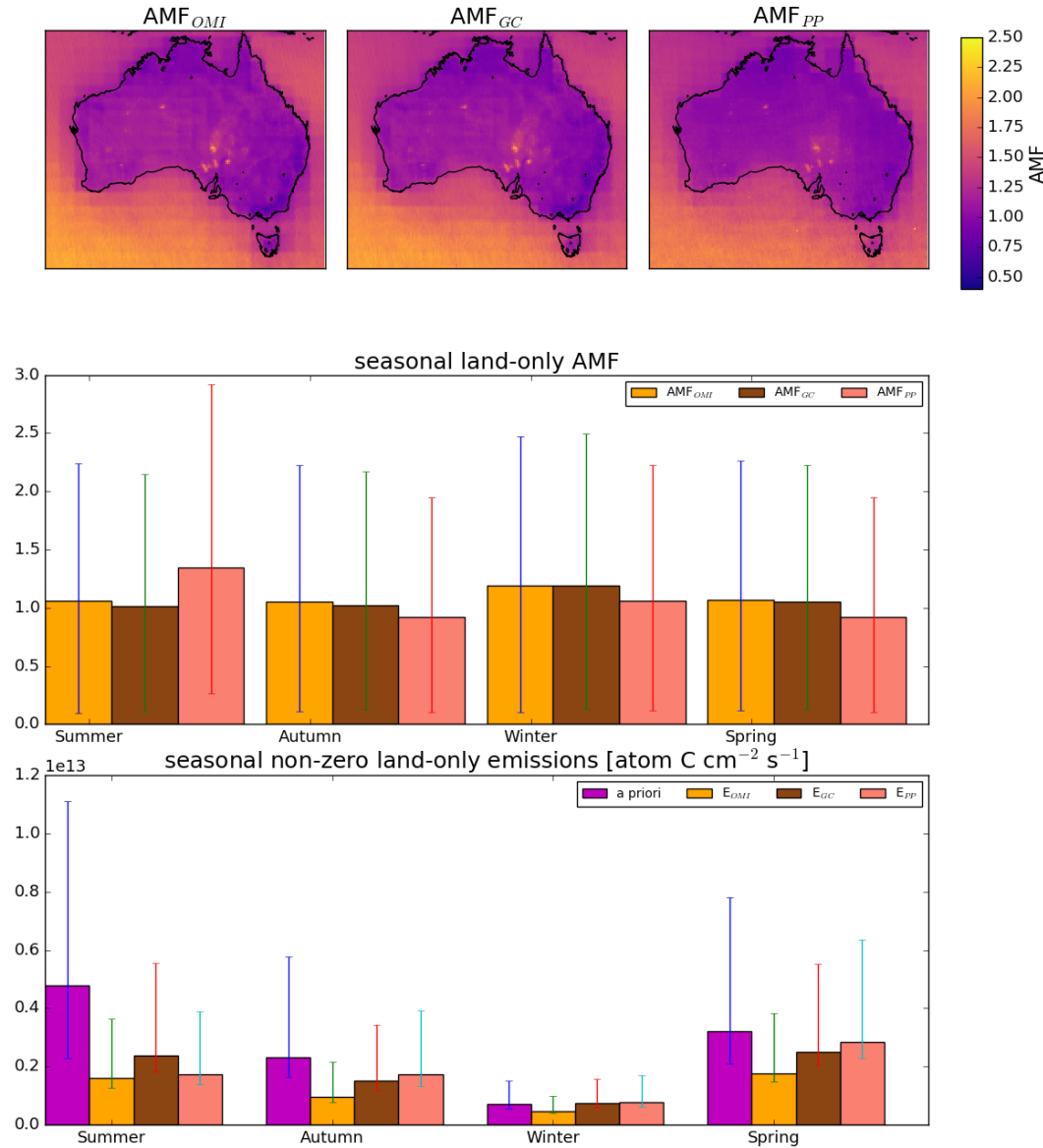


FIGURE 3.32: Top row: averaged OMI Satellite AMF for 2005, from the OMHCCHO data set (left, AMF_{OMI}), recalculated using GEOS-Chem shape factors (middle, AMF_{GC}), and recalculated using GEOS-Chem shape factors and scattering weights (right, AMF_{PP}). Middle row: mean and inter-quartile range over 2005 for each season. Bottom row: mean and inter-quartile range of non-zero emissions based on the three recalculations (with matching subscripts) next to the a priori emissions from GEOS-Chem.

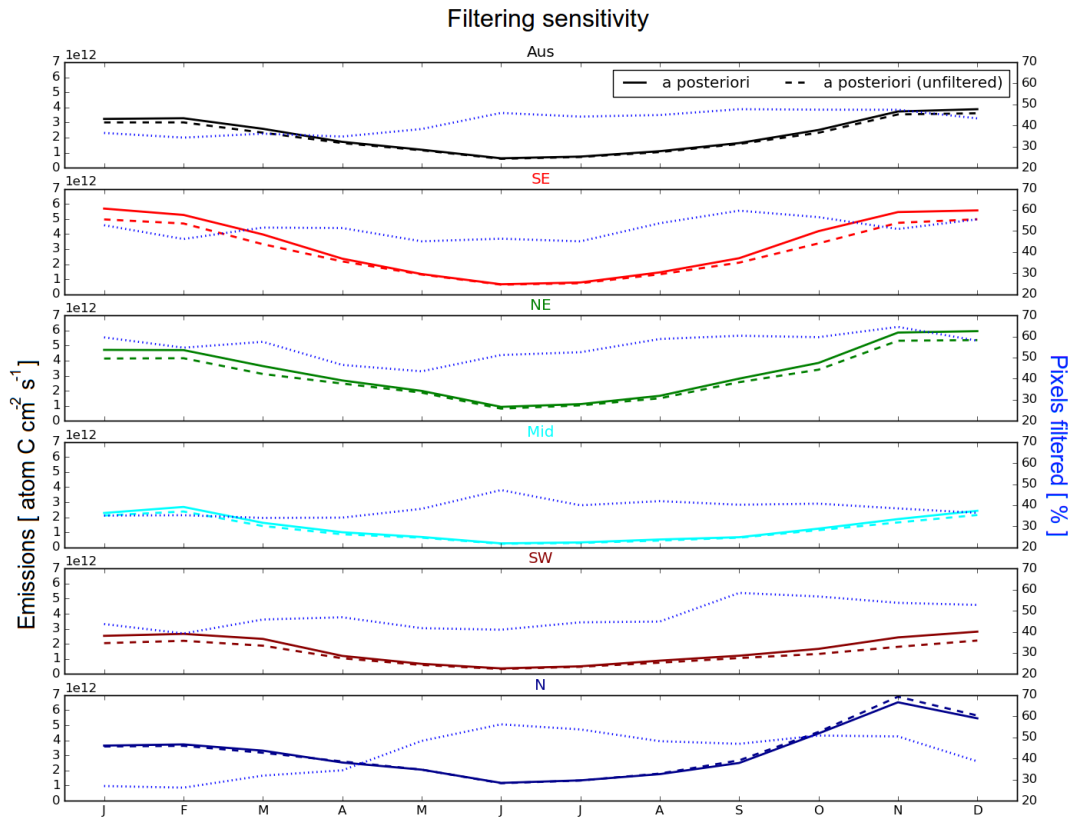


FIGURE 3.33: Multi-year monthly mean values for a posteriori emission estimates calculated with (solid) and without (dashed) applying filters for anthropogenic, pyrogenic, and smearing influences. The portion of pixels within each region which are filtered is shown on the right axis with a blue dotted line.

than 50% of the available good pixels filtered throughout the year, while other regions vary between 20% and 60% with lower filtering rates in summer months.

Each row shows a regionally averaged time series for emissions with (solid) and without (dashed) applying the anthropogenic and pyrogenic filters. Portion of good pixels filtered is also shown (dotted, grey) using the right axis.

3.5 Conclusions and implications

Very few ground based measurements of BVOC concentrations are available in Australia. Emissions from models use largely unverified extrapolations for emission factors and parameterisations in Australia, leading to overestimated isoprene emissions (Emmerson et al. 2016). This leads to uncertainty and error when modelling atmospheric ozone and other trace gases.

In this chapter I created and tested an isoprene emissions estimate (a posteriori)

based on OMI satellite measurements of HCHO, a high-yield product of isoprene oxidation. The a posteriori emissions' effects on ozone and HCHO were tested by running GEOS-Chem with a seasonal (multi-year monthly averaged) gridded ($2^\circ \times 2.5^\circ$) scaling factor calculated from the a posteriori applied to the a priori emissions. Uncertainty in the primary components of the top-down emissions calculation were calculated where possible and potential biases identified.

The a posteriori isoprene emission estimate showed that GEOS-Chem coupled with the MEGAN emissions model overestimates emissions in summer by a factor of 2-5. Total yearly Australian emissions are reduced from 39 Tg yr^{-1} to 21 Tg yr^{-1} (decrease of $\sim 46\%$) in the a posteriori. The overestimate is spatially and temporally diverse and leads to model overestimates of HCHO, which affects ozone levels. Running GEOS-Chem using scaled emissions based on OMI HCHO columns reduced the model HCHO overestimate (when compared to OMI HCHO) in summer by half, from $\sim 100\%$ down to $\sim 50\%$, with most of the difference occurring outside the northern region. Model vertical column HCHO variance is somewhat ($\sim 10\% - 50\%$) lower than that seen by the OMI satellite, and this difference increased after scaling isoprene emissions. Scaling GEOS-Chem emissions also lowered simulated surface ozone concentrations by $\sim 5\%$. A posteriori uncertainty was shown to be on the order of 50% (monthly, per grid square), with large satellite-based uncertainty in winter and a potential bias coming from satellite data of -13% to 40% . The primary uncertainty in the a posteriori emissions comes from the monthly modelled isoprene-to-HCHO yield ($\sim 30\% - 50\%$ uncertainty), although at higher latitudes in winter the satellite uncertainty becomes restrictively high ($> 100\%$).

The reason for the a priori overestimate remains unclear, and both global and Australian emissions estimates for isoprene range widely. It is in part due to the MEGAN emission model's parameterisation of how isoprene responds to parameters such as leaf area indices, plant functional type emission factors, and meteorological factors. In Australia, a mixture of poorly defined emission factors (e.g., Emmerson et al. 2016), unaccounted for soil moisture (e.g., Sindelarova et al. 2014; Emmerson et al. 2019) and poorly understood forest responses to meteorological stresses likely drive uncertainty and model biases (Jiang et al. 2018; Emmerson et al. 2019). A potential improvement to the MEGAN soil parameterisation has been described (Jiang et al. 2018); however, a detailed map of soil properties is not readily available in Australia, and this would be required to apply the parameterisation here. Alternatively soil moisture and the parameterisation of drought processes which affect isoprene emissions could be implemented within GEOS-Chem similar to how it was recently applied to a different CTM in Emmerson et al. (2019).

In the US, bias between OMI and in-situ measurements is as high as 40%, but bias across Australia cannot be determined as there are not enough independent observations. This leads to a wide range for potential emissions (see Figure 3.12) and limits potential top-down refinements to isoprene emissions. Ground-based and aircraft VOC, NO_x , HCHO, and ozone measurements over large areas at relatively fine temporal resolution would help quantify unknown satellite biases while additionally providing constraints for bottom-up models. In the northern region in particular, emissions are affected by monsoonal forcing, but increased cloud coverage during the monsoon

limits satellite coverage. This makes characterisation of forest emissions and their response to sunlight, temperature, and moisture even more important in these areas. In addition to measurements, further analysis determining the sensitivity of modelled emissions to model resolution and changing soil moisture parameters (and parameterisations) would provide the foundation to improve GEOS-Chem and MEGAN modelled emissions along with products like HCHO and ozone.

In the future, other satellites (e.g., GOME-2) could be used to improve emission estimates further, with differing overpass times potentially allowing a measure of diurnal emission patterns. Additionally, an adjoint version of GEOS-Chem could provide details of isoprene transport and ozone production sources. This version of GEOS-Chem could also provide an evaluation of how resolution-limited the linear top-down emission estimates are over Australia. The emission estimate created in this chapter could be refined to higher temporal resolution, with further analysis of uncertainty. Oversampling techniques could be applied near populated areas in order to improve the understanding of isoprene, HCHO, and ozone relationships over cities (e.g., Surl, Palmer, and Abad 2018). Furthermore, publishing the updated underlying emission factors for Australia and implementing the changes in GEOS-Chem would improve the understanding of the natural atmosphere over this relatively remote portion of the planet.

Chapter 4

Stratospheric ozone intrusions

4.1 Foreword

This chapter is unchanged (excepting titles, labels, and numbering) from a paper on which I was the first author, published in the journal of Atmospheric Chemistry and Physics journal: Jesse W Greenslade et al. (2017). “Stratospheric ozone intrusion events and their impacts on tropospheric ozone in the Southern Hemisphere”. In: *Atmospheric Chemistry and Physics*, pp. 1–33. URL: <https://www.atmos-chem-phys.net/17/10269/2017/acp-17-10269-2017.pdf>.

4.2 Introduction

Tropospheric ozone constitutes only 10% of the total ozone column but is an important oxidant and greenhouse gas which is toxic to life, harming natural ecosystems and reducing agricultural productivity. Over the industrial period, increasing tropospheric ozone has been estimated to exert a radiative forcing (RF) of 365 mWm^{-2} (Stevenson et al. 2013), equivalent to a quarter of the CO₂ forcing (Forster et al. 2007). While much tropospheric ozone is produced photochemically from anthropogenic and natural precursors, downward transport from the ozone-rich stratosphere provides an additional natural source of ozone that is particularly important in the upper troposphere (Jacobson and Hansson 2000, and references therein). The contribution of this source to overall tropospheric ozone budgets remains uncertain (Škerlav, Sprenger, and Wernli 2014), especially in the southern hemisphere (SH). Models show that stratospheric ozone depletion has propagated to the upper troposphere (Stevenson et al. 2013). However, work based on the Southern Hemisphere Additional OZonesonde (SHADOZ) network suggests stratospheric mixing may be increasing upper tropospheric ozone near southern Africa (Liu et al. 2015; Thompson et al. 2014). Uncertainties in the various processes which produce tropospheric ozone limit predictions of future ozone-induced radiative forcing. Here we use a multi-year record of ozonesonde observations from sites in the southern hemisphere extra-tropics, combined with a global model, to better characterise the impact of stratospheric ozone on the tropospheric ozone budget in the southern hemisphere.

Stratosphere-to-troposphere transport (STT) primarily impacts the ozone budget in the upper troposphere but can also increase regional surface ozone levels above the legal thresholds set by air quality standards (Danielsen 1968; Lelieveld et al. 2009;

Lefohn et al. 2011; Langford et al. 2012; Zhang et al. 2014; Lin et al. 2015). In the western US, for example, deep STT events during spring can add 20-40 ppbv of ozone to the ground-level ozone concentration, which can provide over half the ozone needed to exceed the standard set by the U.S. Environmental Protection Agency (Lin et al. 2012; Lin et al. 2015). Another hotspot for STT is the Middle East, where surface ozone exceeds values of 80 ppbv in summer, with a stratospheric contribution of 10 ppb (Lelieveld et al. 2009). Estimates of the overall contribution of STT to tropospheric ozone vary widely (e.g. Galani 2003; Stohl et al. 2003; Stevenson et al. 2006; Lefohn et al. 2011). Early work based on two photochemical models showed that 25-50% of the tropospheric ozone column can be attributed to STT events globally, with most contribution in the upper troposphere (Stohl et al. 2003). In contrast, a more recent analysis of the Atmospheric Chemistry and Climate Model Inter-comparison Project (ACCMIP) simulations by Young et al. (2013) found that STT is responsible for $540 \pm 140 \text{ Tg yr}^{-1}$, equivalent to $\sim 11\%$ of the tropospheric ozone column, with the remainder produced photochemically (Monks et al. 2015). This wide range in model estimates exists in part because STT is challenging to accurately represent, and finer model resolution is necessary to simulate small scale turbulence. Observation-based process studies are therefore key in determining the relative frequency of STT events, with models then able to quantify STT impact over large regions. Ozonesondes are particularly valuable for this purpose as they provide multi-year datasets with high vertical resolution.

Lower stratospheric and upper tropospheric ozone concentrations are highly correlated, suggesting mixing across the tropopause mainly associated with the jet streams over the Atlantic and Pacific oceans (Terao et al. 2008). Extra-tropical STT events most commonly occur during synoptic-scale tropopause folds (Sprenger, Croci Maspoli, and Wernli 2003; Tang and Prather 2012; Frey et al. 2015) and are characterised by tongues of high potential vorticity (PV) air descending to lower altitudes. As these tongues become elongated, filaments disperse away from the tongue and mix irreversibly into the troposphere. STT can also be induced by deep overshooting convection (Frey et al. 2015), tropical cyclones (Das et al. 2016) and mid-latitude synoptic scale disturbances (e.g. Stohl et al. 2003; Mihalikova et al. 2012). STT events have been observed in tropopause folds around both the polar front jet (Vaughan, Price, and Howells 1993; Beekmann et al. 1997) and the subtropical jet (Baray et al. 2000). The summertime pool of high tropospheric ozone over the eastern Mediterranean (EM) is mainly attributed to the downward ozone transport, as a result of the enhanced subsidence (Zanis et al. 2014) and the tropopause fold activity (Akritidis et al. 2016) over the region. The EM exhibits a summer maximum of subsidence, which sits between 20°E and 35°E and 31°N to 39°N , while zonally most subtropical tropopause folds occur during winter (Tyrlis et al. 2014, and references therein). They are also observed near cut-off lows (Price and Vaughan 1993; Wirth 1995), so both regional weather patterns and stratospheric mixing are important to understand for STT analysis.

Stratospheric ozone intrusions undergo transport and mixing, with up to half of the ozone diffusing within 12 hours following descent from the upper troposphere (Trickl et al. 2014). The long range transport of enhanced ozone can be facilitated by upper tropospheric winds, with remarkably little convective mixing, as shown by

Trickl et al. (2014) who measure STT air masses two days and thousands of kilometres from their source. Cooper et al. (2004) shows how STT advection can transport stratospheric air over long distances, with a modelled STT event spreading from the northern Pacific to the East coast of the USA over a few days.

The strength (ozone enhancement above background levels), horizontal scale, vertical depth, and longevity of these intruding ozone tongues vary with wind direction and strength, topography, and season. While the frequency, seasonality, and impacts of STT events have been well described in the tropics and northern hemisphere (NH), observational estimates from the SH extra-tropics are noticeably absent in the literature. The role of STT in the SH remains highly uncertain due to the more limited data availability compared to the NH and the temporal sparsity of these datasets (Mze et al. 2010; Thompson et al. 2014; Liu et al. 2015).

Here, we characterise the seasonal cycle of STT events and quantify their contribution to the SH extra-tropical tropospheric ozone budget using nearly a decade of ozonesonde observations from three locations around the Southern Ocean spanning latitudes from 38°S–69°S. In Section 4.3 we describe the observations and methods used to identify STT events and to relate STT occurrence to meteorological events. We show how possible biomass burning smoke plume influence is detected and handled, and we introduce the GEOS-Chem model which is used for ozone flux estimation. Within Section 4.4 we show the seasonality, altitude, depth, and frequency of detected STT events, along with a comparison of our findings to other literature where possible. In Section 4.5 we analyse how well GEOS-Chem captures the tropospheric ozone seasonality and quantity near our three sites. In Section 4.6 an extrapolation of the STT detection frequencies along with GEOS-Chem monthly tropospheric ozone columns is used to estimate STT ozone flux near our three sites. We also compare and contrast our results against relevant literature. Finally, in Section 4.7 we examine in detail the uncertainties involved in our STT event detection technique and ozone flux estimations.

4.3 Data and Methods

4.3.1 Ozonesonde record in the Southern Ocean

Ozonesondes provide a high vertical resolution profile of ozone, temperature, pressure, and humidity from the surface and up to 35 km. In the troposphere, the ozonesondes generally perform 150–300 measurements. Ozone mixing ratio is quantified with an electrochemical concentration cell, using standardised procedures when constructing, transporting, and releasing the ozonesondes (<http://www.ndsc.ncep.noaa.gov/organize/protocols/appendix5/>). Ozonesondes are estimated to provide around 2% precision in the stratosphere, which improves at lower altitudes, and ozonesondes have been shown to be accurate to within 5% when the correct procedures are followed (Smit et al. 2007).

Ozonesondes are launched approximately weekly from Melbourne (38° S, 145° E), Macquarie Island (55° S, 159° E) and Davis (69° S, 78° E), as shown in Fig. 4.1. Melbourne is a major city in the south east of Australia, and may be affected by anthropogenic pollution in the lower troposphere. Macquarie Island is isolated from

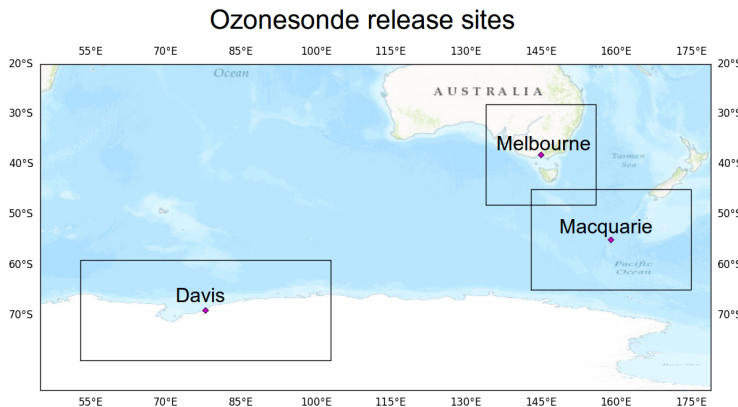


FIGURE 4.1: Ozonesonde release sites and the regions used to examine STT effect on tropospheric ozone levels.

TABLE 4.1: Number of sonde releases at each site over the period of analysis.

Site	Total Releases	Monthly Releases (J, F, M, ...)	Date Range
Davis	240	11, 12, 13, 12, 17, 31, 29, 28, 32, 28, 15, 12	2006/04/13 - 2013/11/13
Macquarie Island	390	32, 31, 45, 28, 34, 33, 28, 35, 29, 33, 31, 31	2004/01/20 - 2013/01/09
Melbourne	456	31, 38, 40, 38, 41, 36, 38, 39, 46, 40, 38, 31	2004/01/08 - 2013/12/18

the Australian mainland, situated in the remote Southern Ocean and unlikely to be affected by any local pollution events. Davis is on the coast of Antarctica and also unlikely to experience the effects of anthropogenic pollution.

For this study, we use the 2004-2013 data for Melbourne and Macquarie Island and the 2006-2013 data for Davis because both ozone and geopotential height (GPH) are available from the World Ozone and Ultraviolet Data Centre archived data in these periods. At Davis, ozonesondes are launched twice as frequently during the ozone hole season and preceding months (June-October) as at other times of year (Alexander et al. 2013). A summary of ozonesonde releases at each site can be seen in Table 4.1.

Characterisation of STT events requires a clear definition of the tropopause. Two common tropopause height definitions are the standard lapse rate tropopause (WMO 1957) and the ozone tropopause (Bethan, Vaughan, and Reid 1996). The lapse rate tropopause is defined as the lowest altitude where the lapse rate (vertical gradient of temperature) is less than $2^{\circ}\text{C km}^{-1}$, provided the lapse rate averaged between this altitude and 2 km above is also below $2^{\circ}\text{C km}^{-1}$. The ozone tropopause is defined as the lowest altitude satisfying the following three conditions for the ozone mixing ratio (OMR) (Bethan, Vaughan, and Reid 1996):

1. Vertical gradient of OMR is greater than 60 ppb km^{-1} ;
2. OMR is greater than 80 ppb ; and

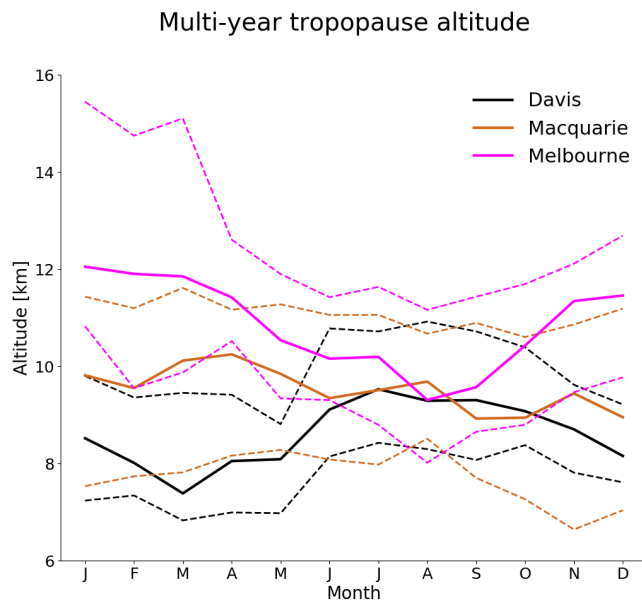


FIGURE 4.2: Multi-year monthly median tropopause altitude (using the ozone defined tropopause) determined from ozonesondes measurements at Davis (2006-2013), Macquarie Island (2004-2013), and Melbourne (2004-2013) (solid lines). Dashed lines show the 10th to the 90th percentile of tropopause altitude for each site.

3. OMR exceeds 110 ppb between 500 m and 2000 m above the altitude under inspection (modified to between 500 m and 1500 m in the Antarctic, including the site at Davis).

The ozone tropopause may misdiagnose the real tropopause altitude during stratosphere-troposphere exchange; however, it is useful at polar latitudes in winter, where the lapse-rate definition may result in artificially high values for tropopause height (Bethan, Vaughan, and Reid 1996; Tomikawa, Nishimura, and Yamanouchi 2009; Alexander et al. 2013). We require lapse rate defined tropopauses to be at a minimum of 4 km altitude. Another commonly used tropopause definition is determined with the use of PV (dynamical tropopause). In the extra-tropics the isosurface where $PV = 2 \text{ PVU}$ ($1 \text{ PVU} = 10^{-6} \text{ m}^2 \text{ s}^{-1} \text{ K kg}^{-1}$) is often used to define the tropopause, allowing the 3D representation of tropopause folds and other tropopause features in a sufficiently resolved model (Škerlak, Sprenger, and Wernli 2014; Tyrlis et al. 2014). The PV is not calculable using the ozonesonde measurements alone, so in this work the ozone tropopause is used when determining STT events or measured tropopause altitude.

Figure 4.2 shows the monthly median ozone tropopause altitudes at each location (solid lines). At Melbourne, the tropopause altitude displays a seasonal cycle with maximum in summer and minimum in winter. This seasonality is missing at Macquarie Island and almost reversed at Davis, which has a minimum during autumn and maximum from winter to spring. Tropopause altitude decreases with latitude from 9-14 km at Melbourne (38° S) to 7-9 km at Davis (69° S).

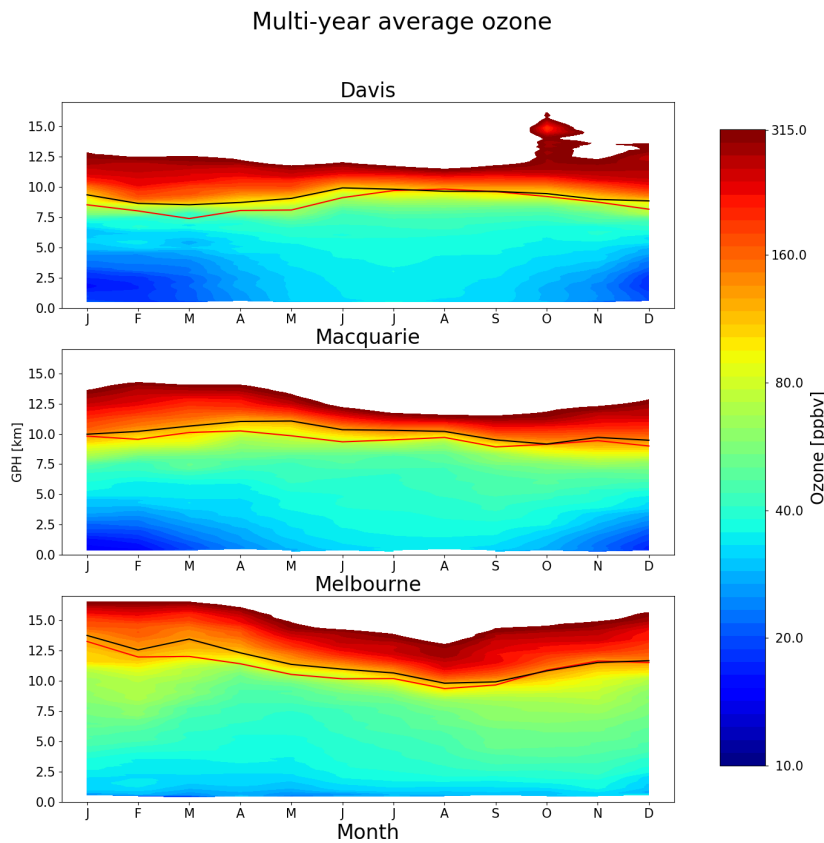


FIGURE 4.3: Multi-year mean seasonal cycle of ozone mixing ratio over Davis, Macquarie Island, and Melbourne as measured by ozonesondes. Measurements were interpolated to every 100 m and then binned monthly. Black and red solid lines show median ozone and lapse-rate defined tropopause altitudes (respectively), as defined in the text.

Figure 4.3 shows multi-year averaged ozone mixing ratios measured by ozonesonde over the three stations. Over Melbourne, increased ozone extending down through the troposphere is apparent from December to March and from September to November. The increased tropospheric ozone in these months is due to STT (in summer), and possible biomass burning influence (in spring), both discussed in more detail in the following sections. Over Davis and Macquarie Island, tropospheric ozone is higher between March and October, although the seasonal differences are small compared to those at Melbourne. The seasonality shown in Fig. 4.3 for Davis is consistent with remote free tropospheric photochemistry determined by solar radiation availability and temperature, resulting in higher ozone in winter (Lelieveld and Dentener 2000). NO₂ stratospheric observations have been conducted in the Southern hemisphere at Lauder, Macquarie Island and Arrival Heights (i.e. Struthers et al. 2004) which displays a winter minima in seasonality consistent with an ozone maxima. Influence from the ozone hole can be seen over Davis in October, with relatively low ozone levels extending up 5-6 km into the stratosphere.

4.3.2 Model description

To provide regional and global context to the ozonesonde observations, we use the GEOS-Chem version 10-01 global chemical transport model (Bey et al. 2001), which simulates ozone along with more than 100 other trace gases throughout the troposphere and stratosphere. Stratosphere-troposphere coupling is calculated using the stratospheric unified chemistry extension (UCX) (Eastham, Weisenstein, and Barrett 2014). Transport is driven by assimilated meteorological fields from the Goddard Earth Observing System (GEOS-5) maintained by the Global Modeling and Assimilation Office (GMAO) at NASA. Ozone precursor emissions are from the Model of Emissions of Gases and Aerosols from Nature (MEGAN) version 2.1 (Guenther et al. 2012) for biogenic emissions, the Emissions Database for Global Atmospheric Research (EDGAR) version 4.2 for anthropogenic emissions, and the Global Fire Emissions Database (GFED4) inventory (Giglio, Randerson, and Van Der Werf 2013) for biomass burning emissions. Our simulation was modified from the standard v10-01 to fix an error in the treatment of ozone data from the Total Ozone Mapping Spectrometer (TOMS) satellite used to calculate photolysis (see http://wiki.seas.harvard.edu/geos-chem/index.php/FAST-JX_v7.0_photolysis_mechanism#Fix_for_TOMS_to_address_strange_cycle_in_OH_output.).

Our simulations span 2005-2012 (following a 1-year spin-up) with horizontal resolution of 2° latitude by 2.5° longitude and 72 vertical levels from the surface to 0.01 hPa. The vertical resolution is finer near the surface at ~ 60 m between levels, spreading out to ~ 500 m near 10 km altitude. For comparison to the ozonesonde observations, the model state was saved every 6 hours within the grid boxes containing each site. When comparing against ozonesondes, GEOS-Chem UTC+0 time samples are used for all sites. This means that the simulated ozone profiles are analysed at local times of 7AM for Davis, and 11AM for Macquarie Island and Melbourne. GEOS-Chem uses the tropopause height provided by GEOS-5 meteorological fields, which are calculated using a lapse-rate tropopause definition using the first minimum above the surface in the function $0.03 \times T(p) - \log(p)$, with p in hPa (Rienecker 2007).

4.3.3 Characterisation of STT events and associated fluxes

We characterise STT events using the ozonesonde vertical profiles to identify tropospheric ozone enhancements above a local background (in moles per billion moles of dry air, referred to here as ppb). The process is illustrated in Figure 4.4 on an example ozone profile. First, the ozone vertical profiles are linearly interpolated to a regular grid with 20 m resolution from the surface to 14 km altitude. Small vertical-scale fluctuations in ozone, which are captured by the high-resolution ozonesondes, can be regarded as sinusoidal waves superimposed on the large vertical scale background tropospheric ozone. As such, the interpolated profiles are bandpass-filtered using a fast Fourier transform (Press et al. 1992) to retain these small vertical scales, between 0.5 km and 5 km (removing low and high frequency perturbations). The high frequency perturbations are removed as they may represent noise in the measurements. The perturbations with scales longer than 5 km represent the vertical gradient of ozone concentration from the surface to the stratosphere. In what follows, these filtered vertical profiles are referred to as perturbation profiles.

Ozone at Melbourne on 2004/01/08

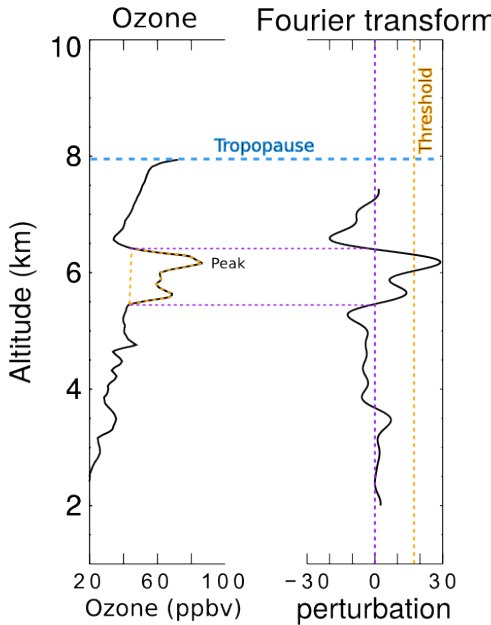


FIGURE 4.4: An example of the STT identification and flux estimation methods used in this work. The left panel shows an ozone profile from Melbourne on 8 January 2004 from 2 km to the tropopause (blue dashed horizontal line). The right panel shows the perturbation profile created from bandpass filtering of the mixing ratio profile. The STT occurrence threshold calculated from the 95th percentile of all perturbation profiles is shown as the orange dashed line, and the vertical extent of the event is shown with the purple dashed lines (see details in text). The ozone flux associated with the STT event is calculated using the area outlined with the orange dashed line in the left panel.

For an event to qualify as STT, a clear increase above the background ozone level is needed, as a bandpass filter leaves us with enhancements minus any noise or seasonal scale vertical profile effects. We next use all the perturbation profiles at each site to calculate the 95th percentile perturbation value for the site. The threshold is calculated from all the interpolated filtered values between 2 km above the surface and 1 km below the tropopause. This is our threshold for tropospheric ozone perturbations, and any profiles with perturbations exceeding this value in individual ozonesondes are classified as STT events. STT events at altitudes below 4 km are removed to avoid surface pollution, and events within 0.5 km of the tropopause are removed to avoid false positives induced by the sharp transition to stratospheric air. We note that this ozone detection methodology detailed above does not allow us to resolve STT events where the ozone flux is spread diffusely across the troposphere without a peak-like structure in the ozonesonde profile. In other words, STT events which might have occurred some distance and time away from the location of the ozonesonde profiles may not be readily detected using the high vertical resolution, but infrequent, ozonesonde launches.

We define the ozone peak as the altitude where the perturbation profile is greatest between 2 km from the surface and 0.5 km below the tropopause. The STT event is confirmed if the perturbation profile drops below zero between the ozone peak and the tropopause, as this represents a return to non-enhanced ozone concentrations. Alternatively, the STT event is also confirmed if the OMR between the ozone peak and the tropopause drops below 80 ppb and is at least 20 ppb lower than the OMR at the ozone peak. If neither of these conditions are met, the profile is rejected as a non-event. This final step removes near-tropopause anomalies for which there is insufficient evidence of detachment from the stratosphere. Vertical ozone profiles recorded by ozonesondes are highly dependent on the time of launch (Sprenger, Croci Maspoli, and Wernli 2003), and it cannot be guaranteed that detected ozone enhancements are fully separated from the stratosphere, although this method minimises that risk by removing detected events too near the tropopause.

We estimate the ozone flux into the troposphere associated with each event by integrating the ozone concentration enhancement vertically over the altitude range for which an STT event is identified (i.e. enhancement near the ozone peak over which the perturbation profile is greater than zero). This estimate is conservative because it does not take into account any ozone enhancements outside of the detected peak that may have been caused by the STT, and also ignores any enhanced ozone background amounts from synoptic-scale stratospheric mixing into the troposphere.

Our method differs somewhat from that used by Tang and Prather (2010) to detect STT events from ozonesonde measurements. Their definition is based on subjective analysis of sondes released from 20 stations ranging in latitude from 35° S to 40° N. They identify an STT event if, starting from 5 km altitude, ozone exceeds 80 ppb and then within 3 km decreases by 20 ppb or more to a value less than 120 ppb. Their technique would miss many events due to the lower ozone concentrations found in the cleaner Southern Hemisphere.

4.3.4 Biomass burning influence

The STT detection algorithm described in Sect. 4.3.3 assumes all ozone enhancements are caused by stratospheric intrusions. In some cases, however, these perturbations may in fact reflect ozone production in lofted smoke plumes. Biomass burning in southern Africa and South America has previously been shown to have a major influence on atmospheric composition in the vicinity of our measurement sites (Oltmans et al. 2001; Gloudemans et al. 2006; Edwards et al. 2006), particularly from July to December (Pak et al. 2003; Liu et al. 2017a). On occasion, smoke plumes from Australian and Indonesian fires can also reach the mid-high southern latitudes, as seen from satellite measurements of carbon monoxide (CO) discussed below.

Large biomass burning events emit substantial quantities of ozone precursors, some of which are capable of being transported over long distances and driving ozone production far from the fire source (Jaffe and Wigder 2012). Ozone production from biomass burning is complex and affected by photochemistry, fuel nitrogen load, and time since emission, among other factors. While ozone production occurs in some biomass burning plumes, this is not always the case; therefore ozone perturbations detected during transported smoke events may or may not be caused by the plume. For this reason all detected STT events which could be caused by smoke plumes are

flagged, following the procedure outlined below. Calculations of seasonality, and ozone flux do not include flagged events, however they are included in summary plots in this work.

Possible biomass burning influence is identified using satellite observations of CO from the AIRS (Atmospheric Infra-red Sounder) instrument on board the Aqua satellite (Texeira 2013). CO is emitted during incomplete combustion and is an effective tracer of long-range transport due to its long lifetime (Edwards 2003; Edwards et al. 2006). In the Southern Hemisphere, biomass burning is the primary source of CO, making CO a good proxy for fire plumes (e.g. Sinha et al. 2004; Mari et al. 2008). To identify possible biomass burning influence, AIRS vertical column CO is visually inspected for all dates with detected STT events. Smoke plumes are diagnosed over areas with elevated CO columns ($\sim 2 \times 10^{18}$ molecules cm $^{-2}$ or higher), and any sonde-detected STT event that occurs near (within ~ 150 km of) a smoke plume is flagged. Removal of these detections reduces the yearly estimated ozone flux by $\sim 15\%$ at Macquarie Island and $\sim 20\%$ at Melbourne.

All days with detected STT events were screened, with the exception of one event during which there were no available AIRS data (January 2010). We find that biomass burning may have influenced 27 events over Melbourne and 21 events over Macquarie Island. These events are flagged in the following sections, and are not used in our calculation of total STT flux. All of the flagged events except for two occurred during the SH burning season (July to December). No events at Davis were seen to be influenced by smoke transport.

4.3.5 Classifying synoptic conditions during STT events

Synoptic scale weather patterns are examined using data from the European Centre for Medium-range Weather Forecasts (ECMWF) Interim Reanalysis (ERA-I) (Dee et al. 2011). This is done using the ERA-I data products over the three sites on dates matching the detected STT events. We use the ERA-I 500 hPa data to subjectively classify the events based on their likely meteorological cause, by visually examining each date where an event was detected. During STT occurrence, the upper troposphere is typically characterised by nearby cyclones, cut-off lows, or cold fronts. Over Melbourne and Macquarie Island, we find that frontal and low pressure activity are prevalent during STT events (see Sect. 4.4). Over Davis, the weather systems are often less clear, however we see a higher portion of probable cut-off lows. The stratospheric polar vortex may create tropopause folds without other sources of upper tropospheric turbulence such as low pressure fronts or cyclones (e.g. Baray et al. 2000; Sprenger, Croci Maspoli, and Wernli 2003; Tyrlis et al. 2014). Cut-off low pressure systems can be seen clearly in synoptic scale weather maps as regions with lowered pressure and cyclonic winds. Low pressure fronts in the higher southern latitudes travel from west to east and lower the tropopause height. We examine two cases in detail to illustrate the relationship between synoptic-scale conditions and STT events over Melbourne. These are included in a supplementary document (Fig. S2 and S3) which show an archetypal cut-off low and low pressure front. To detect cut-off low pressure systems we look for cyclonic winds and a detached area of low pressure within ~ 500 km of a site on days of event detection. For low pressure fronts we look for low pressure troughs within ~ 500 km. Frontal passage is a known cause of STT as stratospheric air descends and

TABLE 4.2: Total number of ozonesonde detected STT events, along with the number of events in each category (see text).

Site	Events	Cut-offs	Frontals	Misc	Fire
Davis	80	44	19	17	0
Macquarie Island	105	19	31	34	21
Melbourne	127	28	31	41	27

streamers of ozone-rich air break off and mix into the troposphere (Sprenger, Croci Maspoli, and Wernli 2003).

4.4 STT event climatologies

Figure 4.5 shows the seasonal cycles of STT frequency at Davis, Macquarie Island, and Melbourne. Frequency is determined as detected event count divided by total launched ozonesondes for each month. STT events in Figures 4.5-4.8 are coloured based on the meteorological classification described in Sect. 4.3.5, with events classified as either low pressure fronts (“frontal”, dark blue), cut-off low pressure systems (“cutoff” teal), or indeterminate (“misc”, cyan). Events that may have been influenced by transported smoke plumes (Sect. 4.3.4) are shown in red. Ozonesonde releases are summarised in Table 4.1 and detected event counts are summarised in Table 4.2.

There is an annual cycle in the frequency of STT events (Fig. 4.5) with a summertime peak at all three sites. This summertime peak is due to a prevalence of summer low-pressure storms and fronts, which increase turbulence and lower the tropopause (Reutter et al. 2015). At Davis, there are more STT detections during winter relative to our other sites, which may be due to the polar vortex and its associated lowered tropopause and increased turbulence. STT events associated with cut-off low pressure systems are more prevalent during summer, while STT events associated with frontal passage occur throughout the year. The high frequency of STT ozone enhancements is comparable to the > 25% frequencies seen over Turkey and east of the Caspian sea in an ERA-I analysis performed by Tyrlis et al. (2014).

The SH summer maximum we see for STT ozone flux can also be seen in Fig. 16 of Škerlak, Sprenger, and Wernli 2014, which shows seasonal flux over the southern ocean, although this is less clear over Melbourne. This seasonality is not clear in the recent ERA-Interim tropopause fold analysis performed by Škerlak et al. (2015), where a winter maximum of tropopause fold frequency ($\sim 0.5\%$ more folds in winter) over Australia can be seen to the north of Melbourne. Their work seems to show slightly higher fold frequencies over Melbourne in summer (Škerlak et al. 2015, Fig. 5), however not to the same extent that our summer peak suggests. Their winter maximum is in the subtropics only - from around 20° S to 40° S, which can be seen as the prevalent feature over Australia in their Fig. 5. Wauben, Fortuin, and Velthoven 1998 look at modelled (CTM driven by ECMWF output) and measured ozone distributions and find more SH ozone in the lower troposphere during austral winter, however they note that the ECMWF fields are uncertain here again due to lack of measurements. Their work shows a generally cleaner lower troposphere in the SH summer but this can not be construed to suggest more or less STT folds in either season. Sprenger,

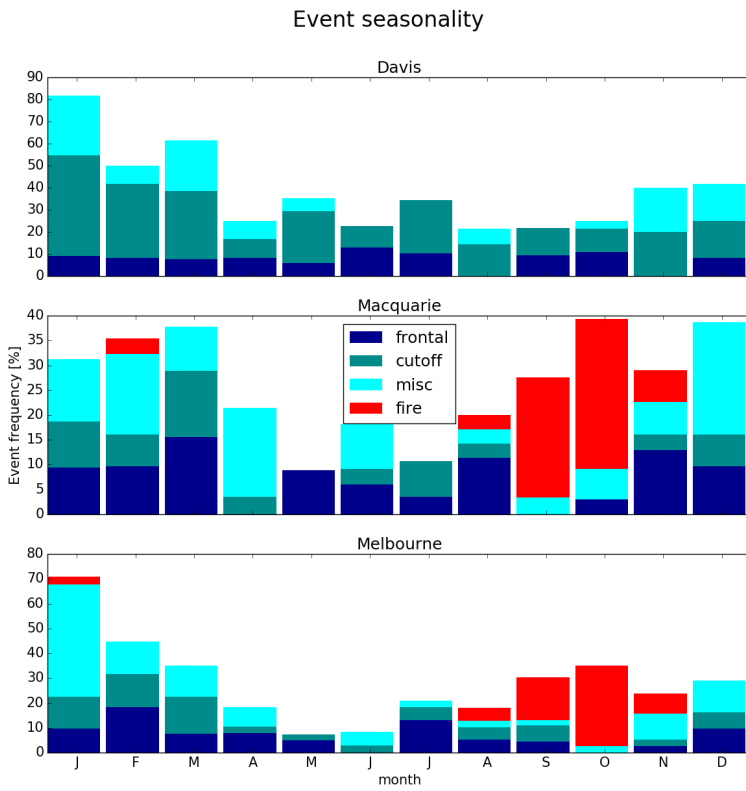


FIGURE 4.5: Seasonal cycle of STT event frequency at Davis (top), Macquarie Island (middle), and Melbourne (bottom). Events are categorised by associated meteorological conditions as described in the text, with low pressure fronts (“frontal”) in dark blue, cut-off low pressure systems (“cutoff”) in teal, and indeterminate meteorology (“misc”) in cyan. Events that may have been influenced by transported smoke plumes are shown in red (see text for details).

Croci Maspoli, and Wernli 2003 examine modelled STT folds using ECMWF output over March 2000 - April 2001, and show that for this year there is a clear austral winter maximum, again over the 20° S to 40° S band. The winter maximum does not include Melbourne, or the southern ocean, which explains why we see a seasonality not readily evident in these global-scale studies.

The measurement sites are not in the regions which have a clear winter maximum seen in Fig. 1 Sprenger, Croci Maspoli, and Wernli 2003, and the large scale winter maximum shown by all three studies seems to be dominated by the system in that region. The seasonality of our three sites is not driven by the larger STT system seen over the southern Indian ocean and middle Australia which dominates prior analysis near or over Australia.

To examine the robustness of the distributions shown in Fig. 4.5, we developed an alternative assessment of the seasonal occurrence of STT events, with results shown in Fig. 4.6. Here STT occurrence is evaluated by consideration of the square of the dry Brunt-Väisälä frequency (N^2) at the heights of the ozone tropopause (z_{OT}) and lapse

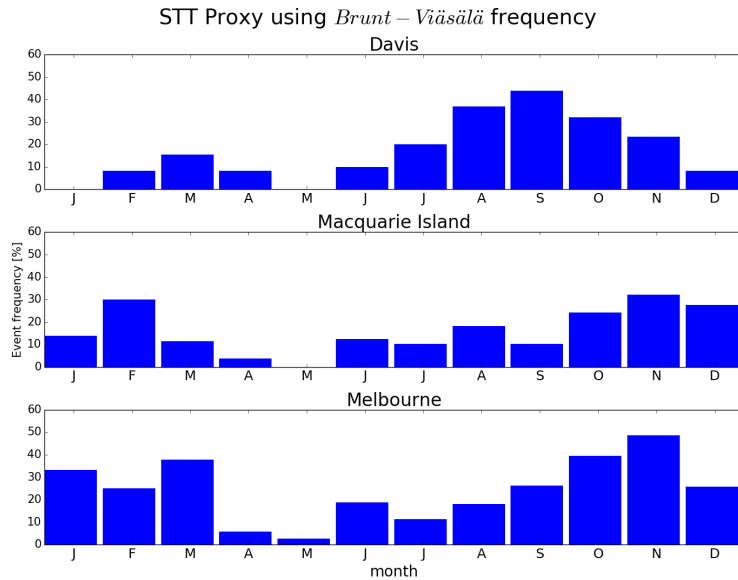


FIGURE 4.6: Seasonal distribution of STT events using the alternative STT proxy, obtained from consideration of the static stability at the ozone and lapse rate tropopauses, for Davis (2006-2013), Macquarie Island (2004-2013), and Melbourne (2004-2013).

rate tropopause (z_{LRT}) in each ozonesonde profile that has been binned to 100 m resolution. We use N^2 to assess atmospheric stability, which is normally distinctly higher in the stratosphere than in the troposphere, and assume that the vertical temperature gradients within the intrusion respond most rapidly to transported heat, which is an additional characteristic of stratospheric air. N^2 is evaluated using 250 m resolution data (to smooth variability in the vertical gradient of potential temperature that is due to small temperature fluctuations likely associated with gravity waves). The altitude binning chosen is a compromise between vertical resolution and the level of variability in N^2 introduced by temperature gradients associated with perturbations from gravity waves and changes near the lapse rate tropopause, and is the minimum that produces a robust seasonal distribution. We define STT as having taken place if $N^2(z_{OT}) > N^2(z_{LRT})$ and $z_{OT} < z_{LRT}$; in this way the characteristically higher static stability and ozone concentration of stratospheric intrusion is regarded as being retained as it penetrates below the lapse rate tropopause. The seasonal distributions shown for the three stations in Fig. 4.6 are generally similar to those shown in Fig. 4.5 (although detected events are less frequent), with the main exception that very few events are identified with the alternative method at Davis in the first half of the year. For our STT proxy, we only detect intrusions where the lowest altitude of the intrusion satisfies the ozone tropopause definition. During summer and autumn, the vertical ozone gradients at Davis are weaker compared with the other seasons, and the detected ozone tropopause tends to lie above the lapse rate tropopause potentially reducing the ability to identify STT events based on the definition of our proxy.

Figure 4.7 shows the altitudes of detected events, based on the altitude of peak tropospheric ozone (local maximum ozone within enhancement altitude) in the ozonesonde

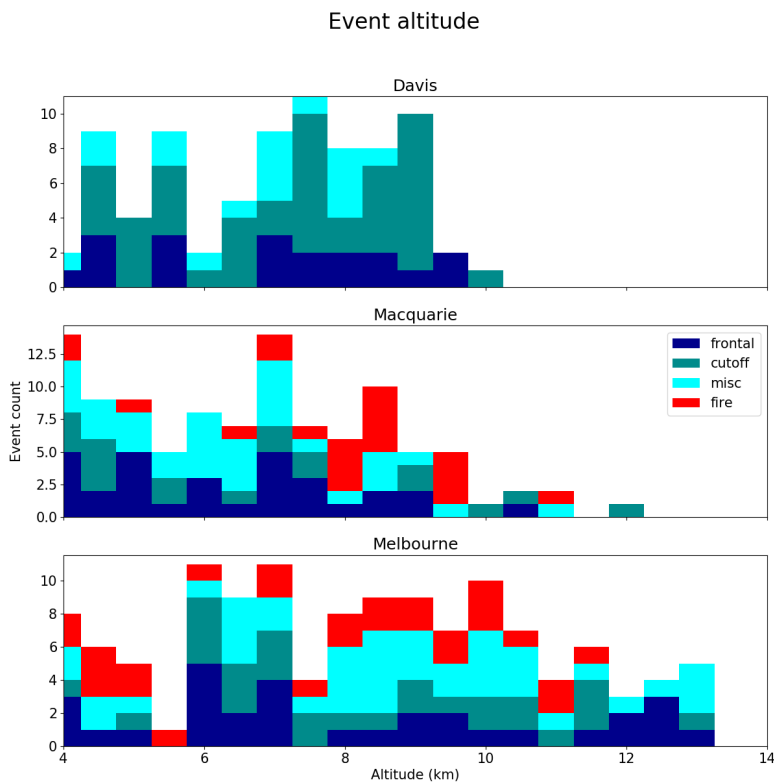


FIGURE 4.7: The distribution of STT events' altitudes at Davis (top), Macquarie Island (middle), and Melbourne (bottom), determined as described in the text. Events are coloured as described in Fig. 4.5.

profile. STT event peaks most commonly occur at 6–11 km above Melbourne and anywhere from 4–9 km at Davis and Macquarie Island. There is no clear relationship between meteorological conditions and event altitude, which may reflect the fact that the ozonesondes observe a snapshot of an event at different stages of its life cycle.

Figure 4.8 shows the distance from the event peak to the ozone defined tropopause, referred to as event depth. The majority of STT events occur within 2.5 km of the tropopause at Davis and Macquarie Island. Over Melbourne, the event depth is more spread out, with peak ozone enhancement generally occurring up to 6 km below the tropopause. Again, there is no clear relationships between meteorological conditions and event depth.

4.5 Simulated ozone columns

Figure 4.9 compares the time series of tropospheric ozone columns (Ω_{O_3}) in molecules cm^{-2} simulated by GEOS-Chem (red) to the measured tropospheric ozone columns (black). GEOS-Chem outputs ozone density (molecules cm^{-3}), and height of each simulated box, as well as which level contains the tropopause, allowing modelled Ω_{O_3} to be calculated as the product of density and height summed up to the box below the

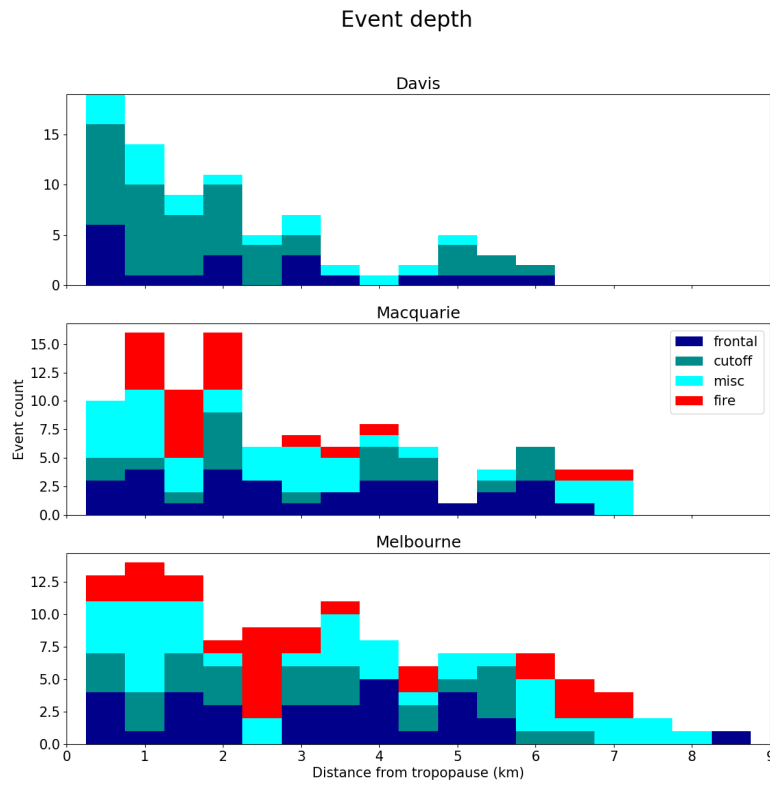


FIGURE 4.8: The distribution of STT events' depths, defined as the distance from the event to the tropopause, at Davis (top), Macquarie Island (middle), and Melbourne (bottom), determined as described in the text.

Events are coloured as described in Fig. 4.5.

tropopause level. In both observations and model, the maximum ozone column at Melbourne occurs in austral summer, with a minimum in winter, while Macquarie Island and Davis show the opposite seasonality.

GEOS-Chem provides a reasonable simulation of the observed seasonality and magnitude of Ω_{O_3} . Reduced major axis regression of observed versus simulated Ω_{O_3} gives a line of best fit with slopes of 1.08 for Davis, 0.99 for Macquarie Island, and 1.34 for Melbourne. The model is only partially able to reproduce the variability in the observations, with paired r^2 values of 0.38 for Davis, 0.18 for Macquarie Island, and 0.37 for Melbourne. Much of the variability is driven by the seasonal cycle, and after removing this effect (by subtracting the multi-year monthly means), the r^2 values decrease to 0.07, 0.11, and 0.30 respectively, although the slope improves at Melbourne to 1.08.

Figure 4.10 shows the observed and simulated ozone profiles at all sites, averaged seasonally. The model generally underestimates ozone in the lower troposphere (up to 6 km) over Davis, although this bias is less pronounced during summer. Over Melbourne, ozone in the lower troposphere is well represented, but the model overestimates ozone from around 4 km to the tropopause. Over Macquarie Island we see

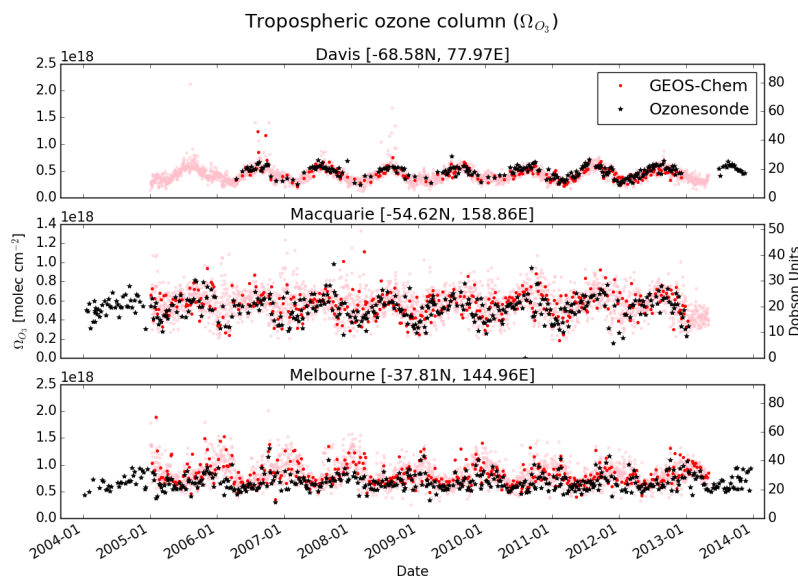


FIGURE 4.9: Comparison between observed (black) and simulated (pink, red) tropospheric ozone columns (Ω_{O_3} , in molec cm^{-2}) from 1 January 2004 to 30 April 2013. For the model, daily output is shown in pink, while output from days with ozonesonde measurements are shown in red. For each site, the model has been sampled in the relevant grid square.

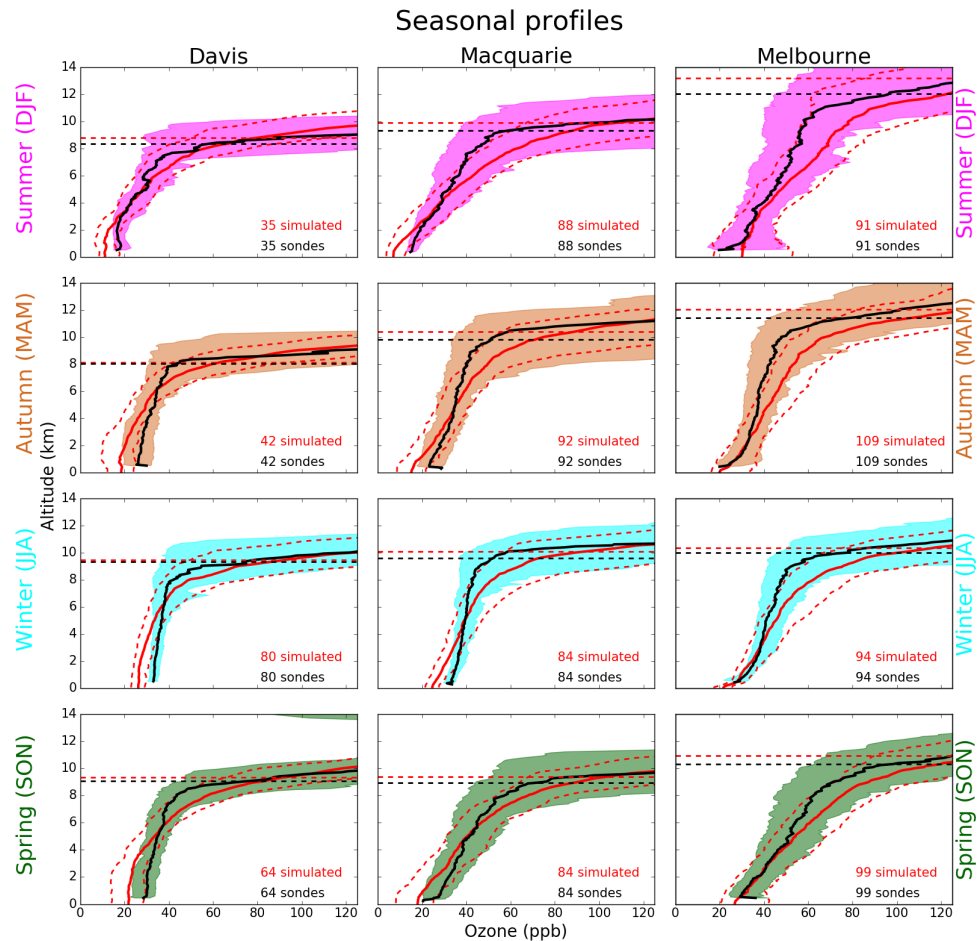


FIGURE 4.10: Observed and simulated tropospheric ozone profiles over Davis, Macquarie Island, and Melbourne, averaged seasonally. Model medians (2005-2013 average) are shown as red solid lines, with red dashed lines showing the 10th and 90th percentiles. Ozonesonde medians (over each season, for all years) are shown as black solid lines, with coloured shaded areas showing the 10th and 90th percentiles. The horizontal dashed lines show the median tropopause heights from the model (red) and the observations (black).

model overestimation of ozone above 4 km, as well as underestimated ozone in the lower troposphere, suggesting that this region is influenced by processes seen at both of our other sites. Also shown is the mean tropopause height simulated by the model (horizontal dashed red line), which is always higher than the observed average, although this difference is not statistically significant. The effect of local pollution over Melbourne during austral summer (DJF) can be seen from the increased mean mixing ratios and enhanced variance near the surface. The gradient of the O₃ profiles is steeper in the measurements than the model, at all sites during all seasons. Recently Hu et al. 2017 examined GEOS-Chem ozone simulations and found a similar overestimation of upper troposphere ozone in the mid southern latitudes when using the GEOS5 meteorological fields.

Figure 4.11 compares modeled (red) and observed (black) ozone profiles on three example days when STT events were detected using the ozonesondes. The figures show the profile for each site with the closest (qualitative) match between model and observations. The resolution (both vertical and horizontal) of GEOS-Chem in the upper troposphere is too low to consistently allow detection of STTs, although in a few cases (e.g., Melbourne in Fig. 4.11) it appears that the event was large enough to be visible in the model output.

4.6 Stratosphere-to-troposphere ozone flux from STT events

4.6.1 Method

We quantify the mean stratosphere-to-troposphere ozone flux due to STT events at each site based on the integrated ozone amount associated with each STT event (see Sect. 4.3.3). Events that may have been influenced by transported biomass burning are excluded from this calculation. Our estimate provides a preliminary estimate of how much ozone is transported from the stratosphere by the events detected by our method. The estimate is conservative for several reasons: it ignores secondary ozone peaks which may also be transported from the stratosphere, it ignores potential ozone enhancements which may have dispersed and increased the local background mixing ratio, and any influence from STT events nearby which may also increase the local background ozone.

Observed tropospheric columns are calculated from the ozonesondes by calculating the ozone number density (molecules cm⁻³) using measured ozone partial pressure (P_{O₃}) and integrating vertically up to the tropopause:

$$\Omega_{O_3} = \int_0^{TP} \frac{P_{O_3}(z)}{k_B \times T(z)} dz$$

where z is the altitude (GPH), TP is the altitude at the tropopause, T is the temperature, and k_B is the Boltzmann constant.

Three regions are used to examine possible STT flux over a larger area using modeled tropospheric ozone concentrations. The regions are shown in Fig. 4.1. The regions are centred at each site, plus or minus ten degrees latitude, and plus or minus 25, 16, and 11 degrees longitude for Davis, Macquarie Island, and Melbourne respectively. These boundaries approximate a rectangle centred at each site with ~ 2000 km side

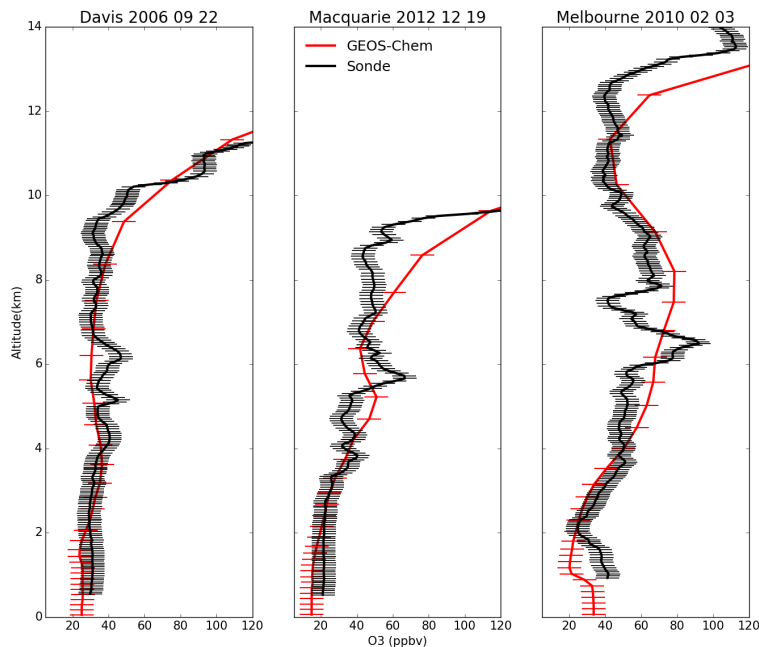


FIGURE 4.11: Example comparisons of ozone profiles from ozonesondes (black) and GEOS-Chem (red) from three different dates during which STT events were detected from the measurements. The dates were picked based on subjective visual analysis. The examples show the best match between model and observations for each site. GEOS-Chem and ozonesonde pressure levels are marked with red and black dashes respectively.

lengths, covering $\sim 4.4, 4.6$, and 4.8 million square km, for Davis, Macquarie Island, and Melbourne respectively.

To determine the ozone column attributable to STT, we determine monthly averaged STT impact (I ; fraction of tropospheric ozone sourced from the stratosphere as shown above) and the monthly mean tropospheric ozone column (from the GEOS-Chem multi-year mean, Ω_{O_3}) over the regions described above. This can be expressed simply as the STT flux per event (flux $_i$ in each month: $\text{flux}_i = \Omega_{O_3} \times I$). Next we determine how many events are occurring per month by assuming only one event can occur at one time, and that no event is measured twice. These assumptions allow a simple estimate of events per month from the relatively sparse dataset and should hold true as long as our regions of extrapolation are not too large. The (P)robability of any sonde launch detecting an event is calculated as the fraction of ozonesonde releases for which an STT event was detected, calculated for each month. We assume events last N days, then find how many events per month we expect by multiplying the days in a month by P and dividing by this assumed event lifetime. For example if we expect to see an event 25% of the time in a month, and events last one day, we expect one event every four days (~ 7.5 events in that month) whereas if we expect events to last a week then we would expect \sim one event in that month. This leads us to multiply our flux $_i$ by P , and then by the term M ($M = \frac{\text{days per month}}{N}$) determined by our assumed event lifetime in order to determine monthly STT ozone flux.

The longevity of ozone events is very difficult to determine, and we have chosen 2 days as a representative number based on several examples in Lin et al. 2012 where intrusions were seen to last from 1-3 days (occasionally longer) and an analysis of one large event by Cooper et al. 2004 showing that most of the ozone had dispersed after 48 hours. Worth noting is the recent work of Trickl et al. 2014, where intrusions are detected > 2 days and thousands of kilometres away from their initial descent into the troposphere over Greenland or the Arctic. In those regions with high wind shear, mixing appears to be slower, which allows ozone intrusions to be transported further without dissipating into the troposphere. Relative uncertainty in our M term is set to 50%, as we assume these synoptic events to generally last from 1-3 days.

4.6.2 Results

The top panel of Fig. 4.12 shows the STT ozone enhancements, based on a vertical integration of the ozone above baseline levels for each ozonesonde where an event was detected. The area considered to be 'enhanced' ozone is outlined with yellow dashes on the left panel of Fig. 4.4. We find that the mean ozone flux associated with STT events is $\sim 0.5\text{--}2.0 \times 10^{16}$ molecules cm^{-2} . The bottom panel shows the mean fraction of total tropospheric column ozone (calculated from ozonesonde profiles) attributed to stratospheric ozone intrusions at each site for days when an STT event occurred. First the tropospheric ozone column is calculated, then the enhanced ozone column amount is used to determine the relative increase. At all sites, the mean fraction of tropospheric ozone attributed to STT events is $\sim 1.0\text{--}3.5\%$. On three separate days over Macquarie and Melbourne, this value exceeds 10%.

The upper panels in figures 4.13-4.15 show the factors I , P , and Ω_{O_3} which are used along with the assumed event lifetime to estimate the STT flux. The tropospheric ozone and area of our region is calculated using the output and surface area from

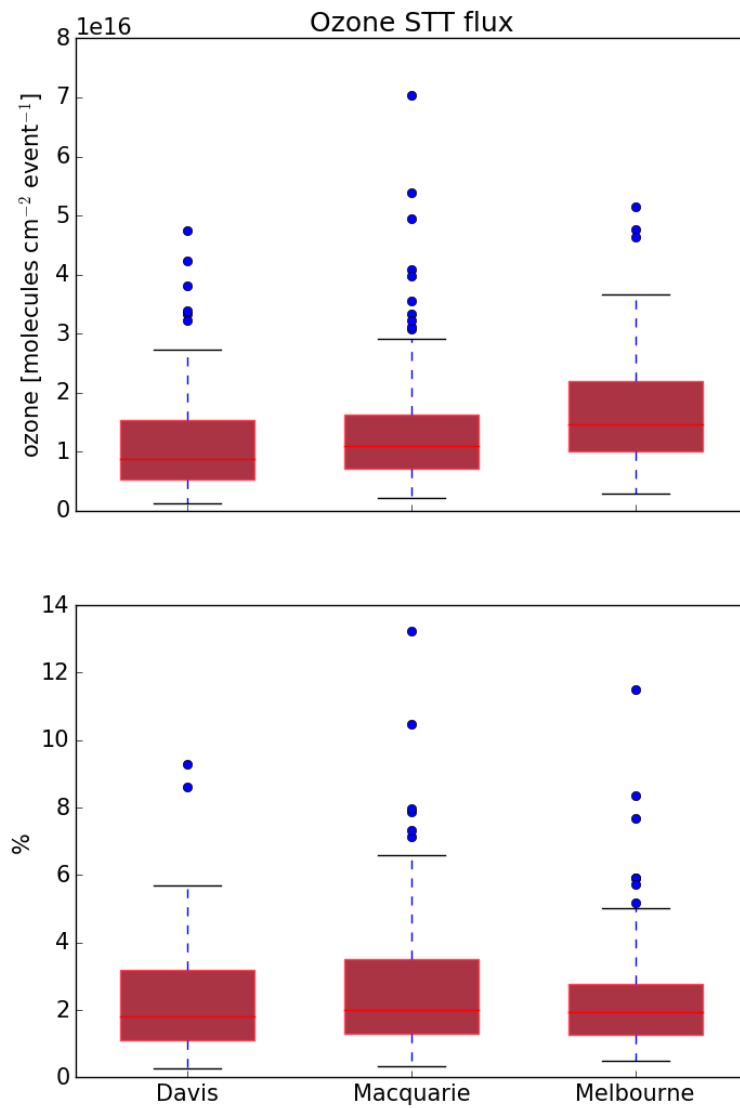


FIGURE 4.12: Top panel: tropospheric ozone attributed to STT events. Bottom panel: percent of total tropospheric column ozone attributed to STT events. Boxes show the inter-quartile range (IQR), with the centre line being the median, whiskers show the minimum and maximum, circles show values which lie more than 1.5 IQR from the median. Values calculated from ozonesonde measurements as described in the text.

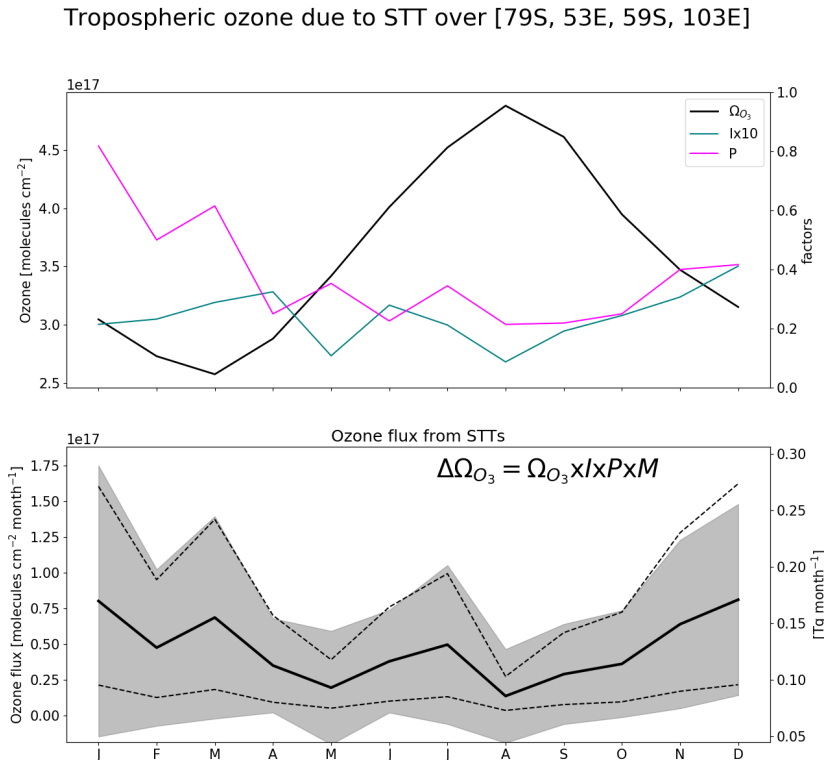


FIGURE 4.13: (Top) Tropospheric ozone, (I)impact per event, and (P)probability of event detection per sonde launch, averaged over the region above Davis. The tropospheric ozone column Ω_{O_3} (black, left axis) is from GEOS-Chem, while the STT probability P (magenta, right axis) and impact I (teal, right axis) are from the ozonesonde measurements. The STT impact is multiplied by ten to better show the seasonality. (Bottom) Estimated contribution of STT to tropospheric ozone columns over the region, with uncertainty (shaded area) estimated as outlined in Sect. 4.7. The black line shows STT ozone flux if event lifetime is assumed to be two days, with dashed lines showing the range of flux estimation if we assumed events lasted from one day to one week.

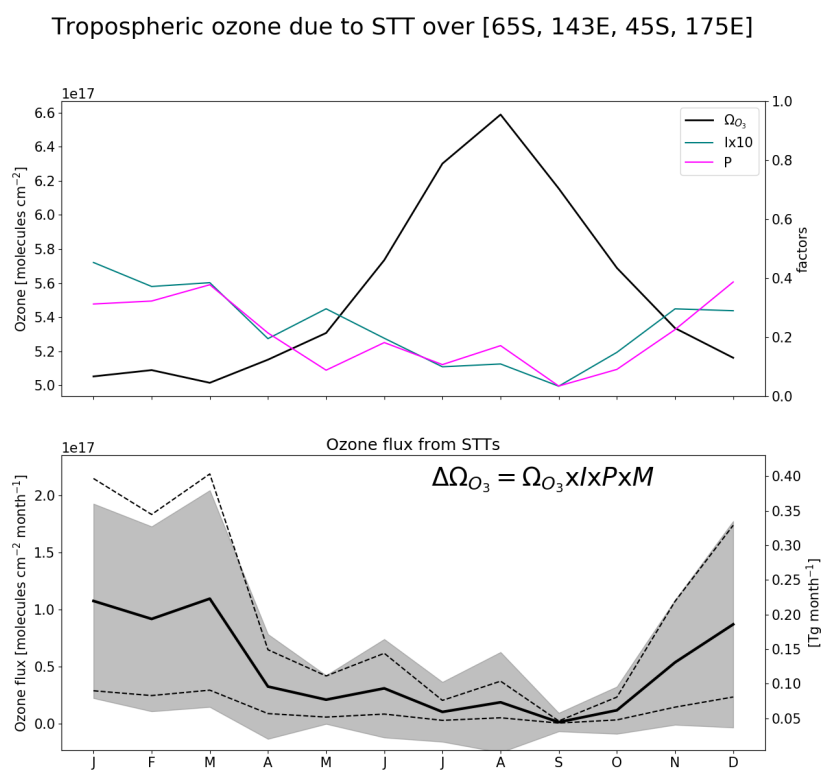


FIGURE 4.14: As described in 4.13, for the region containing Macquarie Island.

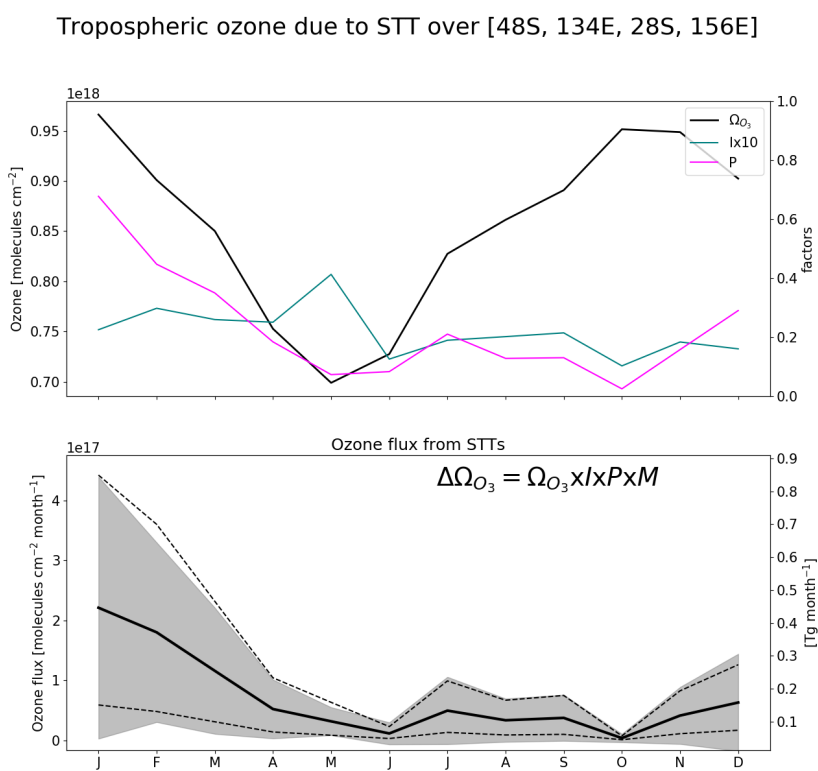


FIGURE 4.15: As described in 4.13, for the region containing Melbourne.

TABLE 4.3: Seasonal STT ozone contribution in the regions near each site, in $\text{kg km}^{-2} \text{ month}^{-1}$. In parentheses are the relative uncertainties.

Region	DJF	MAM	JJA	SON
Davis	54.5 (102%)	47.7 (97%)	30.7 (114%)	18.8 (127%)
Macquarie Island	61.3 (85%)	70.7 (91%)	17.9 (139%)	7.7 (229%)
Melbourne	96.7 (103%)	88.6 (89%)	26.7 (102%)	21.4 (109%)

GEOS-Chem over our three regions. The lower panel of these figures show the results of the calculation when we choose two days for our flux estimation, with dotted lines showing the range of flux calculated if we assume events last from one day to one week. The seasonal cycle of ozone flux is mostly driven by the P term, which peaks in the SH summer over all three sites. Total uncertainty (shaded) is on the order of 100% (see Sect. 4.7.2). We calculate the annual amount based on the sum of the monthly values. The regions over Davis, Macquarie Island, and Melbourne have estimated STT ozone contributions of $\sim 5.7 \times 10^{17}$, $\sim 5.7 \times 10^{17}$, and $\sim 8.7 \times 10^{17}$ molecules $\text{cm}^{-2} \text{ a}^{-1}$ respectively, or equivalently ~ 2.0 , 2.1 , and 3.3 Tg a^{-1} .

4.6.3 Comparison to literature

Škerlak, Sprenger, and Wernli 2014 show an estimate of roughly 40 to 150 $\text{kg km}^{-2} \text{ month}^{-1}$ in these regions, over all seasons (see Fig. 16, 17 in their publication) while we estimate from 0 to 180 $\text{kg km}^{-2} \text{ month}^{-1}$ STT impact, following a seasonal cycle with the maximum in austral summer. We estimate higher maximum flux over Melbourne, (178, and 150 $\text{kg km}^{-2} \text{ month}^{-1}$ in January and February) than in either Davis (89 $\text{kg km}^{-2} \text{ month}^{-1}$ in March) or Macquarie Island (68 $\text{kg km}^{-2} \text{ month}^{-1}$ in January). Our calculated seasonal contributions, along with total uncertainty are shown in Table 4.3.

This result disagrees with several other studies which have found STT ozone fluxes in the SH extra-tropics are largest from autumn or winter to early spring. Roelofs and Lelieveld 1997 used a model carrying a tracer for stratospheric ozone to estimate STT impacts. They see higher SH tropospheric ozone concentrations, as well as STT flux, in the SH winter. Our model also shows ozone column amounts peaking in winter, however flux is maximised in summer due to our detected event frequencies. Elbern, Hendricks, and Ebel 1998 examine STT using ECMWF data for prior to 1996, using PV and Q-vectors to determine STT frequency and strength, and suggest fewer fold events in the SH occur from December to February. Olsen (2003) used PV and winds from the GEOS reanalysis combined with ozone measurements from the TOMS satellite to estimate that the ozone flux between 30° S and 60° S is 210 Tg yr^{-1} , with the maximum occurring over SH winter. Liu et al. (2017a) model the upper tropospheric ozone and its source (emissions/lightning/stratospheric) over the Atlantic ocean between 30° S and 45° S , and suggest that most of this is transported from the stratosphere from March to September, which is when the subtropical jet system is strongest.

The disagreements largely reflect the difference between point source based estimates and zonally averaged estimates, as the meteorological behaviour at our three sites is not the same as the system that dominates the southern hemisphere in general. As detailed in Sect. 4.4, the maximum STT influx which occurs during SH winter is

almost entirely due to the dominant STT system which occurs annually over the southern Indian ocean and middle of Australia. It is difficult to compare remote ozonesonde datasets with area averaged models or re-analyses based on non-co-located measurements (such as ERA).

4.7 Sensitivities and limitations

4.7.1 Event detection

Our method uses several subjectively-defined quantities in the process of STT event detection. Here we briefly discuss these quantities and the sensitivity of the method to each. Using the algorithm discussed in Sect. 4.3.3, we detect 80 events at Davis, 105 (21 fire influenced) events at Macquarie Island, and 127 (27 fire influenced) events at Melbourne.

The cut-off threshold (defined separately for each site) is determined from the 95th percentile of the ozone perturbation profiles between 2 km above the earth's surface and 1 km below the tropopause. We use the 95th percentile because at this point the filter locates clear events with fewer than 5% obvious false positive detections. Event detection is sensitive to this choice; for example, using the 96th, and 97th percentile instead decreased detected events by 2, 9 (2,10%) at Davis, 13, 31 (11, 28%) at Macquarie Island, and 8, 24 (6, 18%) at Melbourne. Event detection is therefore also sensitive to the range over which the percentile is calculated. This range was chosen to remove anomalous edge effects of the Fourier bandpass filter and to discount the highly variable ozone concentration which occurs near the tropopause.

Ozone enhancements are only considered STT events if they occur from 4 km altitude up to 500 m below the tropopause. This range removes possible ground pollution and events not sufficiently separated from the stratosphere, while still capturing many well-defined events that occur within 1 km of the tropopause. An example of a well-defined event that occurs within 1 km of the tropopause is shown in the supplementary (Fig. S2). However, STT events which reach below 4 km are physically possible and we may have some false negative detections due to the altitude restricted detections.

4.7.2 Flux calculations

Flux is calculated as $I \times P \times M \times \Omega_{O_3}$, with each term calculated as described in Sect. 4.6.1. The uncertainty is determined using the standard deviation of the product, with variance calculated using the variance of a product formula, assuming that each of our terms is independent:

$$\text{var}(\Pi_i X_i) = \Pi_i (\text{var}(X_i) + E(X_i)^2) - (\Pi_i E(X_i))^2$$

The standard deviations for the I and Ω_{O_3} terms are calculated over the entire dataset. These terms are considered to be homoskedastic (unchanging variance over time). Uncertainty in assumed event lifetime is set at 50%, as we believe it is reasonable to expect events to last 1-3 days. P is the probability of any ozonesonde detecting an event, and is assumed to be constant (for any month). The overall uncertainty as a

percentage is shown in parentheses in Table 4.3, these values are on the order of 100%, largely due to relative uncertainty in the I factor which ranges from 50-120% for each month.

Small changes in the region don't have a large affect on the per area flux calculations: increasing or decreasing the regions by 1° on each side ($\sim 10\%$ change in area) change the resulting flux by $\sim 1\%$. However due to the large portion of winter STT events being flagged due to potential smoke plume influence, a significant change in the yearly flux is seen when we don't remove these events. Without removing smoke flagged events we see an increase in estimated yearly flux of $\sim 1.1, 2.1 \times 10^{17}$ molecules $\text{cm}^{-2} \text{ yr}^{-1}$ (which is a change of $\sim 15, 20\%$), over Macquarie Island and Melbourne respectively.

Considering the I factor, as discussed in here and in Sect. 4.7, there are several uncertainties in our method that are likely to lead to a low bias, such as the conservative estimate of flux within each event. Although there is little available data on SH ozone events for us to compare against, consider Terao et al. (2008), who estimated that up to 30–40% of the ozone at 500 hPa was transported from the stratosphere, in the northern hemisphere.

Our STT event impact estimates have some sensitivity to our biomass burning filter: including smoke-influenced days increases the mean per area flux by 15-20%. Although events which are detected near fire smoke plumes are removed, some portion of these could be actual STTs. The change in our P parameter when we include potentially smoke influenced events leads to a yearly estimated STT of 11×10^{17} molecules $\text{cm}^{-2} \text{ yr}^{-1}$ over Melbourne, which suggests that up to 2.1×10^{17} molecules $\text{cm}^{-2} \text{ yr}^{-1}$ ozone enhancement could be caused by smoke plume transported precursors. This is a potential area for improvement, as a better method of determining smoke influenced columns would improve confidence in our estimate.

Other possibly important uncertainties in our calculation of STT flux which we don't cover are listed here. Filtering events which occur within 500 m of the tropopause may also lead to more false negatives. This could also cause lower impact estimates due to only measuring ozone enhancements which have descended and potentially slightly dissipated. On the other hand we have no measure of how often the detached ozone intrusion reascends into the stratosphere, which would lead to a reduced stratospheric impact. The estimated tropospheric ozone columns modelled by GEOS-Chem may be biased, for instance Hu et al. 2017 suggest that in general GEOS-Chem (with GEOS-5 met. fields) underestimates STT, with $\sim 360 \text{ Tg a}^{-1}$ simulated globally, compared to $\sim 550 \text{ Tg a}^{-1}$ observationally constrained. Transport uncertainty is very difficult to estimate with the disparate point measurements; it's possible that detected events are (at least partially) advected out of the analysis regions, which would mean we overestimate the influx into the region, and it is also possible that we are influenced by STT events outside the regions of analysis. Uncertainty in event longevity is set to 50%, however this implies a very simplistic model of event lifetimes. A great deal of work could be done to properly model the regional event lifetimes, however this is beyond the scope of our work.

Uncertainties in STT ozone flux detection are ($\sim 100\%$), and could be directly improved with larger or longer datasets. Possible parameterisations and an improved model of event lifetime could also improve the confidence in our estimate of event

impacts, as well as allowing fewer assumptions.

4.8 Conclusions

Stratosphere-to-troposphere transport (STT) can be a major source of ozone to the remote free troposphere, but the occurrence and influence of STT events remains poorly quantified in the southern extra-tropics. Ozonesonde observations in the SH provide a satellite-independent quantification of the frequency of STT events, as well as an estimate of their impact and source. Using almost ten years of ozonesonde profiles over the southern high latitudes, we have quantified the frequency, seasonality, and altitude distributions of STT events in the SH extra-tropics. By combining this information with ozone column estimates from a global chemical transport model, we provided a first, conservative estimate of the influence of STT events on tropospheric ozone over the Southern Ocean.

Our method involved applying a bandpass filter to the measured ozone profiles to determine STT event occurrence and strength. The filter removed seasonal influences and allowed clear detection of ozone-enhanced tongues of air in the troposphere. By setting empirically-derived thresholds, this method clearly distinguished tropospheric ozone enhancements that are separated from the stratosphere. Our method is sensitive to various parameters involved in the calculation; however, for our sites we saw few false positive detections of STT events.

Detected STT events at three sites spanning the SH extra-tropics (38°S , 55°S , and 69°S) showed a distinct seasonal cycle. All three sites displayed a summer (DJF) maximum and an autumn to winter (AMJJA) minimum, although the seasonal amplitude was less apparent at the Antarctic site (Davis) as events were also detected regularly in winter and spring (likely due to polar jet stream-caused turbulence). Analysis of ERA-Interim reanalysis data suggested the majority of events were caused by turbulent weather in the upper troposphere due to low pressure fronts, followed by cut-off low pressure systems. Comparison of ozonesonde-measured ozone profiles against those simulated by the GEOS-Chem global chemical transport model showed the model is able to reproduce seasonal features but does not have sufficient vertical resolution to distinguish STT events.

By combining the simulated tropospheric column ozone from GEOS-Chem with ozonesonde-derived STT estimates, we provide a first estimate of the total contribution of STT events to tropospheric ozone in these southern extra-tropical regions. We estimate that the ozone enhancement due to STT events near our three sites ranges from $300\text{-}570 \text{ kg km}^{-2} \text{ a}^{-1}$, with seasonal maximum in SH summer.

Estimating STT flux using ozonesonde data alone remains challenging; however, the very high vertical resolution provided by ozonesondes suggests they are capable of detecting STT events that models, re-analyses, and satellites may not. Further work is needed to more accurately translate these ozonesonde measurements into STT ozone fluxes, particularly in the SH where data are sparse and STT is likely to be a major contributor to upper tropospheric ozone in some regions. More frequent ozonesonde releases at SH sites could facilitate development of better STT flux estimates for this region.

4.9 Contributions and Acknowledgements

JWG wrote the algorithms, ran the GEOS-Chem simulations, performed the analysis and led the writing of the paper under the supervision and guidance of SPA, RS, and JAF. AK contributed the Davis ozonesonde data and performed the analysis of the alternate STT proxy. All authors contributed to editing and revising the manuscript.

Data availability. All GEOS-Chem model output and the ozonesonde observational data are available from the authors upon request.

We thank Dr. Sandy Burden for help clarifying some of the uncertainties involved in methods within this work. We also thank Dr. Clare Paton-Walsh, who identified the need to account for smoke-influenced events, and provided discussions on how to go about doing such. Ozonesonde data comes from the World Ozone and Ultraviolet Data Centre (WOUDC). The ERA-Interim data were downloaded from the ECMWF website following registration. This research was undertaken with the assistance of resources provided at the NCI National Facility systems at the Australian National University through the National Computational Merit Allocation Scheme supported by the Australian Government. This work was supported through funding by the Australian Government's Australian Antarctic science grant program (FoRCES 4012), the Australian Research Council's Centre of Excellence for Climate System Science (CE110001028), the Commonwealth Department of the Environment ozone summer scholar program. This research is supported by an Australian Government Research Training Program (RTP) Scholarship.

Chapter 5

Summary and Concluding remarks

In this thesis I aimed to improve understanding of natural contributions to ozone over Australia and the southern ocean. Chapter 1 Introduction and Literature Review examined processes leading to ozone creation in the troposphere, primarily isoprene emissions and subsequent chemistry. The secondary cause of ozone, stratosphere to troposphere transport (STT), was also outlined with associated processes and causes discussed. A summary of how the lack of information available over Australia affects modelling and forecasting was provided. Methodologies, tools and data-sets used throughout the thesis were detailed in Chapter 2 Data and Modelling . Chapter 3 Biogenic Isoprene emissions in Australia showed how models are misrepresenting isoprene emissions by a large margin in Australia, along with the description and implementation of a relatively simple method of improvement. Chapter 4 Stratospheric ozone intrusions provided an estimate of stratospheric ozone influx to the troposphere, along with potential classifications and seasonality.

5.1 Outcomes

I aim to recalculate satellite vertical columns of HCHO using updated model a priori information. HCHO from OMI on board the AURA satellite was examined and recalculated in Chapter 2, where influence of the air mass factor (AMF) was discussed in detail. This AMF was created using an older version of GEOS-Chem with out-of-date HCHO chemistry. Recalculation, binning, and analysis of the satellite HCHO vertical columns was performed using GEOS-Chem v10.01, outlined in Section 2.6.1. This was performed using my own partial AMF recalculation code, along with full recalculation code set up in collaboration with Prof. Palmer and Dr. Surl. Subsequent use of the data makes further use of the recalculation as a basic sensitivity analysis of top-down emissions estimations to a priori satellite information.

I aim to determine biogenic isoprene emissions in Australia using a top-down inversion of satellite HCHO, through an estimated yield from GEOS-Chem. In Chapter 3 I determine the linear relationship between total column HCHO and biogenic isoprene emissions over Australia using the global CTM GEOS-Chem. Applying this relationship to satellite based HCHO measurements creates the desired top-down isoprene emissions estimate. This process was described in Section 3.2, using extensive filtering of both satellite data (to exclude non-biogenic HCHO sources) and model yield (to minimise spatial smearing). The uncertainty and limitations of top-down estimates due to satellite and model uncertainty, along with temporal and horizontal

resolution of available data was examined in Section 3.4. Furthermore, this top-down estimation was used to scale a new simulation of HCHO, and O₃ over Australia, described in Section 3.2.9.

I aim to improve understanding of ozone transported to the troposphere from the stratosphere in Australia and the southern ocean. In Chapter 4 the seasonal cycle of STT events was characterised, and their contribution to the SH extra-tropical tropospheric ozone budget quantified using GEOS-Chem to estimate ozone flux extrapolated from three measurement sites. Causal climatology and event seasonality were examined in Section 4.4. STT detection frequencies and modelled tropospheric ozone columns were used to estimate STT ozone flux near three sites in Section 4.6. Findings were compared against relevant literature, and the uncertainties involved in STT event detection and ozone flux estimation have also been examined.

5.2 Isoprene emissions

A new isoprene emissions estimate was created using OMI satellite measurements of HCHO. This estimate was compared against the bottom-up estimate from GEOS-Chem (running MEGAN). Generally months outside of May to August show the a posteriori lower than the a priori, except in the south eastern portion of Australia where only February was notably reduced. MEGAN isoprene emissions appear to be overestimated in Austral summer, suggesting poorly understood emission factors for Australian forests. The overall reduction over Australia was $\sim 46\%$, and the MEGAN based a priori emissions range from 2-5 times higher than the a posteriori. How these emissions affect ozone concentrations was examined through running GEOS-Chem with emissions scaled seasonally to match the a posteriori.

5.3 Ozone over Australia

Ozone production in the troposphere is a complex process involving various compounds. Tropospheric ozone is enhanced through VOC chemistry, stratospheric transport, and pollution. The first two of these processes are highly uncertain, with few studies performed on either topic within Australia. Of these ozone sources, VOC chemistry uncertainty is dominated by poor understanding of biogenic emissions (mainly) of isoprene. Emissions of isoprene have been globally modelled at $\sim 465\text{-}500 \text{ Tg C yr}^{-1}$ (Guenther et al. 2006; Messina et al. 2016). However these appear to be overestimated in Australia, as seen here with top-down estimates at $\sim 21 \text{ Tg C yr}^{-1}$ compared to $\sim 39 \text{ Tg C yr}^{-1}$ using GEOS-Chem (which implements MEGAN).

Tropospheric ozone production was estimated using GEOS-Chem before and after scaling isoprene emissions based on top-down satellite data. Figure 5.1 shows Australian summer surface level ozone with and without scaling isoprene emissions to match the multi-year top-down estimation. The reduction in surface ozone is approximately 5%, and most of this reduction is seen at the surface, as shown by only minimal ($< 1\%$) tropospheric column ozone reduction. This shows that modelled impacts from reduced isoprene emission are seen nearly completely in the surface level, and outweighed by other processes at higher altitudes.

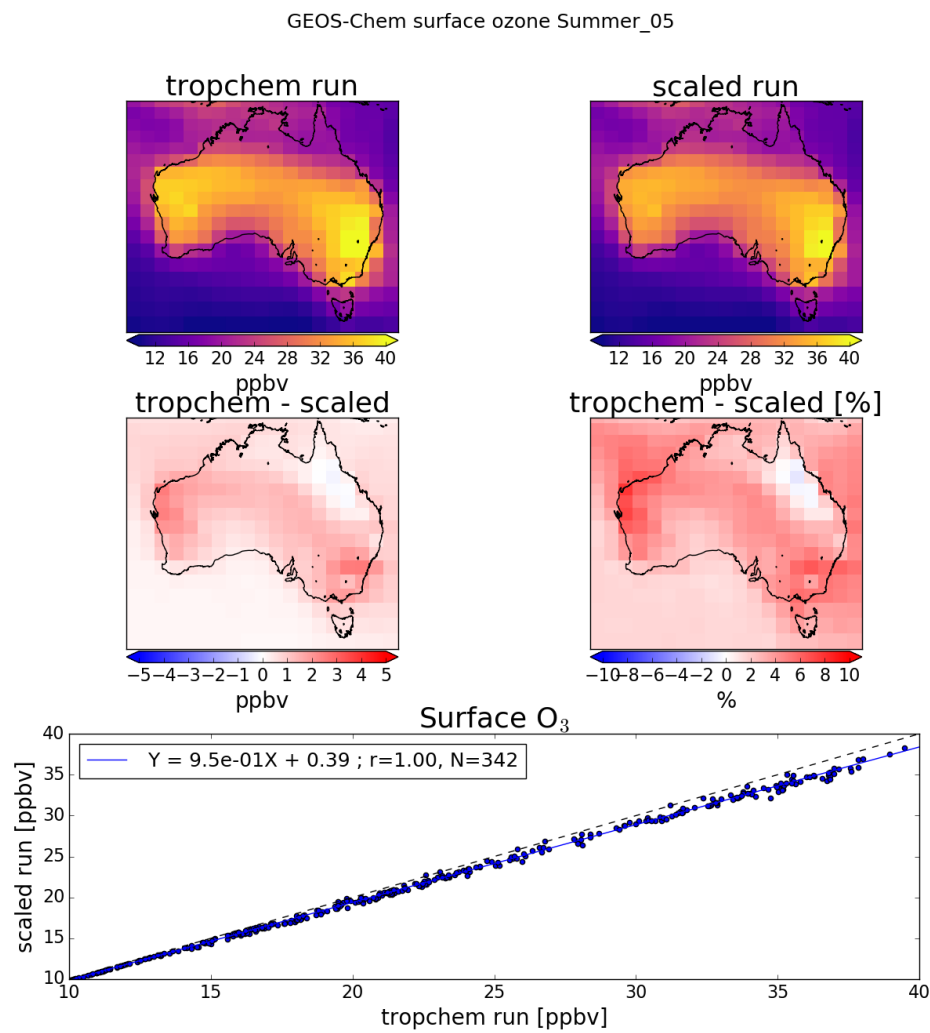


FIGURE 5.1: Top row: ozone maps before (left) and after (right) scaling isoprene emissions in GEOS-Chem for summer. Middle row: absolute (left) and relative (right) differences. The bottom panel shows the linear regression between the runs along with a black dashed line representing the 1-1 ratio.

TABLE 5.1: Isoprene emissions from MEGAN and top-down estimation in Tg a^{-1} , along with ozone tropospheric column amounts in $\text{O}_3 \text{ cm}^{-2} \times 10^{17}$.

Metric	AUS	SEA	NEA	NA	SWA	MID
MEGAN	43(2)	blah				
Ozone	9.70	11.17	11.03	11.19	11.69	9.09
Top-Down	19(2)					
Ozone	9.64	11.11	10.99	11.12	11.63	9.02

Standard deviations shown in parenthesis.

TODO: Update and fill in this table(currently just sample of 2005 values, need to use multi-year average to match text).

Ozone is one of the two measured air pollutants that have not fallen in concentration over the last 10 years (Keywood, Emmerson, and Hibberd 2016). Isoprene emissions are one of the important precursors to ozone production, and this has been examined in Section 3.3. The results have been tabulated for Australia and five sub-regions, shown here in Table 5.1. The sub-regions were detailed in Section 3.3 and shown again here in Figure 5.2. A 5% mean difference in surface ozone levels will directly affect exposure levels and impacts air quality estimates. This effect could be underestimated in cities due to the low horizontal resolution used in this thesis, as isoprene is most likely to impact city fringes (Millet et al. 2016).

Ozone transported from the stratosphere affects surface ozone levels, although this was hard to detect with the methods used in this thesis. We compared the effects of two disparate influences on the tropospheric ozone column. STT analysis over Melbourne suggests up to $\sim 10\%$ of the tropospheric column was due to stratospheric influx, with the average increase caused by influx being ~ 1 to 3.5% . From the biogenic source we see a relatively large ($\sim 50\%$) drop in isoprene emissions causes $\sim 1 - 5\%$ reduced surface ozone concentrations over summer. The direct correlation between reduced emissions and surface ozone reductions was not apparent without taking large area averages, likely due to the effects being down-wind of where isoprene emissions are reduced. Both STT and biogenic ozone sources become more important in summer, as STT occur more frequently and isoprene emissions increase with the summer high temperatures. The impacts were separated by altitude with most STT occurring in the free troposphere, while isoprene emission impacts were largely seen at the surface. Ozone in the free troposphere has the largest effect on climate, while surface ozone matters more when looking at air quality and ecosystem impacts.

5.4 Outputs

Analysis of STT along with an estimate of ozone flux from the stratosphere over a portion of Australia and the southern ocean was published in Greenslade et al. (2017). Ozone production using GEOS-Chem with updated top-down isoprene emissions

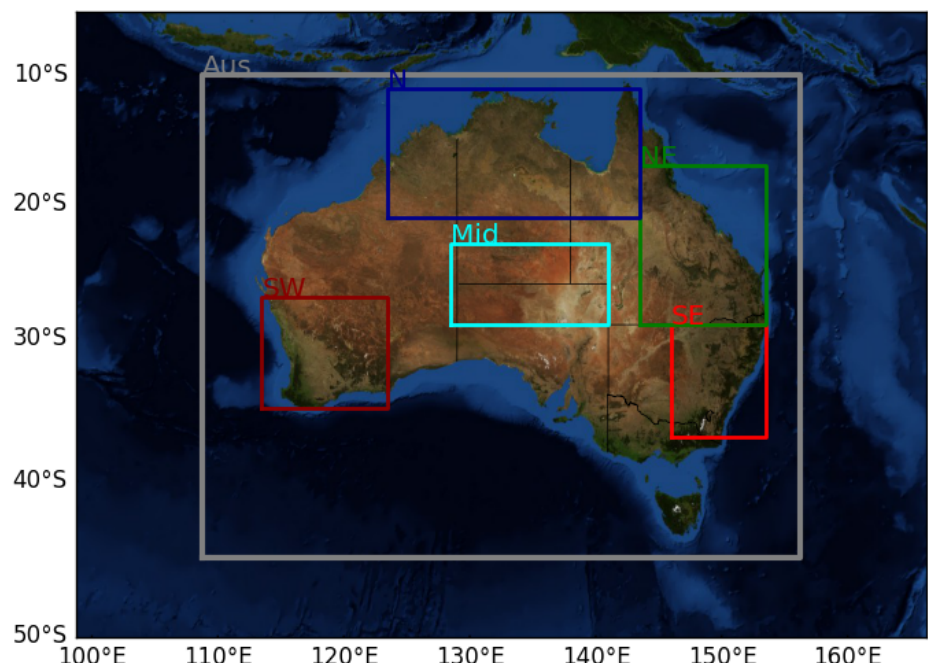


FIGURE 5.2: Sub-regions used in subsequent figures. Australia-wide averages will be black or grey, while results from within the coloured rectangles will match the colours shown here.

was examined in this thesis and may form part of a new publication in the near future with the aim of updating MEGAN isoprene emission factors in Australia.

A top down estimate of isoprene emissions over Australia created using OMI HCHO and GEOS-Chem modelled chemistry in Chapter 3 is currently in preparation to become a publication. Regridded OMI HCHO prepared in this thesis has been used in a publication currently under review (of which I am a co-author), which examines the HCHO trend over Wollongong over the last 20 years.

5.5 Future work

One important parameters dealing with isoprene emission in Australia is the soil moisture activity factor (γ_{SM}) (Sindelarova et al. 2014; Bauwens et al. 2016). Sindelarova et al. (2014) and more recently Emmerson et al. (2019) showed how Australian isoprene emissions could be as much as halved by accounting for lower soil moisture. Generally if soil moisture is too low, isoprene emissions stop (Pegoraro et al. 2004; Niinemets et al. 2010), however in many Australian regions the plants may be more adapted to lower moisture levels (Emmerson et al. 2019). GEOS-Chem runs MEGANv2.1, which has three possible states for isoprene emissions based on the soil moisture (θ):

$$\begin{array}{ll} \gamma_{SM} = 1 & \theta > \theta_1 \\ \gamma_{SM} = (\theta - \theta_w) / \Delta\theta_1 & \theta_w < \theta < \theta_1 \\ \gamma_{SM} = 0 & \theta < \theta_w \end{array}$$

where θ_w is the wilting point, and θ_1 determines when plants are near the wilting point. The wilting point is set by a land based database from Chen and Dudhia (2001), while θ_1 is set globally based on Pegoraro et al. (2004). These moisture states are not implemented in recent GEOS-Chem versions (including v10.01, used in this thesis). Improved isoprene emissions modelling requires this soil moisture problem to be handled. Simply enabling the parameter in its current form is not quite good enough for Australia, due to both the unknown soil moisture and the poorly understood plant responses in this country. Recently an update to this has been shown to improve modelled isoprene emissions in drought conditions (Jiang et al. 2018). Alternatively improving the soil moisture and drought process parameterisation in GEOS-Chem could be performed following a similar process to that shown in Emmerson et al. (2019), using satellite based soil moisture estimates. Calibrating and applying a soil moisture update to Australia would be a worthwhile future project. Testing improvements and sensitivity of modelled VOCs and ozone to a soil moisture update could provide useful information with which to update GEOS-Chem.

Using satellite data to improve isoprene emission estimates such as done in this thesis must be used to analyse model improvements, since fully independent measurements are lacking. Measurements of isoprene emissions in Australia would provide a valuable opportunity to verify improvements in emission estimates. Emissions

measurement would be greatly valuable however they remain expensive and difficult, especially over the large sparse environment which makes up the Australia outback. Working on prioritising measurement priorities for potential campaigns may be worthwhile in a future project, due to the limitations of coverage such operations can reasonably provide. For instance ground-and-aircraft-based VOC, NO_x, HCHO, and ozone measurements would greatly improve the understanding of both satellite biases and model uncertainties over Australia. Additionally, measurements in the northern forested areas of Australia could be used to improve how models handle the monsoonal conditions which are not likely to be represented by satellite measurements due to increased cloud coverage.

This thesis examines isoprene emissions and how they affect ozone concentrations at one resolution, using one satellite as the basis for a top-down inversion. Other satellites (e.g., GOME-2) could be included to allow more robust estimates as well as providing some diurnal resolution as each satellite has its own overpass time. An adjoint version of GEOS-Chem could be implemented over a smaller domain (either spatially or temporally or both) to provide more detailed analysis of both ozone and isoprene transport. This sort of modelling would also provide understanding of the resolution limitations of top-down emissions estimates, along with a clearer look at how sensitive the technique is to various parameters.

Considering ozone flux estimations based on ozone sondes, the process outlined in Chapter 4 could be applied to more ozonesondes. The work as published could be improved to automatically filter potential fire smoke influence using freely available satellite data, which would lead to a very simple and computationally inexpensive method for STT detection. A similar improvement based on online (or user specified) ozone concentration data would allow quick estimation of STT impacts, which are highly uncertain in many areas (especially in the southern hemisphere).

Bibliography

- NOAA. *Earth System Research Laboratory; Global Monitoring Division*. URL: https://esrl.noaa.gov/gmd/ccgg/trends/_ch4/.
- Brasseur, Guy P and Daniel J Jacob (2017). *Modeling of Atmospheric Chemistry*. Cambridge University Press. DOI: 10.1017/9781316544754.
- Atkinson, Roger (2000). "Atmospheric chemistry of VOCs and NO(x)". In: *Atmospheric Environment* 34.12-14, pp. 2063–2101. ISSN: 13522310. DOI: 10.1016/S1352-2310(99)00460-4.
- Fuentes, J. D. et al. (2000). "Biogenic Hydrocarbons in the Atmospheric Boundary Layer: A Review". In: *Bulletin of the American Meteorological Society* 81.7, pp. 1537–1575. ISSN: 00030007. DOI: 10.1175/1520-0477(2000)081<1537:BHITAB>2.3.CO;2. arXiv: arXiv:1011.1669v3. URL: [http://journals.ametsoc.org/doi/abs/10.1175/1520-0477\(2000\)081{\%}3C1537{\%}3ABHITAB{\%}3E2.3.CO{\%}3B2](http://journals.ametsoc.org/doi/abs/10.1175/1520-0477(2000)081{\%}3C1537{\%}3ABHITAB{\%}3E2.3.CO{\%}3B2).
- Travis, Katherine R et al. (2016). "Why do models overestimate surface ozone in the Southeast United States?" In: *Atmos. Chem. Phys* 16, pp. 13561–13577. DOI: 10.5194/acp-16-13561-2016. URL: www.atmos-chem-phys.net/16/13561/2016/.
- Paulot, Fabien et al. (2009b). "Unexpected Epoxide Formation in the". In: *Science* 325.2009, pp. 730–733. ISSN: 0036-8075. DOI: 10.1126/science.1172910.
- Atkinson, Roger and Janet Arey (2003). "Gas-phase tropospheric chemistry of biogenic volatile organic compounds: A review". In: *Atmospheric Environment* 37.SUPPL. 2. ISSN: 13522310. DOI: 10.1016/S1352-2310(03)00391-1.
- Stevenson, D. S. et al. (2013). "Tropospheric ozone changes, radiative forcing and attribution to emissions in the Atmospheric Chemistry and Climate Model Intercomparison Project (ACCMIP)". In: *Atmospheric Chemistry and Physics* 13.6, pp. 3063–3085. ISSN: 16807316. DOI: 10.5194/acp-13-3063-2013.
- Hegglin, Michaela I and Theodore G Shepherd (2009). "Large climate-induced changes in ultraviolet index and stratosphere-to-troposphere ozone flux". In: *Nature Geoscience* 2.10, pp. 687–691. DOI: 10.1038/ngeo604. URL: <http://dx.doi.org/10.1038/ngeo604>.
- Brinksma, E. J. et al. (2002). "Five years of observations of ozone profiles over Lauder, New Zealand". In: *Journal of Geophysical Research* 107.D14, pp. 1–11. ISSN: 0148-0227. DOI: 10.1029/2001JD000737. URL: <http://doi.wiley.com/10.1029/2001JD000737>.
- Hsieh, Nan-Hung and Chung-Min Liao (2013). "Fluctuations in air pollution give risk warning signals of asthma hospitalization". In: *Atmospheric Environment* 75, pp. 206–216. DOI: 10.1016/j.atmosenv.2013.04.043. URL: <http://dx.doi.org/10.1016/j.atmosenv.2013.04.043>.
- Avnery, Shiri et al. (2013). "Global crop yield reductions due to surface ozone exposure: 2. Year 2030 potential crop production losses and economic damage under two scenarios of O₃ pollution". In: *Atmospheric Environment* 71.13, pp. 408–409.

- ISSN: 13522310. DOI: 10.1016/j.atmosenv.2012.12.045. URL: <http://dx.doi.org/10.1016/j.atmosenv.2011.01.002>.
- Yue, Xu et al. (2017). "Ozone and haze pollution weakens net primary productivity in China". In: *Atmospheric Chemistry and Physics* 17.9, pp. 6073–6089. ISSN: 1680-7324. DOI: 10.5194/acp-17-6073-2017. URL: <https://www.atmos-chem-phys.net/17/6073/2017/>.
- Myhre, G and D Shindell (2013). *Chapter 8: Anthropogenic and Natural Radiative Forcing, in Climate Change 2013: The Physical Science Basis, Working Group 1 Contribution to the Fifth Assessment Report of the Intergovernmental Panel on Climate Change*, 2013. Fifth Assessment Report of the Intergovernmental Panel on Climate Change, 2013.
- Monks, P. S. et al. (2015). "Tropospheric ozone and its precursors from the urban to the global scale from air quality to short-lived climate forcer". In: *Atmospheric Chemistry and Physics* 15.15, pp. 8889–8973. ISSN: 1680-7324. DOI: 10.5194/acp-15-8889-2015. URL: <http://www.atmos-chem-phys.net/15/8889/2015/>.
- Lelieveld, J. et al. (2013). "Model calculated global, regional and megacity premature mortality due to air pollution". In: *Atmospheric Chemistry and Physics* 13.14, pp. 7023–7037. ISSN: 16807324. DOI: 10.5194/acp-13-7023-2013.
- Ayers, James D and William R Simpson (2006). "Measurements of N₂O₅ near Fairbanks, Alaska". In: *Journal of Geophysical Research: Atmospheres* 111.D14, n/a-n/a. ISSN: 2156-2202. DOI: 10.1029/2006JD007070. URL: <http://dx.doi.org/10.1029/2006JD007070>.
- Lelieveld, J. et al. (2009). "Severe ozone air pollution in the Persian Gulf region". In: *Atmospheric Chemistry and Physics* 9, pp. 1393–1406. ISSN: 1680-7324. DOI: 10.5194/acp-9-1393-2009.
- Ashmore, M R, Lisa Emberson, and Murray Frank (2003). *Air pollution impacts on crops and forests : a global assessment*. Ed. by Lisa Emberson, Mike Ashmore, and Frank Murray. Imperial College Press London ; River Edge, NJ, xiii, 372 p. : ISBN: 186094292.
- Selin, N E et al. (2009). "Global health and economic impacts of future ozone pollution". In: *Environmental Research Letters* 4.4, p. 044014. ISSN: 1748-9326. DOI: 10.1088/1748-9326/4/4/044014.
- Young, P J et al. (2017). "Tropospheric Ozone Assessment Report (TOAR): Assessment of global-scale model performance for global and regional ozone distributions, variability, and trends". In: *Elementa: Science of the Anthropocene*, pp. 0–84. ISSN: 2325-1026. DOI: 10.1525/elementa.265. URL: http://eprints.lancs.ac.uk/88836/1/TOAR{_}Model{_}Performance{_}07062017.pdf or http://www.igacproject.org/sites/default/files/2017-05/TOAR-Model{_}Performance{_}draft{_}for{_}open{_}comment.pdf.
- Stevenson, D S et al. (2006). "Multimodel ensemble simulations of present-day and near-future tropospheric ozone". In: *Journal of Geophysical Research* 111.D8. DOI: 10.1029/2005jd006338. URL: <http://dx.doi.org/10.1029/2005JD006338>.
- Stohl, Andreas et al. (2003). "A new perspective of stratosphere-troposphere exchange". In: *Bulletin of the American Meteorological Society* 84.11, pp. 1565–1573+1473. ISSN: 00030007. DOI: 10.1175/BAMS-84-11-1565.

- Guenther, A et al. (2006). "Estimates of global terrestrial isoprene emissions using {MEGAN} (Model of Emissions of Gases and Aerosols from Nature)". In: *Atmospheric Chemistry and Physics* 6.11, pp. 3181–3210. DOI: 10.5194/acp-6-3181-2006. URL: <http://dx.doi.org/10.5194/acp-6-3181-2006>.
- Jacobson, M C and H Hansson (2000). "Organic atmospheric aerosols: Review and state of the science". In: *Reviews of Geophysics* 38.38, pp. 267–294. ISSN: 87551209. DOI: 10.1029/1998RG000045. URL: <http://dx.doi.org/10.1029/1998RG000045>.
- Kuang, Shi et al. (2017). "Summertime tropospheric ozone enhancement associated with a cold front passage due to stratosphere-to-troposphere transport and biomass burning: Simultaneous ground-based lidar and airborne measurements". In: *Journal of Geophysical Research: Atmospheres* 122.2, pp. 1293–1311. ISSN: 21698996. DOI: 10.1002/2016JD026078. URL: <http://doi.wiley.com/10.1002/2016JD026078>.
- Cooper, O. et al. (2004). "On the life cycle of a stratospheric intrusion and its dispersion into polluted warm conveyor belts". In: *Journal of Geophysical Research* 109.23, pp. 1–18. ISSN: 01480227. DOI: 10.1029/2003JD004006.
- Young, P. J. et al. (2013). "Preindustrial to present-day changes in tropospheric hydroxyl radical and methane lifetime from the Atmospheric Chemistry and Climate Model Intercomparison Project (ACCMIP)". In: *Atmospheric Chemistry and Physics* 13.10, pp. 5277–5298. ISSN: 16807316. DOI: 10.5194/acp-13-5277-2013.
- Sprenger, Michael, Mischa Croci Maspoli, and Heini Wernli (2003). "Tropopause folds and cross-tropopause exchange: A global investigation based upon ECMWF analyses for the time period March 2000 to February 2001". In: *Journal of Geophysical Research* 108.D12. ISSN: 2156-2202. DOI: 10.1029/2002JD002587. URL: <http://dx.doi.org/10.1029/2002JD002587>.
- Ojha, Narendra et al. (2016). "Secondary ozone peaks in the troposphere over the Himalayas". In: *Atmospheric Chemistry and Physics Discussions* 17.November, pp. 1–25. ISSN: 1680-7375. DOI: 10.5194/acp-2016-908. URL: <http://www.atmos-chem-phys-discuss.net/acp-2016-908/>.
- Lin, Meiyun et al. (2015). "Climate variability modulates western US ozone air quality in spring via deep stratospheric intrusions." In: *Nature communications* 6.May, p. 7105. ISSN: 2041-1723. DOI: 10.1038/ncomms8105. URL: <http://www.nature.com/ncomms/2015/150512/ncomms8105/full/ncomms8105.html>.
- Liu, Junhua et al. (2017a). "Causes of interannual variability over the southern hemispheric tropospheric ozone maximum". In: *Atmos. Chem. Phys* 17.5, pp. 3279–3299. ISSN: 1680-7324. DOI: 10.5194/acp-17-3279-2017. URL: <http://www.atmos-chem-phys.net/17/3279/2017/>.
- Marvin, Margaret R. et al. (2017). "Impact of evolving isoprene mechanisms on simulated formaldehyde: An inter-comparison supported by in situ observations from SENEX". In: *Atmospheric Environment* 164, pp. 325–336. ISSN: 13522310. DOI: 10.1016/j.atmosenv.2017.05.049. URL: https://ac.els-cdn.com/S1352231017303618/1-s2.0-S1352231017303618-main.pdf?{_}tid=3de7eaaa-06ff-11e8-99a9-0000aacb360{\&}acdnat=1517455576{_}09d7334af609ed43470155c1c42fad5fhttp://www.sciencedirect.com/science/article/pii/S1352231017303618.

- Mazzuca, Gina M. et al. (2016). "Ozone production and its sensitivity to NO_x and VOCs: Results from the DISCOVER-AQ field experiment, Houston 2013". In: *Atmospheric Chemistry and Physics* 16.22, pp. 14463–14474. ISSN: 16807324. DOI: 10.5194/acp-16-14463-2016.
- Cape, J. N. (2008). "Surface ozone concentrations and ecosystem health: Past trends and a guide to future projections". In: *Science of the Total Environment* 400.1-3, pp. 257–269. ISSN: 00489697. DOI: 10.1016/j.scitotenv.2008.06.025. URL: <http://dx.doi.org/10.1016/j.scitotenv.2008.06.025>.
- Christian, Kenneth E. et al. (2018). "Global sensitivity analysis of GEOS-Chem modeled ozone and hydrogen oxides during the INTEX campaigns". In: *Atmospheric Chemistry and Physics* 18.4, pp. 2443–2460. ISSN: 1680-7324. DOI: 10.5194/acp-18-2443-2018. URL: <https://www.atmos-chem-phys.net/18/2443/2018/>.
- Delmas, R, D Serca, and C Jambert (1997). "Global inventory of NO_x sources". In: *Nutrient cycling in agroecosystems* 48.x, pp. 51–60. ISSN: 1385-1314. DOI: 10.1023/A:1009793806086. URL: <http://link.springer.com/article/10.1023/A:1009793806086>.
- Romer Present, Paul S., Azimeh Zare, and Ronald C. Cohen (2019). "The changing role of organic nitrates in the removal and transport of NO_x". In: *Atmospheric Chemistry and Physics Discussions* x, pp. 1–18. DOI: 10.5194/acp-2019-471. URL: <https://www.atmos-chem-phys-discuss.net/acp-2019-471/>.
- Cooper, O R, S Gilge, and D T Shindell (2014). "Global distribution and trends of tropospheric ozone : An observation-based review". In: pp. 1–28. DOI: 10.12952/journal.elementa.000029. URL: <https://www.elementascience.org/articles/10.12952/journal.elementa.000029/>.
- Sillman, Sanford (1999). "The relation between ozone , NO and hydrocarbons in urban and polluted rural environments". In: *Atmospheric Environment* 33. DOI: [https://doi.org/10.1016/S1352-2310\(98\)00345-8](https://doi.org/10.1016/S1352-2310(98)00345-8). URL: <http://www-personal.umich.edu/~sillman/web-publications/Sillmanreview99.pdf><https://www.sciencedirect.com/science/article/pii/S1352231098003458>.
- Guenther, Alex et al. (1995). "A global model of natural volatile organic compound emissions". In: *Journal of Geophysical Research* 100.D5, pp. 8873–8892. ISSN: 0148-0227. DOI: 10.1029/94JD02950. URL: <http://onlinelibrary.wiley.com/doi/10.1029/94JD02950/full><http://onlinelibrary.wiley.com/doi/10.1029/94JD02950>
- Glasius, Marianne and Allen H. Goldstein (2016). "Recent Discoveries and Future Challenges in Atmospheric Organic Chemistry". In: *Environmental Science and Technology* 50.6, pp. 2754–2764. ISSN: 15205851. DOI: 10.1021/acs.est.5b05105.
- Guenther, Alex et al. (2000). "Natural emissions of non-methane volatile organic compounds, carbon monoxide, and oxides of nitrogen from North America". In: *Atmospheric Environment* 34.12-14, pp. 2205–2230. ISSN: 13522310. DOI: 10.1016/S1352-2310(99)00465-3.
- Yue, X., N. Unger, and Y. Zheng (2015). "Distinguishing the drivers of trends in land carbon fluxes and plant volatile emissions over the past 3 decades". In: *Atmospheric Chemistry and Physics* 15.20, pp. 11931–11948. ISSN: 16807324. DOI: 10.5194/acp-15-11931-2015.

- Stavrakou, T. et al. (2014). "Isoprene emissions over Asia 1979-2012: Impact of climate and land-use changes". In: *Atmospheric Chemistry and Physics* 14.9. ISSN: 16807324. DOI: 10.5194/acp-14-4587-2014. URL: <https://www.atmos-chem-phys.net/14/4587/2014/acp-14-4587-2014.pdf>.
- Kwon, Hyeong-Ahn et al. (2017). "Sensitivity of formaldehyde (HCHO) column measurements from a geostationary satellite to temporal variation of the air mass factor in East Asia". In: *Atmospheric Chemistry and Physics* 17.7, pp. 4673–4686. ISSN: 1680-7324. DOI: 10.5194/acp-17-4673-2017. URL: <http://www.atmos-chem-phys.net/17/4673/2017/>.
- Hoek, Gerard et al. (2013). "Long-term air pollution exposure and cardio-respiratory mortality: a review". In: *Environmental Health* 12.1, p. 43. DOI: 10.1186/1476-069x-12-43. URL: <http://dx.doi.org/10.1186/1476-069x-12-43>.
- Krewski, D et al. (2009). "Extended follow-up and spatial analysis of the American Cancer Society study linking particulate air pollution and mortality". In: *Res Rep Health Eff Inst* 140, pp. 5–36. ISSN: 1041-5505 (Print) 1041-5505 (Linking). URL: <http://www.ncbi.nlm.nih.gov/pubmed/19627030>.
- Silva, Raquel A et al. (2013). "Global premature mortality due to anthropogenic outdoor air pollution and the contribution of past climate change". In: *Environ. Res. Lett.* 8.3, p. 34005. DOI: 10.1088/1748-9326/8/3/034005. URL: <http://dx.doi.org/10.1088/1748-9326/8/3/034005>.
- Lelieveld, J et al. (2015). "The contribution of outdoor air pollution sources to premature mortality on a global scale". In: *Nature* 525.7569, pp. 367–371. DOI: 10.1038/nature15371. URL: <http://dx.doi.org/10.1038/nature15371>.
- Kanakidou, M et al. (2005). "Physics Organic aerosol and global climate modelling : a review". In: *Atmospheric Chemistry and Physics* 5, pp. 1053–1123.
- Kroll, Jesse H. and John H. Seinfeld (2008). "Chemistry of secondary organic aerosols: Formation and evolution of low-volatility organics in the atmosphere". In: *Atmospheric Environment* 42.16, pp. 3593–3624. ISSN: 13522310. DOI: 10.1016/j.atmosenv.2008.01.003. URL: <http://www.sciencedirect.com.ezproxy.uow.edu.au/science/article/pii/S1352231008000253>.
- Guenther, A. B. et al. (2012). "The model of emissions of gases and aerosols from nature version 2.1 (MEGAN2.1): An extended and updated framework for modeling biogenic emissions". In: *Geoscientific Model Development* 5.6, pp. 1471–1492. ISSN: 1991959X. DOI: 10.5194/gmd-5-1471-2012.
- Brown, S. S. et al. (2009). "Nocturnal isoprene oxidation over the Northeast United States in summer and its impact on reactive nitrogen partitioning and secondary organic aerosol". In: *Atmospheric Chemistry and Physics* 9.9, pp. 3027–3042. ISSN: 16807316. DOI: 10.5194/acp-9-3027-2009.
- Kefauver, Shawn C., Iolanda Filella, and Josep Peñuelas (2014). "Remote sensing of atmospheric biogenic volatile organic compounds (BVOCs) via satellite-based formaldehyde vertical column assessments". en. In: *International Journal of Remote Sensing*. URL: <http://www.tandfonline.com/doi/abs/10.1080/01431161.2014.968690{\#}.VkqEubNM61M>.
- Millet, Dylan B et al. (2006). "Formaldehyde distribution over North America: Implications for satellite retrievals of formaldehyde columns and isoprene emission". In: *J. Geophys. Res.* 111.D24. DOI: 10.1029/2005jd006853. URL: TODO.

- Arneth, A et al. (2008). "Why are estimates of global terrestrial isoprene emissions so similar (and why is this not so for monoterpenes)?" In: *Atmos. Chem. Phys* 8.x, pp. 4605–4620. ISSN: 1680-7375. DOI: 10.5194/acpd-8-7017-2008.
- Niinemets, U. et al. (2010). "The emission factor of volatile isoprenoids: Stress, acclimation, and developmental responses". In: *Biogeosciences* 7.7, pp. 2203–2223. ISSN: 17264170. DOI: 10.5194/bg-7-2203-2010.
- Lathière, J et al. (2006). "Impact of climate variability and land use changes on global biogenic volatile organic compound emissions". In: *Atmospheric Chemistry and Physics* 6.2003, pp. 2129–2146. ISSN: 16807324. DOI: 10.5194/acp-6-2129-2006. URL: www.atmos-chem-phys.net/6/2129/2006/.
- Messina, Palmira et al. (2016). "Global biogenic volatile organic compound emissions in the ORCHIDEE and MEGAN models and sensitivity to key parameters". In: *Atmospheric Chemistry and Physics* 16.22, pp. 14169–14202. ISSN: 16807324. DOI: 10.5194/acp-16-14169-2016. URL: <http://www.atmos-chem-phys.net/16/14169/2016/acp-16-14169-2016.pdf>.
- Sindelarova, K. et al. (2014). "Global data set of biogenic VOC emissions calculated by the MEGAN model over the last 30 years". In: *Atmospheric Chemistry and Physics* 14.17, pp. 9317–9341. ISSN: 16807324. DOI: 10.5194/acp-14-9317-2014. arXiv: [arXiv:1011.1669v3](https://arxiv.org/abs/1011.1669v3).
- Wagner, V (2002). "Are CH₂O measurements in the marine boundary layer suitable for testing the current understanding of CH₄ photooxidation?: A model study". In: *Journal of Geophysical Research* 107.D3, p. 4029. ISSN: 0148-0227. DOI: 10.1029/2001JD000722. URL: <http://doi.wiley.com/10.1029/2001JD000722>.
- Nguyen, Tran B. et al. (2016). "Atmospheric fates of Criegee intermediates in the ozonolysis of isoprene". In: *Phys. Chem. Chem. Phys.* 18.15, pp. 10241–10254. ISSN: 1463-9076. DOI: 10.1039/C6CP00053C. URL: <http://xlink.rsc.org/?DOI=C6CP00053C>.
- Wolfe, G. M. et al. (2016). "Formaldehyde production from isoprene oxidation across NO_x regimes". In: *Atmospheric Chemistry and Physics* 16.x, pp. 2597–2610. ISSN: 16807324. DOI: 10.5194/acp-16-2597-2016. URL: www.atmos-chem-phys.net/16/2597/2016/.
- Nguyen, T. B. et al. (2014). "Overview of the Focused Isoprene eXperiment at the California Institute of Technology (FIXCIT): Mechanistic chamber studies on the oxidation of biogenic compounds". In: *Atmospheric Chemistry and Physics* 14.24. ISSN: 16807324. DOI: 10.5194/acp-14-13531-2014.
- Arneth, Almut et al. (2007). "CO₂ inhibition of global terrestrial isoprene emissions: Potential implications for atmospheric chemistry". In: *Geophysical Research Letters* 34.18, p. L18813. DOI: 10.1029/2007GL030615. URL: <http://doi.wiley.com/10.1029/2007GL030615>.
- Hewitt, C N et al. (2011). "Ground-level ozone influenced by circadian control of isoprene emissions". In: *Nature Geoscience* 4.10, pp. 671–674. DOI: 10.1038/ngeo1271. URL: <http://dx.doi.org/10.1038/ngeo1271>.
- Fan, Jiwen and Renyi Zhang (2004). "Atmospheric oxidation mechanism of isoprene". In: *Environmental Chemistry* 1.3, pp. 140–149. ISSN: 14482517. DOI: 10.1071/EN04045. URL: <http://dx.doi.org/10.1071/en04045>.
- Jiang, Xiaoyan et al. (2018). "Isoprene emission response to drought and the impact on global atmospheric chemistry". In: *Atmospheric Environment* 183, pp. 69–83. ISSN:

- 1352–2310. DOI: 10.1016/J.ATMOSENV.2018.01.026. URL: <https://www.sciencedirect.com/science/article/pii/S1352231018300402>.
- Patchen, Amie K. et al. (2007). "Direct Kinetics Study of the Product-Forming Channel of the Reaction of Isoprene-Derived Hydroxyperoxy Radicals with NO". In: *International journal of Chemical Kinetics* 31.5, pp. 493–499. ISSN: 13000527. DOI: 10.1002/kin. URL: <http://onlinelibrary.wiley.com/wol1/doi/10.1002/kin.20248/full>.
- Mao, Jingqiu et al. (2013). "Ozone and organic nitrates over the eastern United States: Sensitivity to isoprene chemistry". In: *Journal of Geophysical Research Atmospheres* 118.19, pp. 11256–11268. ISSN: 21698996. DOI: 10.1002/jgrd.50817.
- Crounse, John D et al. (2012). "Atmospheric Fate of Methacrolein. 1. Peroxy Radical Isomerization Following Addition of OH and O₂". In: *Physical Chemistry m.*
- Paulot, F, D K Henze, and P O Wennberg (2012). "Impact of the isoprene photochemical cascade on tropical ozone". In: *Atmos. Chem. Phys. Atmospheric Chemistry and Physics* 12, pp. 1307–1325. DOI: 10.5194/acp-12-1307-2012. URL: www.atmos-chem-phys.net/12/1307/2012/.
- Crounse, John D. et al. (2013). "Autoxidation of organic compounds in the atmosphere". In: *Journal of Physical Chemistry Letters* 4.20, pp. 3513–3520. ISSN: 19487185. DOI: 10.1021/jz4019207. URL: <http://pubs.acs.org/doi/abs/10.1021/jz4019207>.
- Crounse, John D. et al. (2006). "Measurement of gas-phase hydroperoxides by chemical ionization mass spectrometry". In: *Analytical Chemistry* 78.19, pp. 6726–6732. ISSN: 00032700. DOI: 10.1021/ac0604235. URL: <https://pubs.acs.org/doi/abs/10.1021/ac0604235>.
- Yu, Karen et al. (2016). "Sensitivity to grid resolution in the ability of a chemical transport model to simulate observed oxidant chemistry under high-isoprene conditions". In: *Atmospheric Chemistry and Physics* 16.7, pp. 4369–4378. ISSN: 16807324. DOI: 10.5194/acp-16-4369-2016. URL: <http://acmg.seas.harvard.edu/publications/2016/Yu\ACP\2016.pdf>.
- Marais, E A et al. (2012). "Isoprene emissions in Africa inferred from {OMI} observations of formaldehyde columns". In: *Atmospheric Chemistry and Physics* 12.3, pp. 7475–7520. DOI: 10.5194/acp-12-6219-2012. URL: <http://dx.doi.org/10.5194/acp-12-6219-2012>.
- Liu, Yingjun et al. (2016b). "Isoprene photochemistry over the Amazon rainforest". In: *Proceedings of the National Academy of Sciences* 113.22, pp. 6125–6130. ISSN: 0027-8424. DOI: 10.1073/pnas.1524136113. URL: <http://www.pnas.org/content/113/22/6125.abstract>.
- Fisher, Jenny A. et al. (2016). "Organic nitrate chemistry and its implications for nitrogen budgets in an isoprene- and monoterpane-rich atmosphere: Constraints from aircraft (SEAC 4 RS) and ground-based (SOAS) observations in the Southeast US". In: *Atmospheric Chemistry and Physics* 16.9, pp. 5969–5991. ISSN: 16807324. DOI: 10.5194/acp-16-5969-2016. URL: <https://www.atmos-chem-phys.net/16/5969/2016/acp-16-5969-2016.pdf>.
- Paulot, F. et al. (2009a). "Isoprene photooxidation: new insights into the production of acids and organic nitrates". In: *Atmospheric Chemistry and Physics* 9.4, pp. 1479–1501. ISSN: 1680-7324. DOI: 10.5194/acp-9-1479-2009.

- Palmer, Paul I et al. (2006). "Quantifying the seasonal and interannual variability of North American isoprene emissions using satellite observations of the formaldehyde column". In: *J.Geophys.Res.* 111, p. D12315. ISSN: 0148-0227. DOI: 10.1029/2005JD006689. URL: <http://dx.doi.org/10.1029/2005JD006689>.
- Liu, Y. J. et al. (2013). "Production of methyl vinyl ketone and methacrolein via the hydroperoxy pathway of isoprene oxidation". In: *Atmospheric Chemistry and Physics* 13.11, pp. 5715–5730. ISSN: 1680-7324. DOI: 10.5194/acp-13-5715-2013. URL: <http://www.atmos-chem-phys.net/13/5715/2013/>.
- Peeters, Jozef and Jean-Francis Muller (2010). "HO_x radical regeneration in isoprene oxidation via peroxy radical isomerisations. II: experimental evidence and global impact". In: *Physical Chemistry Chemical Physics* 12.42, p. 14227. ISSN: 1463-9076. DOI: 10.1039/c0cp00811g. URL: <http://pubs.rsc.org/en/content/articlepdf/2010/cp/c0cp00811g>.
- Mao, J. et al. (2012). "Insights into hydroxyl measurements and atmospheric oxidation in a California forest". In: *Atmospheric Chemistry and Physics* 12.17, pp. 8009–8020. ISSN: 16807316. DOI: 10.5194/acp-12-8009-2012.
- Peeters, J., T. L. Nguyen, and L. Vereecken (2009). "HO_x radical regeneration in the oxidation of isoprene". In: *Physical Chemistry Chemical Physics* 11.28, p. 5935. ISSN: 1463-9076. DOI: 10.1039/b908511d. URL: <http://xlink.rsc.org/?DOI=b908511d>.
- Wolfe, Glenn M. et al. (2012). "Photolysis, OH reactivity and ozone reactivity of a proxy for isoprene-derived hydroperoxyenals (HPALDs)". In: *Physical Chemistry Chemical Physics* 14.20, p. 7276. ISSN: 1463-9076. DOI: 10.1039/c2cp40388a. URL: <http://xlink.rsc.org/?DOI=c2cp40388a>.
- Rollins, A W et al. (2009). "Isoprene oxidation by nitrate radical: alkyl nitrate and secondary organic aerosol yields". In: *Atmos. Chem. Phys. Atmospheric Chemistry and Physics* 9, pp. 6685–6703. URL: www.atmos-chem-phys.net/9/6685/2009/.
- Emmerson, Kathryn M. et al. (2016). "Current estimates of biogenic emissions from eucalypts uncertain for southeast Australia". In: *Atmospheric Chemistry and Physics* 16.11, pp. 6997–7011. ISSN: 1680-7324. DOI: 10.5194/acp-16-6997-2016. URL: <http://www.atmos-chem-phys.net/16/6997/2016/>.
- Stocker, T.F. et al. *IPCC, 2013: Climate Change 2013: The Physical Science Basis. Contribution of Working Group I to the Fifth Assessment Report of the Intergovernmental Panel on Climate Change*. Tech. rep. Cambridge University Press, Cambridge, United Kingdom and New York, NY, USA. DOI: 10.1017/CBO9781107415324.
- Forster, P. et al. (2007). *Changes in Atmospheric Constituents and in Radiative Forcing*. In: *Climate Change 2007: The Physical Science Basis. Contribution of Working Group I to the Fourth Assessment Report of the Intergovernmental Panel on Climate Change* [Solomon, S., D. Qin, M. Man. URL: https://www.ipcc.ch/publications_and_data/ar4/wg1/en/ch2.html (visited on 01/14/2016).
- Fu, Tzung-may et al. (2007). "Space-based formaldehyde measurements as constraints on volatile organic compound emissions in east and south Asia and implications for ozone". In: 112, pp. 1–15. DOI: 10.1029/2006JD007853.
- Dufour, G. et al. (2008). "SCIAMACHY formaldehyde observations: constraint for isoprene emissions over Europe?" In: *Atmospheric Chemistry and Physics* 8.6, pp. 19273–19312. ISSN: 1680-7324. DOI: 10.5194/acpd-8-19273-2008.

- Bauwens, M et al. (2013). "Satellite-based isoprene emission estimates (2007–2012) from the GlobEmission project". In: *Proceedings of the ACCENT-Plus Symposium, Atmospheric Composition Change-Policy Support and Science, Urbino*, pp. 17–20.
- Bauwens, Maite et al. (2016). "Nine years of global hydrocarbon emissions based on source inversion of OMI formaldehyde observations". In: *Atmospheric Chemistry and Physics* March, pp. 1–45. ISSN: 1680-7375. DOI: 10.5194/acp-2016-221. URL: <http://www.atmos-chem-phys-discuss.net/acp-2016-221/>.
- Surl, Luke, Paul I. Palmer, and Gonzalo G. Abad (2018). "Which processes drive observed variations of HCHO columns over India?" In: *Atmospheric Chemistry and Physics* 18.March, pp. 4549–4566. DOI: 10.5194/acp-18-4549-2018. URL: <https://doi.org/10.5194/acp-18-4549-2018>.
- Fortems-Cheiney, A. et al. (2012). "The formaldehyde budget as seen by a global-scale multi-constraint and multi-species inversion system". In: *Atmospheric Chemistry and Physics* 12.15, pp. 6699–6721. ISSN: 16807316. DOI: 10.5194/acp-12-6699-2012. URL: <http://www.atmos-chem-phys.net/12/6699/2012/acp-12-6699-2012.pdf>.
- Palmer, Paul I et al. (2003). "Mapping isoprene emissions over North America using formaldehyde column observations from space". In: *J. Geophys. Res.* 108.D6. DOI: 10.1029/2002jd002153. URL: <http://dx.doi.org/10.1029/2002jd002153>.
- Shim, Changsub et al. (2005). "Constraining global isoprene emissions with Global Ozone Monitoring Experiment (GOME) formaldehyde column measurements". In: *Journal of Geophysical Research Atmospheres* 110.24, pp. 1–14. ISSN: 01480227. DOI: 10.1029/2004JD005629.
- Millet, Dylan B. et al. (2008). "Spatial distribution of isoprene emissions from North America derived from formaldehyde column measurements by the OMI satellite sensor". In: *Journal of Geophysical Research Atmospheres* 113.2, pp. 1–18. ISSN: 01480227. DOI: 10.1029/2007JD008950.
- Zhu, Lei et al. (2014). "Anthropogenic emissions of highly reactive volatile organic compounds in eastern Texas inferred from oversampling of satellite (OMI) measurements of HCHO columns". In: *Environmental Research Letters* 9.11, p. 114004. ISSN: 1748-9326. DOI: 10.1088/1748-9326/9/11/114004. URL: <http://stacks.iop.org/1748-9326/9/i=11/a=114004?key=crossref.3d2869ee02fd4f0792f831ac8cbe117>.
- Levy, Hiram (1972). "Photochemistry of the lower troposphere". In: *Planetary and Space Science* 20.6, pp. 919–935. ISSN: 00320633. DOI: 10.1016/0032-0633(72)90177-8.
- Crutzen, Paul J, Mark G Lawrence, and Ulrich Poschl (1999). "On the background photochemistry of tropospheric ozone". In: *Tellus A* 51.1, pp. 123–146. ISSN: 1600-0870. DOI: 10.1034/j.1600-0870.1999.t01-1-00010.x. URL: <http://dx.doi.org/10.1034/j.1600-0870.1999.t01-1-00010.x>.
- Ayers, G. P. et al. (1997). "Formaldehyde production in clean marine air". In: *Geophysical Research Letters* 24.4. DOI: <https://doi.org/10.1029/97GL00123>.
- Franco, B. et al. (2015). "Retrievals of formaldehyde from ground-based FTIR and MAX-DOAS observations at the Jungfraujoch station and comparisons with GEOS-Chem and IMAGES model simulations". In: *Atmospheric Measurement Techniques* 8.4, pp. 1733–1756. ISSN: 18678548. DOI: 10.5194/amt-8-1733-2015.
- Gonzalez Abad, G. et al. (2015). "Updated Smithsonian Astrophysical Observatory Ozone Monitoring Instrument (SAO OMI) formaldehyde retrieval". In: *Atmospheric*

- Measurement Techniques* 8.1, pp. 19–32. ISSN: 18678548. DOI: 10.5194/amt-8-19-2015.
- Davenport, J. J. et al. (2015). "A measurement strategy for non-dispersive ultra-violet detection of formaldehyde in indoor air : spectral analysis and interferent gases". In: *Measurement Science and Technology* 015802. December 2015, p. 15802. ISSN: 0957-0233. DOI: 10.1088/0957-0233/27/1/015802. URL: <http://dx.doi.org/10.1088/0957-0233/27/1/015802>.
- Lee, Anita et al. (2006). "Gas-phase products and secondary aerosol yields from the ozonolysis of ten different terpenes". In: 111.Ci, pp. 1–18. DOI: 10.1029/2005JD006437.
- Lerner, Brian M. et al. (2017). "An improved, automated whole air sampler and gas chromatography mass spectrometry analysis system for volatile organic compounds in the atmosphere". In: *Atmospheric Measurement Techniques* 10.1, pp. 291–313. ISSN: 18678548. DOI: 10.5194/amt-10-291-2017. URL: <https://www.atmos-meas-tech.net/10/291/2017/amt-10-291-2017.pdf>.
- Hak, C. et al. (2005). "Intercomparison of four different in-situ techniques for ambient formaldehyde measurements in urban air". In: *Atmospheric Chemistry and Physics Discussions* 5.3, pp. 2897–2945. ISSN: 1680-7316. DOI: 10.5194/acpd-5-2897-2005.
- EUMETSAT (2015). GOME2. URL: <http://www.eumetsat.int/website/home/Satellites/CurrentSatellites/Metop/MetopDesign/GOME2/index.html>.
- Marais, E A et al. (2014). "Improved model of isoprene emissions in Africa using Ozone Monitoring Instrument (OMI) satellite observations of formaldehyde: implications for oxidants and particulate matter". In: *Atmospheric Chemistry and Physics* 14.15, pp. 7693–7703. DOI: 10.5194/acp-14-7693-2014. URL: <http://dx.doi.org/10.5194/acp-14-7693-2014>.
- De Smedt, I. et al. (2015). "Diurnal, seasonal and long-term variations of global formaldehyde columns inferred from combined OMI and GOME-2 observations". In: *Atmospheric Chemistry and Physics* 15.21, pp. 12519–12545. ISSN: 16807324. DOI: 10.5194/acp-15-12519-2015. URL: <https://www.atmos-chem-phys.net/15/12519/2015/acp-15-12519-2015.pdf>.
- Zhu, Lei et al. (2016). "Observing atmospheric formaldehyde (HCHO) from space: validation and intercomparison of six retrievals from four satellites (OMI, GOME2A, GOME2B, OMPS) with SEAC4RS aircraft observations over the Southeast US". In: *Atmospheric Chemistry and Physics* 0, pp. 1–24. ISSN: 1680-7375. DOI: 10.5194/acp-2016-162. URL: <http://www.atmos-chem-phys.net/16/13477/2016/acp-16-13477-2016.pdf>.
- Lorente, Alba et al. (2017). "Structural uncertainty in air mass factor calculation for NO₂ and HCHO satellite retrievals". In: *Atmospheric Measurement Techniques* 2, pp. 1–35. ISSN: 1867-8610. DOI: 10.5194/amt-10-759-2017. URL: <https://www.atmos-meas-tech.net/10/759/2017/amt-10-759-2017.html>
- Jacob, Daniel J (1999). *Introduction to Atmospheric Chemistry*. Ed. by Daniel J Jacob. Princeton University Press. URL: <http://acmg.seas.harvard.edu/people/faculty/djj/book/index.html>.

- Zhang, Yang et al. (2012). "Impact of gas-phase mechanisms on Weather Research Forecasting Model with Chemistry (WRF/Chem) predictions: Mechanism implementation and comparative evaluation". In: *Journal of Geophysical Research: Atmospheres* 117.D1, n/a-n/a. DOI: 10.1029/2011JD015775. URL: <http://doi.wiley.com/10.1029/2011JD015775>.
- Zeng, G. et al. (2015). "Multi-model simulation of CO and HCHO in the Southern Hemisphere: comparison with observations and impact of biogenic emissions". In: *Atmospheric Chemistry and Physics* 15.13, pp. 7217–7245. ISSN: 1680-7324. DOI: 10.5194/acp-15-7217-2015. URL: <http://www.atmos-chem-phys.net/15/7217/2015/>.
- Christian, Kenneth E, William H Brune, and Jingqiu Mao (2017). "Global sensitivity analysis of the GEOS-Chem chemical transport model: ozone and hydrogen oxides during ARCTAS (2008)". In: *Atmos. Chem. Phys* 17, pp. 3769–3784. DOI: 10.5194/acp-17-3769-2017. URL: www.atmos-chem-phys.net/17/3769/2017/.
- Miller, C. et al. (2014). "Glyoxal retrieval from the Ozone Monitoring Instrument". In: *Atmospheric Measurement Techniques* 7.11, pp. 3891–3907. ISSN: 1867-8548. DOI: 10.5194/amt-7-3891-2014. URL: <http://www.atmos-meas-tech.net/7/3891/2014/>.
- Wild, Oliver and Michael J. Prather (2006). "Global tropospheric ozone modeling: Quantifying errors due to grid resolution". In: *Journal of Geophysical Research Atmospheres* 111.11, pp. 1–14. ISSN: 01480227. DOI: 10.1029/2005JD006605.
- VanDerA, R J et al. (2008). "Trends seasonal variability and dominant {NO} x source derived from a ten year record of {NO} 2 measured from space". In: *J. Geophys. Res.* 113.D4. DOI: 10.1029/2007jd009021. URL: <http://dx.doi.org/10.1029/2007jd009021>.
- Lawson, Sarah J. et al. (2017). "Biomass burning at Cape Grim: Exploring photochemistry using multi-scale modelling". In: *Atmospheric Chemistry and Physics* 17.19, pp. 11707–11726. ISSN: 16807324. DOI: 10.5194/acp-17-11707-2017. arXiv: 0006240 [astro-ph].
- Oltmans, J et al. (2001). "Ozone in the Pacific tropical troposphere from ozonesonde observations". In: *Journal of Geophysical Research* 106.D23, pp. 32503–32525.
- Gloudemans, Annemieke et al. (2006). "Evidence for long-range transport of carbon monoxide in the Southern Hemisphere from SCIAMACHY observations". In: *European Space Agency, (Special Publication)* 33.SP-636, pp. 1–5. ISSN: 03796566. DOI: 10.1029/2006GL026804.
- Edwards, D. P. et al. (2006). "Satellite-observed pollution from Southern Hemisphere biomass burning". In: *Journal of Geophysical Research* 111.14, pp. 1–17. ISSN: 01480227. DOI: 10.1029/2005JD006655.
- Pak, B.C.a et al. (2003). "Measurements of biomass burning influences in the troposphere over southeast Australia during the SAFARI 2000 dry season campaign". In: *Journal of Geophysical Research* 108.13, pp. 1–10. ISSN: 0148-0227. DOI: 10.1029/2002JD002343. URL: <http://www.scopus.com/inward/record.url?eid=2-s2.0-0742322536&partnerID=40&md5=cafaeef03b948fb456696583ed3ab9a5>.
- Liu, Junhua et al. (2016a). "Causes of interannual variability of tropospheric ozone over the Southern Ocean". In: *Atmospheric Chemistry and Physics Discussions* October, pp. 1–46. ISSN: 1680-7316. DOI: 10.5194/ACP-2016-692.

- Russell-Smith, Jeremy et al. (2007). "Bushfires 'down under': patterns and implications of contemporary Australian landscape burning". In: *International Journal of Wildland Fire* 16.4, p. 361. ISSN: 1049-8001. DOI: 10.1071/wf07018. URL: <https://www.researchgate.net/publication/228969191> Bushfires 'down under' Patterns and implications of contemporary Australian landscape burning.
- Huang, Guanyu et al. (2018). "Validation of 10-year SAO OMI Ozone Profile (PROFOZ) Product Using Aura MLS Measurements". In: *Atmospheric Measurement Techniques* 11, pp. 17–32. ISSN: 1867-8610. DOI: 10.5194/amt-11-17-2018. URL: <https://www.atmos-meas-tech.net/11/17/2018/amt-11-17-2018.pdf>.
- Zeng, Guang et al. (2017). "Attribution of recent ozone changes in the Southern Hemisphere mid-latitudes using statistical analysis and chemistry-climate model simulations". In: *Atmospheric Chemistry and Physics* 17.17, pp. 10495–10513. ISSN: 16807324. DOI: 10.5194/acp-17-10495-2017.
- Alexander, S. P. et al. (2013). "High resolution VHF radar measurements of tropopause structure and variability at Davis, Antarctica (69 S, 78 E)". In: *Atmospheric Chemistry and Physics* 13.6, pp. 3121–3132. ISSN: 16807324. DOI: 10.5194/acp-13-3121-2013. URL: <http://www.atmos-chem-phys.net/13/3121/2013/>.
- Škerlak, B, M Sprenger, and H Wernli (2014). "A global climatology of stratosphere-troposphere exchange using the ERA-Interim data set from 1979 to 2011". In: *Atmospheric Chemistry and Physics* 14.2, pp. 913–937. DOI: 10.5194/acp-14-913-2014. URL: <http://www.atmos-chem-phys.net/14/913/2014/>.
- Emmerson, Kathryn M et al. (2019). "Sensitivity of isoprene emissions to drought over south-eastern Australia : Integrating models and satellite observations of soil moisture". In: *Atmospheric Environment* 209.April, pp. 112–124. ISSN: 1352-2310. DOI: 10.1016/j.atmosenv.2019.04.038. URL: <https://doi.org/10.1016/j.atmosenv.2019.04.038>.
- Stavrakou, T et al. (2009). "Evaluating the performance of pyrogenic and biogenic emission inventories against one decade of space-based formaldehyde columns". In: *Atmospheric Chemistry and Physics* 9.3, pp. 1037–1060. DOI: 10.5194/acp-9-1037-2009. URL: <http://dx.doi.org/10.5194/acp-9-1037-2009>.
- Palmer, Paul I et al. (2001). "Air mass factor formulation for spectroscopic measurements from satellites' Application to formaldehyde retrievals from the Global Ozone Monitoring Experiment". In: *Journal of Geophysical Research* 106.D13.
- Eskes, HJ and K F Boersma (2003). "Averaging kernels for DOAS total-column satellite retrievals". In: *Atmospheric Chemistry and Physics* 3.1, pp. 1285–1291. ISSN: 1680-7324. DOI: 10.5194/acp-3-1285-2003. URL: <http://dx.doi.org/10.5194/acpd-3-895-2003>.
- Lamsal, L N et al. (2014). "Evaluation of OMI operational standard NO₂ column retrievals using in situ and surface-based NO₂ observations". In: *Atmos. Chem. Phys* 14, pp. 11587–11609. DOI: 10.5194/acp-14-11587-2014. URL: www.atmos-chem-phys.net/14/11587/2014/.
- Leue, C et al. (2001). "Quantitative analysis of {NO} x emissions from Global Ozone Monitoring Experiment satellite image sequences". In: *J. Geophys. Res.* 106.D6, p. 5493. DOI: 10.1029/2000jd900572. URL: <http://dx.doi.org/10.1029/2000jd900572>.

- Martin, Randall V et al. (2002b). "Interpretation of TOMS observations of tropical tropospheric ozone with a global model and in situ observations". In: 107. DOI: 10.1029/2001JD001480.
- Goldberg, Daniel L. et al. (2017). "A high-resolution and observationally constrained OMI NO₂ satellite retrieval". In: *Atmospheric Chemistry and Physics* 17.18, pp. 11403–11421. ISSN: 16807324. DOI: 10.5194/acp-17-11403-2017.
- Ahn, Changwoo, Omar Torres, and Pawan K. Bhartia (2008). "Comparison of Ozone Monitoring Instrument UV Aerosol Products with Aqua/Moderate Resolution Imaging Spectroradiometer and Multiangle Imaging Spectroradiometer observations in 2006". In: *Journal of Geophysical Research Atmospheres* 113.16, pp. 1–13. ISSN: 01480227. DOI: 10.1029/2007JD008832.
- Texeira, Joao (2013). *AIRS/Aqua L3 Daily Standard Physical Retrieval (AIRS-only) 1 degree x 1 degree V006*: Accessed 2/Dec/2015. DOI: doi:10.5067/AQUA/AIRS/DATA303.
- Vasilkov, A et al. (2017). "Accounting for the effects of surface BRDF on satellite cloud and trace-gas retrievals: a new approach based on geometry-dependent Lambertian equivalent reflectivity applied to OMI algorithms". In: *Atmospheric Measurement Techniques* 10.1, pp. 333–349. DOI: 10.5194/amt-10-333-2017. URL: <http://www.atmos-meas-tech.net/10/333/2017/>.
- Vigouroux, C. et al. (2009). "Ground-based FTIR and MAX-DOAS observations of formaldehyde at Réunion Island and comparisons with satellite and model data". In: *Atmospheric Chemistry and Physics Discussions* 9, pp. 15891–15957. ISSN: 1680-7316. DOI: 10.5194/acpd-9-15891-2009.
- Dee, D P et al. (2011). "The ERA-Interim reanalysis: configuration and performance of the data assimilation system". In: *Quarterly Journal of the Royal Meteorological Society* 137.656, pp. 553–597. ISSN: 1477-870X. DOI: 10.1002/qj.828. URL: <http://dx.doi.org/10.1002/qj.828>.
- Paton-Walsh, C et al. (2017). "The MUMBA campaign: measurements of urban, marine and biogenic air Clare". In: *Earth system science data*, pp. 349–362.
- Guérette, Elise-Andrée et al. (2018). "Emissions of trace gases from Australian temperate forest fires: emission factors and dependence on modified combustion efficiency". In: *Atmospheric Chemistry and Physics* 18.5, pp. 3717–3735. ISSN: 1680-7324. DOI: 10.5194/acp-18-3717-2018. URL: <https://www.atmos-chem-phys.net/18/3717/2018/>.
- Dunne, Erin et al. (2018). "Comparison of VOC measurements made by PTR-MS, adsorbent tubes-GC-FID-MS and DNPH derivatization-HPLC during the Sydney Particle Study, 2012: A contribution to the assessment of uncertainty in routine atmospheric VOC measurements". In: *Atmospheric Measurement Techniques* 11.1, pp. 141–159. ISSN: 18678548. DOI: 10.5194/amt-11-141-2018. URL: <https://www.atmos-meas-tech.net/11/141/2018/amt-11-141-2018.pdf>.
- Cheng, M et al. (2016). "Factors controlling volatile organic compounds in dwellings in Melbourne, Australia". In: *Indoor Air* 26.2, pp. 219–230. DOI: 10.1111/ina.12201. URL: <https://onlinelibrary.wiley.com/doi/abs/10.1111/ina.12201>.
- Lawson, S. J. et al. (2015). "Seasonal in situ observations of glyoxal and methylglyoxal over the temperate oceans of the Southern Hemisphere". In: *Atmospheric Chemistry and Physics* 15.1, pp. 223–240. ISSN: 1680-7324. DOI: 10.5194/acp-15-223-2015. URL: <http://www.atmos-chem-phys.net/15/223/2015/>.

- ABS (2013). *Melbourne population*. URL: [http://www.abs.gov.au/ausstats/abs@.nsf/Previousproducts/3218.0>MainFeatures52012-13?opendocument&tabname=Summary&prodno=3218.0&issue=2012-13&num={\&}view="](http://www.abs.gov.au/ausstats/abs@.nsf/Previousproducts/3218.0>MainFeatures52012-13?opendocument&tabname=Summary&prodno=3218.0&issue=2012-13&num={\&}view=) (visited on 05/10/2017).
- Deeter, M. N. (2002). *Calculation and application of MOPITT averaging kernels*. URL: <https://www.acom.ucar.edu/mopitt/avg\krnl\app.pdf> (visited on 09/20/2004).
- Schenkeveld, V. M. Erik et al. (2017). "In-flight performance of the Ozone Monitoring Instrument". In: *Atmospheric Measurement Techniques* 10.5, pp. 1957–1986. ISSN: 1867-8548. DOI: 10.5194/amt-10-1957-2017. URL: <http://www.atmos-meas-tech-discuss.net/amt-2016-420/> <https://www.atmos-meas-tech.net/10/1957/2017/>.
- Wikipedia (2016). *Solar zenith angle*. DOI: 10.1016/B978-012369407-2/50005-X.. URL: <http://sacs.aeronomie.be/info/sza.php>.
- Kurosu, T and K Chance (2014). *OMIReadme*. URL: https://www.cfa.harvard.edu/atmosphere/Instruments/OMI/PGEReleases/READMEs/OMHCHO__v3.0.pdf.
- Barkley, Michael P. et al. (2013). "Top-down isoprene emissions over tropical South America inferred from SCIAMACHY and OMI formaldehyde columns". In: *Journal of Geophysical Research Atmospheres* 118.12, pp. 6849–6868. ISSN: 21698996. DOI: 10.1002/jgrd.50552. URL: <http://dx.doi.org/10.1002/jgrd.50552>.
- Instrument, O M I (2002). "OMI Algorithm Theoretical Basis Document Volume I". In: I.August, pp. 1–50.
- Spurr, R.J.D., T.P. Kurosu, and K.V. Chance (2001). "A linearized discrete ordinate radiative transfer model for atmospheric remote-sensing retrieval". In: *Journal of Quantitative Spectroscopy and Radiative Transfer* 68.6, pp. 689–735. DOI: 10.1016/S0022-4073(00)00055-8. URL: <https://www.sciencedirect.com/science/article/pii/S0022407300000558>.
- Martin, Randall V. et al. (2002a). "An improved retrieval of tropospheric nitrogen dioxide from GOME". In: *Journal of Geophysical Research D: Atmospheres* 107.20. ISSN: 01480227. DOI: 10.1029/2001JD001027.
- Abad, Gonzalo González et al. (2016). "Smithsonian Astrophysical Observatory Ozone Mapping and Profiler Suite (SAO OMPS) formaldehyde retrieval". In: *Atmospheric Measurement Techniques* 9.7, pp. 2797–2812. ISSN: 18678548. DOI: 10.5194/amt-9-2797-2016.
- Chen, D. et al. (2009). "Regional CO pollution in China simulated by the high-resolution nested-grid GEOS-Chem model". In: *Atmospheric Chemistry and Physics Discussions* 9.2, pp. 5853–5887. ISSN: 1680-7324. DOI: 10.5194/acpd-9-5853-2009. URL: <http://dx.doi.org/10.5194/acpd-9-3825-2009>.
- Giglio, Louis, James T. Randerson, and Guido R. Van Der Werf (2013). "Analysis of daily, monthly, and annual burned area using the fourth-generation global fire emissions database (GFED4)". In: *Journal of Geophysical Research* 118.1, pp. 317–328. ISSN: 21698961. DOI: 10.1002/jgrg.20042.
- Wuebbles, Donald J and Katharine Hayhoe (2002). "Atmospheric methane and global change". In: *Earth-Science Reviews* 57.3-4, pp. 177–210. ISSN: 0012-8252. DOI: 10.1016/S0012-8252(01)00062-9. URL: <https://www.sciencedirect.com/science/article/pii/S0012825201000629?via%3Dihub>.

- Horowitz, Larry W. et al. (1998). "Export of reactive nitrogen from North America during summertime: Sensitivity to hydrocarbon chemistry". In: *Journal of Geophysical Research* 103.D11, pp. 13451–13476. ISSN: 0148-0227. DOI: 10.1029/97JD03142. URL: <http://doi.wiley.com/10.1029/97JD03142><http://www.agu.org/pubs/crossref/1998/97JD03142.shtml>.
- Crounse, John D et al. (2011). "Peroxy radical isomerization in the oxidation of isoprene". In: *Physical Chemistry Chemical Physics* 13.30, pp. 13607–13613. ISSN: 1463-9076. DOI: doi:10.1039/c1cp21330j. URL: <http://dx.doi.org/10.1039/C1CP21330J>.
- Jozef, Peeters et al. (2014). "Hydroxyl Radical Recycling in Isoprene Oxidation Driven by Hydrogen Bonding and Hydrogen Tunneling: The Upgraded LIM1 Mechanism". In: *Journal of Physical Chemistry*.
- Taraborrelli, D. et al. (2012). "Hydroxyl radical buffered by isoprene oxidation over tropical forests". In: *Nature Geoscience* 5.3, pp. 190–193. ISSN: 17520894. DOI: 10.1038/ngeo1405. URL: <http://dx.doi.org/10.1038/ngeo1405><https://www.nature.com/articles/ngeo1405.pdf>.
- Niinemets, U. et al. (1999). "A model of isoprene emission based on energetic requirements for isoprene synthesis and leaf photosynthetic properties for Liquidambar and Quercus". In: *Plant, Cell and Environment* 22.11, pp. 1319–1335. ISSN: 01407791. DOI: 10.1046/j.1365-3040.1999.00505.x.
- Bank, World. *World Bank Nitrogen Oxide Emissions*. URL: <https://data.worldbank.org/indicator/EN.ATM.NOXE.AG.ZS>.
- Eastham, Sebastian D., Debra K. Weisenstein, and Steven R H Barrett (2014). "Development and evaluation of the unified tropospheric-stratospheric chemistry extension (UCX) for the global chemistry-transport model GEOS-Chem". In: *Atmospheric Environment* 89, pp. 52–63. ISSN: 13522310. DOI: 10.1016/j.atmosenv.2014.02.001. URL: <http://dx.doi.org/10.1016/j.atmosenv.2014.02.001>.
- Spurr, R. J D (2002). "Simultaneous derivation of intensities and weighting functions in a general pseudo-spherical discrete ordinate radiative transfer treatment". In: *Journal of Quantitative Spectroscopy and Radiative Transfer* 75.2, pp. 129–175. ISSN: 00224073. DOI: 10.1016/S0022-4073(01)00245-X.
- Martin, Randall V et al. (2003). "Global inventory of nitrogen oxide emissions constrained by space-based observations of NO₂ columns". In: 108.2, pp. 1–12. DOI: 10.1029/2003JD003453.
- De Smedt, I et al. (2008). "Twelve years of global observations of formaldehyde in the troposphere using GOME and SCIAMACHY sensors". In: *Atmos. Chem. Phys.* 8.16, pp. 4947–4963. ISSN: 1680-7324. DOI: 10.5194/acp-8-4947-2008. URL: <http://www.atmos-chem-phys.net/8/4947/2008/>.
- De Smedt, I. et al. (2012). "Improved retrieval of global tropospheric formaldehyde columns from GOME-2/MetOp-A addressing noise reduction and instrumental degradation issues". In: *Atmospheric Measurement Techniques* 5.11, pp. 2933–2949. ISSN: 18671381. DOI: 10.5194/amt-5-2933-2012. URL: <https://www.atmos-meas-tech.net/5/2933/2012/amt-5-2933-2012.pdf>.
- Shao, Yaping et al. (2007). "Numerical simulation of the October 2002 dust event in Australia". In: *J. Geophys. Res.* 112.D8. DOI: 10.1029/2006jd007767. URL: <http://dx.doi.org/10.1029/2006jd007767>.

- Carlisle, Wendy (2012). *The coal seam gas rush*. URL: <http://www.abc.net.au/news/2011-11-24/coal-seam-gas-by-the-numbers-map/3664318>.
- Liu, Zhen et al. (2017b). "Theoretically derived mechanisms of HPALD photolysis in isoprene oxidation". In: *Physical Chemistry Chemical Physics* 19.13, pp. 9096–9106. ISSN: 14639076. DOI: 10.1039/c7cp00288b.
- Zhu, Lei et al. (2013). "Variability of HCHO over the Southeastern United States observed from space : Implications for VOC emissions". In: vol. 1.
- Zheng, Y. et al. (2015). "Relationships between photosynthesis and formaldehyde as a probe of isoprene emission". In: *Atmospheric Chemistry and Physics* 15.15, pp. 8559–8576. ISSN: 16807324. DOI: 10.5194/acp-15-8559-2015.
- Torres, Omar O. (2008). *OMI/Aura Near UV Aerosol Optical Depth and Single Scattering Albedo L3*. DOI: 10.5067/Aura/OMI/DATA3003. URL: https://disc.gsfc.nasa.gov/datasets/OMAERUVd__V003/summary (visited on 05/30/2019).
- Phillips, Frances et al. (2017). *Measurements of trace gases relevant to air quality in Western Sydney, Australia, from May 2016 to September 2017 as part of the Western Air Shed and Particulate Study for Sydney (WASPSS)*. DOI: 10.1594/PANGAEA.884317. URL: <https://doi.pangaea.de/10.1594/PANGAEA.884317> (visited on 05/30/2019).
- Winters, Anthony J et al. (2009). "Emissions of isoprene, monoterpene and short-chained carbonyl compounds from Eucalyptus spp. in southern Australia". In: *Atmospheric Environment* 43.19, pp. 3035–3043. ISSN: 13522310. DOI: 10.1016/j.atmosenv.2009.03.026.
- Abbot, Dorian S. (2003). "Seasonal and interannual variability of North American isoprene emissions as determined by formaldehyde column measurements from space". In: *Geophysical Research Letters* 30.17, pp. 1999–2002. ISSN: 0094-8276. DOI: 10.1029/2003GL017336. URL: <http://doi.wiley.com/10.1029/2003GL017336>.
- Curci, G. et al. (2010). "Estimating European volatile organic compound emissions using satellite observations of formaldehyde from the Ozone Monitoring Instrument". In: *Atmospheric Chemistry and Physics* 10.23, pp. 11501–11517. ISSN: 16807316. DOI: 10.5194/acp-10-11501-2010. URL: <https://www.atmos-chem-phys.net/10/11501/2010/acp-10-11501-2010.pdf>.
- Thomas, W et al. (1998). "Detection of biomass burning combustion products in Southeast Asia from backscatter data taken by the GOME spectrometer". In: *Geophysical Research Letters* 25.9, pp. 1317–1320. DOI: 10.1029/98GL01087. URL: <http://onlinelibrary.wiley.com/doi/10.1029/98GL01087/epdf>.
- Streets, David G et al. (2013). "Emissions estimation from satellite retrievals: A review of current capability". In: *Atmospheric Environment* 77, pp. 1011–1042. DOI: 10.1016/j.atmosenv.2013.05.051. URL: <http://dx.doi.org/10.1016/j.atmosenv.2013.05.051>.
- Kaiser, Jennifer et al. (2018). "High-resolution inversion of OMI formaldehyde columns to quantify isoprene emission on ecosystem-relevant scales: application to the southeast US". In: *Atmospheric Chemistry and Physics* 18.8, pp. 5483–5497. DOI: 10.5194/acp-18-5483-2018. URL: <https://www.atmos-chem-phys.net/18/5483/2018/acp-18-5483-2018.pdf>.
- Chance, K. et al. (2000). "Satellite observations of formaldehyde over North America from GOME". In: *Geophysical Research Letters* 27.21, pp. 3461–3464. ISSN: 00948276. DOI: 10.1029/2000GL011857. URL: <http://dx.doi.org/10.1029/2000gl011857>.

- Stavrakou, T. et al. (2015). "How consistent are top-down hydrocarbon emissions based on formaldehyde observations from GOME-2 and OMI?" English. In: *Atmospheric Chemistry and Physics* 15.20, pp. 11861–11884. ISSN: 1680-7324. DOI: 10.5194/acp-15-11861-2015. URL: <http://www.atmos-chem-phys.net/15/11861/2015/acp-15-11861-2015.html>.
- Keywood, MD, KM Emmerson, and MF Hibberd (2016). *Australia state of the environment 2016*. Canberra. DOI: 10.4226/94/58b65c70bc372. URL: <https://soe.environment.gov.au/theme/atmosphere>.
- Millet, Dylan B. et al. (2016). "Nighttime Chemistry and Morning Isoprene Can Drive Urban Ozone Downwind of a Major Deciduous Forest". In: *Environmental Science and Technology* 50.8, pp. 4335–4342. ISSN: 15205851. DOI: 10.1021/acs.est.5b06367. URL: <https://pubs.acs.org/doi/pdfplus/10.1021/acs.est.5b06367>.
- Greenslade, Jesse W et al. (2017). "Stratospheric ozone intrusion events and their impacts on tropospheric ozone in the Southern Hemisphere". In: *Atmospheric Chemistry and Physics*, pp. 1–33. URL: <https://www.atmos-chem-phys.net/17/10269/2017/acp-17-10269-2017.pdf>.
- Liu, Junhua et al. (2015). "Origins of tropospheric ozone interannual variation over Réunion: A model investigation". In: *Journal of Geophysical Research*, pp. 1–19. DOI: 10.1002/2015JD023981. URL: <http://onlinelibrary.wiley.com/doi/10.1002/2015JD023981/abstract>.
- Thompson, A. M. et al. (2014). "Tropospheric ozone increases over the southern Africa region: Bellwether for rapid growth in Southern Hemisphere pollution?" In: *Atmospheric Chemistry and Physics* 14.18, pp. 9855–9869. ISSN: 16807324. DOI: 10.5194/acp-14-9855-2014.
- Danielsen, Edwin F. (1968). *Stratospheric-Tropospheric Exchange Based on Radioactivity, Ozone and Potential Vorticity*. DOI: 10.1175/1520-0469(1968)025<0502:STEBOR>2.0.CO;2.
- Lefohn, Allen S. et al. (2011). "The importance of stratospheric-tropospheric transport in affecting surface ozone concentrations in the western and northern tier of the United States". In: *Atmospheric Environment* 45.28, pp. 4845–4857. ISSN: 13522310. DOI: 10.1016/j.atmosenv.2011.06.014. URL: <http://dx.doi.org/10.1016/j.atmosenv.2011.06.014>.
- Langford, A. O. et al. (2012). "Stratospheric influence on surface ozone in the Los Angeles area during late spring and early summer of 2010". In: *Journal of Geophysical Research* 117.3, pp. 1–17. ISSN: 01480227. DOI: 10.1029/2011JD016766.
- Zhang, L et al. (2014). "Sources contributing to background surface ozone in the {US} Intermountain West". In: *Atmospheric Chemistry and Physics* 14.11, pp. 5295–5309. DOI: 10.5194/acp-14-5295-2014. URL: <http://dx.doi.org/10.5194/acp-14-5295-2014>.
- Lin, Meiyun et al. (2012). "Springtime high surface ozone events over the western United States: Quantifying the role of stratospheric intrusions". In: *Journal of Geophysical Research* 117.19, pp. 1–20. ISSN: 01480227. DOI: 10.1029/2012JD018151.
- Galani, E. (2003). "Observations of stratosphere-to-troposphere transport events over the eastern Mediterranean using a ground-based lidar system". In: *Journal of Geophysical Research* 108.D12, pp. 1–10. ISSN: 0148-0227. DOI: 10.1029/2002JD002596. URL: <http://www.agu.org/pubs/crossref/2003/2002JD002596.shtml>.

- Terao, Yukio et al. (2008). "Contribution of stratospheric ozone to the interannual variability of tropospheric ozone in the northern extratropics". In: *Journal of Geophysical Research* 113.D18. DOI: 10.1029/2008jd009854. URL: <http://dx.doi.org/10.1029/2008jd009854>.
- Tang, Q. and M. J. Prather (2012). "Five blind men and the elephant: What can the NASA Aura ozone measurements tell us about stratosphere-troposphere exchange?" In: *Atmospheric Chemistry and Physics* 12.5, pp. 2357–2380. ISSN: 16807316. DOI: 10.5194/acp-12-2357-2012. URL: <http://dx.doi.org/10.5194/acpd-11-26897-2011>.
- Frey, W. et al. (2015). "The impact of overshooting deep convection on local transport and mixing in the tropical upper troposphere/lower stratosphere (UTLS)". In: *Atmospheric Chemistry and Physics* 15.11, pp. 6467–6486. ISSN: 1680-7324. DOI: 10.5194/acp-15-6467-2015. URL: <http://www.atmos-chem-phys.net/15/6467/2015/>.
- Das, Siddarth Shankar et al. (2016). "Influence of tropical cyclones on tropospheric ozone: possible implications". In: *Atmospheric Chemistry and Physics* 16, pp. 4837–4847. DOI: 10.5194/acp-16-4837-2016. URL: www.atmos-chem-phys.net/16/4837/2016/.
- Mihalikova, M et al. (2012). "Observation of a tropopause fold by MARA VHF wind-profiler radar and ozonesonde at Wasa, Antarctica: comparison with ECMWF analysis and a WRF model simulation". In: *Annales Geophysicae* 30.9, pp. 1411–1421. DOI: 10.5194/angeo-30-1411-2012. URL: <http://www.ann-geophys.net/30/1411/2012/>.
- Vaughan, G., J. D. Price, and A. Howells (1993). "Transport into the troposphere in a tropopause fold". In: *Quarterly Journal of the Royal Meteorological Society* 120.518, pp. 1085–1103. ISSN: 00359009. DOI: 10.1002/qj.49712051814.
- Beekmann, M. et al. (1997). "Regional and global tropopause fold occurrence and related ozone flux across the tropopause". In: *Journal of Atmospheric Chemistry* 28.1-3, pp. 29–44. ISSN: 01677764. DOI: 10.1023/A:1005897314623.
- Baray, J. L. et al. (2000). "Planetary-scale tropopause folds in the southern subtropics". In: *Geophysical Research Letters* 27.3, pp. 353–356. ISSN: 00948276. DOI: 10.1029/1999GL010788.
- Zanis, P. et al. (2014). "Summertime free-tropospheric ozone pool over the eastern Mediterranean/middle east". In: *Atmospheric Chemistry and Physics* 14.1, pp. 115–132. ISSN: 16807316. DOI: 10.5194/acp-14-115-2014.
- Akritidis, Dimitris et al. (2016). "On the role of tropopause folds in summertime tropospheric ozone over the eastern Mediterranean and the Middle East". In: *Atmospheric Chemistry and Physics* 16.21, pp. 14025–14039. DOI: 10.5194/acp-16-14025-2016. URL: <http://www.atmos-chem-phys.net/16/14025/2016/>.
- Tyrlis, Evangelos et al. (2014). "On the linkage between the Asian summer monsoon and tropopause fold activity over the eastern Mediterranean and the Middle East". In: *Journal of Geophysical Research* 119.6, pp. 3202–3221. ISSN: 2169897X. DOI: 10.1002/2013JD021113. URL: <http://doi.wiley.com/10.1002/2013JD021113>.

- Price, J. D. and G. Vaughan (1993). "The potential for stratosphere-troposphere exchange in cut-off-low systems". In: *Quarterly Journal of the Royal Meteorological Society* 119.510, pp. 343–365. DOI: 10.1002/qj.49711951007. URL: <http://onlinelibrary.wiley.com/doi/10.1002/qj.49711951007/abstract>.
- Wirth, Volkmar (1995). "Diabatic heating in an axisymmetric cut-off cyclone and related stratosphere-troposphere exchange". In: *Quarterly Journal of the Royal Meteorological Society* 121.521, pp. 127–147. ISSN: 00359009. DOI: 10.1002/qj.49712152107. URL: <http://doi.wiley.com/10.1002/qj.49712152107>.
- Trickl, T. et al. (2014). "How stratospheric are deep stratospheric intrusions?" In: *Atmospheric Chemistry and Physics* 14.18, pp. 9941–9961. ISSN: 16807324. DOI: 10.5194/acp-14-9941-2014.
- Mze, N. et al. (2010). "Climatology and comparison of ozone from ENVISAT/GOMOS and SHADOZ/balloon-sonde observations in the southern tropics". In: *Atmospheric Chemistry and Physics* 10.16, pp. 8025–8035. ISSN: 16807316. DOI: 10.5194/acp-10-8025-2010.
- Smit, Herman G J et al. (2007). "Assessment of the performance of ECC-ozonesondes under quasi-flight conditions in the environmental simulation chamber: Insights from the Juelich Ozone Sonde Intercomparison Experiment (JOSIE)". In: *Journal of Geophysical Research* 112.19, pp. 1–18. ISSN: 01480227. DOI: 10.1029/2006JD007308.
- WMO, World Meteorological Organization (1957). "Meteorology A Three-Dimensional Science". In: *Geneva, Second Session of the Commission for Aerology* 4, pp. 134–138.
- Bethan, S., G. Vaughan, and S. J. Reid (1996). "A comparison of ozone and thermal tropopause heights and the impact of tropopause definition on quantifying the ozone content of the troposphere". In: *Quarterly Journal of the Royal Meteorological Society* 122.532, pp. 929–944. ISSN: 00359009. DOI: 10.1002/qj.49712253207. URL: <http://doi.wiley.com/10.1002/qj.49712253207>.
- Tomikawa, Yoshihiro, Yashiro Nishimura, and Takashi Yamanouchi (2009). "Characteristics of Tropopause and Tropopause Inversion Layer in the Polar Region". In: *SOLA* 5, pp. 141–144. DOI: 10.2151/sola.2009-036. URL: <http://dx.doi.org/10.2151/sola.2009-036>.
- Lelieveld, Jos and Frank J. Dentener (2000). "What controls tropospheric ozone?" In: *Journal of Geophysical Research* 105.D3, pp. 3531–3551. ISSN: 01480227. DOI: 10.1029/1999JD901011. URL: <http://doi.wiley.com/10.1029/1999JD901011>.
- Struthers, H. et al. (2004). "Past and future simulations of NO₂ from a coupled chemistry-climate model in comparison with observations". In: *Atmospheric Chemistry and Physics* 4.8, pp. 2227–2239. ISSN: 1680-7324. DOI: 10.5194/acp-4-2227-2004. URL: <http://www.atmos-chem-phys.net/4/2227/2004/>.
- Bey, Isabelle et al. (2001). "Global Modeling of Tropospheric Chemistry with Assimilated Meteorology: Model Description and Evaluation". In: *Journal of Geophysical Research* 106, pp. 73–95. ISSN: 0148-0227. DOI: 10.1029/2001JD000807.
- Rienecker, Michele (2007). "File Specification for GEOS-5 DAS Gridded Output". In: pp. 1–54. URL: https://gmao.gsfc.nasa.gov/products/documents/GEOS-5.1.0__File__Specification.pdf.
- Press, William H et al. (1992). *Numerical Recipes in C (2Nd Ed.): The Art of Scientific Computing*. New York, NY, USA: Cambridge University Press. ISBN: 0-521-43108-5.

- Tang, Q. and M. J. Prather (2010). "Correlating tropospheric column ozone with tropopause folds: The Aura-OMI satellite data". In: *Atmospheric Chemistry and Physics* 10.19, pp. 9681–9688. ISSN: 16807316. DOI: 10.5194/acp-10-9681-2010.
- Jaffe, Daniel a. and Nicole L. Wigder (2012). "Ozone production from wildfires: A critical review". In: *Atmospheric Environment* 51, pp. 1–10. ISSN: 13522310. DOI: 10.1016/j.atmosenv.2011.11.063. URL: <http://dx.doi.org/10.1016/j.atmosenv.2011.11.063>.
- Edwards, D. P. (2003). "Tropospheric ozone over the tropical Atlantic: A satellite perspective". In: *Journal of Geophysical Research* 108.D8, p. 4237. ISSN: 0148-0227. DOI: 10.1029/2002JD002927. URL: <http://doi.wiley.com/10.1029/2002JD002927>.
- Sinha, Parikhit et al. (2004). "Transport of biomass burning emissions from southern Africa". In: *Journal of Geophysical Research* 109, p. D20204. ISSN: 01480227. DOI: 10.1029/2004JD005044.
- Mari, C H et al. (2008). "Tracing biomass burning plumes from the Southern Hemisphere during the AMMA 2006 wet season experiment, Atmos". In: *Atmospheric Chemistry and Physics* 8, pp. 3951–3961. ISSN: 1680-7324. DOI: 10.5194/acpd-7-17339-2007.
- Reutter, P. et al. (2015). "Stratosphere-troposphere exchange (STE) in the vicinity of North Atlantic cyclones". In: *Atmospheric Chemistry and Physics* 15.19, pp. 10939–10953. ISSN: 16807324. DOI: 10.5194/acp-15-10939-2015.
- Škerlak, Bojan et al. (2015). "Tropopause folds in ERA-Interim: Global climatology and relation to extreme weather events". In: *Journal of Geophysical Research* 120.10, pp. 4860–4877. ISSN: 21698996. DOI: 10.1002/2014JD022787.
- Wauben, Wiel M F, J Paul F Fortuin, and Peter F J Van Velthoven (1998). "Comparison of modeled ozone distributions observations". In: *Journal of Geophysical Research* 103, pp. 3511–3530.
- Hu, Lu et al. (2017). "Global budget of tropospheric ozone: evaluating recent model advances with satellite (OMI), aircraft (IAGOS), and ozonesonde observations". In: *Atmospheric Environment*, pp. 1–36. DOI: 10.1016/j.atmosenv.2017.08.036.
- Roelofs, Geert Jan and Jos Lelieveld (1997). *Model study of the influence of cross-tropopause O₃ transports on tropospheric O₃ levels*. DOI: 10.1034/j.1600-0889.49.issue1.3.x.
- Elbern, H, J Hendricks, and A Ebel (1998). "A Climatology of Tropopause Folds by Global Analyses". In: *Theoretical and Applied Climatology* 59.3, pp. 181–200. ISSN: 1434-4483. DOI: 10.1007/s007040050023. URL: <http://dx.doi.org/10.1007/s007040050023>.
- Olsen, Mark a. (2003). "A comparison of Northern and Southern Hemisphere cross-tropopause ozone flux". In: *Geophysical Research Letters* 30.7, p. 1412. ISSN: 0094-8276. DOI: 10.1029/2002GL016538. URL: <http://doi.wiley.com/10.1029/2002GL016538>.
- Pegoraro, E. et al. (2004). "Effect of drought on isoprene emission rates from leaves of *Quercus virginiana* Mill." In: *Atmospheric Environment* 38.36, pp. 6149–6156. ISSN: 13522310. DOI: 10.1016/j.atmosenv.2004.07.028. URL: <http://linkinghub.elsevier.com/retrieve/pii/S1352231004007198>.
- Chen, Fei and Jimy Dudhia (2001). "Coupling an Advanced Land Surface–Hydrology Model with the Penn State–NCAR MM5 Modeling System. Part I: Model Implementation and Sensitivity". In: *Monthly Weather Review* 129. URL: <https://journals>.

[ametsoc.org/doi/pdf/10.1175/1520-0493\(2001\)291293C0569\(%\)3ACAALSH\(%\)3E2.0.CO\(%\)3B2](https://ametsoc.org/doi/pdf/10.1175/1520-0493(2001)291293C0569(%)3ACAALSH(%)3E2.0.CO(%)3B2).